Local Chemical Properties of Nanostructured Au-Pd Bimetal Model Catalysts

Dissertation

zur Erlangung des Doktorgrades Dr. rer. nat.
der Fakultät für Naturwissenschaften
der Universität Ulm

vorgelegt von

Martin Ruff
aus Herbrechtingen

2000

Amtierender Dekan:	Prof. Dr. Othmar Marti
1. Gutachter:	Prof. Dr. Dieter M. Kolb
2. Gutachter:	Prof. Dr. Hartmut Jex
3. Gutachter:	Prof. Dr. Rolf Jürgen Behm
Tag der Promotion:	3. Juli 2000

Für Anita

Contents

Introduction **vii**

I Methods and experimental details 1

1 Experimental methods **3**
1.1 Scanning tunneling microscopy (STM) 3
1.2 High resolution electron energy loss spectroscopy (HREELS) . . . 8
1.3 X-ray photoelectron spectroscopy (XPS) and Auger electron spectroscopy (AES) 13

2 Experimental details **17**
2.1 Design of the sample holder 23
2.2 TPD system 24
2.3 Sample preparation 26

II Growth and alloying of Au on Pd(111) 29

3 Au growth on Pd(111) **33**
3.1 Submonolayer Au films 35
3.1.1 Qualitative aspects 35
3.1.2 Determination of the Au adatom diffusion barrier on Pd(111) 42
3.2 Monolayer and multilayer Au films 45
3.2.1 Morphology of 1 ML Au for different deposition temperatures 45
3.2.2 Multilayer Au/Pd(111) films: Morphology and strain relief patterns 49
3.3 Conclusions: Au growth on Pd(111) 55

4 AuPd(111) surface alloy formation **57**
4.1 Annealing of partially Au covered Pd(111) 60
4.1.1 Changes in film morphology by annealing 60
4.1.2 Au-Pd(111) intermixing behaviour on the atomic scale . . 70

4.2 Annealing of completely Au covered Pd(111) 80
4.2.1 Changes in film morphology by annealing 81
4.2.2 Au-Pd(111) intermixing behaviour on the atomic scale . . 83
4.3 Au deposition at elevated temperatures 86
4.4 Element distribution in the surface 92
4.5 Interdiffusion kinetics 96
4.6 Conclusions: AuPd(111) surface alloy formation 106

III Adsorption and reaction on Au-Pd surfaces 111

5 CO/Au-Pd surfaces 113
5.1 Earlier results for CO adsorption 113
5.1.1 Theory: The nature of the metal–CO bond 114
5.1.2 Earlier experimental studies 120
5.2 TPD results 137
5.2.1 CO adsorption on Pd(111) 138
5.2.2 CO adsorption on layered Au/Pd(111) surfaces 141
5.2.3 CO adsorption on AuPd(111) surface alloys 150
5.2.4 Quantitative evaluation of the TPD spectra 158
5.3 HREELS results: CO/Au-Pd(111) surfaces 178
5.3.1 CO adsorption on Pd(111) 178
5.3.2 CO adsorption on layered Au/Pd(111) surfaces 184
5.3.3 CO adsorption on AuPd(111) surface alloys 195
5.4 HREELS results: CO/Pd-Au(110) surfaces 209
5.5 Conclusions: CO adsorption on Au-Pd(111) surfaces 215

6 C_2H_4/ Au-Pd(111) surfaces 219
6.1 Earlier studies on C_2H_4/Pd 219
6.1.1 General aspects of C_2H_4 chemisorption and decomposition reactions 220
6.1.2 Earlier experimental results for C_2H_4/Pd 222
6.2 TPD results 230
6.3 HREELS results 237
6.3.1 C_2H_4 adsorption and decomposition on Pd(111) 237
6.3.2 C_2H_4 adsorption and decomposition on AuPd(111) surface alloys 244
6.3.3 C_2H_4 adsorption on completely Au covered Pd(111) 251
6.4 XPS results 254
6.5 STM results 255
6.6 Discussion and concluding remarks 259

Resume 269

Zusammenfassung **271**

Acknowledgments/Danksagung **277**

Bibliography **279**

List of Figures **297**

List of Tables **299**

List of Appreviations **303**

List of STM Images **305**

Curriculum Vitae **309**

Introduction

The interaction between molecules and metal surfaces constitues an important topic in the current physical and chemical research. One of the reasons for this can be found in the economic importance of heterogeneously catalysed reactions, which, to a large part, are governed by chemisorption phenomena. Taking into account, that about 20% of the world gross national product depends on heterogeneous catalysis [1], it becomes obvious that even small improvements of catalytic processes might have a tremendous economic impact.

Atomic scale investigations of adsorption phenomena are interesting not only with respect to possible applications, but also from an academic point of view. From the perspective of solid state physics, crystal surfaces can be regarded as defects because of the reduced symmetry that is encountered at surfaces. For this reason, the theoretical concepts used in solid state physics, which take advantage of the crystal symmetry might not be applicable to describe surface phenomena. On the other hand, any microscopic theory describing the properties of matter in the solid state has also to account for phenomena that take place at non-ideal sites of the solid, especially at its surface. As has been shown by many studies in the past and as should be emphasized also in the present work, modern experimental surface science methods are able to provide a very detailed understanding of the processes occuring at surfaces. Hence, by experimental investigations of surface properties testing benchmarks for theoretical concepts become available, and the understanding of fundamental properties of matter can be deepened.

The aim of this work is to gain insight into the atomic mechanisms that govern chemisorption and reaction processes occuring on bimetallic surfaces. Catalysts often contain two or even more metallic components, because it has been found for many heterogeneously catalysed reactions, that the activity (the number of converted molecules per unit time and per unit metal surface area) and, often more important, the selectivity (the number of the desired molecular products relative to the total conversion rate) can be improved by using alloy particles. Besides the small metallic particles with typical sizes of only a few nm, a real catalyst contains also other components that may be decisive for its performance. Usually, the metal particles are dispersed over the surface of a high area support, often oxides such as SiO_2, Al_2O_3, or MgO. Also so-called promoters, for instance alkali metals, may be added to the catalyst, either merely to stabilize the active

metal particles or as participants in the catalytic processes. It is obvious that a real catalyst constitutes a very complex system containing many parameters, that are difficult to investigate experimentally with sufficient precision. Even if detailed knowledge about the catalyst's structure and microscopic composition was obtainable, there would still remain the difficulty to draw conclusions from the observed overall catalytic behaviour to the role of the different available reaction sites. Taking a bimetallic catalyst as an example, the metal particles might expose several different low index crystal faces to the gas phase. On each of these crystal faces a large number of different local arrangements of the two elements is possible. Furthermore, a high amount of defect sites, like edge or corner atoms, exists on small particles. These defect sites can again consist of different atoms. There is no doubt, that the interpretation of experiments which are performed using real catalysts (or dispersed model catalysts) has to be backed by a detailed knowledge of the processes that are taking place on the different metal surfaces present in the catalyst.

A first step to reach this knowledge consists in investigations carried out on well-defined single crystalline surfaces. As reflected by the division of the experimental results that were obtained in this work into two parts — one concerning the preparation of the Au-Pd(111)surfaces[1] and the other on the adsorption and reaction properties of these surfaces — it is a formidable task to prepare and analyse bimetallic surfaces in a way, where all chemically important parameters (surface composition, distribution of the elements in the surface layer, abundance of defect sites like steps, etc.) are determined. For this purpose, the possibility to obtain real-space images of the surface with atomic precision, that is provided by scanning tunneling microscopy (STM), is of inestimable value. For instance, since no long range order is observed in AuPd(111) surface alloys, STM is the only experimental method that is capable of determining the local composition of the surface layer on the atomic scale. The combination of STM with the powerful spectroscopic tools of high resolution electron energy loss spectroscopy (HREELS) and temperature programmed desorption spectroscopy (TPD) provides the unique capability to investigate the local chemical properties of disordered surface alloys[2]. This work provides one of the first examples where variable temperature STM, HREELS, and TPD were combined in one UHV apparatus and where the STM characterization and the chemical investigations could be carried out on indentical surfaces. The price that has to be paid for this variety of experimental methods consists in several compromises on the design of the measuring setup, especially the sample holder.

[1]The nomenclature that is used in the present work to denote the different types of Au-Pd(111) surfaces will be explained on page 31.

[2]The investigation of alloy surfaces would be largely equivalent, but by using bulk alloys more constraints are imposed on the available surface compositions compared to the preparation of surface alloys by a deposition-annealing procedure as applied in this work.

The system Au-Pd has been chosen for various reasons. First, Au-Pd catalysts are used in the chemical industry for certain partial oxidation reactions of ethylene [2–5]. They are also promising candidates as fuel cell anode catalyst for the oxidation of H_2 in the presence of trace CO contaminations [6]. Therefore, in the "chemical" part of this thesis, C_2H_4 and CO will be used as probe molecules to investigate the chemical activity of bimetallic Au-Pd(111) surfaces. Second, with Au being chemically inert and Pd being reactive, the interpretation of chemical processes on bimetallic Au-Pd surfaces should be facilitated. Third, the investigation of the alloy formation process starting from Au/Pd(111) films, may be considered as a prototype study on near surface metal interdiffusion that gives insight into the atomic processes occuring at a close-packed interface of two completely miscible metals. Fourth, Au itself is increasingly considered as metal with interesting catalytic properties. Especially for the low temperature oxidation of CO, oxide supported Au catalysts are already commercially available [7]. Investigations on the chemical activity of pure Au films on Pd(111) with different morphological features, particularly with a highly different proportion of Au step edge sites, provide information on the nature of the active sites on Au catalysts. Considering the many-sidedness of problems that are to be investigated in this work, it could not be avoided to exceed the size, that would seem to be appropritate for a PhD thesis.

The thesis is devided into three parts. In the first part a short introduction is given into the experimental methods that were employed in this work. Also, the experimental setup and some technical aspects of the measurement equipment are explained. The second part deals with the results that were obtained for the Au-Pd(111) system. First, the growth of thin Au films on Pd(111) at $T \leq 400\,K$ is analysed. By measuring temperature dependent island densities the Au adatom diffusion barrier on Pd(111) is evaluated. Second, various aspects of the formation of AuPd(111) surface alloys are addressed in that part. Different mechanisms that lead to alloy formation are identified based on atomically resolved STM images. Also, the intermixing kinetics between Au and Pd is analysed by "time-resolved" Auger spectroscopy. One objective of the second part is to provide the information that is necessary to prepare specific Au-Pd(111) surfaces for subsequent adsorption and reaction studies. These are presented in the third part of this thesis. Using CO and C_2H_4 as probe molecules the chemical properties of AuPd(111) surface alloys with varied surface composition and of layered Au/Pd(111) surfaces with different film structures are investigated. A short section on CO adsorption investigations on Pd-Au(110) surfaces is added to the third part.

Part I

Methods and experimental details

Chapter 1

Principles of the experimental methods

In the following, the physical background of the main experimental methods that were applied in this work will be briefly outlined. Since the aim of these investigations was to gain maximum information about the investigated systems from a combination of several powerful experimental methods and since it was not intended to develop one of these methods beyond the level that had been reached by other experimental groups which concentrate on a single method, this chapter will be restricted to those aspects that are of immediate importance for the present work. LEED measurements have been preformed only as complementary experiments on some of the Au-Pd(111) surfaces, but they do not provide additional information to the STM results and are omitted in the presentation of the experimental data for the sake of brevity. Hence, an outline of the LEED method is not necessary. In the latest stages of the experimental time for this work it was possible to record TPD spectra. TPD is a conceptually very simple method and requires basically only an operating mass spectrometer. Therefore it is also omitted in this chapter. The main difficulty of TPD measurements is their interpretation, and this point will be thoroughly discussed in section 5.2.4. For the remaining experimental tools, several aspects of STM, HREELS, and the electron spectroscopies AES and XPS will be addressed in the following.

1.1 Scanning tunneling microscopy (STM)

The invention of STM by G. Binnig and H. Rohrer in the year 1981 marks the begin of a new era in surface science [8]. The fascination of this instrument, that might be ascribed to an unique combination of conceptual simplicity and general applicability, has attracted numerous researchers from different fields of science. The idea behind STM, using a sharp tip as a local probe, has triggered the evolution of a whole family of novel measurement methods, the Scanning Probe

Microscopes (SPMs), among which the Atomic Force Microscope (AFM) and the Scanning Near-field Optical Microscope (SNOM) might be the most important representatives. An introduction to these methods and several examples for their applications can be found, for instance, in a book by Wiesendanger [9].

The principle of STM can be explained with few words: Based on the quantum-mechanical tunnel effect, small particles are able to cross a "forbidden region". For instance, if two conducting materials are brought together in close proximity, separated only by a narrow (= few atomic distances) insulating gap ("tunnel gap", e. g., air or vacuum), it is possible for electrons to be transferred from one conductor to the other conductor, without being able to exist within the small gap. A "tunnel current" (I_t) will flow if a bias voltage (U_t) is applied between the two conductors. The magnitute of I_t is very sensitive to the width of the tunnel gap. For STM, this effect is applied in a system, where one of the conductors consists of a sharp metal tip, that is scanned over the second conductor — the sample surface. The tip is moved by a piezoelectric drive, which allows subatomic precision in the positioning of the tip. In the following x and y will span the scanning plane and z is the direction normal to the sample surface. The tunnel effect is exploited either to control the distance between tip and surface, using a feedback loop, such that a constant tunnel current is flowing ("constant current mode"), or to obtain a variable tunnel current as measurement signal by scanning the tip at constant z ("constant height mode"). In the constant current mode the voltage that is applied to the piezo element controlling the z position of the tip provides the measurement signal that contains information on the topography and possibly also on other features of the sample. Usually this voltage is mapped onto a colour scale, where brighter colours represent "higher" areas of the surface.

A more precise determination of the working principle of STM requires a theoretical description of the tunnel current between tip and sample. So far, it is not possible to predict the appearance of an arbitrary surface (e. g., a bimetallic surface) in STM images by theory, i. e., the experimental application of the STM method is far ahead of the quantitative explanation of the results by theory. The problem is inherent to the method itself, because of the strong dependence of the measurement results on the tip conditions. As an example, in atomically resolved STM images of AuPd(111) surface alloys the Pd atoms are reproducibly imaged brighter (=higher) than the Au atoms. However, the height difference between the two species is very sensitive to the condition of the tip, ranging from less than 0.1 Å to more than 1 Å in extreme cases. Therefore, a general theory of STM should be able to predict the former phenomenon (Pd reproducibly brighter than Au), but it can not be expected that the height difference is quantitatively predicted by theory.

Here is not the right place to discuss the different theoretical approaches to STM imaging, but at least one important result should be mentioned. Shortly

after the first reports on STM images from metals and semiconductors had been published, Tersoff and Hamann presented an approximate solution to the STM problem [10]. They assumed a spherically shaped tip (radius R, centre at $\vec{r}_0$) considering only s-type tip wave functions. In the limit of low temperatures and small applied bias voltages the following tunnel current can be obtained:

$$I_t \propto U_t \cdot n_t(E_F) \cdot e^{2\kappa R} \cdot \sum_{\nu} |\psi_\nu(\vec{r}_0)|^2 \cdot \delta(E_\nu - E_F) \tag{1.1}$$

with n_t being the density of states at the Fermi level for the tip and $\kappa = \sqrt{2m\Phi}/\hbar$ the decay rate of the wave functions in vacuum, where Φ is the effective local potential barrier height and m is the electron mass. Hence, the local density of states (LDOS) of the surface at the Fermi level ($n_s(E_F, \vec{r}_0)$), evaluated at the centre of the tip curvature, enters into the expression for $\mathrm{I_t}$:

$$n_s(E_F, \vec{r}_0) = \sum_{\nu} |\psi_\nu(\vec{r}_0)|^2 \cdot \delta(E_\nu - E_F). \tag{1.2}$$

With s being the distance between the front end of the tip and the surface (i. e., $s+R$ is the distance between the centre of the tip and the surface) and considering the exponential decay of the surface wave functions in vacuum it can be written:

$$|\psi_\nu(\vec{r}_0)|^2 \propto e^{-2\kappa(s+R)}. \tag{1.3}$$

Hence, the tunnel current from equation 1.1 depends exponentially on the tip–sample separation s:

$$I_t \propto e^{-2\kappa s}. \tag{1.4}$$

In the Tersoff-Hamann picture, the STM images represent contour maps of constant LDOS at E_F of the surface. In some cases this might be an appropriate description, but there are also severe limitations to this approach. First, equation 1.1 is only valid for small bias voltages. Second, for typical tip materials (W, Pt, Ir) the assumption of the tip states having only s-character is not valid. Third, in very close proximity between tip and sample the interaction between tip and sample atoms leads to dynamic changes of the tip and/or the sample structure, which might result in a significant enhancement of the atomic corrugation measured on the surface.

From the above short introduction to the principle of STM it should be obvious that STM images contain information of both the sample surface and the STM tip. A nice illustration of this point can be seen in fig. 1.1, where the same AuPd(111) surface alloy is imaged with two different tip conditions. In fig. 1.1(a) a monatomic sharp tip enables each atom to be imaged as an individual dot. On a homogeneous surface this would be difficult to prove, because it could not be

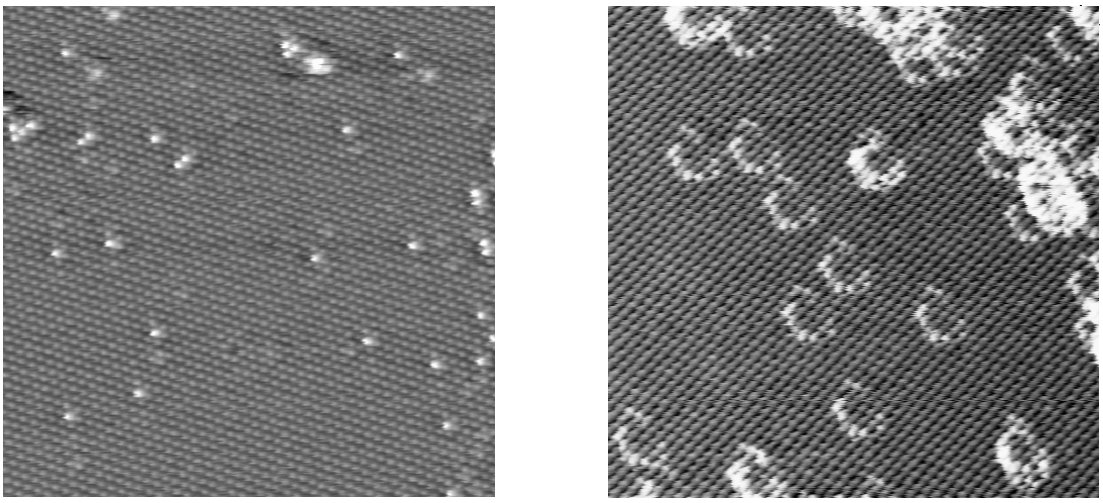

(a) atomically sharp tip; $I_t = 25\,nA$, $U_t = +1\,mV$; 130 Å × 130 Å

(b) tip with "ring structure"; $I_t = 32\,nA$, $U_t = +2\,mV$; 135 Å × 130 Å

Figure 1.1: STM images of two different areas on a dilute AuPd(111) surface alloy ($\sim 1\%$ Pd) recorded under low tunnel resistance conditions. Between the two images the tip configuration has changed markedly.

excluded that the periodic atomic-like structure is just the result of a superposition of images from a multiple tip. Only the fact that single impurity atoms (Pd) are imaged as individual structures, demonstrates true atomic resolution. This becomes clear if fig 1.1(b) is examined. Here, the Au atoms seem to form still an atomically resolved hexagonal lattice. But no individual Pd atoms are visible anymore. Ring-like structures are observed, which can be interpreted, however, as the images of Pd atoms. In this case, it would be even possible to extract information about the tip structure from the STM image by comparison with the atomically resolved surface. Hence, with small structures on the surface (here: Pd impurity atoms) it is in principle possible to obtain an "STM image" from a small part of the tip.

It is appropriate to concluded this section on the STM method by some comments about the possibility to distinguish atoms of different chemical nature in STM images, because an important part of the STM analysis of AuPd(111) surface alloys presented below relies on this so-called "chemical contrast". It might not be surprising that non-metallic surface atoms like O or S are easily distinguishable from substrate metal atoms because of their different electronic structure [11]. On the other hand, it is less clear whether the two metallic components of a bimetallic surface are imaged with a sufficiently large difference in

the apparent height to make them distinguishable in STM images. The number of bimetallic systems where this has been achieved in a reproducible manner (i. e., without requiring a non-metallic impurity atom to form the micro-tip) suggests that chemical contrast is a relatively general phenomenon. Three classes of systems exhibiting chemical contrast can be distinguished:

1. Chemical contrast is generally obtained in atomically resolved STM images with corrugation differences considerably above the differences of the atom sizes[1]. Here, the contrast is very sensitive to the tunnel parameters and might be reversed, i. e., the bigger atoms might appear lower. Examples: vide infra.

2. The different elements can be routinely distinguished, but the corrugation is only of the order of the atom size difference (Δd) with the larger atom appearing higher. Typical example: PbCu (Pb-Cu(111) [12] and Pb-Cu(100) [13, 14]) with Pb atoms being imaged $\sim 0.7\,$Å higher than Cu atoms; $\Delta d = 0.9\,$Å.

3. A distinct chemical contrast is only observed under special tip conditions, i. e., most likely with a non-metallic impurity atom forming the micro-tip. Examples: Au-Cu(100) [15] and Cu-Au(110) [16].

The present system (AuPd) clearly belongs to the first class, since in almost all STM images, that were recorded during this work and where individual atoms could be resolved, a distinction between Au and Pd was possible with the smaller element (Pd) being imaged brighter (i. e. higher). Other systems of this class are AuNi (Au-Ni(110) [17], Au-Ni(111) [18, 19], and Ni-Au(110) [20]) with Ni usually being imaged brighter, CuPd (Pd-Cu(100) [21] and Pd-Cu(111) [22]) with Pd imaged brighter, and PtRh ($Pt_{50}Rh_{50}$(100) [23, 24]) with Rh imaged brigher. From the comparison of the cases where noble metals are combined with elements from the Pt group (Ni, Pd, Pt) it seems to be a general observation that under high resolution tunnel conditions (i. e., small tip–sample separations due to high I_t and low U_t) the noble metals appear darker. Even though the Tersoff-Hamann approach might be questionable for very small tip–sample distances, it should be noted that this observation is in qualitative agreement with the prediction by equation 1.1, in so far as the noble metals exhibit only a low (bulk) LDOS at E_F due to the completely filled d bands. Of course, the latter argument suffers from the different decay rates of sp states and d states into vacuum, but since for the present purpose only atomically resolved images were considered with the tip in close proximity to the surface, the analogy to the bulk LDOS might be justified.

[1] To a first approximation the atom sizes of the constituents in binary alloys can be taken as the atom sizes of the pure metals (Vegard's law), i. e., the respective lattice nearest neighbour distances.

For PtRh bulk alloys the Tersoff-Hamann model was employed by Hofer and coworkers [24] to simulate STM scans over the surface. With the first-principles full-potential augmented plane waves (FLAPW) method the LDOS was calculated at variable distances (up to 5 Å) over the surface. The simulated apparent height difference between Pt and Rh atoms ((0.15 ± 0.02) Å, Rh brighter) is in good agreement with the measured value (0.22 Å) for an assumed tip–sample distance of 3 Å. In this case, it was found that the chemical contrast is largely caused by changes in the electronic structure of Pt and of Rh due to alloying. While the LDOS at E_F decreases for Pt, it increases for Rh in the alloy compared to the pure metals. Hence, the contrast should depend on the chemical environment of the atoms. For AuPd(111), however, there is no indication from experiment for such alloying effects, since the observed apparent height differences between Au and Pd atoms exhibit no correlation with the surface composition.

Finally, it should be noted that the above mentioned chemical contrast between Au and Pd atoms (Pd higher than Au) occurs mainly in high resolution images, whereas in images with higher tunnel resistances (i. e., with larger tip–sample separations) Au rich areas are usually imaged *higher* than Pd rich areas. For example, in Au aggregations at former Pd step edges, that are observed after submonolayer Au deposition, the Au area is imaged 0.1 Å – 0.2 Å higher than the neighbouring Pd terrace, which is close to the difference in step height of the (111) oriented surfaces of the pure metals (0.1 Å). From these considerations it can be concluded that great care has to be employed when interpreting STM images from bimetallic surfaces. General statements can be derived only by comparing many STM images taken under different tunnel conditions from a specific system. The different contrast mechanisms observed on AuPd(111) surface alloys will be discussed in some more detail in section 4.1.1.

1.2 High resolution electron energy loss spectroscopy (HREELS)

High resolution electron energy loss spectroscopy (HREELS) is an important experimental method to study the vibrational properties of surfaces. Since an electron beam is used as a probe of the vibrations, the application of HREELS requires UHV conditions. Hence, it has been mainly applied to study the surfaces of well-defined single crystals under a highly controlled environment. Due to a continuous improvement of the performance (resolution and intensity) of HREEL spectrometers during the past two decades, this method has reached a state, where it is already close to the physical limit, that is given by the lifetime broadening of adsorbate vibrational bands ($\approx$ 1 meV). Compared to other techniques that provide information about surface vibrations, e. g., infrared spectroscopies, it has a considerably lower resolution. On the other hand, HREELS

exhibits the advantage of being applicable in a wide energy range with the lower limit determined by the width and the shape of the elastic beam (in this study this limit was about 20 meV) and the upper limit given by the energy of the primary electron beam. The main advantage of HREELS is, however, that it is not only sensitive to "dipole-active" vibrations, but it can also be used to detect vibrational modes that are not visible using optical spectroscopies. In the following, a short explanation of the mechanisms that lead to inelastic scattering of electrons from metal[2] surfaces will be given with emphasis on those aspects that are essential for the interpretation of the HREELS results presented in part III of this thesis.

In HREELS experiments it is a general observation, that the angular distribution of inelastically scattered electrons is either very narrow and close to the direction of the specularly reflected beam or relatively broad with no pronounced maximum around the specular direction. It is appropriate to introduce two different scattering concepts not only from the empirical point of view, but also based on theoretical considerations. It can be shown that preferred scattering into the specular direction (i. e., small momentum transfer parallel to the surface during the scattering process) is a direct consequence of the scattering potential exhibiting a long-range dipole characteristic [25]. On the other hand, large angular deflections from the specular direction (i. e., large momentum transfer parallel to the surface) require an interaction of the electrons with short-range contributions to the surface potential, that can only be described by a microscopic theory. The two classes of inelastic electron scattering are called **dipole scattering** (observed near the specular direction) and **impact scattering** (broad angular distribution). A third scattering mechanism, **negative ion resonances**, is observed in special cases. Here, the electron and the adsorbate molecule form a short-lived ($10^{-10}\,\mathrm{s} - 10^{-15}\,\mathrm{s}$) negative ion. The cross section for this scattering mechanism is very sensitive to the electron energy. Also the excitation of vibrational overtones is usually enhanced for negative ion resonances. In the present work, this mechanism has not been identified and therefore it will not be further discussed.

Dipole scattering A general outline of the theory describing the small angle inelastic scattering of electrons from surfaces is given by Ibach and Mills in [25]. In this book, the discussion is not restricted to harmonic oscillators on the surface, as would be sufficient if only adsorbate vibrations were to be described, but a general form of the charge distribution in the near-surface region is preferred as starting point of the calculations in order to include also bulk excitations (plasmons, interband transitions, and phonons). For the present purpose it is

[2] HREELS is in principle also applicable on semiconductor surfaces, but due to the less efficient screening of charges on semiconductor surfaces by the free charge carriers the description of the electron–surface interaction for semiconductors is more complicated than for metals.

not necessary to use this general description, since HREELS was exclusively used for the analysis of adsorbate vibrations, that can be described using harmonic potentials. A quantum-mechanical treatment of this problem was presented, for instance, by Persson [26] and by Lenac et al. [27]. In the following a metal surface in the x-y plane is considered. The electron is approaching the surface from the positive z direction with θ_i being the incident angle measured from the surface normal. An incoming electron induces an image charge in the metal. The resulting electric field between electron and surface image charge can be written as:

$$\vec{E}(t) = \int d\omega \vec{E}(\omega) e^{-i\omega t}, \tag{1.5}$$

where only the z components (E_z) are non-zero at the surface. At the location of an adsorbed molecule the amplitude of the electric field is:

$$E = \frac{e}{2\pi\epsilon_0}\frac{1}{r^2}, \tag{1.6}$$

with r being the distance between electron and molecule. The interaction between the electrical field and the molecule can be described by the following Hamiltonian with $\vec{\mu}$ being the dipole moment operator for the molecule:

$$H = \vec{\mu}\vec{E} = \mu_z E. \tag{1.7}$$

The excitation of a vibrational mode with frequency ω_0 can only be performed by Fourier components of E with $\omega = \omega_0$ (equation 1.5), i. e., by

$$E(\omega_0)e^{-i\omega_0 t} \tag{1.8}$$

Hence, only this component of the electric field has to be considered. Since typical vibrational frequencies are far below the plasmon frequencies of metals ($\hbar\omega_0 \leq 500\,\mathrm{meV}$ and $\hbar\omega_p \approx 10\,\mathrm{eV}$), the electrons of the metal can follow the change in the external electric field, and the representation of the metal electron response by an image charge is possible.

Before the result for the scattering cross section will be presented, the small angular spread of electrons scattered by the dipole mechanism can be shown to follow from momentum conservation parallel to the surface [28]. With $\vec{k}$ being the electron wave vector, $\vec{Q}$ being the momentum transfer during the scattering process, the subscript $\parallel$ denoting components parallel to the surface, and $i(f)$ as label for the initial (final) state of the electron, the momentum conservation within the surface plane can be written as:

$$\vec{k}_{\parallel,i} - \vec{k}_{\parallel,f} = \vec{Q}_{\parallel} + n\vec{G}. \tag{1.9}$$

$\vec{G}$ is a reciprocal lattice vector of the substrate with $n \in \mathcal{N}$. If the molecule is excited from the ground state to the first vibrational state it can be written:

$$E_i - E_f = \hbar\omega_0 \tag{1.10}$$

with

$$E = \frac{\hbar^2 k^2}{2m_e} = \frac{m_e v_e^2}{2}. \tag{1.11}$$

Assuming $n = 0$ it follows:

$$\frac{\hbar^2 k_i^2}{2m_e} = \frac{\hbar^2(\vec{k}_i - \vec{Q}_\parallel)^2}{2m_e} + \hbar\omega_0. \tag{1.12}$$

For $\hbar\omega_0 \ll E_i$, $|\vec{Q}_\parallel|$ is only small and the term with $|\vec{Q}_\parallel|^2$ can be neglected in 1.12. The momentum transfer follows as

$$|\vec{Q}_\parallel| = |\vec{k}_i|\frac{\hbar\omega_0}{2E_i} = \frac{\omega_0}{v_e}. \tag{1.13}$$

Taking the typical values of $E_i = 5\,\mathrm{eV}$ and $\hbar\omega_0 = 100\,\mathrm{meV}$ one obtains $\frac{|\vec{Q}_\parallel|}{|\vec{k}_i|} \approx 0.01$. For the angular deviation of the outgoing electron from the specular direction ($\Delta\theta = \theta_f - \theta_i$) it follows (using $\Delta\theta/\theta_i \ll 1$):

$$\Delta\theta \approx \frac{\hbar\omega_0}{2E_i}\, cos\theta_i. \tag{1.14}$$

For $\theta_i = 60°$ only a deflection of $\Delta\theta \approx 0.3°$ from the specular direction will be noticed in the inelastically scattered beam.

Returning to the result for the scattering cross section, the following expression was derived by Persson [26]:

$$\frac{d\sigma}{d\omega} = \left(\frac{me}{\pi\epsilon_0\hbar^2}\right)^2 \mu^2 \left|\frac{\vec{k}_f}{\vec{k}_i}\right|^2 \frac{1}{cos\theta_i}\frac{|\vec{k}_{i,\parallel} - \vec{k}_{f,\parallel}|^2}{|\vec{k}_i - \vec{k}_f|^4}, \tag{1.15}$$

with μ being the dynamic dipole moment for the excitation from the vibrational state $|\Phi_i\rangle$ to the state $|\Phi_f\rangle$:

$$\mu = \int \Phi_f \mu_z \Phi_i dr = \langle\Phi_f|\mu_z|\Phi_i\rangle. \tag{1.16}$$

Based on symmetry considerations it is possible to derive a selection rule for dipole scattering. Only those modes with $\mu \neq 0$ contribute to the signal. This condition requires that $\langle\Phi_f|\mu_z|\Phi_i\rangle$ is even with respect to all symmetry operations of the point group of the adsorbate complex. Since μ_z is totally symmetric

like any vector that is normal to the surface, the product $\Phi_i \Phi_f^*$ has also to be totally symmetric. If excitations from the ground state are considered, which is necessarily a totally symmetric state, it follows that also the excited state, i. e., the vibrational mode considered, has to transform symmetrically with respect to all point group symmetry operations of the adsorbate complex. This leads to the so-called *metal surface selection rule* (MSSR), which states that only totally symmetric modes are observed as fundamentals in dipole scattering. It should be noted that this selection rule is equivalent to the formulation that only vibrations with a component of the dynamic dipole moment perpendicular to the surface are observed in dipole scattering. These include vibrations, where all nuclei move only parallel to the surface, but where due to charge redistributions between surface and adsorbate an oscillating dipole exists perpendicular to the surface. As an example for the latter case the CH_2 and C–C stretching modes and the in-plane CH_2 bending modes of flat-lying C_2H_4 molecules can be mentioned.

Ibach gave an expression for the intensity of a dipole loss (I_{inel}), that provides some additional information for the interpretation of experimental results [25]:

$$I_{inel} \propto I_I \frac{sin^2\theta_I}{(\hbar\omega_0)^3 cos\theta_I} \Delta E, \tag{1.17}$$

where I_I is the monochromatic current incident on the sample and ΔE is the energy resolution. Since $I_I \propto (\Delta E)^2$ the intensity of a dipole peak decreases with the third power of the resolution. Also the scattering geometry (via θ_I) and the vibrational energy ($(1/\hbar\omega_0)^3$) determine the peak intensity. For low adsorbate coverages the intensity should be proportional to the coverage, but for coverages near to saturation, even a decrease of the HREELS intensity can be observed with increasing coverage. An example for this behaviour has been reported by Pfnür et al. [29] for CO/Ru(0001), where a maximum in the dipole intensity is reached at 0.4 ML, while for saturation coverages (0.7 ML) only about 80% of the maximum intensity is observed. As a final remark, one has also to keep in mind, that modern HREEL spectrometers have acceptance angles of the analyzer that are far below 1° and therefore only part of the inelastically scattered electrons are collected. This might also influence the relative intensity of dipole losses and could make the direct comparison of intensities between different experiments impossible.

Impact scattering One essential feature of dipole scattering is that the scattering event itself produces only a small change in electron momentum. The reflection of the electron (i. e., the change in k_z) is occuring as an additional process directly at the surface. On the other hand, it is also possible that the electron interacts with surface atoms or with adsorbates (here only adsorbate vibrations are considered) in a way, where it loses energy *and* suffers a strong change in momentum in a single process. This requires the electron to "see" the

short range potential of the adsorbates. In other words, the electron hits the adsorbate and therefore this class of scattering events is termed impact scattering. Due to the broad angular distribution of the electrons scattered by the impact mechanism, only few electrons travel within the small acceptance angle of a typical HREEL spectrometer. Therefore, the signals from modes that are excited by impact scattering are usually much weaker than the peaks that can be observed in the specular direction from dipole scattering processes. The best way to observe impact scattering is to move the analyzer out of the specular direction, because then the contributions form dipole active modes will be greatly reduced, while the intensity from impact scattering varies only slowly with angle and might even be higher in "off-specular" measurements.

The calculation of cross sections for impact scattering requires a detailed knowledge of the interaction parameters between the electron and the surface. Similar to the approach taken for the quantitative evaluation of LEED experiments with multiple scattering events included in the description, a scattering amplitude has to be calculated depending on the wave vectors for incoming and scattered electrons and on the position of the nuclei. An expansion of the scattering amplitude in powers of the displacements of the nuclei up to the linear term in the displacements is the first step towards a solution of the problem [25]. Since the qualitative description of the difference between dipole scattering and impact scattering is sufficient for the present purpose, further technical details about the derivation of expressions describing the impact scattering process can be omitted. Further details may be found, for instance, in [25].

1.3 X-ray photoelectron spectroscopy (XPS) and Auger electron spectroscopy (AES)

Although photoelectron spectroscopy and Auger electron spectroscopy rely on different physical effects, they exhibit several common features and therefore it is convenient to discuss them in one section. Since only few XPS and AES results will be presented in the later parts of this thesis, a short introduction into these techniques is sufficient. Further details may be found in the introductory books by Ertl and Küppers [30] and by Briggs and Seah [31].

Both types of spectroscopy use electrons that are emitted from the sample as probe for the chemical properties of the near-surface region of the sample. The surface sensitivity of these methods is given by the small (up to 10 atomic layers) inelastic mean free path of electrons with the typically observed kinetic energies below 2000 eV in solid samples. The difference of the methods consists in different processes that lead to the emission of the electrons. A schematic drawing to show the principles of XPS and AES is displayed in fig. 1.2. For XPS the sample is illuminated by soft x-ray photons. Usually either the characteristic

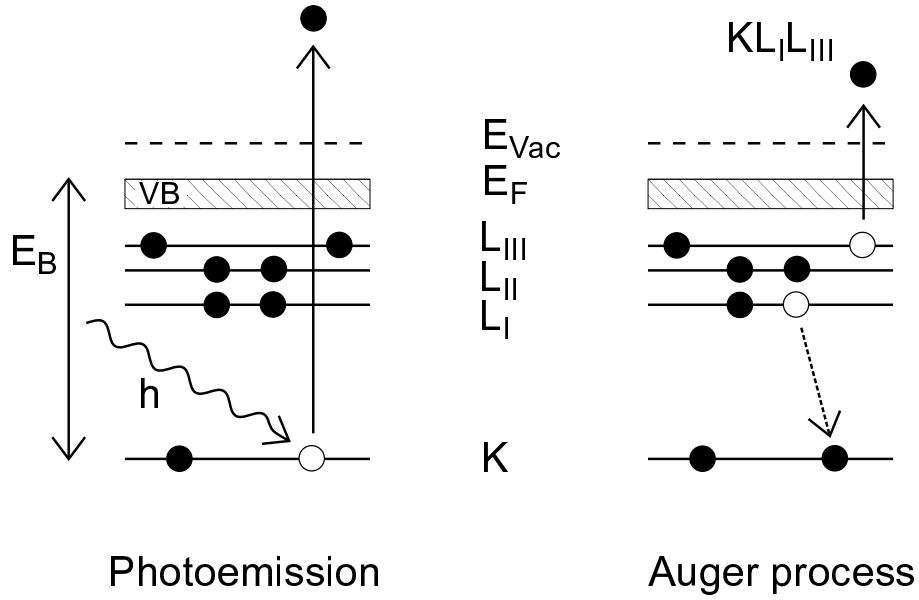

Figure 1.2: Illustration for the elementary processes exploited in XPS and AES.

x-ray radiation from a Mg or an Al anode (K_α radiation with $h\nu = 1253.6\,\mathrm{eV}$ and $h\nu = 1486.6\,\mathrm{eV}$, respectively) is used, or monochromatized synchrotron light, the energy of which can be adapted to the investigated problem. In a very simple description, where second order effects — like final state effects, that are caused by the rearrangement of the electrons in response to the creation of a hole — are omitted, the XPS process may be described as the emission of an electron caused by the absorption of a photon. The kinetic properties of the electron, that can be detected in an electron analyzer, carry information about the system, the most important parameter being the binding energy of the electron (E_B):

$$E_B = h\nu - E_{kin} - e\phi_{sp}. \tag{1.18}$$

For the determination of E_B the work function of the spectrometer (ϕ_{sp}), that has to be electrically connected with the sample, has to be corrected. An XPS spectrum is usually recorded by retarding the electrons in an electrostatic lens system such that the kinetic energies of the electrons are reduced to the constant analyzer pass energy. The retarding electric field is scanned over the desired energy range and the kinetic energy scale is converted to a binding energy scale. In metals this is most conveniently done by referring the energies to the metal Fermi level, that mark the onset of high energy electron emission.

The Auger effect is a radiationless deexcitation process. An example is shown in fig. 1.2, where a core hole has been initally created in the K shell. The nature of the initial excitation is not important and experimentally usually electron impact (typically with 1–5 keV electron energy) or x-ray excitation is employed. The core

hole is then filled by an electron from an upper level. The energy gained therein is transferred in a radiationless process to a third electron, that may leave the sample with a characteristic kinetic energy. Once again, the latter is independent of the radiation used for creating the core hole. In the example shown in fig. 1.2 the Auger electron is called a KL_1L_3 electron, because a K electron was removed from the atom in the initial excitation, an L_1 electron is filling the hole in the K shell and an L_3 electron is emitted in the Auger process. For an estimate of the kinetic energy of this Auger electron it has to be considered that the energy levels are altered by the ionization of the atom. If $\tilde{E}_{LIII}$ denotes the binding energy of the electron in subshell L_{III} for the ionized atom (hole in the L_I subshell), then the kinetic energy of the KL_1L_3 electron is given by:

$$E(KL_1L_3) = E_K - E_{LI} - \tilde{E}_{LIII} - e\phi_{sp}. \tag{1.19}$$

Again, final state effects and complications that might arise if the valence band is involved instead of the sharp core levels are neglected in this description.

So far it has been shown, that both XPS and AES provide spectra of electrons that show distinct features at energies that are characteristic for the investigated element. In the present work, however, these methods were primarily employed to gain information about heterogeneous samples. For instance, the Au coverage on the Pd(111) sample could be derived either from AES or from XPS measurements. Concluding this section, the principles of a quantitative evaluation of XP or AE spectra shall be briefly outlined using the example Au/Pd(111). In that case the XPS or AES peaks that are characteristic for Pd are attenuated by a Au overlayer on the sample. If d is the thickness of this overlayer and $\lambda_Y(X)$ is the so-called escape depth (or attenuation length) of electrons (with a certain kinetic energy) emitted by element X in a matrix consisting of element Y, then the measured intensity of the Pd peak becomes

$$I_{Pd} = I^0_{Pd}\, e^{-d/cos\theta\lambda_{Au}(Pd)}, \tag{1.20}$$

where I^0_{Pd} denotes the peak intensity measured from the pure Pd sample and θ is the angle between the surface normal and the direction to the electron analyzer. The peak intensities from the Au overlayer are increasing with increasing film thickness, and it can be written:

$$I_{Au} = I^0_{Au}\,(1 - e^{-d/cos\theta\lambda_{Au}(Au)}), \tag{1.21}$$

where the term in brackets has been obtained from $\int_0^d e^{-x/cos\theta\lambda} dx$. Hence, the relative intensity of a Au derived peak to a Pd derived peak becomes

$$\frac{I_{Au}}{I_{Pd}} = \frac{I^0_{Au}}{I^0_{Pd}} \frac{(1 - e^{-d/cos\theta\lambda_{Au}(Au)})}{e^{-d/cos\theta\lambda_{Au}(Pd)}}. \tag{1.22}$$

For a two component system, where a homogeneous film is deposited onto an also homogeneous sample, the overlayer coverage can be derived from the measurement of AES or XPS peak intensities. This simple formalism can be adapted to more complicated situations like three dimensional growth or alloy formation. In section 4.5 the latter case will be discussed in some more detail.

Chapter 2

The UHV chamber and experimental details

section[UHV chamber]UHV chamber: basic concepts and instrumental equipment

All experiments that are presented in this thesis were performed using a home-built UHV chamber. It was designed by E. Kopatzki and M. Hugenschmidt based on an earlier model developed by S. Günther. The most important feature of this apparatus is the capability of combining variable temperature STM with other analysis methods like AES, LEED, and XPS as well as with sample preparation facilities in one UHV chamber. The basic outline of these UHV chambers is described extensively in [32]. The modifications allow for adding a separate UHV-chamber for HREELS measurements. During the experimental work for this thesis it was decided that a facility for TPD measurements would be of great advantage for the interpretation of the HREELS data. Since neither the sample holder nor the UHV chamber were especially laid out for TPD experiments, many problems were encountered. The solutions to these problems will be described below. One of the advantages of being able to obtain STM and TPD data from the same surface is, that the latter is a very sensitive standard method in surface science, which is available in many laboratories. Therefore, TPD can be used as a link between the accurate STM characterization of the surfaces and other powerful methods — like photoelectron spectroscopy using synchrotron radiation — that are not available in the STM apparatus. As an example, it will be shown below that the peak positions and shapes in CO TPD spectra from AuPd(111) surface alloys are very sensitive to the Pd concentration in the surface layer. Therefore, by comparing CO TPD spectra with the "STM calibrated" spectra presented in section 5.2.3 of this thesis, also in other laboratories a determination of the Pd concentration could be possible with high accuracy.

An overview over the main parts of the chamber is given by the photograph shown in fig. 2.1 and by the schematic drawings shown in fig. 2.2. Two recipients

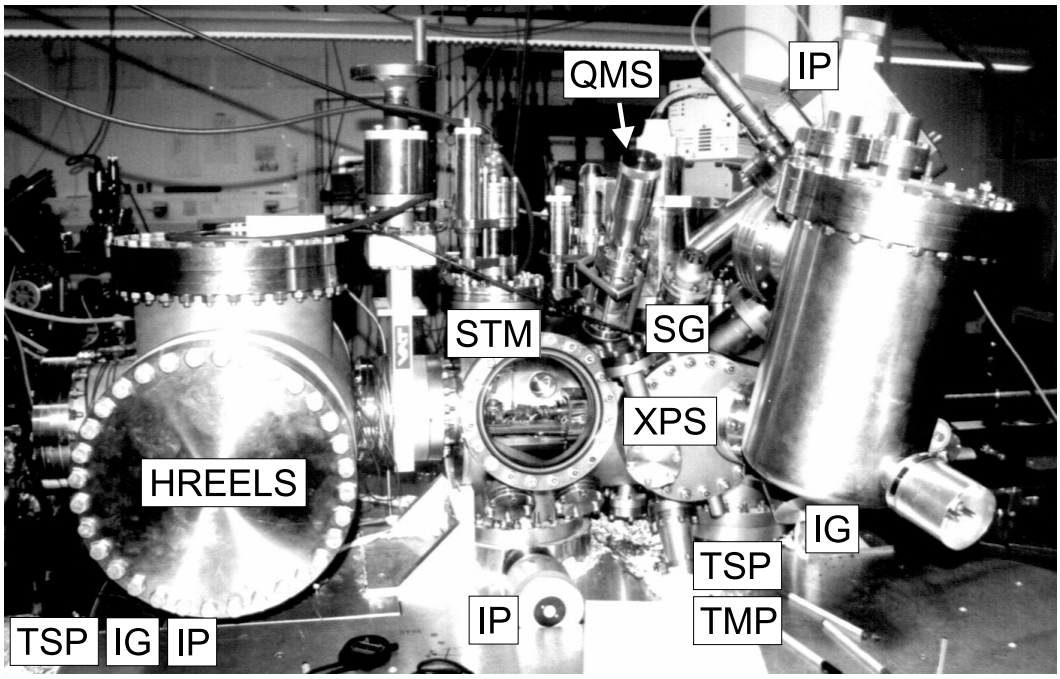

Figure 2.1: Photograph of the UHV chamber that was used in this work. The positions of the HREEL spectrometer, the STM, the QMS, the XP spectrometer, the sputter gun (SG), the ionization gauges (IG), and the different pumps (TSP, TMP, and IP) are indicated. On the back-side of the chamber the following facilities were installed: LEED optics, metal evaporation source, and gas dosing system

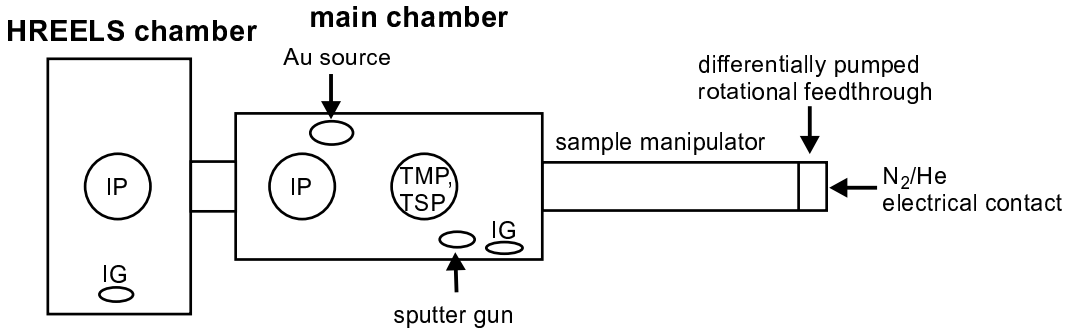

(a) vacuum system and preparation facilities

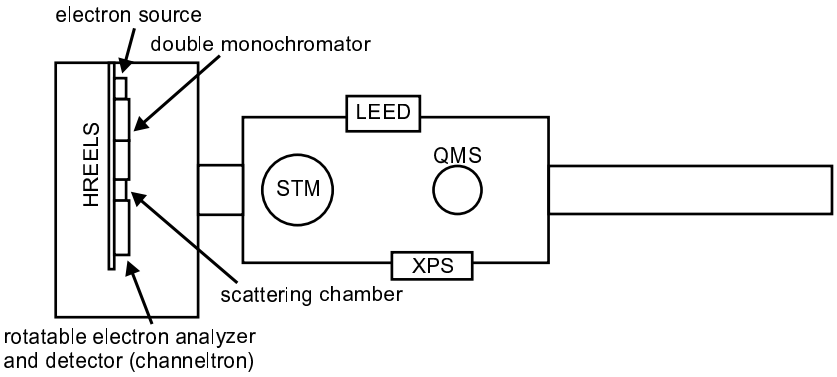

(b) measuring system

Figure 2.2: Schematic topview drawings of the UHV chamber used for this work.

(main chamber and HREELS chamber), that can be separated by a gate valve, form a T-shaped apparatus, which is shown in sideview in fig. 2.1. The concept of this UHV chamber is based on the requirement, that full temperature control of the sample should be possible during all preparation and measurement steps. Hence, the sample is permanently connected to a long horizontal manipulator (Fisons/VG, OMNIAX 600) that allows the sample to be positioned in any of the required measurement or preparation positions: from the TPD/sputtering level at the right-hand side to the HREELS level at the left-hand side of fig. 2.1. In order to avoid vibrations it is necessary to detach the sample holder from the manipulator during the STM measurements leaving several cables for electrical contact and a copper braid for thermal contact as the only connections to the manipulator.

The main chamber (base pressure $5 \cdot 10^{-11}$ mbar – $1 \cdot 10^{-10}$ mbar) is equipped with an oil-free turbo molecular pumping (TMP) system (Varian Turbo-V250 backed by a Varian Turbo-V70LP and a membrane pump), an ion pump (IP, Varian VacIon Plus 500), and a titanium sublimation pump (TSP). Both the ion pump and the turbo pumps can be separated from the main chamber by two independent valves. During gas dosing the ion pump is closed off, during STM measurements the turbo pumps are switched off and separated from the chamber. Since the oil-free turbo pumps do not have to be vented when they are switched off, it can be avoided to introduce contaminants like water into the system. Only a few mbar of N_2 are usually admitted into the TMPs in order to stop their rotation within a few minutes. Otherwise, more than two hours would be necessary to stop the vibrations from the turbo pumps. Because of the only small amount of nitrogen in the TMP system, the turbo pumps can be connected to the main chamber again after only about 10 min of pumping without a significant increase in the chamber pressure. Therefore, several sample preparation and STM measuring cycles can be performed in one day, which is for example important for adsorption measurements on a series of different AuPd(111) surface alloys, because after each annealing step the sample had to be analysed again by STM. An additional ion pump (Varian VacIon Plus 250) together with a liquid nitrogen coolable TSP allows the HREELS chamber to be separated from the main chamber during sample preparation and during gas dosing. The two pumps in the HREELS chamber are also required to achieve a good local pressure ($\leq 5 \cdot 10^{-11}$ mbar) even during adsorption experiments. The pressure in the system can be measured by two ionization gauges (IG, Granville-Phillips, nude Bayard-Alpert type) located in the main chamber and in the HREELS chamber, respectively.

Originally, the chamber was equipped with an Auger electron spectrometer (AES, Perkin-Elmer 10-155) consisting of a cylindrical mirror analyzer (CMA) with an electron gun on the cylinder axis. After some time it was replaced by an XPS system consisting of a double X-ray source (Fisons/VG, XR3E2) for

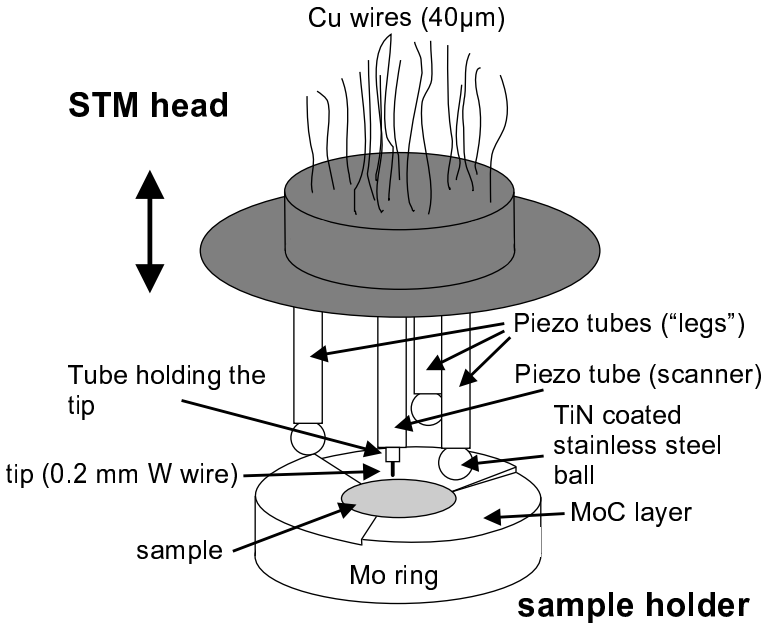

Figure 2.3: Sketch of the "beetle-type" STM and the sample holder.

Mg($K\alpha$) and Al($K\alpha$) radiation, respectively, and a hemispherical energy analyzer (CLAM2, Fisons/VG). The metal evaporation source used for Au evaporation was home-built by C. Guenther [33]. The material, that is to be evaporated, is put into resistively heatable W- or Mo-baskets. A Ta heat shield, that can be flashed for degassing by electron bombardment, prevents the surroundings from being warmed up, which allowed the chamber pressure to remain in the lower 10^{-10} mbar region during metal evaporation.

The STM measurement system was designed by J. Wiecherts (electronics) and by S. Guenther (mechanics, [32]) on the basis of the "beetle-type" STM built by Besocke [34]. A new STM head had to be built for the experiments of this thesis, but since no major changes were made, it is sufficient to describe only the basic features of the microscope. The design of the STM head and the sample holder is illustrated by the drawing in fig. 2.3. Three parallel piezo tubes ("outer piezos") with TiN coated stainless steel balls glued to one of their ends are forming the three "legs" of the microscope. They are fixed to the head in the corners of an equilateral triangle. A fourth piezo tube in the centre of the triangle is holding the tip, that is made from 0.2 mm W wire by an electrochemical etching procedure. All four piezos are identical concerning their piezoelectric properties and their dimensions. Specifically, they have 5 independent electrodes: one at the inner surface of the tube and 4 segments at the outer surface, by which it is possible to move all four piezos tubes independently in x, y, and z. For the STM measurements shown below the outer piezos were used for the tip–sample approach and the inner piezo was performing the scanning movement and the

adjustment of the tip–sample distance. In principle, also the outer piezos can be used for scanning. For STM measurements each of the legs is standing on one of three slightly inclined ramps, that are shaped into the Mo ring[1] holding the sample. Thereby, a rotation of the STM head (achieved by applying suitable voltage pulses to the different segments of the outer piezos) results in a very small vertical movement of the microscope allowing the controlled positioning of the tip with respect to the sample surface (with accuracy of a few Å). This design is relatively well-suited for measurements at variable temperatures (see [32]), and the complete sample surface is accessible for STM. The latter point is especially advantageous, since the sample is also used for area intergrating measurements (HREELS, TPD), and the homogenity of the whole sample can in principle be checked by STM. All STM images that are presented in this thesis were recorded using the constant current mode of the STM. The images are displayed in a gray-scale representation with brighter colours corresponding to higher areas.

A commercial VSI "Delta 0.5" spectrometer was used for the HREELS measurements. Its design was developed by H. Ibach and is described in [35]. Cylindrical deflector analyzers are used as energy dispersive systems in the double monochromator and the single analyzer. The analyzer is rotatable by $\sim 60°$ allowing measurements in the specular direction with a maximum angle of 60° to the surface normal. This geometry was used for most of the HREELS measurements presented below. The specified performance of the instrument is a beam current of $\geq 5\,\mathrm{pA}$ at a resolution of 1 meV (FWHM) in the direct beam (i. e., without sample). These values were only achievable with the magnets of the ion pumps removed from the system. Otherwise, the best performance was 2 pA at 0.97 meV. However, the limiting factor for measurements on the sample is the sample holder. Usually, sample holders that are used for HREELS measurements are constructed as slender as possible in order to avoid electric stray fields (from work function differences or from isolating parts that possibly get charged during the measurement) or magnetic stray fields, which might disturb the low energy electron beam. While the latter problem could be avoided by using non-magnetic materials in the construction of the sample holder (see below), it was not possible to get completely rid of the former problem, even though the potential of the sample holder is controlled independently from the sample potential. The performance that could be achieved in the elastically reflected beam was a resolution of 3 meV with a count rate of a few hundred kcps. Most of the HREELS results of this work will be presented after a normalization of the intensities such that all spectra that are collected in one figure have an equal height of the elastic peak. While this procedure ensures that deviations in the intensities, which are caused by the non-perfect reproducibility of the electron beam quality from spectrum to spectrum are eliminated, it does not guarantee a linear relationship between

[1]The Mo ring is coated by a thin MoC layer in order to prevent scratches in its surface by the hard TiN coated spheres at the STM legs.

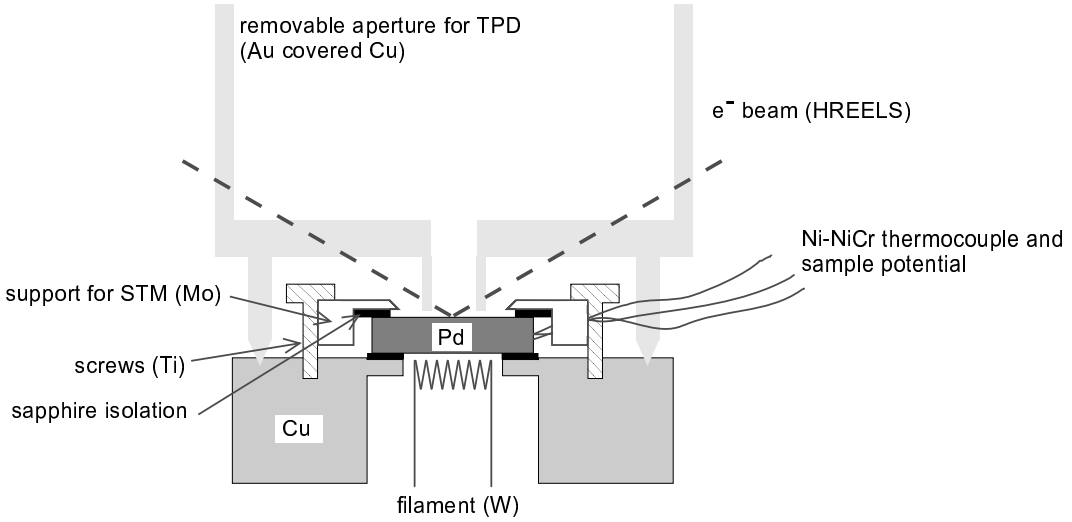

Figure 2.4: Sketch of a cut through the sample holder. The course of the electron beam for HREELS measurements is indicated by the dashed line. Also the removable aperture for TPD measurements is included.

intensities and adsorbate coverages (see section 1.2).

Gas dosing for adsorption measurements was either done via backfilling the main chamber (for HREELS measurements) with the valves to the ion pump and to the HREELS chamber closed or via a dosing system (for TPD, vide infra). The exposures that are given in part III of the thesis are derived from the ionization gauge readings devided by the ionization gauge sensitivity, where necessary (for C_2H_4: 2.1 from [36]).

2.1 Design of the sample holder

One of the main experimental difficulties that are encountered if several demanding experimental methods are to be combined in one apparatus is to find a suitable design of the sample holder. For this work, it was necessary to modify a sample holder that was originally outlined for being used in combination with a beetle-type STM. The basic design was developed in the group of K. Kern at the University of Lausanne. Its features are largely determined by the requirements of the STM system, i. e., a Mo ring surrounding the sample is necessary as support of the STM head, and by the HREELS related limitations, i. e., the choice of non-magnetic materials and the necessity to cover all isolating parts by a conducting shield. A cut through the sample holder is sketched in fig. 2.4. The sample is electrically isolated from its surroundings by two sapphire rings (black). For sample potential control and for temperature measurement three thin (0.1 mm) Ni(NiCr) wires are spot-welded to the edge of the crystal. Three Ti screws connect the

sandwitch structure, that consists of the Mo-support for the STM head, the two sapphire rings, and the Pd crystal, to a small Cu block. The latter is connected via a Cu braid to the cryostat that can be operated either with liquid nitrogen or with liquid helium. The thermal isolation of the Cu block was considerably improved in the course of this work. In the original sample holder six Ti screws (M 1.6) were directly connecting the Cu block to a base plate made from Ta. The latter was in relatively good thermal contact to a second bigger Cu part, which in turn is essentially at room temperature. The lowest temperature that could be achieved with this setup was $\sim$150 K. By insertion of small tubes made from quarz glas[2], which exhibits a very low thermal conductivity at low temperatures, between the Ti screws and the Cu block a very good thermal isolation could be achieved. After this change sample temperatures below 100 K could be reached with liquid nitrogen cooling.

As can be seen in fig. 2.4 the electron beam of the HREEL spectrometer is passing the Mo ring and the Ti screws in relatively close proximity. Also, the position of the sample holder has to be controlled very precisely in order to avoid reflections from other parts of the sample holder than the sample. This situation is certainly not the best condition for an optimum HREELS performance. Hence, it can not be expected to reach the theoretically possible resolution with this sample holder.

2.2 TPD system

For TPD measurements also severe problems are caused by the setup of the sample holder. Even though a direct and fast heating of the sample via electron bombardment is possible, it can not be avoided that also the sample holder is heated up during the temperature ramp. Therefore, desorption from the sample holder and from the cooling system causes the pressure in the chamber to rise up to the mid 10^{-9} mbar range during TPD if dosing is performed by backfilling the chamber. The quality of the TPD spectra could be improved by two major changes of the experimental setup:

1. A closed cover with a port for differential pumping (by a 20 l/s ion pump) had to be built for the quadrupol mass spectrometer (QMS). An opening towards the sample is the only connection to the UHV chamber. For several reasons, that will be given below, the cover was designed to consist of two parts. One is fixed to the QMS and the other part (the "aperture") is put in vacuum onto the sample holder for TPD measurements. The three legs of the aperture are inserted into three depressions drilled into the

[2] As alternative material for the thermal isolation TiAlV alloys can be used; iron based alloys (stainless steel) that are also good thermal isolators at low temperatures should be avoided because of possible magnetic stray fields.

sample holder, and therefore the position of the aperture with respect to the sample is almost exactly defined. Using the positioning system of the manipulator, it is possible to connect the aperture and the QMS cover such that only a very small signal caused by the increasing chamber pressure is registered in the QMS during heating the sample. With this cover, the background problems arising from the degassing of the sample holder could be sufficiently reduced.

2. A closer inspection of the sample holder (see fig. 2.4) reveals that a second source for possible background signals exists, namely the outer parts of the Pd crystal itself. Only the area that is accessible through the hole in the Mo ring (diameter: 6 mm) is properly prepared by ion sputtering and Au evaporation and is therefore providing an useful signal. But during dosing not only this part is covered by adsorbates but also a considerable area of the crystal that is shadowed by the Mo ring. In the best case, this area is restricted to the diameter of the upper sapphire ring (7 mm), which would amount to 36% of the preparable area in the centre of the crystal. The importance of this problem can be illustated by the following example: If a AuPd(111) surface alloy with 10% Pd in the surface layer is prepared in the central part of the crystal surface, about 0.1 ML CO will be the saturation coverage in this area. However, in the outer region up to 0.75 ML CO can be adsorbed depending on the degree of contamination on this part of the crystal[3]. Hence, almost three times more CO molecules might be released during a TPD run from the outer region than from the central region. By using a relatively small aperture that is placed directly over the crystal centre this problem could be partially resolved. An even better solution was found by using the aperture, that was originally designed for the QMS system, also as doser. This was done by attaching a stainless steel tube to the dosing valve. The tube fits to the upper opening of the aperture. The latter is moved together with the sample between the dosing position and the QMS position. If a slit of about 1 mm is left open between the aperture and the dosing tube, a small pressure rise in the chamber can be used to estimate the exposure of the surface. The ratio between the gas pressure over the sample surface and the pressure rise in the chamber was determined to be about 200 under these conditions, but it could be chosen also higher by narrowing the 1 mm slit. The decisive advantage of the doser is, that the outer parts of the crystal are exposed to a lower gas pressure than the inner parts, which results in a decrease of the contribution from the free Pd areas in the TPD spectra. Of course, it had to be checked whether the coverage gradient over the sample surface and possible diffusion effects influence the

[3] Due to the high annealing temperatures ($\sim$1200 K) that are used for crystal preparation the contaminants are also removed from the outer crystal areas by diffusion into the bulk.

shape and position of the TPD spectra from the central crystal parts. It was found that there is no significant difference in the peak shapes between measurements, where the above described dosing system was used, and measurements, where dosing was performed via the background pressure in the chamber. However, in the latter case a somewhat increased peak intensity (by $\sim 20\%$) was noticed.

Finally, it has to be justified why the described unusual design of the aperture/cover system was preferred over a simple cup that is completely fixed to the QMS. As has been made clear above, it is decisive to be able to put the opening of the QMS cover as close as possible to the sample surface in order to eliminate desorption signals from the outer sample parts and from the chamber background. This can be easily achieved in the described aperture/cover system, since the aperture position could be carefully adjusted ex situ, before it is put into the UHV system. For each TPD measurement sequence the aperture is put into the marked position on the sample holder, which can be done with reproducible accuracy. On the other hand, the distance between the opening in a hypothetical QMS cover and the sample surface can not be controlled visually because of the Mo ring that conceals the sample. Therefore, the reproducibility of TPD intensities from such a system would probably suffer from inaccuracies in the distance between the sample surface and the aperture.

2.3 Sample preparation

For the few experiments on a Au(110) crystal, that are included in chapter 5, a sample was used, that had been prepared during the earlier work of S. Günther and A. Hitzke. A detailed preparation procedure for this crystal is described in [37]. The major part of the experimental work was performed on a new (111) oriented Pd crystal (Matek, $\geq$ 99.999% Pd). The initial sample preparation method was largely developed by B. Gleich during his diploma thesis and is explained in [38]. Therefore, it is sufficient to give a short summary of the sample preparation in the following.

First, the Pd crystal was electrochemically etched in order to remove the top few μm, that had been damaged by the preceeding mechanical polishing of the surface. Subsequently, short sputtering (Ar^+, 1000 eV) and annealing (1200 K) cycles were sufficient to produce a sharp LEED pattern. The terraces visible in STM images were already relatively large (up to 2000 Å), but impurity islands were still present. From AES measurements it could be inferred that strongly segregating sulfur from the crystal bulk was the most likely reason for the defects. From the differences in surface energies of Pd and S a segregation energy of $\sim$0.6 eV can be estimated, which is sufficient for a considerable S enrichment in the surface even at high temperatures (at 900 K and in assumed thermodynamic

equilibrium the enrichment factor is ∼2300). Therefore, it was determined that sputtering at elevated temperatures (high diffusion rate of S!) was the most suitable method to remove the S contamination from the crystal. After sputtering with an estimated (low) rate of ∼ 0.2 ML/min, that was adjusted to the estimated S segregation speed, for 14 h at 900 K, the sulfur contamination could be reduced to a value below the detection limit of AES (≤ 0.01 ML).

STM images showed still a relatively high density of defects. Since small amounts of carbon are not detectable by AES (the C(KLL) peak overlaps with the Pd(MNN) peak), it was assumed that C contaminations were still present on the surface. Even after repeated oxygen adsorption, flashing, and sputtering cycles no significant changes were detected by STM. A considerable improvement of the preparation results was achieved by changing the sputtering procedure. Originally, the sample and the sample holder were at ground potential and were bombarded by 1000 eV Ar^+ ions. Thereby also the carbidized Mo ring was sputtered and C atoms could be scattered in the Ar gas ($3 \cdot 10^{-5}$ mbar) and could hit the sample. This effect is largely reduced by applying a negative bias voltage (500 V) to the sample and leaving the Mo ring at ground potential, which causes the ions to be focused onto the sample. The acceleration voltage of the ions is reduced to 500 eV. Of course, they can still hit also the Mo ring, but the sputter rate on the sample (1000 eV ions) is now considerably higher than the sputter rate on the sample holder (500 eV ions). Using this sputtering procedure and a short subsequent flash to 1200 K, a clean and well ordered surface was routinely observable by STM. The terrace widths were found to be relatively inhomogeneous across the crystal surface on the length scale of a few tens of μm. Large terraces (≥ 1000 Å) were usually detected only after checking several areas on the sample. The majority of the areas that were visited by STM exhibited typical terrace widths of a few 100 Å. The largest terraces (up to 1 μm) could be detected in the vicinity of bulk defects like screw dislocations. Atomically resolved STM images typically showed about 0.1% ML impurity atoms on substitutional sites in the surface layer. It is likely that most of these atoms were Au atoms that had diffused into deeper crystal layers in previous alloying experiments. Additionally, a small amount of C (≤ 0.05 ML) was frequently detectable in XP spectra even after repeated oxygen adsorption – annealing cycles. Besides CO adsorbed from the residual gas during the measurement, also C atoms in subsurface sites can be assumed as origin of the C signal. The amount of C atoms *on* the surface can be neglected, because STM did not show any indications for the presence of such adatoms.

Part II

Growth and alloying of Au on Pd(111)

The main objective of this work is to gain insight into the local chemical properties of bimetallic Au-Pd(111) surfaces. This requires that the surface structure and composition is characterized on the atomic length scale. STM is an experimental method that offers an ideal combination of virtues for studying bimetallic surfaces on the atomic scale. An overview over the recent literature on this topic can be found in the reviews by Besenbacher [39], Brune and Kern [40], Besenbacher et al. [19], and by Brune [41]. The examination of growth and interdiffusion processes of Au on Pd(111) constitues a formidable task in itself, and it would not be adequate to treat this part of the work merely as a tiresome preparatory step for subsequent adsorption and reaction studies. On the contrary, the relevation of the atomic processes that govern film growth and surface alloy formation is of considerable interest both from a scientific and from a practical point of view. Having said this, it has to be admitted that for some aspects that will be touched in this part of the thesis the discussion of the experimental results might appear to be not detailed enough. This can not be avoided considering the many-sidedness of this work. For example, in the chapter about Au growth on Pd(111) the section on the evaluation of temperature dependent island densities will be restricted to the most important arguments, because it is based on the broad body of similar investigations that have been reported for other systems in the past and that provide "standard methods" for the evaluation of film growth kinetics. On the other hand, several aspects of the Au-Pd(111) alloy formation were considered to be worth a more profound analysis, because in this field still many basic questions either wait to be answered or are not even formulated. One guideline for these growth and alloying studies was the question how to prepare Au-Pd(111) surfaces with specific properties, that could be exploited in subsequent adsorption or reaction studies. For example, it is not trivial to obtain a surface that is completely covered by 1 ML of Au and contains as little second layer Au islands as possible. Or, in the case of surface alloys, preparation methods have been investigated that lead either to homogeneous surface compositions or to well-defined inhomogenities.

In this work different types of surfaces were prepared by Au deposition on Pd(111) and partly by subsequent steps. The following nomenclature will be used to distinguish between these types:

- **Au-Pd(111):** General notation for bimetallic systems prepared by Au deposition on Pd(111) (including surface alloys).
- **Au/Pd(111):** "Layered" Au-Pd(111) systems, i. e., each crystal layer consists of only one element, and intermixing between the two components can be neglected.
- **AuPd(111):** Surface alloys, i. e., the surface layer and possibly also several sub-surface layers exhibit a mixed composition.

It should be mentioned that the application of the term "surface alloy" is controversial in the literature. Sometimes it is restricted to systems, where the surface stabilizes the alloy structure and a qualitatively different behaviour is found at the surface compared to the bimetallic bulk phase (thermodynamically stable surface alloys). In the surface science literature "surface alloy" is also widely used to denote mixed bimetallic phases at or near the surface, which are stabilized by high energy barriers for bulk diffusion (kinetically stabilized surface alloys). In the following "surface alloy" will be applied in the second, broader sense.

Chapter 3

Au growth on Pd(111)

Investigations about metal-on-metal growth have been one of the "classical" applications of STM from the beginning [42]. An overview over a large part of this work can be found in recent reviews by Besenbacher [39] and by Brune [41]. The main advantages of STM over other structure sensitive methods are its universal applicability on conducting materials, the direct observation of atomic structures in real space, and the possibility to obtain information on different length scales in a single experiment. The latter is of utmost importance for metal-on-metal growth studies, because it might well be, that processes which are only observable on the atomic scale profoundly influence the evolution of the mesoscopic film structure (island densities, island shapes or film morphologies). As an example for this kind of phenomena it can be mentioned that in certain heteroepitaxial systems (e. g., for Ni/Ag(111) [43]) atomic exchange processes have been found to strongly influence the island nucleation behaviour. Hence, a correct interpretation of island densities in such systems is only possible if the alloying process is taken into account.

For the present growth system Au on Pd(111) several different aspects have been addressed in this work using STM. The general motivation behind these studies was the preparation of well-defined surfaces that could be employed in subsequent adsorption and reaction experiments. For this purpose the following points had to be investigated with STM:

- Au coverage determination. In principle, it was possible to measure the Au coverage for each experiment directly by STM. Additionally, STM images were used for a calibration of an AES or XPS based coverage determination. Thus, the coverage of Au/Pd(111) films that were used for adsorption experiments could also be determined simply by recording AE or XP spectra.

- Average island sizes and amount of Au edge sites. It will be shown in part III that Au step edge sites exhibit a considerably different chemical behaviour compared to Au terrace sites. In order to show this effect, information of

the average Au island sizes and the island shapes had to be obtained.

- Smoothness of Au films. Even if the integral Au coverage is known from spectroscopic measurements the film morphology still has to be investigated. An important question in this respect is, for instance, how much Au is needed to cover the Pd(111) substrate completely at a certain temperature.

In addition to STM experiments that were performed in order to accomplish the above tasks, it was found worthwhile to study two aspects of Au growth on Pd(111) in more detail: First, the Au adatom diffusion barrier on Pd(111) was determined from the measurement of temperature dependent island densities. Second, for multilayer Au films the nature of the strain relief pattern was analysed on the atomic scale. The presentation of the experimental results will be devided into two sections on submonolayer Au films and on films with $\Theta_{Au} \geq 1\,ML$, respectively.

Several experimental studies have been performed on the Au/Pd(111) system in the past. Kuk, Feldman, and Silverman (KFS, [44]) investigated the structure of Au/Pd(111) films grown at room temperature by HEIS (high-energy ion scattering), LEED, and AES. From LEED measurements KFS determined the in-plane lattice constant of the surface layer to correspond to the Pd value of 3.89 Å for 1 ML Au and to continuously increase up to the value for Au (4.08 Å), which is reached at Θ_{Au}=10 ML. In the intermediate region two values are reported at 4 ML (3.96 Å) and at 6.5 ML (4.03 Å), respectively. The ion (1.8 MeV He^+) scattering experiments yielded several important results:

- The first ML of Au grows pseudomorphically.
- For all investigated Au film thicknesses (up to 11 ML) only fcc stacking has been observed.
- Misfit dislocations are found in films with $\Theta_{Au} \geq 2\,ML$.
- In ion channeling experiments an *increase* of the ion yield from Pd atoms above the value observed on pure Pd(111) is observed for $\Theta_{Au} \geq 2\,ML$, indicating that also the substrate is distorted in the direction parallel to the surface.

In an electron reflection study Jaklevic found that the growth of Au on Pd(111) at room temperature proceeds close to layer-by-layer growth [45]. Approximately three layers are growing pseudomorphically, while for $\Theta_{Au} \geq 3\,ML$ the formation of dislocations is inferred from the experiments. Eisenhut reports a combined XPD (photoelectron diffraction), AES, and LEED investigation on the Au/Pd(111) system at room temperature [46]. Her results differ somewhat from the above mentioned studies, insofar as she found a pronounced deviation from

layer-by-layer growth. Already at 0.4 ML Au emission of photoelectrons from third layer Au atoms was observed. The transition from pseudomorphic to non-registered growth was found at a critical film thickness of 3 ML, which is in accordance with the results of Jaklevic but differs from the critical film thickness of 1 ML determined by Kuk et al.. The fcc stacking of the Au overlayers up to at least 12 ML was confirmed by the XPD measurements.

3.1 Submonolayer Au films

3.1.1 Qualitative aspects

An overview over STM measurements on submonolayer Au films prepared at different temperatures is given in figs. 3.1 and 3.3. The Au coverage is 0.10 ML except for the highest deposition temperatures (379 K and 400 K), where 0.24 ML and 0.4 ML Au have been deposited, respectively. For these figures STM images from relatively large terraces have been selected in order to illustrate the variation of island densities with deposition temperature. In one of the large-scale images (fig. 3.3(c)) also several monatomic high surface steps are visible and it is obvious that a (temperature dependent) minimum terrace width exists for the nucleation of Au islands (at 379 K $\sim$600 Å). The deposited Au atoms are found not only in islands on the terraces but also in aggregations at the former Pd step edges, i. e., the step edges act as traps for incoming Au atoms. In STM height profiles across former Pd steps and the neighbouring Au aggregations differences of around 0.2 Å are usually found between the level of the Pd terrace (lower) and the Au level (higher). "Usually" means with a normal metallic tip and with the high resistance tunnel parameters (the tip is relatively far away from the surface) that were employed for these overview images ($I_t \leq 10$ nA and $U_t \geq 100$ mV). It will be shown below that a different kind of contrast mechanism could be obtained with low resistance tunnel parameters, where Au atoms or Au rich areas are imaged darker (lower) than Pd atoms or areas. Atomically resolved images were almost exclusively observed with the latter contrast mechanism (Pd bright, Au dark).

In fig. 3.3(c) it can be seen that at step edges that separate relatively small, island-free terraces, the amount of Au is closely related to the width of the *lower* terrace, and is almost independent of the width of the *upper* terrace. From this observation it can be inferred that interlayer Au transport across a step edge to the lower terrace is hindered by a reflective energy barrier. This phenomenon is well-known in metal-on-metal epitaxy with the additional energy barrier at the step edges usually referred to as "Ehrlich-Schwoebel" (ES) barrier [47, 48]. In kinetically controlled growth experiments the ratio between the ES barrier and the terrace diffusion barrier largely determines the film roughness [49]. In this study it was not attempted to evaluate the height of the ES barrier for Au/Pd(111), and this aspect will not be discussed in more detail.

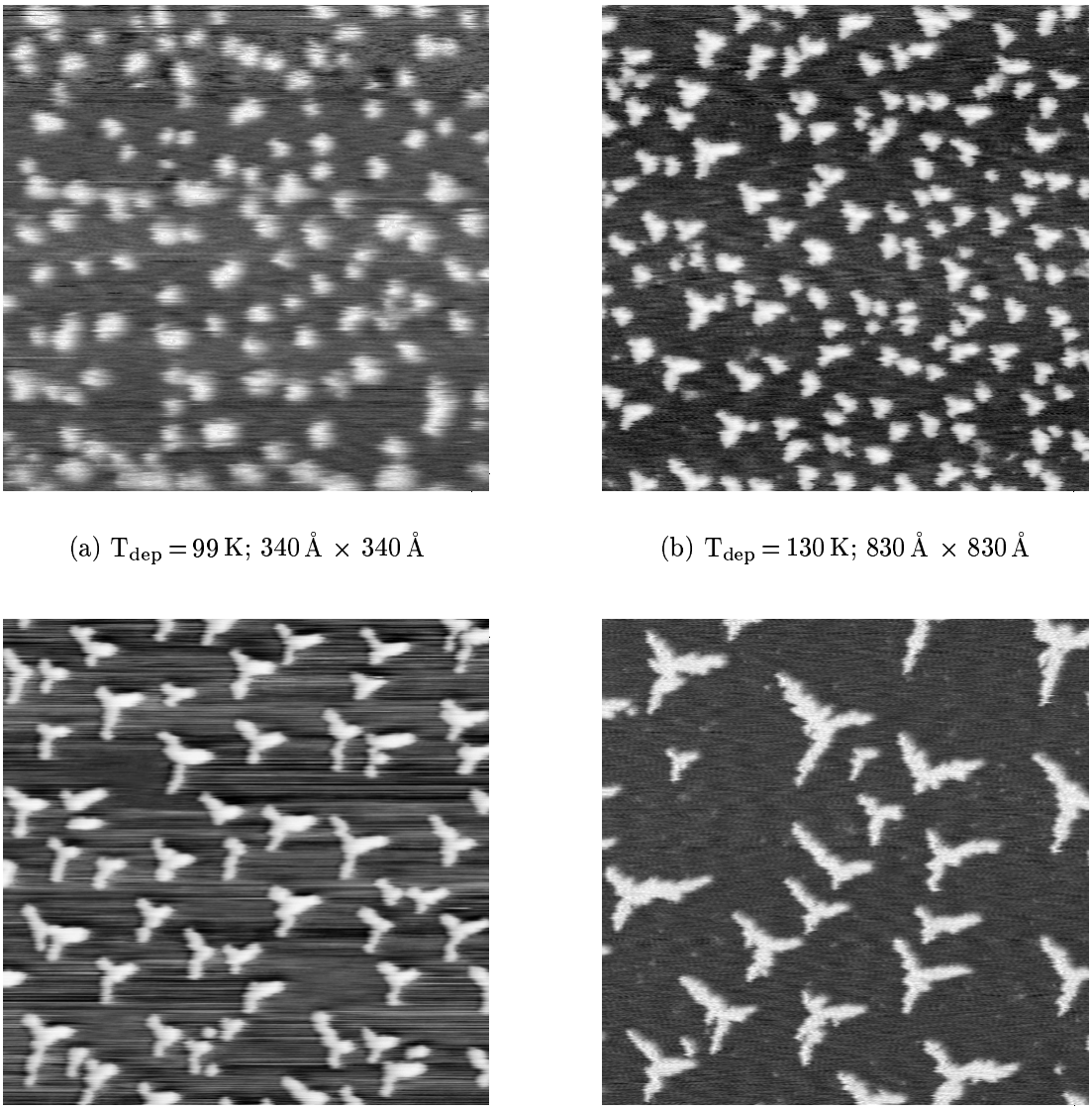

(a) $T_{dep} = 99\,K$; 340 Å × 340 Å

(b) $T_{dep} = 130\,K$; 830 Å × 830 Å

(c) $T_{dep} = 180\,K$, 1540 Å × 1240 Å

(d) $T_{dep} = 225\,K$, 1380 Å × 1370 Å

Figure 3.1: STM images of 0.1 ML Au deposited at low temperatures; Au flux: 0.01 ML/s.

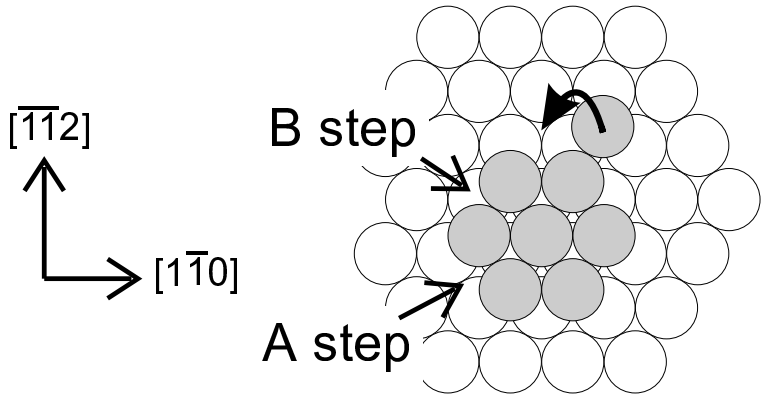

Figure 3.2: Model for corner diffusion on fcc(111) surfaces.

It is evident at first sight that the Au island density strongly depends on the deposition temperature over the whole temperature range, as predicted by nucleation theory for homogeneous nucleation. As immediate consequence of the increasing island density observed at lower temperatures, the average island size is decreasing with temperature. For 0.1 ML deposited at 99 K each island contains on average only about 16 Au atoms. For this reason and because of the limited resolution obtained in STM measurements at low temperatures the island shapes in fig. 3.1(a) could not be determined very well. In all other cases a clear tendency to form dendritic island shapes can be seen at least for larger islands. Qualitatively, there is no significant difference between the island shapes detectable upon Au deposition at 180 K ($\sim$500 atoms per island) and the island shapes formed at 355 K (with up to 28,000 atoms in larger islands).

Dendritic shapes are frequently encountered in non-equilibrium growth processes throughout nature, for example in the formation of snowflakes. In metal-on-metal growth it is a common phenomenon on hexagonal surfaces (see [41] for several examples). During the last years the atomic processes that lead to the formation of the dendritically shaped islands on fcc(111) surfaces could be revealed by a combination of STM experiments, effective medium theory (EMT) calculations, and kinetic Monte Carlo (KMC) simulations [50–52]. It was found that the decisive atomic process that leads to the dendritic islands with threefold symmetry consists in anisotropic corner diffusion. This is illustrated in fig. 3.2. On fcc(111) surfaces two types of step edges can be distinguished: "A steps" which expose (100) oriented facets, and "B steps", which expose (111) facets [53]. Therefore, the six sides of a hexagonal island are not equivalent. For an atom that is attached to a corner site (see fig. 3.2) the energy barrier for diffusion to the A step is generally different from the barrier for diffusion to the B step. Intuitively one would expect the former being lower because along its path the atom does not have to cross an unfavourable on-top position. For Ag/Pt(111) this has been

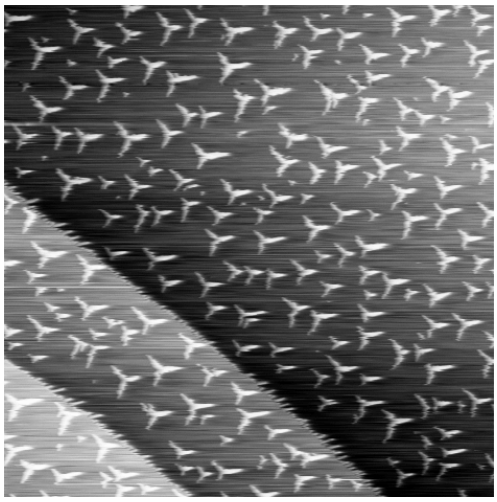

(a) 0.1 ML Au; $T_{dep} = 298$ K; 8000 Å × 8000 Å

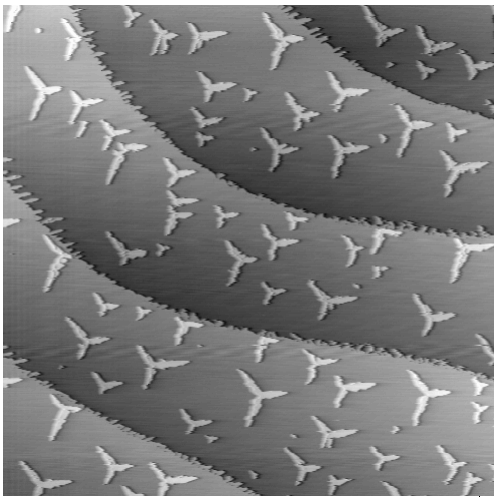

(b) 0.1 ML Au; $T_{dep} = 355$ K; 8400 Å × 8300 Å

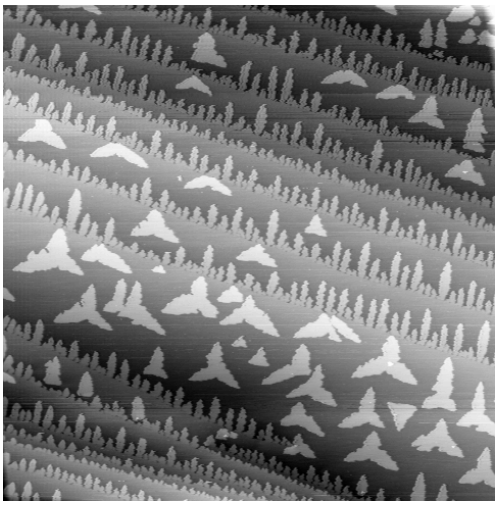

(c) 0.24 ML Au; $T_{dep} = 379$ K, 9000 Å × 9000 Å

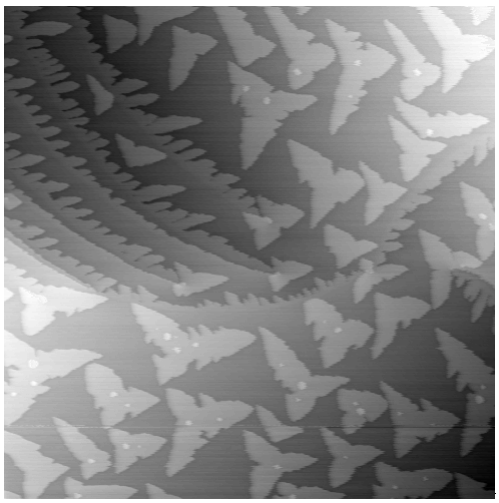

(d) 0.4 ML Au; $T_{dep} = 400$ K, 8350 Å × 8350 Å

Figure 3.3: STM images of 0.1 ML – 0.4 ML Au deposited at $T \geq 298$ K; Au flux: 0.01 ML/s.

confirmed by EMT calculations [51]. Once a small protrusion has been formed on an otherwise compact island, this is exposed to a slightly larger flux of incoming atoms. Hence, such protrusions tend to continue to grow. For the incoming atoms the anisotropic corner diffusion leads to preferred growth directions that are perpendicular to the A steps. For a detailed explanation how the mechanism operates for larger islands and how it finally results in the experimentally observed shapes see [51]. This mechanism is also confirmed theoretically in a recent publication by Ovesson et al. [54]. They report kinetic Monte Carlo simulations with energy barriers obtained from DFT based calculations. They find that the corner diffusion anisotropy together with non-equivalent edge diffusion barriers along A and B steps are the decisive factors in the formation of dendritic island shapes.

An interesting consequence of the island shapes with threefold symmetry is that these allow to decide whether only islands with one type of stacking (fcc or hcp) are formed or whether both stacking possibilities are realized. This can be explained with the help of the model shown in fig. 3.2. If it is assumed that the hexagonal island is moved downward until the atoms have reached again threefold hollow sites (i. e., by $(1/\sqrt{3})\cdot$nn distance), it becomes obvious that this shift from an fcc to an hcp island (and vice versa) results in former A steps becoming B steps and vice versa. Since the dendritic shape is pinned to the orientation of A steps it follows that the dendrites which grow from an hcp nucleus will be rotated by 60°. In the STM experiments on Au/Pd(111) the observation of a rotated island was a very rare event. One example can be found in the lower right-hand corner of fig. 3.3(c). Therefore, the energy difference between fcc sites and hcp sites is large enough to prevent the growth of islands with unfavourable stacking. It has been mentioned above, that ion scanneling experiments [44] and XPD measurements [46] showed independently that Au grows exclusively with fcc stacking on Pd(111). From atomically resolved STM images showing the former Pd step edges — see for instance fig. 4.9(a) after annealing at 600 K — this conclusion could be confirmed.

In figs. 3.3(c), 3.3(d), and 3.5(a) it can be seen that increasing the Au coverage to 0.24 ML – 0.5 ML leads to a considerable increase in the branch thickness of the dendritic islands. Although it has not been studied systematically how each of the two parameters Au coverage and temperature influence the island shapes, from the STM images presented in this section it seems to be likely that the deposition temperature has only a small effect on the island shapes. This can be demonstrated at least for 180 K $\leq$ T $\leq$ 355 K and 0.1 ML Au (figs. 3.1(c),(d) and 3.3(a),(b)). With increasing Au coverage the branch thickness of the dendritic islands increases and triangular shapes are visible for 0.5 ML deposited at 400 K (fig. 3.3(d)). These triangles might be close to the equilibrium island shape for submonolayer Au/Pd(111) films. In this case B steps with (111) facets would be the energetically more favourable steps.

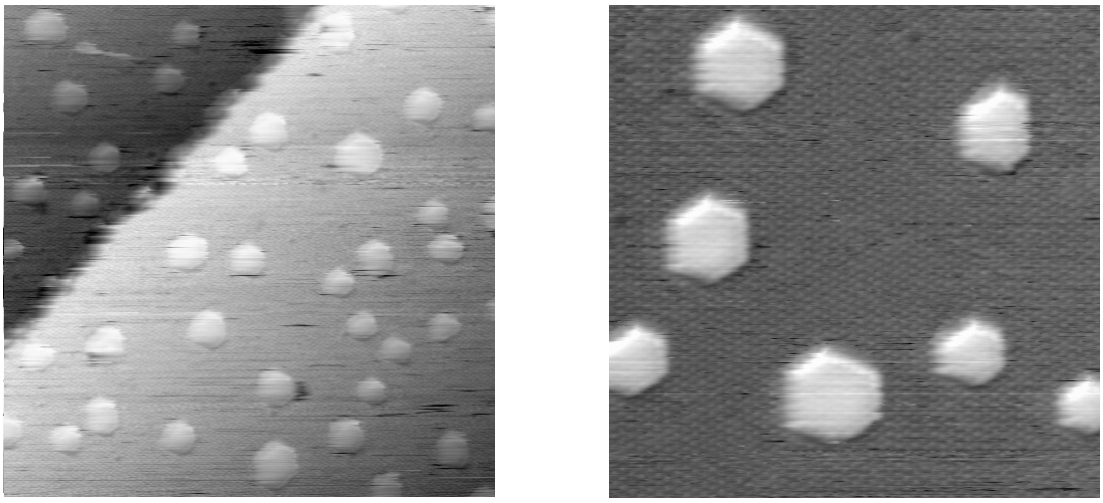

(a) 340 Å × 340 Å (b) 130 Å × 130 Å

Figure 3.4: Room temperature STM images of 0.1 ML Au deposited at 99 K (see fig. 3.1(a)) and warmed up to 300 K (10 h prior to the STM measurement).

Dendritic island shapes have also consequences for the reactivity of the surfaces. First, the total amount of Au atoms that are located at island edges is larger for dendritic islands compared to compact islands. Second, in the latter case mostly regular island edge atoms exist (coordination number 7), while in the former case a considerable amount of kink sites (coordination number 6) and possibly also of even lower coordinated sites is present on the surface. In part III of this thesis the reactivity of such sites towards CO adsorption will be examined. It was for example tested, how CO TPD spectra on 0.25 ML Au deposited at 114 K change with the number of TPD runs to 350 K. The result of annealing a low temperature deposited Au film (0.1 ML; T_{dep} = 99 K) at moderate temperatures (300 K) is shown in fig. 3.4. A comparison with the situation before annealing (fig. 3.1(a)) reveals that the island density is reduced to about one third[1], i. e., the average island size is still very small (∼50 atoms per island) and the relative amount of Au step edge atoms is still high (40% – 50%). However, the island shapes have changed to compact hexagonal islands. The comparison between figs. 3.3(a) and 3.4 reveals that the film morphology is largely governed by kinetic effects. In both images 0.1 ML Au/Pd(111) are shown at room temperature. The difference consists in the deposition temperature being 99 K vs. 298 K. For a system in thermodynamic equilibrium the memory of the preparation conditions would be lost and the same film structure should be visible in both cases. From

[1]Six STM images have been analysed for each of these two surfaces containing 703 islands and 155 islands for the non-annealed and for the annealed film, respectively.

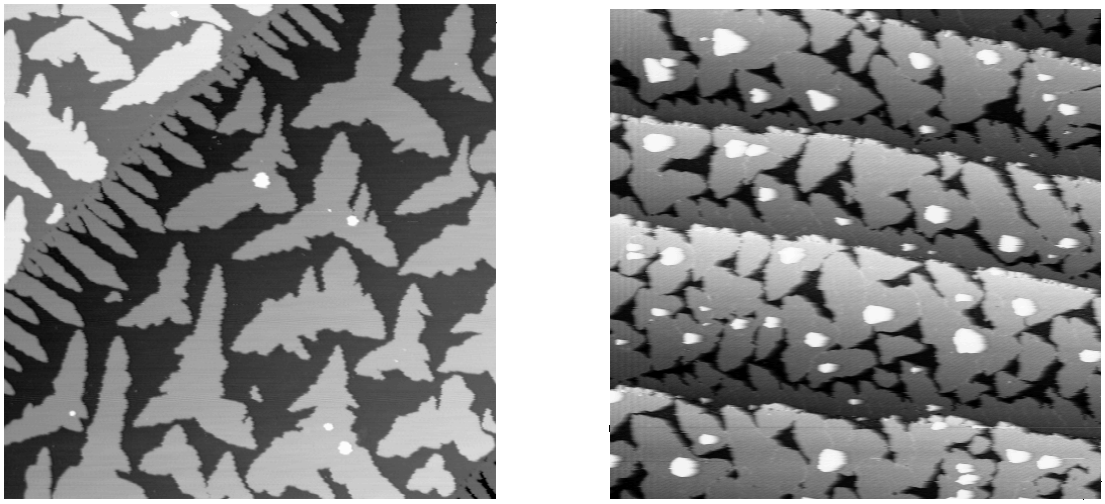

(a) 0.5 ML Au; $T_{dep} = 318$ K; 3400 Å × 3200 Å

(b) 0.7 ML Au; $T_{dep} = 305$ K; 3400 Å × 3250 Å

Figure 3.5: STM images of 0.5 ML and 0.7 ML Au deposited around room temperature; Au flux: ∼0.01 ML/s.

this observation it follows that the evaporation of Au atoms from island edges onto the terraces is a very slow process at 300 K, because otherwise the small islands in fig. 3.4 would have vanished. This can also be supported by a direct argument, because during STM experiments, where individual islands are observed over a period of several minutes, neither changes in the island shapes nor in the island sizes are noticed.

The effect of increasing the Au coverage around room temperature is shown in fig. 3.5. 0.5 ML and 0.7 ML have been deposited at 318 K and at 305 K, respectively. While in the former case most of the islands do not touch their neighbours, coalescence plays an important role in the latter case. As has been mentioned in the introduction to this chapter, there has been some controversy about whether or not this system exhibits layer-by-layer growth at room temperature. From the presence of second layer islands in fig. 3.5 it is evident that no perfect layer-by-layer growth occurs. However, it is also clear that the statement by Eisenhut about third layer Au atoms being present on 0.4 ML Au films can not be confirmed. Even with 0.7 ML Au only a low coverage of second layer islands is detectable and the nucleation of third layer island has not started yet. The film morphology for higher Au coverages will be presented below.

3.1.2 Determination of the Au adatom diffusion barrier on Pd(111)

The basic processes occuring during metal-on-metal epitaxy can be described in many cases by simple rate equations ("mean-field nucleation theory"). These describe the time evolution of clusters of different sizes during the deposition process and possibly also during a certain period of time after deposition. In the end, several quantities describing the film can be calculated and compared to experimental results, for example island densities or island size distributions. In the following, the assumptions will be explained, that have to be made in order to derive the equation that will be applied to evaluate the temperature dependent island densities measured for Au/Pd(111). It is not attempted to give any kind of overview over the broad field of nucleation theory. A review on this subject was given for instance by Venables in [55] and more recently by Brune [41]. In order to keep the rate equations relatively simple, the following assumptions have to be made:

- Only the case of "complete condensation" is considered, i. e., reevaporation of atoms from the surface into vacuum is not allowed.

- Only adatoms are mobile. Clusters consisting of 2 or more atoms do not move.

- The migration of the adatoms consists of hops between their equilibrium positions ("random walk") on the surface. The hopping rate is given by

$$h = \nu_0 e^{-\beta E_d} \tag{3.1}$$

  with $\beta = \frac{1}{kT}$, ν_0 being a frequency factor, and E_d being the diffusion barrier between two energy minima. The tracer diffusion coefficient D follows then from the Einstein relation: $D = \frac{1}{4}h$, if every quantity is related to the elementary atomic distances, or $D = \frac{1}{4}hl^2$ with l being the distance covered by one hop, if the quantities are given relative to an unit area.

- Coalescence of islands is negligible, i. e., only low coverages are described by the rate equations.

- With low coverages, also the effect of direct impingement of atoms on clusters or islands can be neglected.

Using these assumptions, a relatively simple set of rate equations can be derived that describes the time evolution of the densities n_j of clusters containing j atoms. With F being the flux of atoms onto the surface, σ_j being the so-called capture

numbers, that describe the island size dependence of the capture rate for adatoms, and γ_j being the probability for clusters of size j to lose an atom, one can write:

$$\frac{dn_1}{dt} = F - 2\sigma_1 D n_1^2 - n_1 \sum_{j\geq 2} \sigma_j D n_j + 2\gamma_2 n_2 + \sum_{j\geq 2} \gamma_j n_j \tag{3.2}$$

$$\frac{dn_j}{dt} = n_1(\sigma_{j-1} D n_{j-1} - \sigma_j D n_j) + \gamma_{j+1} n_{j+1} - \gamma_j n_j, \qquad (j > 1) \tag{3.3}$$

For an analytical solution of the rate equations additional approximations have to be made. The most important simplification consists in the definition of a "critical cluster size" i. During the nucleation and growth process there will be a cluster size, which mark the transition from preferred decay to preferred growth. However, in the "real" nucleation process it is still possible for clusters larger than i to lose atoms. In the concept of a critical cluster size this is not allowed, and therefore only the sum of all clusters (or islands) larger than i, which is termed n_x, has to be regarded in the the next step towards a solution of the rate equations. In the very beginning of the deposition process the density of adatoms (n_1) increases linearly with time. Then, first clusters are being formed and the adatom density growth rate is slowed down. Finally, a steady state will be reached, that is characterized by a constant adatom density, i. e., $\frac{dn_1}{dt} = 0$. For this steady state regime the following solution of the rate equations has been derived by Venables [56]:

$$n_x = const\, F^{\chi} e^{\left(\frac{iE_d + E_i}{(i+2)kT}\right)} \tag{3.4}$$

with the scaling exponent $\chi = i/(i+2)$ and the binding energy of the critical cluster E_i. Using this equation two sets of experiments — measuring $n_x^{T=const}(F)$ and $n_x^{F=const}(T)$, respectively — are needed to obtain both the critical cluster size i and the monomer diffusion barrier E_d. The latter follows directly for $i = 1$ and has to be corrected by the binding energy of the critical cluster E_i if $i \geq 1$.

For the system Au/Pd(111) island densities have been measured over a wide temperature range (99 K – 400 K) for $F = 0.01$ ML/s. An Arrhenius plot of the results is presented in fig. 3.6. It is obvious that between 120 K and 225 K the data points can be fit perfectly by a straight line as expected from equation 3.4 for a temperature intervall, where the critical cluster size stays constant. The slope of this line is 79.3 meV, and the statistical error can be estimated to be below 10% (see dashed lines in fig. 3.6). Unfortunately, the attempt to determine i in this temperature range was not successful, because the data points that were obtained from flux dependent measurements at 180 K scatter considerably (probably because of flux instabilities during deposition) and do not allow to decide between the two reasonable possibilities of $i = 1$ and $i = 2$. If $i = 1$ is assumed, a Au adatom diffusion barrier of (222 ± 22) meV follows from the STM measurements.

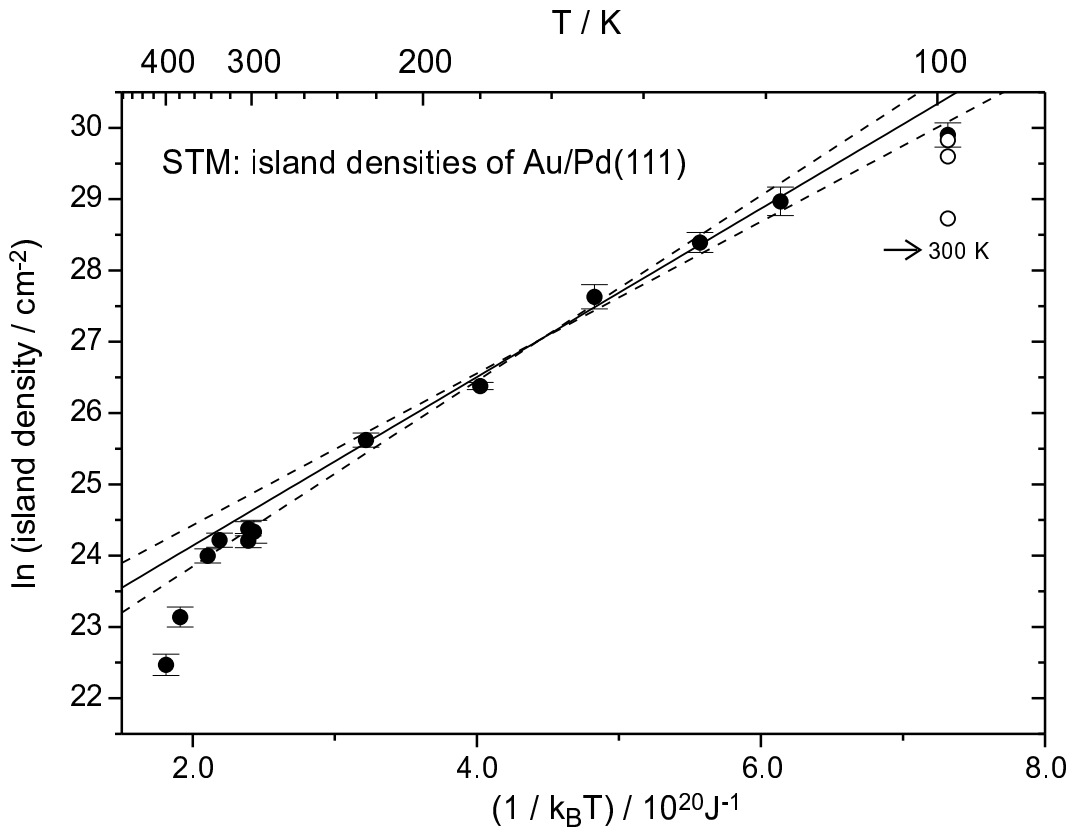

Figure 3.6: Arrhenius plot of Au island densities on Pd(111) measured by STM; Au flux: 0.010 ML/s. In the region 120 K–300 K the data points were fit linearly (slope: 73.9 meV; solid line) and two lines with 10% lower and higher slopes, respectively, (dashed lines) have been added to the figure as an estimate of the statistical error. The open circles at 99 K show the results of the following film preparations (from high to low island densities): 0.06 ML and 0.03 ML deposited and measured at 99 K and 0.1 ML deposited at 99 K and measured after $\sim$10 h at 300 K.

For $i = 2$ the situation is less clear because the Au dimer binding energy on Pd(111) (E_2) has to be known. From equation 3.4 the following relationship between the slope m of the Arrhenius plot and E_d can be obtained ($i = 2$): $E_d = (4m - E_2)/2$. Consequently, for a physically reasonable positive value for E_d, E_2 has to be below 296 meV. For example for $E_2 = 250(200)$ meV E_d becomes 23(48) meV. Since for the related growth system Ag/Pt(111) a dimer binding energy of 320 ± 20 meV was estimated by Brune et al. [57] a value lower than 200 meV in the case of Au/Pd(111) seems unrealistic. On the contrary, for Au dimers even higher binding energies should be expected than for Ag dimers based on the higher cohesive energy of Au compared to Ag, which supports the assumption of $i = 1$ in the linear region. There is another, more direct argument for $i = 1$ being true. A low temperature breakpoint of the Arrheniusplot can be seen around 110 K. This is slightly below the value, where for Ag/Pt(111) the transition from $i = 1$ to $i = 2$ is observed. However, the above mentioned value of $E_2 = 320$ meV for the binding energy of Ag dimers on Pt(111) is an immeditate consequence of this transition temperature obtained by assuming the dimer decay to proceed on the time scale of seconds at T=120 K. This would mean (still assuming $i = 2$ for T $\geq$ 120 K) that the dimer binding energy of Au on Pd(111) is similar to that of Ag on Pt(111) (320 ± 20 meV). As it was shown above, this leads to an unrealisticly low and even to a negative Au adatom diffusion barrier on Pd(111).

In short, for the Au adatom diffusion barrier on Pd(111) a value of (222 ± 22) meV can be derived although some uncertainties about the justification of $i = 1$ remain. This value appears to be reasonable if it is compared to the Pd self-diffusion energy barrier determined by Steltenpohl to 350 meV [58] and to the work of Brune et al. on Ag/Pt(111) with $E_d = 157 \pm 10$ meV [57]. The much lower value for E_d that would result if $i = 2$ was correct ($\sim$50 meV) deviates strongly from these reference values.

3.2 Monolayer and multilayer Au films

3.2.1 Morphology of 1 ML Au for different deposition temperatures

The purpose of this short section is to discuss the possibility of preparing a homogeneous 1 layer thick Au film on Pd(111). In fig. 3.7 several STM images for $\sim$1 ML Au deposited at different temperatures onto Pd(111) are displayed. The image sizes are almost identical except of fig. 3.7(a), where low temperature deposition (110 K) leads to structures on a smaller length scale than in the other cases and therefore an image on a smaller area was selected. Due to the limited resolution of the STM at low temperatures the structure of the first Au layer could

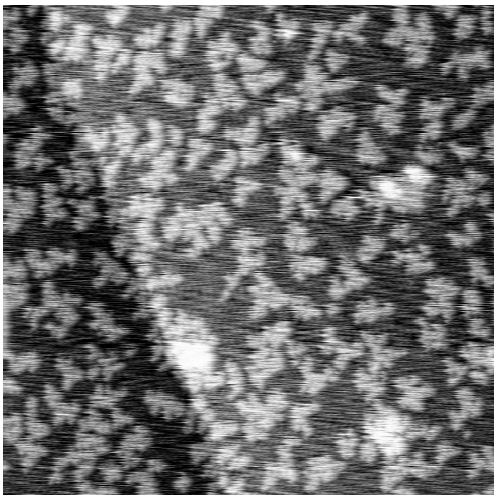

(a) 1.1 ML, $T_{dep} = 110$ K, 825 Å × 820 Å; $I_t = 1.3$ nA, $U_t = +650$ mV

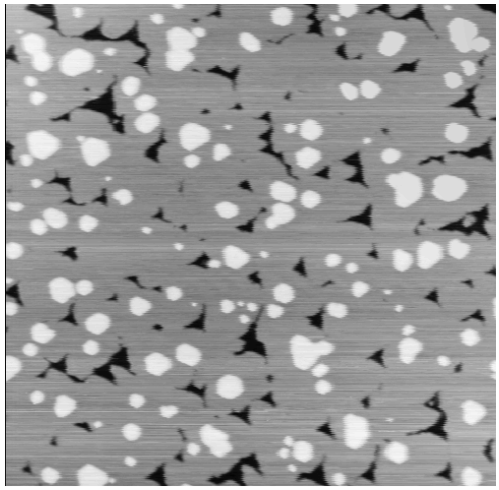

(b) 1.05 ML, $T_{dep} = 310$ K, 3300 Å × 3300 Å; $I_t = 1.0$ nA, $U_t =$ -500 mV

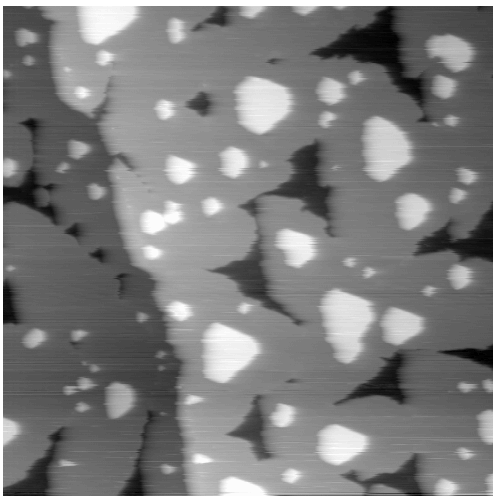

(c) 0.94 ML, $T_{dep} = 354$ K, 3390 Å × 3200 Å; $I_t = 2.0$ nA, $U_t =$ -900 mV

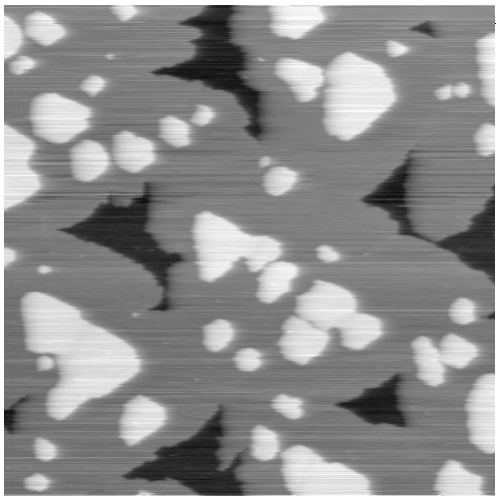

(d) 1.05 ML, $T_{dep} = 400$ K, 3300 Å × 3300 Å; $I_t = 1.8$ nA, $U_t =$ -1.0 V

Figure 3.7: STM images of ~ 1 ML Au deposited at different temperatures. Note the smaller image size in (a).

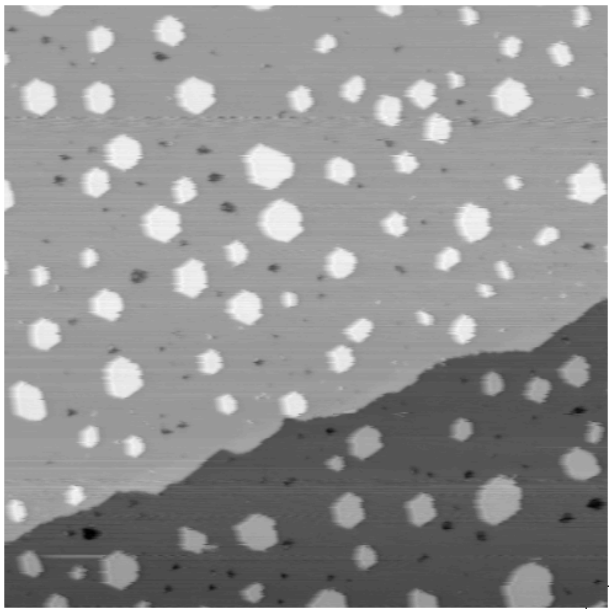

Figure 3.8: STM image of 1.1 ML Au deposited at 110 K and annealed at 400 K for 5 min; 820 Å × 820 Å.

not be resolved in this image and the dominating visible features are second layer Au islands. Also some small islands in the third Au layer can be seen. On the other images (T_{dep}=310/354/400 K) both holes in the first Au layer and islands in the second Au layer are apparent, but no third layer islands exist on these films. In table 3.1 the filling factors of the different layers on large terraces are compared for these films. These were obtained by analysing six STM images for the films deposited at 110 K and at 310 K, one for the film deposited at 354 K, and two for the film deposited at 400 K. Taking into account that for the 354 K film the Au coverage was slightly below 1 ML, a clear trend can be observed between 310 K and 400 K towards flatter growth at *lower* temperatures. This is contra-intuitive, since in a naive approach one could assume that a higher adatom mobility leads to an enhanced interlayer mass transport at higher temperatures. On areas with a smaller average terrace width this behaviour is indeed observed. For instance, on the film with 1.05 ML Au deposited at 400 K the nucleation of second layer islands is not observed on terraces smaller than 500 Å and consequently in these areas almost no free Pd patches are visible.

On sufficiently large terraces several factors determine the film morphology: The island density and hence the average island size in the first layer depends strongly on deposition temperature. Generally, on larger islands it is easier for impinging adatoms to form a second layer island. But also the mobility of the adatoms in the second layer will be higher at elevated temperatures with the consequence of a larger mean island separation. Consequently, at higher temper-

$T_{dep}(T_{anneal})$/K	Au coverage/ML	filling of 1. layer	filling of 2. layer
110 (400)	∼1.1	0.98	0.09
310	1.05	0.95	0.10
354	0.94	0.86	0.08
400	1.05	0.89	0.16

Table 3.1: Filling of different layers for 1 ML Au. The accuracy of the values is about ±0.03 ML.

atures second layer islands will only form on larger first layer islands than at lower temperatures. For homoepitaxial systems, these effects have been analysed by J. Meyer et al. using an analytical model [49]. Additionally, as a "second-order" effect, the island shapes might depend on temperature leading to concomittant changes in the effective ES barriers. However, the latter effect should be only small in the case of Au/Pd(111) as can be judged from the similarity of the shapes observable in figs. 3.7(b)–(d). It seems that the two factors that were mentioned first almost cancel each other for this system with a small advantage on the side of increased nucleation in the second layer at higher temperatures.

In table 3.1 also the values for the film that was deposited at 110 K are included, but only after annealing at 400 K for 5 min. An STM image of this surface is shown in fig. 3.8. It can be seen that this preparation method leads to the best results concerning the filling of the first layer. Because of the enhanced chemical activity of Au edge atoms it might prove disadvantageous that many small holes with a relatively large total boundary length are left in the first layer. Consequently, it seems that for a complete covering of the Pd substrate substantially higher Au coverages than 1 ML are needed. On page 185 an image with 1.5 ML Au (T_{dep}=320 K) will be presented (fig. 5.19(a)), which demonstrates that with this coverage the density and the total area of holes in the first layer have become negligibly small. It should be added that the STM images that have been selected as illustration for the present discussion show exceptionally large terraces. On smaller terraces, the nucleation of second layer islands is inhibited if the terrace width is smaller than a temperature-dependent critical value. The proportion of free Pd areas, that are contributing to area-integrating spectroscopic measurements (e. g., HREELS and TPD), are averaged values over macroscopic distances (mm), and should be below the values given in table 3.1. Only for the low temperature deposited film almost no difference between large and small terraces should be expected because of the small dimensions of the hole and island structure.

3.2.2 Multilayer Au/Pd(111) films: Morphology and strain relief patterns

It has been pointed out in the section on submonolayer Au films, that the structure of the Au/Pd(111) surfaces presented in this section are largely determined by kinetic factors. Therefore, it can not be attempted to derive any conclusion about the growth mode of Au on Pd(111) in the thermodynamic sense [59]. Instead, the objective of the following presentation of STM measurements on multilayer Au films is to gain insight into the strain relaxation mechanisms of Au/Pd(111). A short introduction to this topic will be given first in order to provide some background information for the following discussion.

The importance of strain effects in heteroepitaxial growth continues to trigger many investigations on this subject (for a recent review see [40]). The origin of the strain in heteroepitaxial layers of deposit B on substrate A is the so-called lattice misfit $m = (a_B - a_A)/a_A$, which is a measure for the difference in the lattice constants a of the overlayer and the substrate material, respectively. The strain is roughly proportional to the layer thickness. Therefore, it is often found, that a few layers grow pseudomorphically and that after a critical layer thickness defects are incorporated into the layer (and/or into the substrate) in order to reduce the strain. Depending on the sign of the misfit, two types of strain can be distinguished: compressive strain for positive m (the overlayer material has the larger lattice constant) and tensile strain for negative m (the substrate material has the larger lattice constant). As examples for these different classes the systems Cu/Ru(0001) ($m = -5.8\%$, tensile strain) [60], Ag/Ru(0001) ($m = 6.8\%$, compressive strain) [61], and Ag/Pt(111) ($m = 4.3\%$, compressive strain) [57, 62, 63] can be mentioned.

Annealed (500 K – 600 K) Cu films on Ru(0001) exhibit a pseudomorphic first monolayer, while for local coverages ≥ 2 ML a sequence of different strain-relaxation patterns is observed that are characterized by a continuously decreasing lattice parameter in the Cu overlayer. For example, in the second layer a characteristic double stripe pattern appears, where the Cu atoms have reached almost their Cu bulk spacing in the direction perpendicular to the stripes. But they have still the Ru spacing in the direction parallel to the stripes. The stripes separate regions with different stacking (hcp and fcc) and appear higher (brighter) in the STM images, because the Cu atoms are located near to bridge positions, which results — in a simple hard sphere model — indeed in geometrically higher atom positions compared to atoms in hollow sites. These effects are illustrated in fig. 3.11 on page 54 for the relief of compressive strain. A similar behaviour is found in the Au(111)-$(22 \times \sqrt{3})$ herringbone reconstruction, that can serve as another example for relief of tensile strain in the surface layer [64].

As examples for systems that exhibit compressive strain in the overlayer and that are therefore of higher relevance for the following discussion of Au/Pd(111)

two cases will be mentioned. A surprising STM observation has been reported by Hwang et al. on the Ag/Ru(0001) system [61]: The first monolayer of Ag exhibits a strain relief pattern that has many common features with the well-known ($22 \times \sqrt{3}$)-herringbone reconstruction of Au(111) (coexistence of fcc and hcp regions separated by domain walls), but it differs in one important respect from this reference system. On Ag/Ru(0001) the regions with the surface atoms located in hollow sites (either fcc or hcp) are imaged brighter (higher) than the areas where the atoms occupy lower coordinated sites. If the substrate is considered to be frozen and the Ag atoms are modelled by hard spheres, the STM images for Ag/Ru(0001) could not be regarded as a realistic measure of the surface topography and strong electronic effects would have to be assumed. However, Hwang et al. showed by EAM calculations that the Ru(0001) substrate exhibits a substantial inhomogeneous vertical relaxation, which is sufficient to account for the height difference observed in the STM images. Consequently, the STM measurements could be explained without taking electronic effects into account.

For Ag/Pt(111), which exhibits a similar misfit as Au/Pd(111) (4.3.% for Ag/Pt(111) compared to 4.7% for Au/Pd(111)), the appearance of dark stripes separating regions with different stacking has been reported in an STM study by Brune et al. [57] prior to the above mentioned work on Ag/Ru(0001). However, in this publication the mentioned electronic effects were put forward as explanation for the discrepancy between the surface topography as imaged by STM and the topography that would be expected from a hard sphere model. In a later paper, also for Ag/Pt(111) substrate buckling was confirmed as origin of the unexpected surface morphology [63]. The stacking of Ag on Pt(111) has been analysed by Rangelov et al. using photoelectron diffraction [62]. Depending on deposition or annealing temperature either hcp (room temperature deposition) or fcc stacking (annealing at 750 K) has been found to prevail for the second Ag layer on a pseudomorphic first layer. Unfortunately, neither for Ag/Ru(0001) nor for Ag/Pt(111) any atomically resolved STM images are included in the above mentioned publications and therefore no direct information on the atomic structure of the surfaces is available.

Examples of STM results that were obtained in this work for multilayer Au films on Pd(111) are displayed in figs. 3.9 (large-scale images) and 3.10 (atomically resolved images). Before these images will be analysed, one important observation from submonolayer films should be recalled. The absence of any corrugation on the length-scale of a few hundred Å shows indirectly that the first Au layer grows pseudomorphically. Otherwise, the existence of inequivalent sites would lead to some kind of strain-relief pattern. For coverages above one monolayer, however, such patterns are clearly visible in the STM images. Second layer Au islands grow pseudomorphically up to an island size of about 250 Å. In larger second layer Au areas distinct double stripes, that are imaged lower by about 0.1 Å–0.2 Å than the surrounding areas, are indicative for a lo-

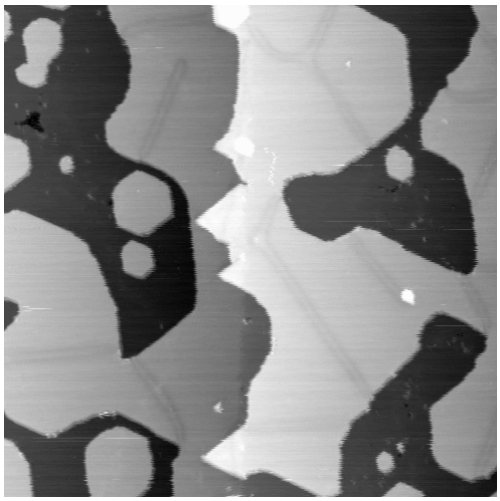

(a) 1.7 ML, $T_{dep} = 317\,K$, 1400 Å × 1300 Å

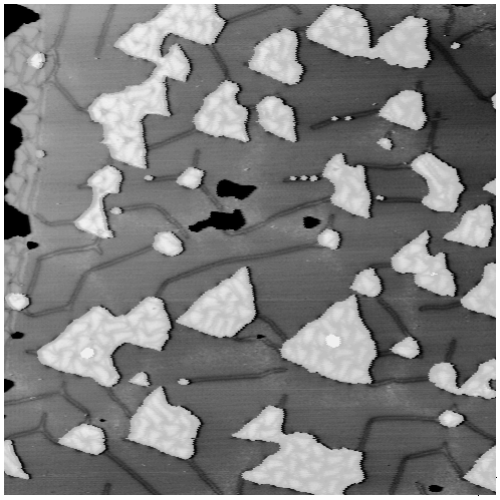

(b) 2.2 ML, $T_{dep} = 400\,K$, 3470 Å × 3310 Å

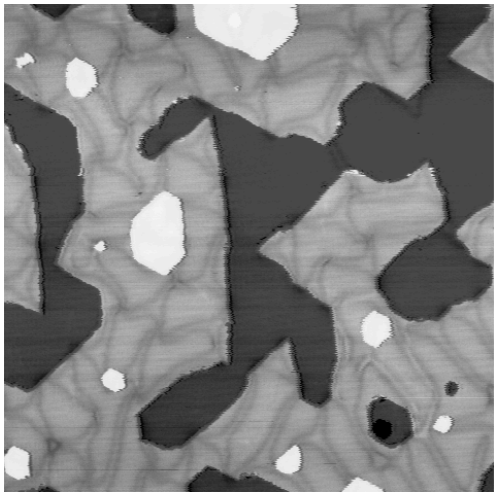

(c) 2.7 ML, $T_{dep} = 300\,K$, 1370 Å × 1070 Å

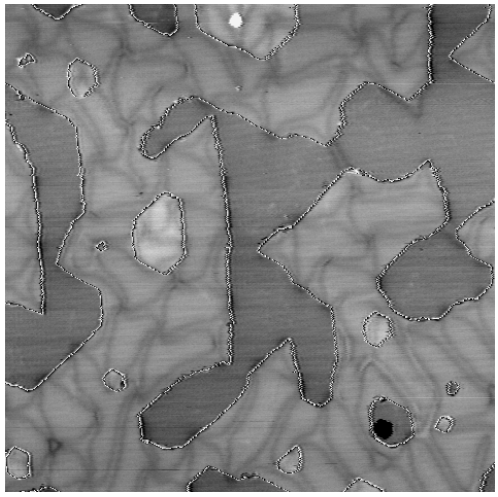

(d) high contrast colouring of (c)

Figure 3.9: STM images of multilayer Au films deposited at temperatures above 300 K. Note the larger image size in (b).

cal deviation from pseudomorphic growth (see fig. 3.9(a)). Sometimes, especially when using low resistance tunnel parameters for atomic resolution, the double stripes are imaged as only a single stripe, as can be seen in fig. 3.10(a). The distance between these double stripes varies strongly and depends on the local film morphology (step edges, 3rd layer islands, holes) as can be seen in fig. 3.9(b). However, there is no significant correlation between the stripe pattern and the deposition temperature in the range 300 K – 400 K. Typically, the double stripes are 200 Å– 300 Å (i. e., about 70 – 110 atom spacings) apart. These distances are considerably larger than the spacings between the stripes observed on the related system Ag/Pt(111), where typically only about 35 Å separate neighbouring double stripes in the second layer. In the third Au layer on Pd(111) the stripe pattern becomes considerably denser as can be seen in figs. 3.9(c) and 3.9(d). Very frequently, three double stripes originate in spiral structures that are typically about 150 Å apart and are often found to be decorated by fourth layer Au islands. Depending on the local film structure (islands, holes), the stripe pattern in the third Au layer can either be described to consist of pairs of stripes that run more or less parallel or to consist of triangular structures. Within the former structure, the separation of the two stripes within a double stripe is about 10 atoms spacings (28 Å), while two neighbouring double stripes are about 100 Å apart.

The atomic surface structure of the stripes found in the second Au layer as well as the spiral structures and the double stripes in the third Au layer are displayed in fig. 3.10. The corrugation visible in the two latter cases is unusual compared to the large-scale images (fig. 3.9) as it shows a distinct elevation of the area within a double stripe. This might be the consequence of the lower tunnel resistance used for recording the atomically resolved images. Besides the already mentioned stripe structures also disordered and less distinct height modulations are detectable in fig. 3.10(b) on the third Au layer. In the examples that were mentioned above for relief of tensile strain in the surface layer (Au(111) and Cu/Ru(0001)) a common observation is the transition from fcc to hcp stacking, which is accompanied by a distinct lateral displacement of the surface atoms from the positions of an ideal hexagonal lattice. The white straight lines that have been added to the STM images of fig. 3.10 should help to recognize possible lateral displacements of the surface atoms in the case of Au/Pd(111). On the second Au layer (fig. 3.10(a)) the deviations of the atom positions from the straight line are too small to be unambiguously detectable in the STM images. In the third layer the hexagonal arrangement of the surface atoms seems to be also almost undisturbed by the double stripes (fig. 3.10(b)). Only in the immediate vicinity of a spiral considerable deviations of the close-packed atom rows from straight lines become obvious (fig. 3.10(b)).

A straightforward explanation for the occurance of the double stripes in the second Au layer would be a film structure, where the surface layer is locally, i. e.,

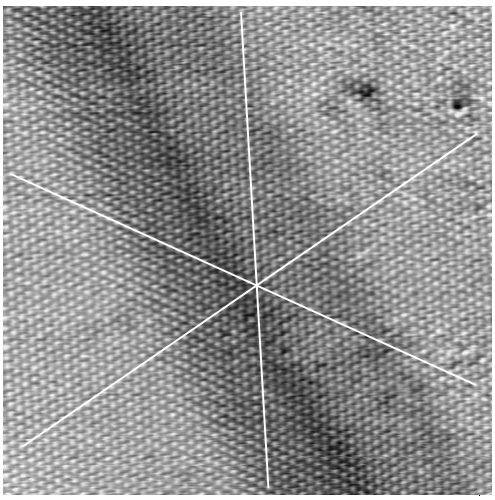

(a) 1.4 ML, area on second Au layer; 140 Å × 140 Å, $I_t = 32$ nA, $U_t = +4$ mV

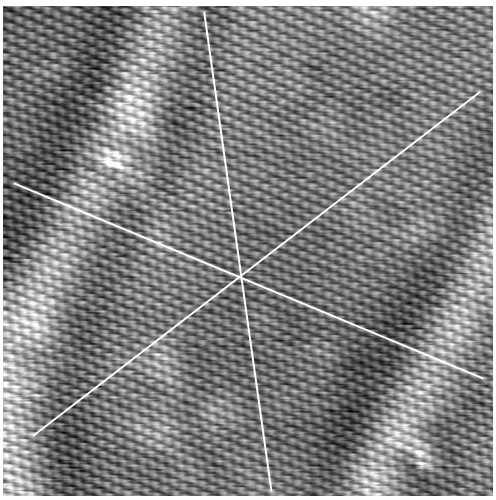

(b) 2.7 ML, area on third Au layer; 125 Å × 125 Å, $I_t = 10$ nA, $U_t = +2$ mV

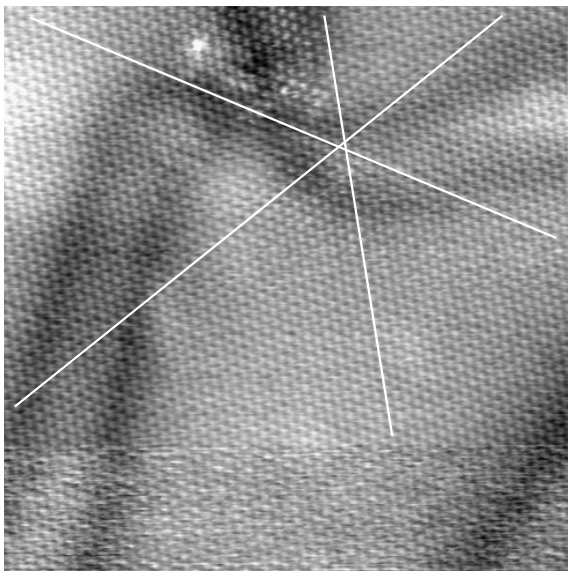

(c) 2.7 ML, area on third Au layer; 140 Å × 140 Å, $I_t = 10$ nA, $U_t = +5$ mV

Figure 3.10: Atomically resolved STM images of strain relief patterns on multilayer Au films deposited around room temperature. The white straight lines are drawn along the close-packed atom rows in order to emphasize lattice distortions.

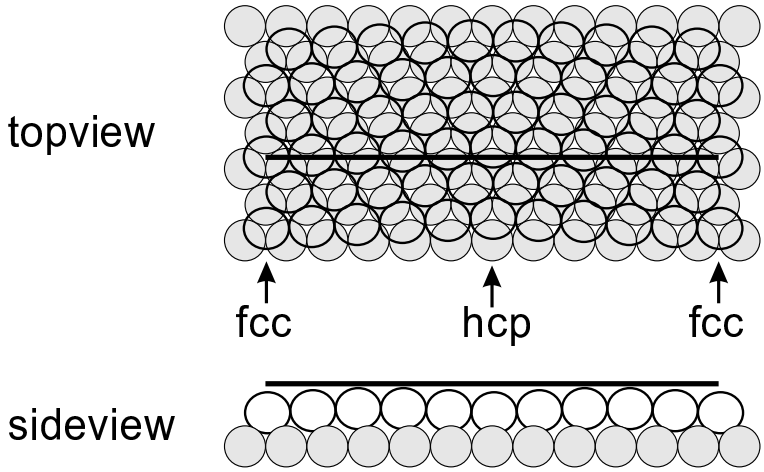

Figure 3.11: Hard sphere model for a possible relief mechanism of compressive strain in the surface layer (surface atoms: open circles; second layer atoms: gray circles). The black lines are drawn to emphasize the lateral and vertical undulations of the atom rows if the atom positions change gradually, i. e., via bridge sites, from fcc to hcp sites and back to fcc sites.

at the stripe positions, expanded in the direction perpendicular to the stripes. This is illustrated in fig. 3.11. However, three observations can be put forward as arguments against this proposition:

1. In atomically resolved STM images no significant difference in the atom spacings can be detected. For instance in fig. 3.10(a) constant atom spacings are found along the white line that is perpendicular to the dark stripe. If the latter would be caused by the accommodation of (n-1) surface layer Au atoms on n second layer atoms, the lattice constant in the ~ 20 atoms wide stripe should be $\sim 5\%$ larger than in the other sections of the white line.

2. No lateral displacements of the atoms in the direction parallel to the dark stripe (fig. 3.10(a)) is visible. In the case of a locally expanded surface layer a transition from fcc to hcp stacking and back to fcc stacking is to be expected. This would be accompanied by a measurable lateral undulation of the atom rows, as is demonstrated in the topview model shown in fig. 3.11.

3. The fact that the second layer stripes appear darker than their surroundings is in contradiction to the transition that is mentioned in the preceeding point, because it would require the occupation of "higher" bridge positions, which is illustrated in the sideview model of fig. 3.11.

As has been shown by the above discussion, the stripe patterns in the second and the third Au layers can not be explained simply by placing a locally expanded

surface layer onto an unmodified hexagonal underlayer. Since for other systems that exhibit compressive strain and that also show dark stripes in STM images (Ag/Ru(0001) and Ag/Pt(111)) substrate relaxations have been demonstrated by EAM calculations to be responsible for the stripe patterns [61, 63], also in the present case such deeper lattice distortions are likely to occur. However, STM shows only the positions of the surface layer atoms and therefore no direct information on the nature of these distortions is available. With experimental methods that are sensitive to the positions of subsurface atoms (HEIS [44] and XPD [46]) it has been found earlier that lateral lattice distortions occur from the second Au layer on. A direct proof for substrate Pd atoms to move out of registry with deeper Pd layers was provided by high energy ion scattering experiments along the $[00\bar{1}]$ direction that were performed by Kuk et al. [44]. They found for $\theta_{\mathrm{Au}} \geq 2\,\mathrm{ML}$ higher He^+ ion yields from Pd atoms than observed from pure Pd(111). Therefore, not only Au overlayer atoms have to be laterally displaced, but also Pd substrate atoms.

In short, it has been shown that the first layer of Au grows pseudomorphically on Pd(111). First dislocation structures are observed already in the second Au layer, but their density is only very small. This might be the reason for the deviations between the results from earlier XPD (3 pseudomorphic layers [46]) and HEIS (1 pseumorphic layer [44]) measurements. The atomic structure of the strain relief patterns indicate the importance of subsurface relaxation effects. Despite the slightly larger misfit for Au/Pd(111) compared to Ag/Pt(111) the strain effects are generally more pronounced in the latter case (higher density of dislocation stripes in the second adlayer). This might be explainable qualitatively by the larger tendency of Au to form a surface layer that is contracted compared to the bulk spacing, as can be seen from the stable reconstructions on all low index Au surfaces. If the atom density in the Au(111)-$(22 \times \sqrt{3})$ surface is compared to the atom density within the Pd(111) surface, it is found that the deviation is not very large ($1.45 \cdot 10^{15}\mathrm{cm}^{-2}$ for the Au-$(22 \times \sqrt{3})$ surface compared to $1.39 \cdot 10^{15}\mathrm{cm}^{-2}$ for close-packed atom layers in the Au bulk and to $1.53 \cdot 10^{15}\mathrm{cm}^{-2}$ for Pd(111)). Hence, it is not surprising that the first Au layer on Pd(111) grows pseudomorphically. Also for thicker Au films the surface layer tends to have only a slightly lower atom density than the Pd(111) substrate, whereas subsurface Au layers most likely adopt average lattice constants that are above the values for Pd(111) and also above the value for the Au surface layer. This might be the reason for the observed buried dislocation lines.

3.3 Conclusions: Au growth on Pd(111)

Au overlayer structures were prepared on Pd(111) by deposition of 0.1 ML – $\sim$3 ML Au at T $\leq$ 400 K. The amount of interdiffusion between Au and Pd is

found to be negligible at these temperatures. Using Au fluxes around 0.01 ML/s and coverages up to 0.4 ML, dendritically shaped Au islands are observed in a broad temperature intervall (180 K–400 K). From the measurement of temperature dependent island densities the Au adatom diffusion barrier on Pd(111) could be determined to (222±22) meV assuming a critical cluster size of 1 for $T \leq 225$ K. At no temperature a perfect layer-by-layer growth has been observed. In a series of experiments with $\Theta_{Au} \approx 1$ ML it has been revealed that on sufficiently large terraces second layer Au islands are formed prior to the completion of the first layer. The "flattest" 1 ML thick Au overlayer could be obtained by Au deposition at 110 K and subsequent annealing at 400 K. While the first Au layer grows pseudomorphically, multilayer Au films are characterized by strain relief patterns that appear as dark stripes in most of the STM images. From atomically resolved STM images it was inferred that the surface morphology can not be explained by assuming a distorted surface layer on a rigid substrate. Relaxations in subsurface layers are necessary to accout for the surface structures.

Chapter 4

AuPd(111) surface alloy formation

Bimetallic systems can be classified according to their miscibility in the solid phase. One important class consists of systems that are miscible at any composition in the bulk. Au-Pd belongs to this class. Furthermore, Au, Pd, and the AuPd alloys exhibit the fcc crystal structure, and the lattice mismatch between Au and Pd is only modest with 5%. Another characteristic feature of the Au-Pd system is the weak tendency to form ordered structures. Two ordered phases have been detected (Au_3Pd and $AuPd_3$) for $T \leq 1123\,K$ and for $T \leq 1143\,K$, respectively, which both exhibit the cubic $AuCu_3$ structure [65]. With Au-Pd(111) a system has been chosen that is supposedly as "simple" as possible with regard to alloy formation. For instance, the Pd(111) substrate is not reconstructed and therefore no complications due to the lifting or formation of reconstructions are to be encountered[1]. Also, around room temperature, where for most experiments Au deposition was carried out, the exchange rate between Au and Pd atoms is negligible. Therefore, most annealing experiments started from the well-defined film compositions and structures that have been analysed in the previous chapter. The investigation of near-surface interdiffusion processes of Au-Pd(111) can be regarded as a prototype study, the results of which might be applicable also to other systems with the above mentioned properties.

In table 4.1 several examples for metal-on-metal systems are given, for which the formation of surface alloys[2] has been investigated experimentally. A recent review on this topic that concentrates on systems which are immiscible in the bulk is given by Besenbacher, Nielsen, and Sprunger in [19]. The classification

[1] With Au coverages below 4 ML, the tendency of Au to form reconstructed surfaces is not strong enough to result in a reconstructed surface layer.

[2] Here, the term "surface alloy" is used to describe all systems, where one or more mixed layers exist on an otherwise pure bulk material (this nomenclature is also used, for instance, in [19]).

class	examples	references
reconstructed substrates	Ni-Au(111)-$(22 \times \sqrt{3})$	[66, 67]
	Pd-Au(111)-$(22 \times \sqrt{3})$	[68]
	Ni-Au(110)-(1×2)	[69]
	Cu-Au(110)-(1×2)	[16, 70]
open substrates	Mn-Cu(100)	[71–73]
	Ni-Cu(100)	[74]
	Pd-Cu(100)	[21, 75]
	Ag-Cu(100)	[76]
	Pb-Cu(100)	[13, 14]
	Mn-Ag(100)	[77]
	Rh-Ag(100)	[78]
	Pd-Ni(110)	[79]
	Au-Ni(110)	[17]
	Au-Ag(110)	[80]
close-packed substrates	Co-Re(0001)	[81]
	Pt-Ru(0001)	[82]
	Au-Ni(111)	[18, 19]
	Sn-Pd(111)	[83]
	Re-Pt(111)	[84]
	Co-Pt(111)	[85]
	Ag-Pt(111)	[86]
	Sn-Pt(111)	[87, 88]
	Pb-Cu(111)	[12]
	Pd-Cu(111)	[22]
	Pt-Cu(111)	[89]
	Ni-Ag(111)	[43]
	Cu-Pb(111)	[90, 91]

Table 4.1: Examples for metal-on-metal systems that have been reported to form surface alloys. They are sorted into three classes according to the substrate structure. The latter was chosen as sorting criterion, because it determines the elementary exchange processes that lead to surface alloy formation.

into the three different classes of reconstructed, open, and close-packed substrates accounts for the fact that the energy barriers for the atomic exchange processes that are necessary for alloy formation strongly depend on the substrate structure. On reconstructed surfaces and on open surfaces either a part or all surface atoms are less strongly bonded to the surface than on close-packed surfaces. Hence, in the latter case, the formation of surface alloys generally requires higher temperatures in order to allow the necessary exchange processes. Since the Au-Pd(111) system belongs to the alloy class on non-reconstructed close-packed substrates, previous investigations on systems of the same class might provide supplementary information for the interpretation and discussion of the experimental data presented in this chapter. However, only for two of these systems (Pb-Cu(111) by Nagl et al. [12] and Pd-Cu(111) by Aaen et al. [22]) extensive STM measurements have been performed that concentrate on similar aspects of the alloying process as the present study.

For Au-Pd(111) the formation of an alloyed surface phase has been reported by Weissman-Wenocur and coworkers [92]. They analysed the electronic structure of Au-Pd(111) surface alloys, that were prepared by depositing 0.1 ML to 10 ML Au at room temperature and annealing for a few seconds at $\sim$670 K. For the microscopic aspects that will be addressed in this section not much information can be extracted from that work. In a combined LEED, AES, TPD, and HREELS work of Baddeley et al. on the alloy formation and the chemical activity of Au-Pd(111) several important observations have been reported. From the decrease of the relative Au AES intensity upon annealing at $T \geq 600$ K they inferred that Au-Pd interdiffusion starts at this temperature. From LEED measurements on a 4 ML Au film, they concluded that the lattice parameter in the surface layer of this film corresponds to the Au bulk value. Upon annealing, the lower lattice constant of Pd(111) is gradually approached with a first decrease observable at 600 K. At no stages of the annealing process any ordered structures were observed.

The presentation of the experimental results will be devided into 5 sections. It will be shown that upon annealing of submonolayer Au films — or more precisely of films where the Pd substrate is still partially exposed — different interdiffusion processes occur at the same time, while on completely Au covered surfaces the observed alloy structures can be explained by assuming only one type of process. Consequently, the two cases of submonolayer and monolayer Au films on the one hand and multilayer Au films on the other hand will be treated separately. In a third, short section a few experiments on the formation of surface alloys by Au deposition at elevated temperatures will be presented. These were mainly performed to explore an additional method for the preparation of AuPd(111) surface alloys with specific compositional properties, that might be useful for reaction studies. One important aspect of the surface alloys will be investigated in the fourth section for submonolayer and multilayer Au films, namely the distribution of the elements on the atomic scale. I. e., it will be examined whether

the elements are randomly distributed or whether deviations from a statistical (maximum entropy) distribution can be observed. While in the first four sections on STM results the discussion will be restricted mainly to qualitative aspects (e. g., the identification of different elementary diffusion and exchange processes) it was attempted to obtain quantitative information on the interdiffusion kinetics by studying the alloying process using AES combined with numerical simulations.

4.1 Annealing of partially Au covered Pd(111)

Annealing of submonolayer Au films on Pd(111) produces two different, but closely related effects:

1. The film morphology is changed with the general tendency to replace small structures like islands or narrow Au fingers growing off Pd step edges by larger structures with smoother boundaries. While these phenomena can be interpreted as an equilibration process of the surface morphology that is also to be expected for homoepitaxial systems, a closer look reveals that the morphological changes observed on Au-Pd(111) surfaces are accompanied by the formation of inhomogenities in certain parts of the surface. Large-scale STM images show slight variations of the surface height (0.1–0.2 Å), that can not be explained by a mere coexistence of pure Pd and pure Au surface areas as it is the case for the Au/Pd(111) surfaces prior to annealing.

2. From atomically and chemically resolved STM images the surface composition of the different areas that are distinguishable in larger-scale images can be determined with high accuracy. This provides the information that is necessary to draw conclusions regarding the atomic processes which lead to the morphological and compositional changes on the surface.

4.1.1 Changes in film morphology by annealing

Submonolayer Au films, that are deposited around room temperature show first significant changes in their structure after annealing at 550 K. This is demonstrated in fig. 4.1, where two STM images of a 0.2 ML film recorded before and after the annealing step, respectively, are compared. The image sizes, the step widths, and the step directions in both images are almost equal and therefore the two images can be directly compared with each other, even though they do not display the same surface area. Fig. 4.1(b) has been coloured by using the full colour range for each terrace and therefore an artificial white to black transition is visible at the island and step edges. This colouring method yields high contrast, and small height variations on the different terraces are emphasized. It will be applied for most of the images presented in this section. In fig. 4.1(a) relatively

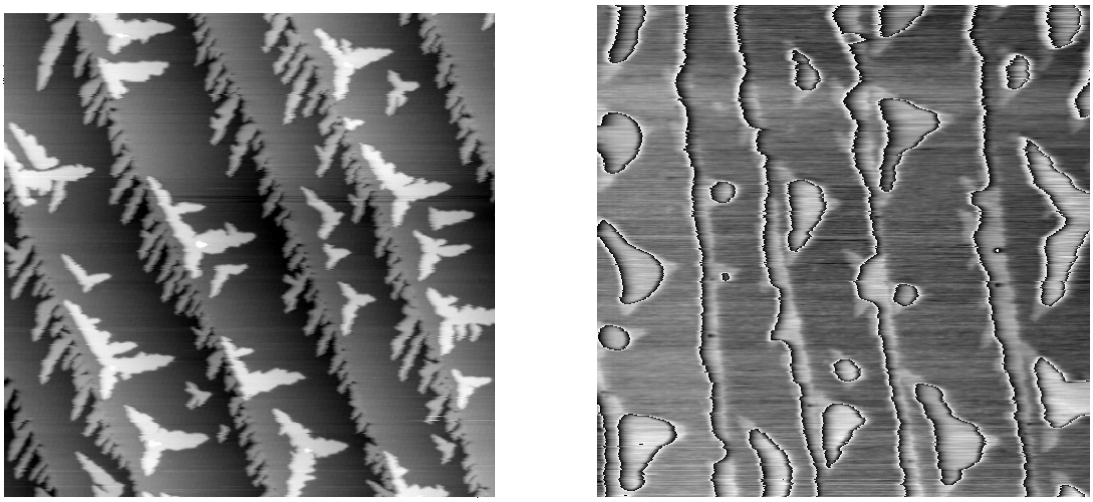

(a) before annealing; $I_t = 5\,nA$, $U_t = +150\,mV$

(b) after 5 min at 550 K; $I_t = 1.8\,nA$, $U_t = +1.1\,V$

Figure 4.1: STM images of 0.2 ML Au deposited at 303 K and annealed for 5 min at 550 K. In (b) each terrace has been coloured using the complete colour range to enhance the contrast. Image sizes: 3350 Å × 3350 Å.

large dendritic Au islands (typical sizes: 200 Å–600 Å) and Au aggregations at the former Pd step edges can be seen as typical Au derived features. Depending on the step direction, the Au aggregations exhibit also dendritic shapes with fingers growing off the steps, that are up to 600 Å long and typically 50 Å broad. Since the deposition temperature of 303 K is too low for exchange processes on the surface to be activated, the terraces contain only Pd atoms and the islands and the finger-shaped aggregations at the steps are formed solely by Au atoms. In the centre of some of the larger islands small second layer Au clusters can be found.

After annealing for 5 min at 550 K (fig. 4.1(b)) the most obvious change in the film morphology is the disappearance of the relatively thin Au fingers that have been observed at the step edges prior to heating the sample. Also the smaller islands have lost their dendritic shapes and are now oval to round. The largest islands maintain their approximate shape, but also here, small protrusions have vanished and the corners are rounded off. These observations can be explained by a general trend to minimize the total step length of the film and might also be found in homoepitaxial films. On images with high contrast, as the one shown in fig. 4.1(b), an additional surprising observation can be made: In the vicinity of the islands and the step edges the terraces exhibit imprints, the shape of which resemble the island and step structures observable before annealing the film.

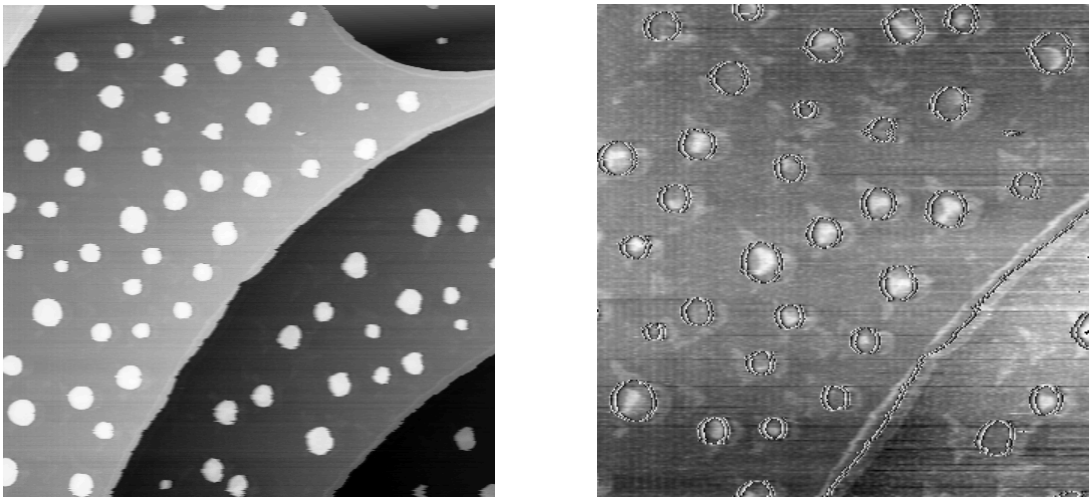

(a) Image size: 6800 Å × 6500 Å

(b) Image size: 4500 Å × 4300 Å

Figure 4.2: STM images of 0.1 ML Au deposited at 303 K and annealed for 5 min at 600 K; $I_t = 6$ nA, $U_t = +8$ mV. Fig. b displays a part of fig. a, where each terrace has been coloured using the complete colour range to enhance the contrast.

Under normal tunnel conditions ($I_t \leq 10$ nA and $U_t \geq 100$ mV), these imprints are imaged about 0.1 Å higher than the sourrounding terrace. Because of the obviously different shapes of the remaining islands and the imprints it can be excluded that they are caused by a double tip, which in general could also produce shadows on the same height scale as the imprints. A closer look reveals that the imprints do not correspond exactly to the shapes that are visible in images like fig. 4.1(a). For example, the imprint structures near the step edges are not as narrow and long as the original Au fingers. For the islands this is less clear since from the beginning the islands have been more compact than the fingers.

In a similar experiment 0.1 ML Au have been deposited around room temperature and annealed for 5 min at 600 K. The result is shown in fig. 4.2, where image 4.2(b) is cut out of image 4.2(a) and is coloured by the method described above. With this high contrast colouring the influence of a weak double tip can be observed as shadows about 160 Å to the right of the "real" structures. Nevertheless, the imprints of the former islands can still be distinguished. The differences to the former experiment consist in a lower Au coverage (0.1 ML instead of 0.2 ML) and in a higher annealing temperature (600 K instead of 550 K). These differences result in three major modifications of the film morphology after annealing:

- The islands are now almost perfectly round. No indications for the former dendritic shapes are detected.

- A part of the islands appear to have vanished completely, because some trigonal imprints of former islands are found without an island in the immediate vicinity. This shows that ripening processes play an important role under the investigated annealing conditions.

- On some larger islands the central region is imaged about 0.2 Å higher than the outer parts of the islands. A similar effect is observed at the step edges, where also a bright stripe is visible in the inner region of the former Au aggregation.

From these observations already a number of conclusions can be drawn regarding the alloying process of submonolayer Au films on Pd(111):

1. The only explanation for the observed inhomogenities on the terraces ("imprints") and on the islands is an inhomogeneous composition of the respective surface areas.

2. Under the tunnel conditions that were used for the images shown in the above figures and for most of the non-annealed films presented in the previous chapter, pure Au aggregations at Pd step edges usually appear higher than the level of the upper Pd terrace. Therefore, it is likely that Au rich areas are imaged brighter also on mixed surfaces. This point will be further discussed below.

3. The alloying process starts to occur at $T \leq 550\,K$ with the formation of the imprints being the first indication of a mixed surface composition.

4. The brighter central regions of larger islands (fig. 4.2(b)) have a higher Au content than the outer parts of the islands. If these brigher inner island regions are combined with the shapes of the surrounding imprints it can be seen that these two features together result in a shape that correspond to a dendritic island as it might have existed at an early stage of the annealing process. Hence, major changes in the island composition are only observed in those areas that have not been part of the original island shape.

5. From the above point it can further be concluded that the exchange of Au and Pd atoms is enhanced at the step edges compared to the inner regions of Au islands or of Au aggregations at steps.

In the next section (4.1.2) some remarkable observations will be reported regarding the composition of 1 ML Au films that have been annealed at 600 K. Here, the larger-scale structure of these films will shortly be presented in fig. 4.3 for two films with almost identical initial Au coverage but different Au deposition temperature. While for fig. 4.3(a) the film was initially prepared at 310 K (see

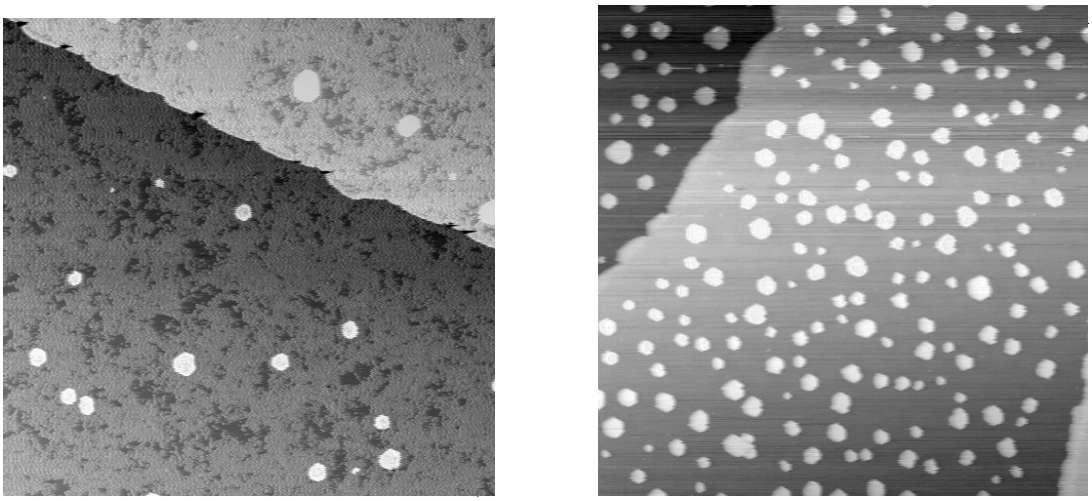

(a) 1.05 ML Au; T_{dep} =310 K; I_t = 3.2 nA, U_t = -850 mV

(b) 1.1 ML Au; T_{dep} =110 K; I_t = 5.0 nA, U_t = +1.1 V

Figure 4.3: STM images of ∼1 ML Au/Pd(111) after annealing for 5 min at 600 K. Image sizes: 3400 Å × 3400 Å.

fig. 3.7(b)), fig. 4.3(b) shows a similar experiment with an Au deposition temperature of 110 K. The islands that can be seen in both images are second layer islands and the first layer is completely covered for the film in fig. 4.3(a). The film with the low deposition temperature exhibits even after relatively long (5 min) annealing at 600 K still a considerable amount of small holes in the first layer, that can not be seen in large-scale images as fig. 4.3(b), but that have been detected in images from smaller areas. These holes are partly responsible for the higher amount of second layer atoms in that image compared to the 310 K deposited film. But also the initial Au coverage was slightly higher. The strikingly different island densities in both STM images show that annealing at 600 K for several minutes is not sufficient to elimiate the structural differences of 1 ML Au films on Pd(111) that have been prepared at different temperatues. In fig. 4.3(a) the first layer appears very inhomogeneous with small dark areas distributed over the terraces. This contrast is due to a special tip condition, where the tip obviously is sensitive to small differences in the chemical composition of the alloyed layer. On other images this contrast has been lost and the overall appearance of the terraces becomes homogeneously flat. The main reason, why this image has been selected, is that it nicely demonstrates the inhomogenity of the surface. This effect will be discussed in section 4.1.2, where atomically resolved images of the same surfaces as shown in fig. 4.3 will be presented.

The effect of annealing submonolayer Au films at higher temperatures has

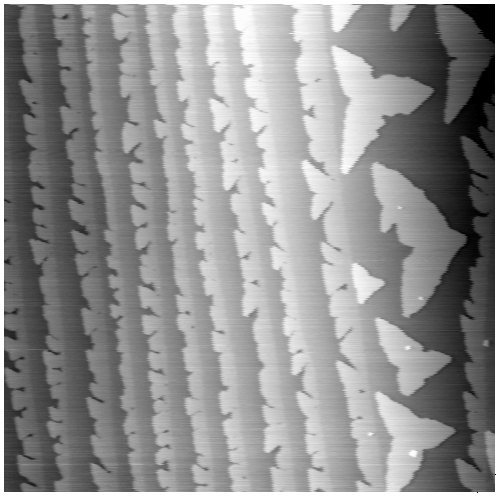

(a) before annealing, 5600 Å × 5600 Å; $I_t = 3.2\,nA$, $U_t = +900\,mV$

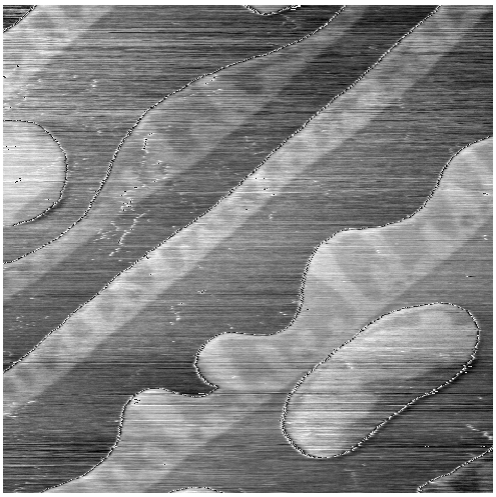

(b) after 5 min at 600 K, 3400 Å × 3400 Å; $I_t = 3.2\,nA$, $U_t = +500\,mV$

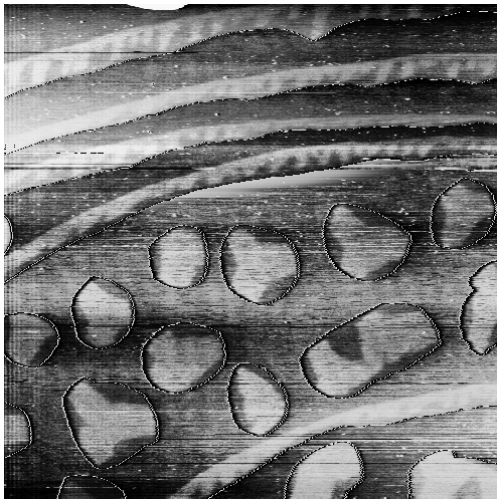

(c) after 5 min at 650 K, 6750 Å × 6750 Å; $I_t = 3.2\,nA$, $U_t = +750\,mV$

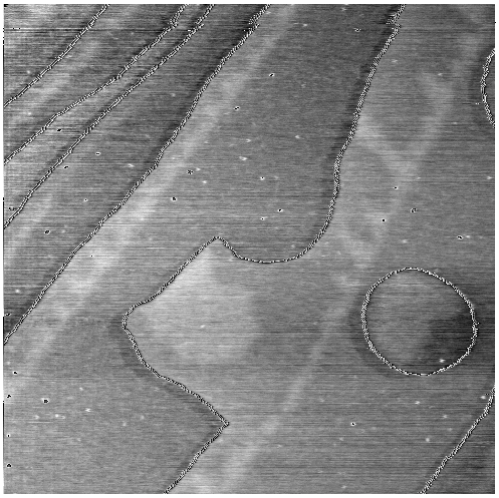

(d) after 5 min at 700 K, 3400 Å × 3400 Å; $I_t = 3.2\,nA$, $U_t = +800\,mV$

Figure 4.4: STM images of 0.4 ML Au deposited at 400 K and annealed for 5 min at $T \geq 600\,K$. In figs. b–d each terrace has been coloured using the complete colour range to enhance the contrast.

been explored using a 0.4 ML film. The results are illustrated by STM images in fig. 4.4. The deposition temperature for this film was 400 K, and therefore the island density and the island shapes differ from those observed on films deposited at 300 K. Large trigonally shaped islands are formed on broad terraces ($\geq$ 1000 Å), as can be seen in fig. 4.4(a). On smaller terraces only step flow growth occurs. The three images of the annealed film (5 min at 600 K, 650 K, and 700 K, respectively) have again been coloured by using several full gray scales across the image for contrast enhancement. The bright areas within the islands or the aggregations at the steps are more distinct in these images compared to the previous figures. The shape of these areas at the former Pd steps seem to be quite different as compared to the shape of the original Au aggregations visible in fig. 4.4(a). The reason for this discrepancy consists simply in the different step directions present in the images. The bright areas — especially those that are visible within the islands of fig. 4.4(c) — resemble again the shapes of the Au structure prior to annealing. It is obvious that annealing at 700 K is not sufficient to obtain a homogeneous surface composition. At the step edges, the brighter areas seem to have shrunk at the expense of the darker areas. For this film, no indications of imprint formation on the terraces have been observed after any annealing step. However, the inhomogeneous islands and step aggregations show unequivocally that intermixing processes have occured. It can not be excluded that the imprints are simply overlooked because of the small average height difference to the surrounding terrace. But it is also possible that imprints are only formed if special initial conditions are met, for example if the average curvature (and consequently the kink density) along the Au steps is high enough.

The STM images in fig. 4.5 show submonolayer Au films (0.3 ML and 0.6 ML) on Pd(111) that have been annealed at 780 K. For both coverages morphological features that differ from the pure Pd(111) surface can be found only on broad terraces ($\geq$ 2000 Å). Depending on the Au coverage either circular islands or round holes are formed at 780 K. The latter exhibit a slight tendency towards hexagonal shapes. As will be shown below, the local composition on such surfaces is relatively homogeneous despite of the clearly distinguishable morphological features (islands and holes). This means that the ripening process, which finally leads to the elimination of the islands or the holes, is much slower than the atom exchange processes that result in a lateral equilibration of the surface composition. Because of the homogeneous Au distribution in these surface alloys annealing of submonolayer films to T $\approx$ 780 K was chosen as one of the standard sample preparation methods for subsequent adsorption experiments. The images in fig. 4.5 serve as illustration of the film morphology for these adsorption studies. Specifically, it can be seen that no additional defect sites like misfit dislocations are created by the annealing procedure and that the large-scale structure of the surface alloy is almost identical to the structure of the pure Pd(111) crystal. The number of additional step edge sites found at the islands or at the holes can be neglected

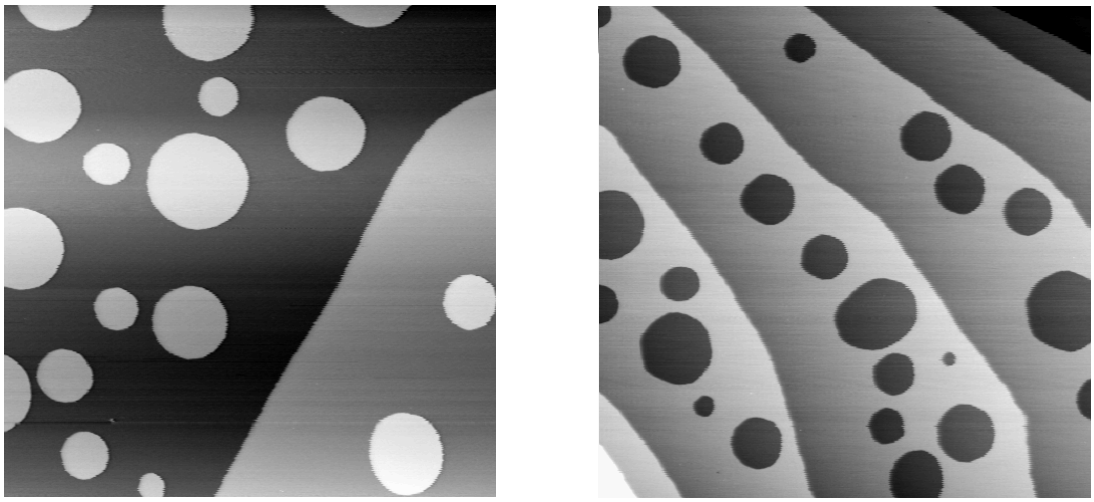

(a) 0.3 ML Au; 6600 Å × 6600 Å;
$I_t = 3.2$ nA, $U_t = +850$ mV

(b) 0.6 ML Au; 6700 Å × 6500 Å;
$I_t = 2.0$ nA, $U_t = -900$ mV

Figure 4.5: STM images of submonolayer Au films after annealing for 30 s at 780 K.

in this respect, because in most parts of the crystal the terraces are considerably narrower than those that are displayed in fig. 4.5. Therefore, the variations of the chemical properties of the surface alloys prepared by annealing at 780 K are only related to the chemical composition of the film (i. e., the Au concentration) and not to structural features like step edges or dislocations.

In several of the above STM images it was demonstrated that annealing of submonolayer Au/Pd(111) surfaces leads to the formation of round islands. This is surprising because circular island edges contain many kink atoms, whereas in hexagonally or triangularly shaped islands the formation of kinks can be avoided. It is important to note that the round island shapes have been observed after different cooling procedures. If the heating was simply switched off after the annealing step, the cooling rate from 780 K to 600 K was very high (≥ 10 K/s). On the other hand, if the heating power was gradually reduced, much lower cooling rates could be obtained. Fig. 4.5(a) was recorded after cooling the sample with ~ 0.4 K/s, but round islands were also found in experiments with fast cooling. For pure Au islands on Pd(111) it has been shown in the previous chapter that depending on the preparation conditions either hexagonal shapes (small Au islands obtained by low temperature Au deposition and subsequent annealing at room temperature), dendritic shapes (0.1 ML Au deposited between 100 K and 300 K), or triangular shapes (0.4 ML Au deposited at 400 K) are preferred. Since Au/Pd(111) overlayer structures can only be prepared at $T \leq 400$ K in order

to avoid alloy formation, these islands might not have adopted their equilibrium shapes yet, but no tendency towards formation of round islands is detectable. Therefore, it is likely that the round islands are characteristic for alloyed surfaces. Since at 780 K the atom migration along island edges is very fast, the islands have certainly adopted their equilibrium structure after a few seconds at this temperature. However, it is difficult to estimate the "critical" temperature where island edge diffusion is becoming to slow to significantly alter the island shapes during cooling. It can be stated that the round shapes are the equilibrium island shapes at this unknown temperature. From the STM images in fig. 4.1 it can be inferred that 550 K is below this critical temperature, such that 600 K can be taken as a rough estimate for it.

The only other system, where, to my knowledge, round islands have been observed, is Ag-Pt(111) [93]. Schuster et al. found circular islands after annealing of 0.55 ML Ag on Pt(111) at T $\geq$ 620 K. However, several differences exist between the two systems. First, Ag-Pt(111) does not form a "real" surface alloy with intermixing of the elements on the atomic scale, but small Ag clusters ($\sim$10 Å) are incorporated into the surface. Second, on Ag-Pt(111) it is observed that larger island structures split into smaller islands upon heating. On the other hand, on Au-Pd(111) Ostwald ripening occurs with larger islands continuously growing at the expense of smaller islands. Because of these differences the driving force behind the formation of round islands seems to be different for both systems. Schuster et al. interprete their findings as indication for a stress relief mechanism via island formation. In the present case, the presence of islands seem to be merely due to the fact that the ripening process is not yet finished. There is no indication for a AuPd(111) surface with islands being energetically more favourable than a surface with all the deposited Au atoms (and the Pd atoms released by exchange processes) being attached to former substrate steps. Since it is unlikely that a stress relief mechanism is responsible for the formation of the round islands on AuPd(111), another driving force has to be sought for this phenomenon. Generally, the number of step edge atoms in a round island is smaller compared to a hexagonal island containing the same amount of atoms. On the other hand, the amount of kink atoms is higher on round islands. It can be suggested that on the alloyed AuPd(111) surfaces kink atoms (coordination number 6) and regular step edge atoms (coordination number 7) have about the same binding energy. The driving force for the preference of round islands over hexagonal islands might then be found in the decreased amount of total step edge atoms. However, this effect is only small: even for a relatively large island with a diameter of $\sim$500 Å the maximum difference between the number of step edge atoms for a hexagonal and for a round island shape can be estimated to be around 4%. Another factor that has to be taken into account is the entropy term that enters into the calculation of the surface free energy. Since the entropy contribution is proportional to temperature, at higher temperatures less-ordered

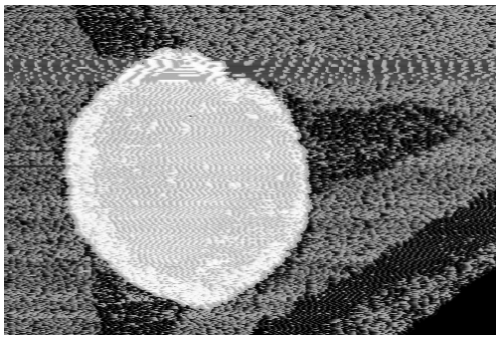

(a) 840 Å × 560 Å; $I_t = 2.8\,nA$, $U_t = +200\,mV$

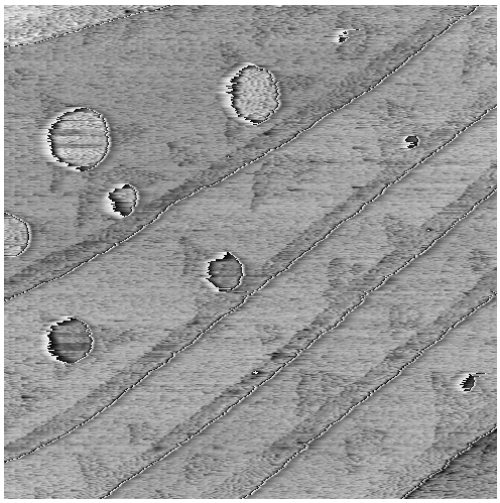

(b) 3400 Å × 3400 Å; $I_t = 2.8\,nA$, $U_t = +20\,mV$

Figure 4.6: STM images of 0.2 ML Au deposited at 307 K and annealed for 5 min at 600 K. In fig. b each terrace has been coloured using the complete colour range to enhance the contrast.

structures are preferred. Comparing round islands with hexagonal or triangular islands it can be stated that the latter represent a higher-ordered state insofar as their orientation is pinned to the crystal directions and hence the rotational degree of freedom is lost.

In a final set of STM images for this section it will be demonstrated that the contrast mechanism which allows the distinction of Au rich and Pd rich areas depends on the tip conditions and on the tunnel parameters. In fig. 4.6 0.2 ML Au/Pd(111) have been annealed for 5 min at 600 K. Similarly as in the previous figures, trigonal imprints in the terraces are clearly distinguishable in the vicinity of the few remaining islands. On the narrower terraces imprints can be seen even though no islands exist on these terraces. While the latter observation is a good illustration of the above mentioned ripening processes — large structures are growing at the expense of small structures to minimize the step energy — the main attention should be payed to the observation that in fig. 4.6 the Au rich imprints are imaged darker (lower) than the surrounding Pd rich terraces. Also the Au aggregations at the steps appear lower than the level of the neighbouring terraces.

It will be shown below that for tunnel conditions, where the tip is very close to the surface and where it is possible to obtain atomically resolved images, i. e., for low tunnel resistances, usually Au atoms are imaged darker than Pd atoms.

If the image size is too large for the individual atoms to be resolved, still the Au rich areas appear darker for these low resistance conditions. However, in all previous images of this section Au rich areas appear higher than the Pd rich terraces. This difference in element specific contrast can be explained by the fact that in both cases different electronic states of the surface give the main contributions to the tunnel current. Since the extension of electronic states into vacuum depends on their energy and on their orbital quantum number l, it can be expected that the balance between Pd derived states and Au derived states varies considerably if the distance between surface and tip is altered. In a more simple-minded nomenclature the conditions where Au is imaged brighter might be called "topographical" mode, because Au atoms are "bigger", i. e., form lattices with larger lattice constants and with higher steps, and the other case might be called "chemical" mode, because here clearly the differences in the electronic structure of Pd and Au are responsible for the contrast. As an additional effect, the direct tip – sample interaction, that could lead to displacements of tip or sample atoms, might be stronger for Pd atoms than for Au atoms. Not only the tunnel resistance, but also the actual state of the tip decides about the contrast mechanism. For this reason, no clear threshold value of the tunnel resistance exists for the transition between the two different imaging modes. While, for instance, for the image shown in fig. 4.2 a topographical contrast is observed using a relatively low tunnel resistance of 1.3 MΩ the chemical contrast seen in figs. 4.6(a) and 4.6(b) is obtained with the higher resistances of $R_t = 71$ MΩ and 7.1 MΩ, respectively. It is important to note that even with reversed contrast, the general features of the film morphology and composition are not changed, only the interpretation of the darker and the brigher areas has to be reversed.

As has been shown in this section, STM is sensitive to variations of the surface composition even on relatively large-scale images. Next, it will be demonstrated that on the atomic scale the composition of the different areas can be determined exactly. Thereby, valuable information on the alloy formation process is available.

4.1.2 Au-Pd(111) intermixing behaviour on the atomic scale

In this section, the large-scale morphological changes that were presented above as the consequences of annealing submonolayer Au films will be examined on the atomic scale. For the interpretation of the atomically resolved STM images that will be presented in this section and also in the later parts of this thesis, it is necessary to emphasize that in almost all atomically resolved STM images that were obtained on the Au-Pd(111) system Au atoms are imaged darker (lower) than Pd atoms. In very rare cases a reversed contrast could be obtained, but then the tip was not very stable, and it is likely that adorbate atoms on the tip were responsible for these occurences. The assignment of the two species to the atomic

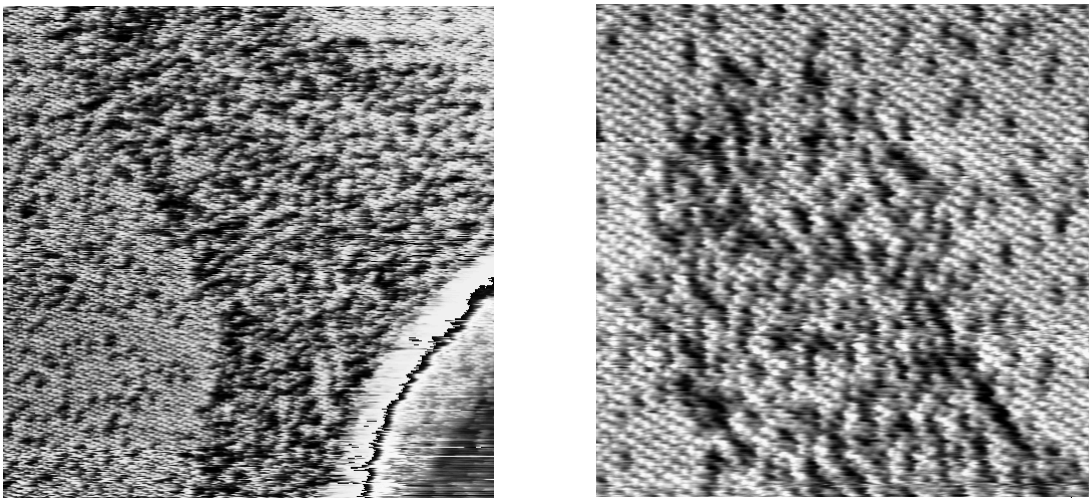

(a) 245 Å × 260 Å; $I_t = 16$ nA, $U_t = +1$ mV

(b) 138 Å × 108 Å; $I_t = 22$ nA, $U_t = +1$ mV

Figure 4.7: STM images of 0.2 ML Au deposited at 307 K and annealed for 5 min at 600 K. In (a), the terrace and the island (lower right-hand corner) have each been coloured using the complete colour range to enhance the contrast.

structures in the STM images was unequivocal in most experiments, because the surface concentrations of the species could be estimated independently — e. g., if only 0.2 ML Au were deposited it is clear that the majority species corresponds to Pd atoms.

The first features that will be analysed are the imprints on the terraces, which are observed mainly in the vicinity of islands. An example is displayed in fig. 4.7 for the same film as shown in fig. 4.6, i. e., for 0.2 ML Au annealed at 600 K for 5 min. In fig. 4.7(a) a part of an island is visible in the lower right-hand corner, and the largest part of the image is filled by the imprint. Fig. 4.7(b) was recorded on the same imprint only a few Å above the image shown in fig. 4.7(a). The resolution of these images is not perfect, and only the Pd atoms can be distinguished as individual bright spots. In any case, it is clear that the imprints exhibit a mixed composition with about an equal amount of Pd and of Au atoms. Together with the observation, that on large islands the inner regions appear brighter and hence contain more Au atoms than the outer parts (see figs. 4.2(b) and 4.4 that exhibit topographical contrast) it can be concluded that the incorporation of Au atoms into the terrace regions forming the imprints occurs during the migration of the island egdes across these regions and is not caused by interlayer exchange processes in the inner parts of the islands. A similar alloying process has been found previously by Hugenschmidt et al. in the system Ni/Au(110)(1 × 2). They ob-

served an increased amount of Ni atoms incorporated into the substrate in the vicinity of islands. This was interpreted by the authors as indication for an island assisted alloying mechanism that is operating while the island is migrating along the troughs of the missing row reconstruction. However, in this case it could not be decided which regions of the islands were responsible for this exchange process. For the Au-Ag(111) system, that is structurally more closely related to the present study, a recent molecular dynamics study by Haftel and Rosen [94] revealed that in the vicinity of adatoms a so-called adatom catalyzed double exchange (CDE) event with a very low activation energy of only 0.047 eV – 0.083 eV becomes possible. Considering the high activation barrier for regular exchange processes on the terraces with 0.421 eV – 0.805 eV, the CDE mechanism should be very important for the Au-Ag(111) alloying process below room temperature. Even though the authors do not consider processes occuring at the edges of large islands, their results can be taken as indication for the existence of highly collective exchange processes on fcc(111) surfaces that require the presence of adatoms or adislands on the surface.

Coming back to the discussion of the STM images shown in fig. 4.7 it can be stated that also on the open terraces alloying has occured leading to a mixed terrace composition, which appears to be relatively homogeneous. As average over many images containing in total 23,000 atoms a Au content of $(8 \pm 1.5)\%$ is found on the terraces. The regions with Au rich imprints have not been included in these numbers. It is quite remarkable that the borderline between the imprints and the rest of the terrace is very sharp, which indicates that the vacancy mediated intralayer diffusion is not relevant at 600 K. The homogeneous distribution of Au atoms across the terraces has then to be explained by a three step process: evaporation of Au atoms from the island edges or from the edges of the Au aggregations at former substrate steps, subsequent fast diffusion of the Au adatoms on the terrace, and finally exchange with a substrate Pd atom after many diffusion steps.

It is interesting to note that the Au concentration on the terraces is, within certain limits, relatively independent of the initial Au coverage. This can be demonstrated by comparing annealing experiments (5 min at 600 K) starting from a 0.1 ML film and a 0.2 ML film, respectively. While atomically resolved images of the latter experiment have just been presented, a corresponding image for a relatively highly stepped area of the 0.1 ML film is shown in fig. 4.8. Here, a Au concentration of $(9 \pm 1)\%$ is found on the terraces by evaluating 3 images containing in total 6500 atoms. This Au concentration is slightly above the value observed for the 0.2 ML film. In both cases only those areas of the surface are included in the evaluations that correspond to the former Pd terraces and that appear to be relatively homogeneous. Islands, Au rich imprints or Pd rich aggregations at step edges have been omitted. It can be concluded that the two-dimensional Au gas on the terraces, which has to be assumed to explain the

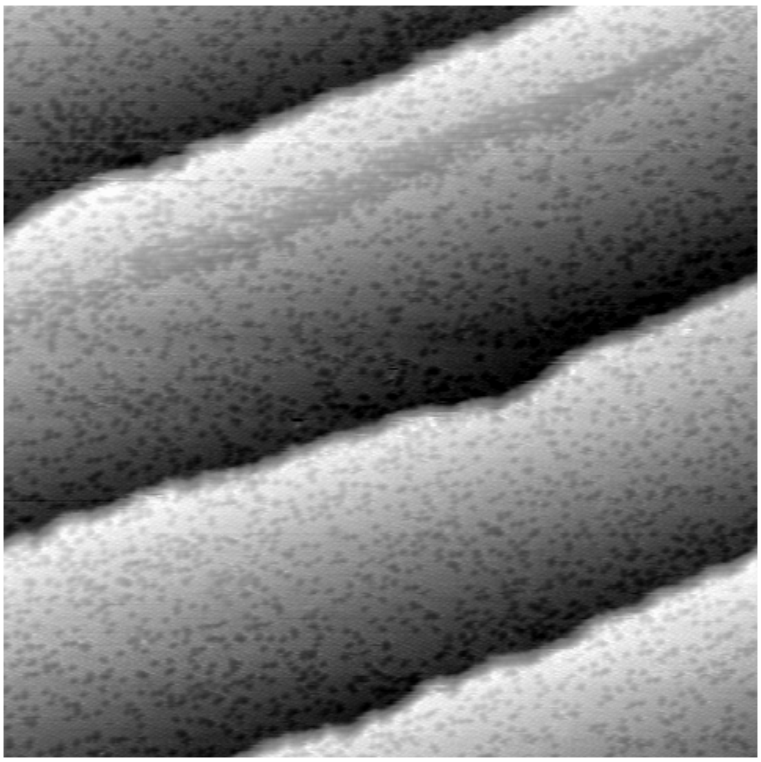

Figure 4.8: STM image of 0.1 ML Au deposited at 303 K and annealed for 5 min at 600 K. Image size: 450 Å × 450 Å; $I_t = 22$ nA, $U_t = +5$ mV.

homogeneous Au distribution, has about the same density and composition in both cases. It is likely that for other initial Au coverages between 0.1 ML and 0.2 ML and possibly also for slightly higher Au coverages a Au concentration of 8–9% would be observed on the terraces after annealing at 600 K for 5 min. This value could constitute an upper boundary for the amount of Au that can be transferred from islands and step edges to the open terraces at 600 K. A possible reason, why such an upper boundary might exist can be seen in fig. 4.8. While at two of the three visible step edges no indications for an inhomogeneous composition can be found, the third one in the upper part of the image displays a feature that is typical for step edges with a not too small lower terrace, namely the occurence of an inner stripe, that consists almost completely of Au atoms, and a broader outer stripe composed mainly of Pd atoms. It should be expected, that after the formation of such Pd rims, the evaporation of Au atoms from the step edges is substantially reduced. However, since in the STM images only the situation is visible after cooling the sample down to room temperature, no statements can be made about the composition of the step edges at elevated temperatures, where at least a part of the atoms are removed from the steps and are migrating on the terraces.

The Au concentrations on the terraces are not only found to be largely independent of the initial Au coverage within a certain interval, but they are also relatively homogeneous. Specifically, no strong Au gradients towards upward or downward steps are visible in images like fig. 4.8. As an example, for the 0.2 ML Au film, that was annealed at 600 K (see figs. 4.6 and 4.7), an evaluation of an area (containing 1623 atoms) next to a former downward step of the substrate yields 6.8% Au, while in an area (containing 1153 atoms) next to an upwardward step 8.8% Au atoms are found. This is in distinct contrast to the behaviour observed for the initial alloy formation process of Mn on Cu(100) (300 K) in an STM investigation by Flores, Junghans, and Wuttig (FJW, [72,73]). In the latter system the density of incorporated Mn atoms strongly depends on the distance to a substrate or an island step. Also a dependency on the step orientation and hence on the kink density of the step is noticed by FJW. They propose an alloying mechanism, where the incorporation of Mn atoms proceeds via annihilation of vacancies that are generated at kink sites and that migrate relatively slowly into the terraces. This mechanism is confirmed by calculations [95]. It is obvious that in the AuPd(111) alloying system no such process is likely to occur, because it would require a very fast diffusion of vacancies within the surface in order to produce a homogeneous distribution of Au atoms.

In fig. 4.9 atomically resolved images are shown for the annealing sequence of 0.4 ML Au, that has been already presented in the overview images of fig. 4.4. All images of fig. 4.9 display an area that is at or close to a downward step. In fig. 4.9(a) the step can be seen in the upper left-hand corner, while the former substrate step is discernible in the lower right-hand corner as division line between a Pd rich area and a Au rich area. Most of this image shows the Au rich aggregation at the former Pd step edge, but Pd rich areas can be distinguished in the upper left-hand and in the lower right-hand parts of the image. The latter belongs to the former Pd terrace and the former is an example of the Pd rims that decorate the step edges and that have been discussed above. In the other three images of fig. 4.9 only the transition from the Pd terrace area to the Au aggregation is visible and not the step edge itself. Fig. 4.9(b) was recorded in close vicinity of fig. 4.9(a) and it nicely demonstrates the sharpness of the still visible original Pd step edge. Additional annealing at higher temperatures (650 K and 700 K) causes this division line to become more and more blurred, as can be seen in figs. 4.9(c) and (d). After annealing for 5 min at 700 K the compositional difference between the Au rich parts of the surface and the free Pd rich open terrace areas are still significant with 60% Au vs. 26% Au (taken from areas containing 2300 and 4000 atoms, respectively), but the concentration gradient has become considerably less abrupt. While the presence of sharp division lines between Au rich and Pd rich areas shows that intra-surface layer atom migration via vacancy diffusion is not important under the respective conditions, a smoother transition between two areas with different composition does not

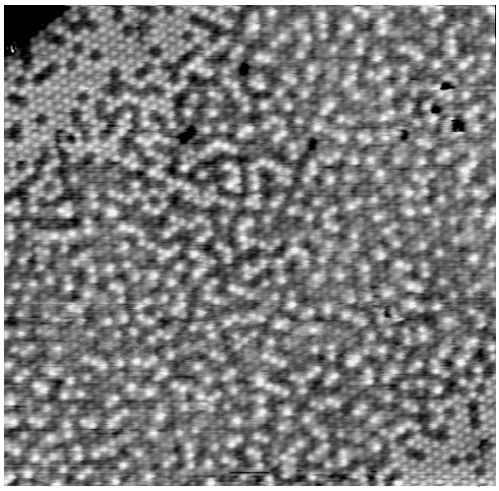

(a) after 5 min at 600 K, 140 Å × 140 Å; $I_t = 32$ nA, $U_t = +50$ mV

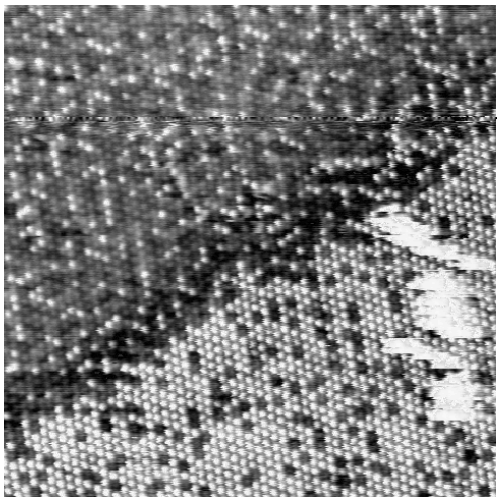

(b) after 5 min at 600 K, 135 Å × 135 Å; $I_t = 10$ nA, $U_t = +5$ mV

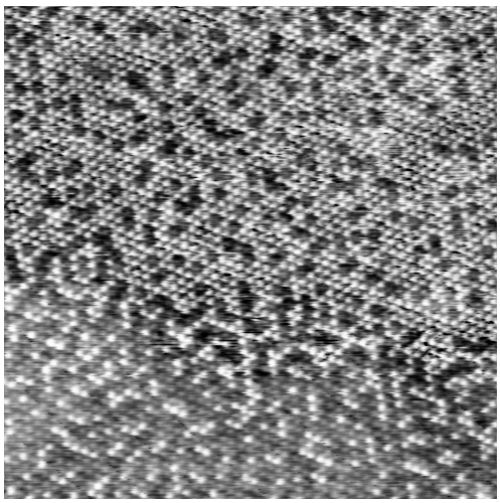

(c) after 5 min at 650 K, 140 Å × 130 Å; $I_t = 10$ nA, $U_t = +1$ mV

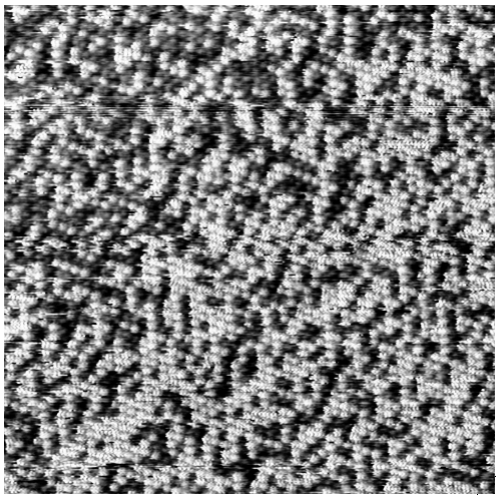

(d) after 5 min at 700 K, 135 Å × 130 Å; $I_t = 10$ nA, $U_t = +1$ mV

Figure 4.9: STM images of a 0.4 ML Au film prepared at 400 K and successively annealed for 5 min at $T \geq 600$ K.

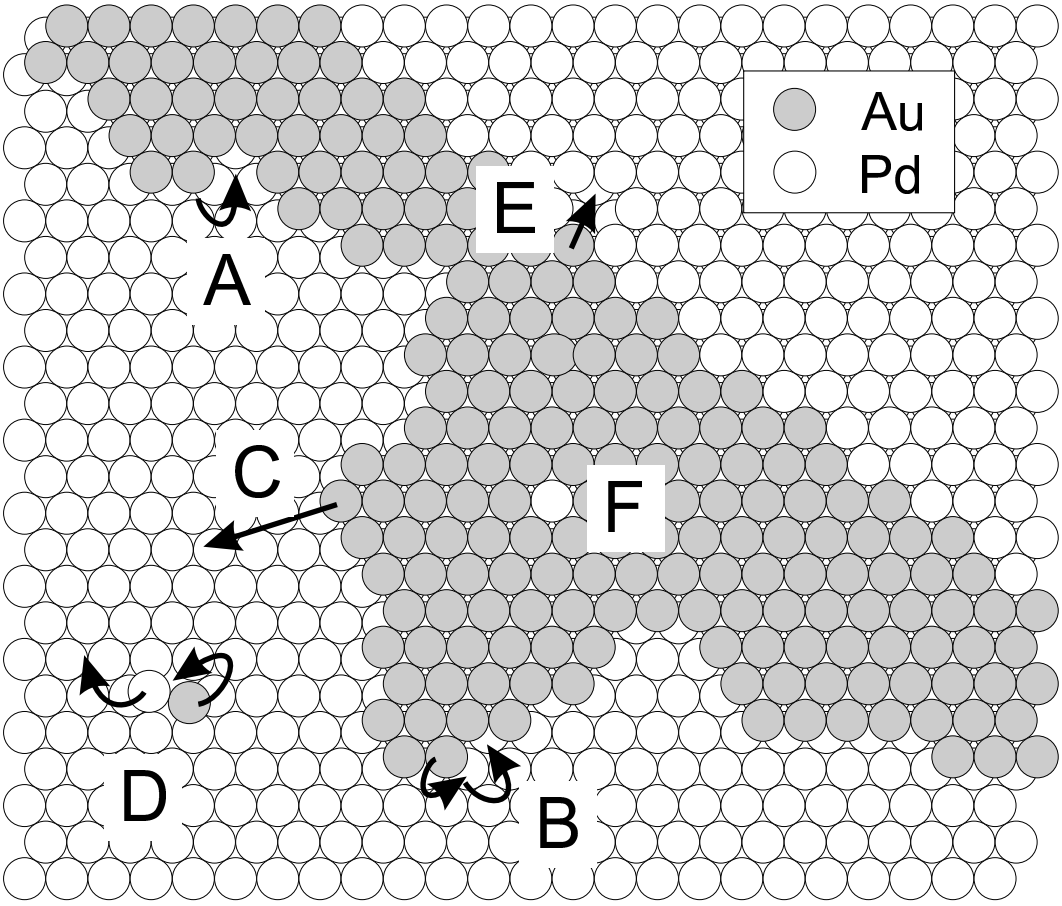

Figure 4.10: Illustration of different elementary processes in the formation of AuPd(111) surface alloys from submonolayer Au films. A short description of the labeled processes is given in table 4.2.

allow an unequivocal conclusion. Besides the mentioned vacancy diffusion also enhanced alloying via the adatom gas results in an equilibration of the surface composition and leads to blurred border lines between different areas.

In fig. 4.10 some basic alloying steps have been visualized in a simple model. They are shortly described in table 4.2. Only the situation for the Au aggregations at steps is shown in the figure, but for Au islands the same processes are possible. Up to now the following processes have been identified to occur at 600 K: The migration of atoms along step edges (A) causes the island shapes to change from triangular to round. Along this edge migration, exchange processes with the substrate occur (B), which leaves Au atoms in the terrace as an imprint of the former island shape. It can be expected that process A occurs already at lower temperatures than process B, and that therefore the imprint represents an intermediate island shape rather than the shape that is observed directly after

label	description
A	Au edge diffusion
B	Edge diffusion coupled with Au-Pd exchange
C	Detachment of Au edge atom
D	Exchange of Au adatom and Pd terrace atom
E	Intralayer vacancy diffusion
F	Interlayer Au-Pd exchange

Table 4.2: Description of the elementary processes for the AuPd(111) surface alloy formation from submonolayer Au films that are illustrated in fig. 4.10.

Au deposition. Detachment of Au atoms (C) and subsequent exchange processes on the terraces (D) are responsible for the homogeneous Au distribution found in the terraces far away from steps. Intralayer vacancy diffusion processes (E) do not play a significant role at 600 K, because sharp border lines are visible between the different areas (see fig. 4.9(b)). The interlayer atom exchange (F) is clearly observable after annealing at 650 K, where in the inner, Au rich parts of large islands an Pd concentration of $26 \pm 2\%$ has been found (the corresponding images are not shown here). It can not be decided whether processes of the type E play an important role at any stage of the annealing experiment, because the possible effects of these vacancy mediated intralayer diffusion processes, e. g., the removal of sharp border lines between areas of different composition, can also be caused by other processes.

Some important secondary processes have not been included in fig. 4.10 in order to keep the illustration as simple as possible. For example, the Pd atoms that are released by the terrace exchange process D might migrate from an upper terrace to the Au aggregation at the downward step and could exchange with a Au atom. Or the Pd adatoms might hit a step edge and get incorportated into the step. This process probably leads to the formation of the distinct Pd decorations of the steps seen for instance in figs. 4.8 and 4.9(a). Of course the question arises, how additional Au atoms can be released after the first few rows of Pd atoms have been added to the step. Either the Au atoms are able to penetrate the Pd confinement directly, which would require several subsequent vacancy mediated intralayer diffusion steps of type E to occur and therefore seems to be unlikely. Or, at 600 K and above most of the Pd atoms are still part of the two-dimensional adatom gas on the surface, and only after cooling the sample they condense at the step edges. A third possibility would be, that the width of the Pd rims is not homogeneous and that at locations where they are thinnest, Au is able to diffuse through the Pd rim.

Next, it shall be demonstrated, how the exchange processes that have been identified in the experiments presented above for submonolayer Au coverages affect the alloy formation process in the case of Au coverages around 1 ML. In the

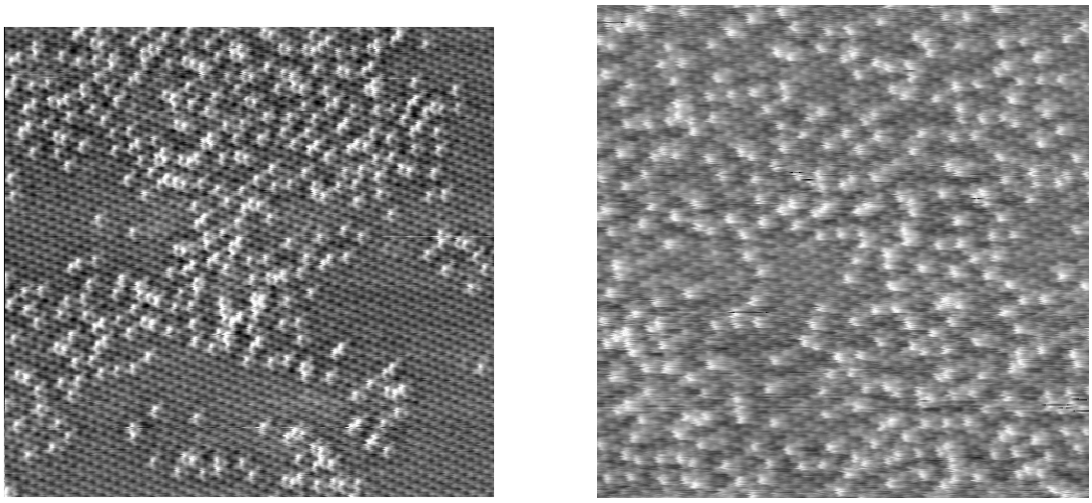

(a) 1.05 ML Au; 145 Å × 140 Å; T_{dep} =310 K; I_t = 14 nA, U_t = +1 mV

(b) 1.1 ML Au; 110 Å × 120 Å; T_{dep} =110 K; I_t = 32 nA, U_t = -4 mV

Figure 4.11: Atomically resolved STM images of ∼ 1 ML Au/Pd(111) after annealing for 5 min at 600 K.

chapter about Au growth on Pd(111) it has been shown that second layer Au islands nucleate before the first layer is completely filled (see fig. 3.7). Therefore, even for Au coverages slightly above 1 ML a small part of the Pd surface remains uncovered, and first layer Au step edges exist on such films. It has been demonstrated above that annealing for 5 min at 600 K causes the Au films to become flat, which means that Au atoms from second layer islands fill up most of the holes in the first Au layer (see fig. 4.3). It can be expected that the distribution of first layer holes in the films has a considerable influence on the alloy structure after annealing, because the important alloying process B (see fig. 4.10) occurs only at step edges. First indications of inhomogenities that are possibly caused by steps in the first Au layer have been detected in fig. 4.3(a), that displays a large-scale image of the same film as shown in fig. 4.11(a) (1.05 ML Au deposited at 310 K and annealed for 5 min at 600 K). The latter, atomically resolved STM image exhibits a striking pattern, which is made up by an inhomogeneous distribution of the (bright) Pd atoms. While in the major part of the image local Pd concentrations between 10% and 20% can be found, there exist relatively large completely Pd free areas containing up to a few hundred Au atoms. It should be emphasized that several similar images have been recorded on this surface, and on no image of the same size as fig. 4.11(a) the Pd distribution is homogeneous. On the other hand, atomically resolved images of a film that has been deposited at 110 K (see fig. 4.11(b); 1.1 ML after 5 min annealing at 600 K) reveal a much

more homogeneous Pd distribution. If the overall Pd concentrations of both films are compared, a significantly higher Pd concentration is found on the low temperature deposited film: 15.7% from images with 24,000 atoms vs. 12.3% from images with 17,000 atoms[3]. These observations can be explained by the following scenario:

- Only very few direct interlayer exchange processes (type F in fig. 4.10) occur, because these would result in a random distribution of Pd atoms in the surface. In that case, no large Pd free areas would be observable.

- Because of the limited mobility of the adsorbed atoms at low temperatures it is likely that the film that was deposited at 110 K initially contains a high number of small holes. At the boundary of the holes the step edge assisted alloying process (type B) becomes possible. Compared to the film that was deposited at 310 K and that contains less but larger holes, the low temperature film comprises a higher total boundary length of first layer holes. Hence, a higher Pd concentration in the surface is expected after annealing the film.

- The relatively homogeneous distribution of surface Pd atoms on the low temperature deposited film can then be explained by the fact that at higher temperatures the holes start to move across the surface before they are filled. It is clear that a large number of small holes is able to cover the surface more homogeneously during their migration and hence produce a smoother distribution of Pd atoms than a smaller number of larger holes, that are to be expected on the film deposited at 310 K.

The importance of edge assisted alloying processes can also be inferred from a two step annealing experiment. While after the first 5 min annealing step of the 1.05 ML film, that is shown in figs. 3.7(b), 4.3(a), and 4.11(a) before and after annealing, respectively, an average Pd concentration of 12.3% is determined, only a relatively small increase to 17.4% Pd is found after a second annealing step using the same heating parameters. If during the first and the second annealing steps exchange processes between the surface and the subsurface layer would occur with the same rate, a Pd concentration of about 23% would be expected in the surface layer. Hence, it can be concluded that the interlayer mass transport is less efficient during the second annealing step. Since after the first annealing step the amount of holes in the first layer is negligibly small, it is likely that the decrease in the Pd accumulation rate on the surface is due to the lack of type B exchange processes. Then, the increase in the Pd content by $\sim 40\%$

[3]Since the typical length scale of the inhomogenities ($\sim$ 50 Å) is smaller than the sizes of the evaluated STM images ($\sim$ 150 Å $\times$ 150 Å), the ratio between Pd rich and Pd free areas is similar in the images.

during the second annealing step has to be attributed to processes of type F. In the discussion above it has been pointed out that such processes are not very frequent during the first annealing step, because of the presence of large Pd free areas. This shows that the simple picture that is conveyed by the model in fig. 4.10 is not sufficient to explain all subtle details of the alloying experiments. For example, thermodynamic aspects, like the concentration dependent Au–Pd mixing enthalpies or the Au segregation energy, have been completely neglected. These are addressed in a recent publication by Sadigh et al. on the structural and thermodynamic properties of thermally equilibrated PdAu/Ru(0001) surface alloys [96]. Also the kinetic barriers for the different exchange processes might depend on the local composition of the surface and the subsurface layer.

Up to now, several cases of inhomogeneous surface alloys have been presented. They were obtained by depositing $\Theta_{\mathrm{Au}} \leq 1\,\mathrm{ML}$ around room temperature and subsequent annealing at temperatures up to 700 K. For most of the adsorption experiments presented in part III of this thesis, however, a homogeneous distribution of Au atoms is desired in order to allow the interpretation of area integrating spectroscopic experiments using HREELS or TPD. One example for an STM image from such surfaces will be presented in section 5.3.3 (see fig. 5.31 on page 202 for 83% Pd in the surface obtained by annealing 0.8 ML Au for 30 s at 1000 K). Generally, it is found that annealing at $T \geq 780\,\mathrm{K}$ is sufficient to eliminate major differences in the local alloy composition for $\Theta_{\mathrm{Au}} \leq 1\,\mathrm{ML}$. For instance, the local Au concentration on the round islands visible in the STM image of fig. 4.5(a) does not differ significantly from values determined on the terraces. While on an island a Au concentration of 22% is determined from one STM image, on the terraces between 22% and 26% Au are found (each value is calculated by counting atoms in an area that contains at least 450 atoms). On the other hand, at 780 K and for submonolayer Au coverages the diffusion of Au into subsurface layers is still very limited. Only between 10% and 20% of the Au atoms are removed from the surface during 30 s at 780 K[4] and for $\Theta_{\mathrm{Au}} \leq 0.5\,\mathrm{ML}$. This allows the Au concentration that remains in the surface layer after annealing to be determined by the amount of deposited Au.

4.2 Annealing of completely Au covered Pd(111)

The interpretation of annealing experiments using surfaces that are completely covered by Au during the initial deposition step is facilitated, because several of the basic alloying processes that are illustrated in fig. 4.10 are not possible on such surfaces. Similarly as in the previous section the presentation of the

[4]This annealing procedure was empirically determined to produce the desired results. Any other temperature in the range between 700 K and 800 K could probably also be used if the annealing duration is adjusted.

STM measurements will be divided into a first part concerning changes of the large-scale film structure and a second part on atomic-scale investigations of the alloying processes. The former part might be considered largely as supplementary information to the more important results that are reported in the latter part.

4.2.1 Changes in film morphology by annealing

An overview over the results of four different experiments is given in fig. 4.12. For coverages ranging from 2.2 ML to 3.5 ML the effect of annealing at $625 \leq T \leq 825$ K on the large-scale film structure was examined. It is obvious that annealing at these temperatures is not sufficient to produce a homogeneous surface with flat terraces. In all of the images the dominating structural features are the stripe patterns that have been described already for the non-annealed films in chapter 3. Mild annealing at $T \leq 700$ K results in either an irregular pattern of stripes, that are separated by several 100 Å (for a local coverage of 2 ML), or in a well-ordered pattern of triangular and hexagonal shapes (local coverage: 3 ML or 4 ML). Annealing at 625 K has almost no effect on the larger-scale film structure. There are still relatively small hexagonally shaped islands present on the surface and also several holes in the second layer have not been filled up yet. At 700 K, islands survive only on large terraces and have a minimum size of 500 Å for an initial coverage of 3.5 ML (fig. 4.12(c)). The ordering of the stripe patterns in the 3rd and 4th layer improves with slightly smaller periodicities observed in the 4th layer compared to the 3rd layer. The structural consequences of a Pd enrichment in the near-surface crystal layers become evident in fig. 4.12(d), that shows a 2.6 ML Au film after annealing at 825 K for 1 min. Due to the similar Au coverage this image can be compared with fig. 4.12(b) (annealing at 700 K). While in areas with a local coverage of two layers the stripe pattern is not altered markedly, on the "higher" areas the distance between the stripes is considerably increased compared to fig. 4.12(b), and the high degree of order is lost. Qualitatively, the appearance of third layer areas is becoming similar to the overall structure of second layer areas. It should be mentioned that annealing of the 2.2 ML film that was also used for the experiment shown in fig. 4.12(a) for 2 min at 900 K results in a large-scale surface structure that is not distinguishable from the pure Pd(111) surface. Therefore, the corresponding STM images have been omitted in the sequence of fig. 4.12. Particularly, no stripes are observable after annealing at 900 K. However, this film contains still 58% Au in the surface layer (see fig. 4.13(c) for an atomically resolved image of this surface). Obviously, this amount of Au can be accommodated within a crystal structure that is pseudomorphic to Pd(111).

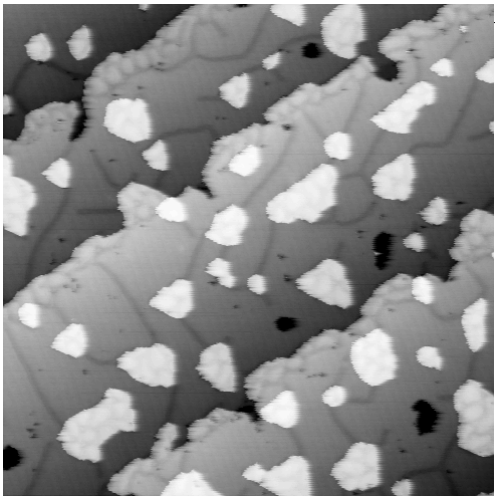

(a) 2.2 ML after 1 min at 625 K, 3600 Å × 3300 Å; $I_t = 0.32$ nA, U_t = -200 mV

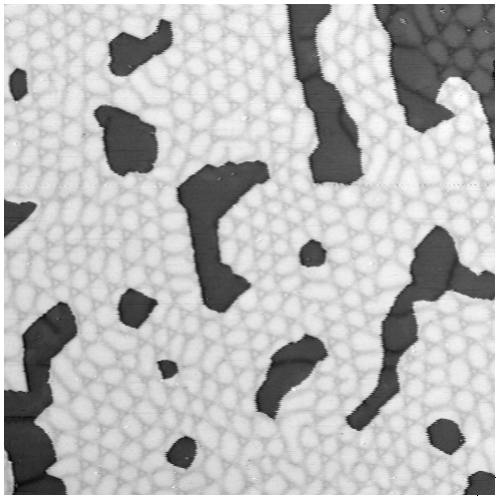

(b) 2.7 ML after 2 min at 700 K, 3200 Å × 3000 Å; $I_t = 3.2$ nA, U_t = +1.3 V

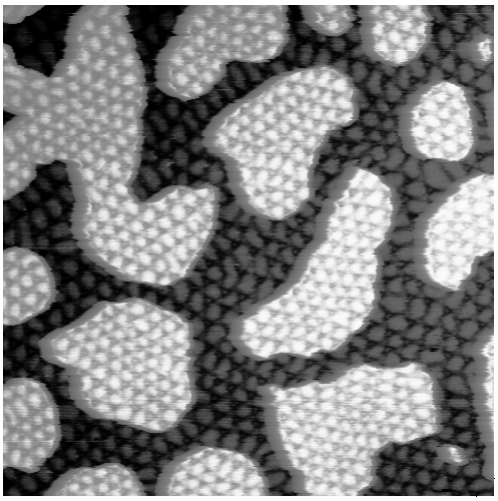

(c) 3.5 ML after 5 min at 700 K, 3600 Å × 3400 Å; $I_t = 16$ nA, U_t = -1.2 V

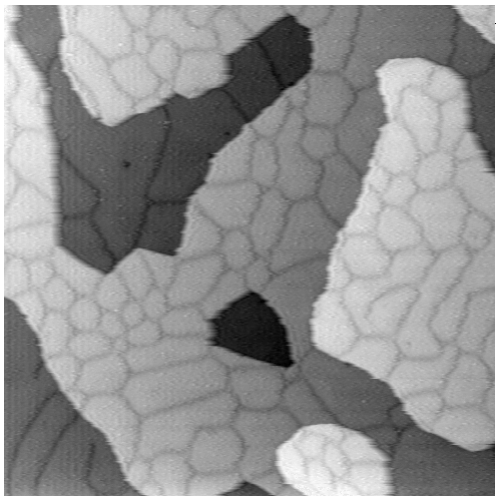

(d) 2.6 ML after 1 min at 825 K, 3400 Å × 3200 Å; $I_t = 0.63$ nA, U_t = +1.1 V

Figure 4.12: STM images of multilayer Au films, that were deposited around room temperature and subsequently annealed at temperatures ≥ 625 K.

integral Θ_{Au}/ML	annealing	local Θ_{Au}/ML	c_{Pd}/%	images
1.7	5 min, 580 K	2	3.5 ± 0.7	4.13(a)
2.2	1 min, 625 K	2	4.9 ± 0.6	4.12(a)
2.2	1 min, 675 K	2 3	10.3 ± 0.7 8.4 ± 0.5	4.13(b)
2.2	2 min, 900 K	2/3	42 ± 2	4.13(c)
2.6	1 min, 825 K	2/3	24 ± 2	4.12(d)
2.7	2 min, 700 K	2 3	13.5 ± 1 11.9 ± 1.0	4.12(b), 4.14(a), 4.14(b)

Table 4.3: Local Pd concentrations on some of the AuPd(111) surface alloys that are presented in this and in the previous section.

4.2.2 Au-Pd(111) intermixing behaviour on the atomic scale

On submonolayer Au films there exist several effects which lead to a different composition of the areas in the vicinity of island edges and of step edges compared to the open terraces. First, the former substrate steps are decorated by Au during the film deposition, which leads to the formation of Au rich stripes adjacent to the original substrate step edges during annealing. Secondly, step edges act as traps for Pd atoms that are released by Au–Pd exchange processes on the terraces and therefore for several alloying parameters it has been observed that the step edges are preferentially terminated by Pd atoms. Thirdly, efficient step edge assisted alloying processes yield an increased Pd concentration in those areas of the islands or of the atom aggregations at substrate steps that have changed their position during the annealing process. Since after annealing at temperatures around 780 K and above also for submonolayer Au films no significant difference in the alloy composition at or near step edges has been observed, it is likely that the complicated inhomogeneous concentration profiles that are found near step edges after annealing at intermediate temperatures (600 K – 700 K) are merely caused by kinetic effects. Turning to the present case of multilayer Au films, it can be stated that initially the terraces and the step edges exhibit the same composition, namely they consist exclusively of Au atoms. Therefore, on these surfaces it might be easier to distinguish between thermodynamic properties — like differences in the step energies for the two elements — and kinetic effects.

In fig. 4.13 several atomically resolved STM images containing a surface step are displayed. In all of these images the Pd atoms are displayed brighter than the surrounding Au atoms. The results of counting the number of Pd atoms in several images of these surfaces are collected in table 4.3. Where possible it is differentiated between the various local Au coverages. In fig. 4.13(a) the first stages of alloying are observed on a second layer Au island. The distribution of

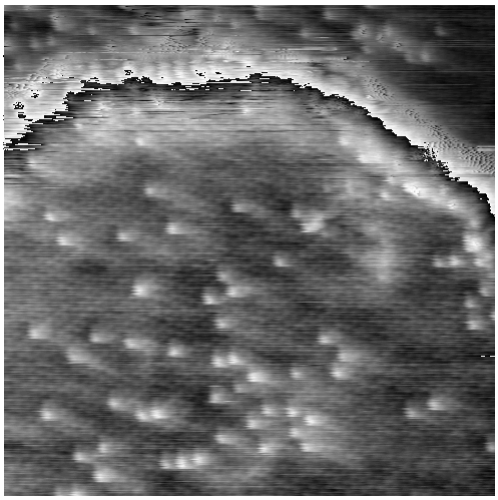

(a) 1.7 ML after 5 min at 580 K, 140 Å × 130 Å; $I_t = 10$ nA, U_t = -5 mV

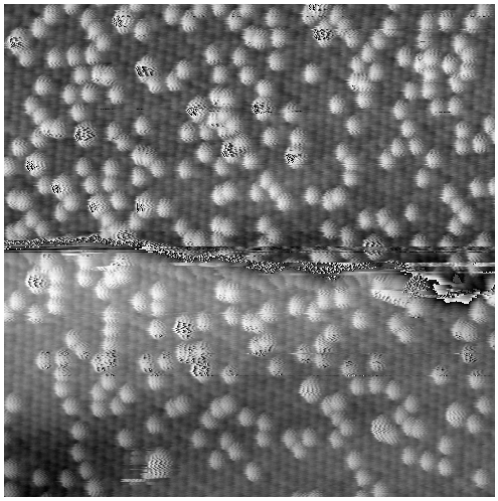

(b) 2.2 ML after 1 min at 675 K, 130 Å × 135 Å; $I_t = 10$ nA, U_t = -3 mV

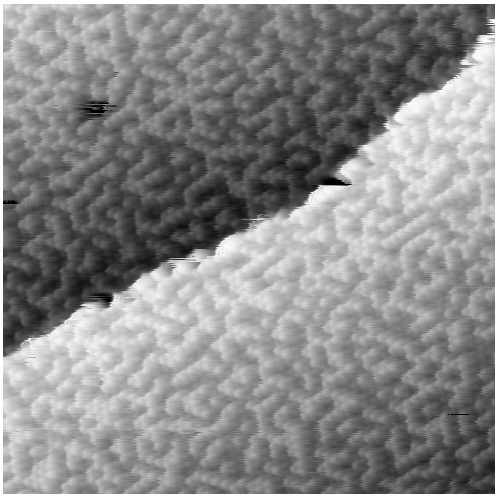

(c) 2.2 ML after 2 min at 900 K, 133 Å × 133 Å; $I_t = 3.2$ nA, U_t = -4 mV

Figure 4.13: STM: Influence of surface steps on the local composition of AuPd(111) surface alloys prepared by annealing multilayer Au films. In (a) and (b) each of the upper and the lower level of the surface has been coloured with the complete grayscale, which results in an artificial stripe at the step edge. The higher level is found in the bottom region of both images.

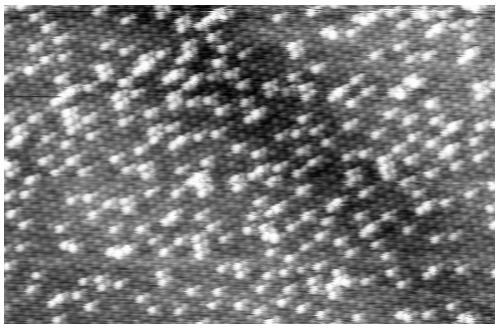

(a) 2 ML local coverage; 135 Å × 100 Å; $I_t = 10$ nA, $U_t = +1$ mV

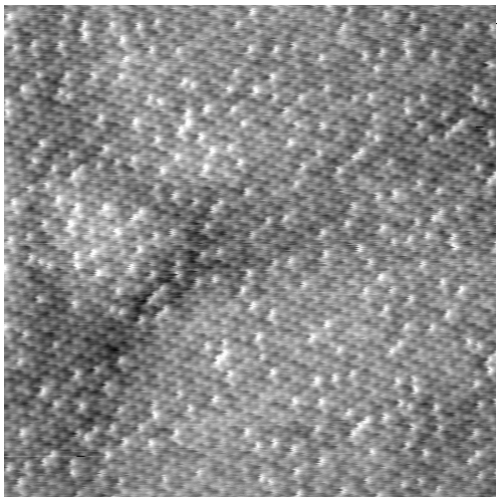

(b) 3 ML local coverage; 136 Å × 126 Å; $I_t = 10$ nA, $U_t = +1$ mV

Figure 4.14: STM: Influence of the strain relief stripes of multilayer Au films on the local alloy composition; 2.7 ML after 2 min at 700 K (see fig. 4.12(b) for a large-scale image from the same film).

the Pd atoms that are found within this island appears to be relatively homogeneous. In the centre of the island a slightly higher Pd concentration is observable, but in other pictures this could not be confirmed to be generally true. It is clear, however, that the regions near the island edges do not exhibit a strongly altered composition, as it was observed on submonolayer films. The same conclusion can be drawn from an inspection of fig. 4.13(b), where a step is shown that separates two areas with local Au coverages of 2 ML and of 3 ML, respectively. In this image also the region on the lower terrace is well-resolved. No gradient of the Pd concentration is detectable neither on the lower terrace nor on the upper terrace. The difference between the average composition of second and of third layer areas (10% vs. 8% Pd, see table 4.3) is not large, but still significant. Such differences are not observable on films that have been annealed at higher temperatures, e. g., at 825 K or at 900 K as the film shown in fig. 4.13(c)[5]. On these surface alloys the chemical composition is homogeneous across the entire surface including the regions near step edges. Directly at the step edges it is difficult to decide about the nature of the atoms, and therefore no exact evaluation of the step edge composition is possible. It seems that also the step edge consists of a

[5] At first sight, the alloy structure of this film appears to be unusual in so far as the Pd atoms seem to form relatively long chains. By a statistical evaluation of this structure (see fig. 4.20) this will be shown to be merely an optical illusion.

mixture of Pd and Au atoms. In summary, no indications for specific properties of step edges regarding the kinetics or the thermodynamics of the alloy formation process are found on multilayer Au films.

Besides step edges there exists another class of large-scale surface inhomogenities on multilayer Au/Pd(111) films, namely the characteristic pattern of dark stripes. In fig. 4.14 two examples are presented for the chemical composition of areas close to second (a) and to third layer (b) stripes. In none of these images an obvious difference of the Pd concentration is observed between areas situated on the stripes and areas that are located on the higher level between the stripes. For fig. 4.14(a) a local Pd concentration of $(15.2 \pm 1.5)\%$ is determined in a 35 Å broad area covering the stripe and $(14.6 \pm 1.1)\%$ Pd are found in the other areas of the image. Hence, these stripes do not significantly influence the alloying process. Specifically, it can be excluded that an additional fast diffusion channel exists at the stripes, which is of some importance for the results that will be presented in section 4.5 on the alloying kinetics, since it shows that the presence of dislocation stripes can be neglected in the evaluation of AES interdiffusion experiments.

A very simple conclusion can be drawn from the STM measurements on the formation of multilayer AuPd(111) surface alloys. While for $\Theta_{Au} \leq 1\,\mathrm{ML}$ a complex interplay of several different atomic processes has to be assumed in order to explain all observable features, only a single type of process, namely interlayer atom exchange, has to be postulated for the multilayer Au films.

4.3 Au deposition at elevated temperatures

The objectives of the following experiments, where Au was deposited at elevated sample temperatures (550 K and 600 K) were twofold: First, it should be investigated how the balance between the different alloying processes that are illustrated in fig. 4.10 is altered if the film is deposited at higher temperatures compared to the above presented alloy preparation method (Au deposition at $T \leq 400\,\mathrm{K}$ and subsequent annealing). Secondly, Au deposition at temperatures where intermixing processes are possible might produce a surface composition that is not obtainable by other procedures. It is clear that a serious investigation of the effects produced by Au deposition at elevated temperatures would require a large number of experiments, because both the Au coverage and the deposition temperature are important parameters and have to be varied in these experiments. In this work only two STM measurements have been performed to investigate Au deposition at elevated temperatures. They can only be used to show some qualitative features of the high temperature Au deposition procedure and are not sufficient for a comprehensive quantitative evaluation.

In fig. 4.15 an atomically resolved STM image of a AuPd(111) surface alloy is presented, which was prepared by depositing 0.1 ML Au at 600 K. The following

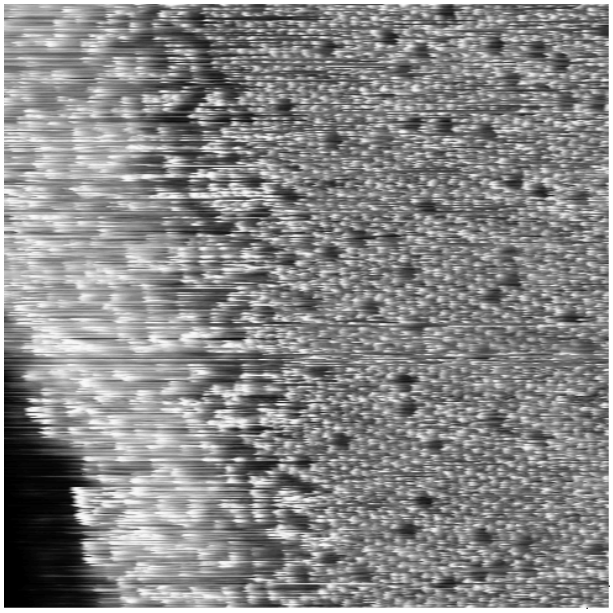

Figure 4.15: STM image of 0.1 ML Au deposited at 600 K; image size: 140 Å × 135 Å, $I_t = 45$ nA, $U_t = +2$ mV.

qualitative differences to the corresponding conventional annealing experiment (0.1 ML Au deposited at 303 K and annealed for 5 min at 600 K; figs. 4.2 and 4.8) can be noticed:

- At former Pd step edges the division line between the Pd rich upper terrace and the Au aggregation is less sharp.
- No Pd rich rim exists at the step edges.
- Islands are only found on very large terraces. In the present STM experiment one single island (Au concentration on the island: 67%) was detected on a 3000 Å wide terrace.

It has been demonstrated above, that on submonolayer Au films which are heated to temperatures above 550 K, the evaporation of Au atoms from step edges and the formation of a two-dimensional lattice gas is required to explain the homogeneous distribution of Au atoms in the former Pd terraces (processes C and D in fig. 4.10). During the deposition process, the adsorbed atoms also form an lattice gas, the steady-state density of which depends on the substrate temperature. Since the adatoms might get incorporated into steps, the adatom density in the vicinity of these traps should be lower compared to the value far away from steps. This phenomenon is responsible for the well-known island depletion zones that are observed in growth experiments near surface steps. In the present context, the question arises whether also in alloying experiments a similar depletion zone

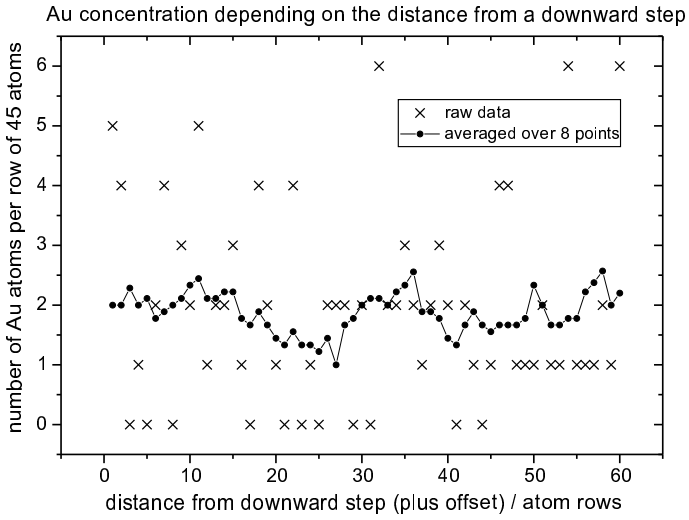

(a) first set of STM images

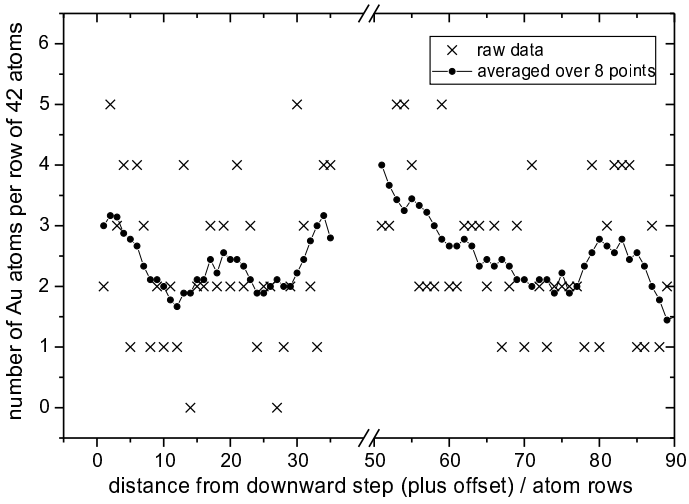

(b) second set of STM images

Figure 4.16: Statistical analysis of the Au distribution relative to a downward substrate step for 0.1 ML Au deposited at 600 K. The position of the original substrate step is not exactly determinably, and an unknown offset of a few atom rows has to be added to the numbers on the x-axis. Due to bad statistics averaged curves are included in the figures. The results of each figure are obtained from two adjacent STM images. For (b) the images do not overlap and therefore a small gap (1–10 atom rows) is indicated on the x-axis.

for incorporated Au atoms is observable. In order to answer this question two sets of two directly adjacent STM images have been recorded, for which the relative position to the next downward step is known (one of these images is shown in fig. 4.15). The other STM image of the same size was recorded on the right hand side of this image on a terrace that was about 600 Å wide. In fig. 4.16(a) a statistical analysis of the Au concentration is presented. The STM images that were used for the analysis presented in fig. 4.16(b) do not overlap. Therefore a gap of 1–10 atom rows exists on the x-axis. Fortunately, the close-packed atom rows are approximatley parallel to the former Pd step edge, such that simply the number of Au atoms in the approximately vertical atom rows had to be counted. Each atom row in fig. 4.16(a) contains 45 atoms (42 atoms for the images evaluated in fig. 4.16(b)). On average only about two Au atoms per atom row were counted in both cases. Therefore, several adjacent data points have to be averaged in order to obtain a meaningful result. As can be seen from the data points that are shown in fig. 4.16, no clear correlation between the position of the atom rows and the Au content can be detected. While in fig. 4.16(a) the smoothed curve is almost perfectly constant, in fig. 4.16(b) some modulations might be detectable. Due to the low amount of Au atoms that were evaluated, these weak modulations are statistically not significant. This evaluation is only sensitive to effects on a length scale of a few 10 Å. If the modulation of the Au concentration occurs with a typical length scale of a few 100 Å then the difference would be too small to be detected in fig. 4.16. On the other hand, the average Au concentrations found on the two sets of STM images deviate relatively strongly: 4.2% Au for fig. 4.16(a) and 5.7% Au for fig. 4.16(b). Therefore, there seems to exist a significant difference of the Au content on different terraces. Unfortunately, only for one of the two cases the terrace width is known (600 Å for the terrace that is visible in fig. 4.15 and that is used for the evaluation presented in fig. 4.16(a)). At this point, it can only be concluded that no strong modulations of the Au concentrations are observed within one terrace, but that some variations are detected if different terraces are compared with each other.

In the next two sets of STM images (figs. 4.17 and 4.18) the result of depositing 1.2 ML Au at 550 K is shown. In the overview image displayed in fig. 4.17 three second layer islands are visible on broad terraces ($\sim$4000 Å). They are located in the vicinity of former substrate steps, which can still be recognized by a sharp line dividing an area with only one adlayer (darker) and an area with two adlayers (brighter). From the contrast difference at these former step edges it can be inferred that Au rich areas are imaged brighter under the present tunnel conditions, which is also what would be expected for a "normal" tip. In fig. 4.17(b), where each terrace has been coloured using the complete gray scale in order to enhance the contrast, a distinct modulation of the terrace height can be recognized throughout the image. Irregularly shaped bright bands run approximately perpendicular to the steps across the terraces. This indicates that during the

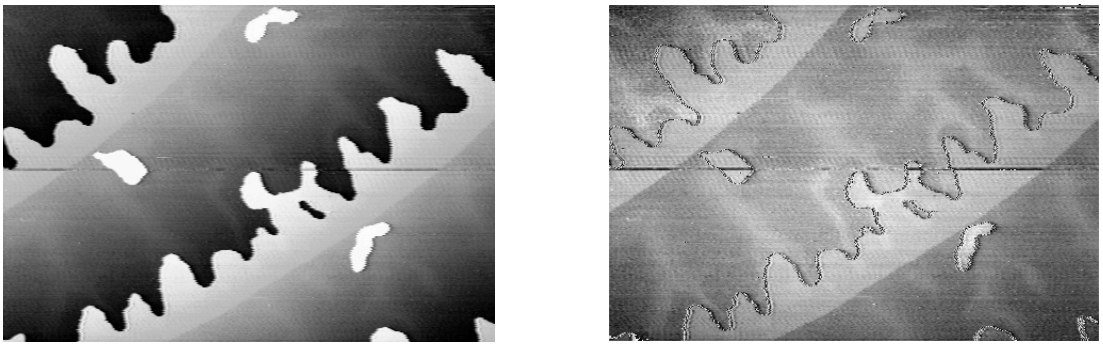

(a) low contrast colouring

(b) high contrast colouring

Figure 4.17: STM image of 1.2 ML Au deposited at 550 K; image size: 6200 Å × 4200 Å, $I_t = 3.2$ nA, $U_t = +600$ mV.

deposition process — which took 110 s and after which the sample heating was immediately switched off — inequivalent areas exist on large terraces. The most likely explanation for this is, that despite the high sample temperature large islands are being formed upon Au deposition and eventually coalesce. In the centre of these islands the Pd concentration is expected to be higher than in the areas that are filled up during the last stages of completion of the first monolayer.

Two factors contribute to this effect. First, with increasing island sizes, the amount of atoms that adsorb on the Au rich islands and consequently do not encounter the Pd rich substrate increases. Second, the open substrate surface gets more and more enriched by Au atoms during the deposition process with the consequence that the probability for an exchange process between a Au adatom and a Pd surface atom decreases. Hence, the darker areas in fig. 4.17(b) most likely mark the positions, where islands have been formed initially. This shows that, at a Au flux of $1.1 \cdot 10^{-2}$ ML/s, 550 K are not enough to prevent island formation on 3000 Å wide terraces. It should be possible to observe these islands directly by investigating lower Au coverages.

In fig. 4.18 an impression of the atomic structure of this film is given. The majority of the image displays an area within the second adlayer. A step edge is visible in the upper left corner of the image and in the opposite corner the position of the former substrate step is weakly discernible as border line to a relatively Pd rich area. The local Pd concentration on the second adlayer is 3.5% in this image. In total 20 atomically resolved images each containing between 800 and 8200(!) atoms have been obtained from this film, which gives very good statistics for the Pd concentrations. Since even the largest of these images (235 Å × 235 Å) is considerably smaller than the length scale of the inhomogenities in fig. 4.17, the gradient of the Pd concentration in each of these images is very

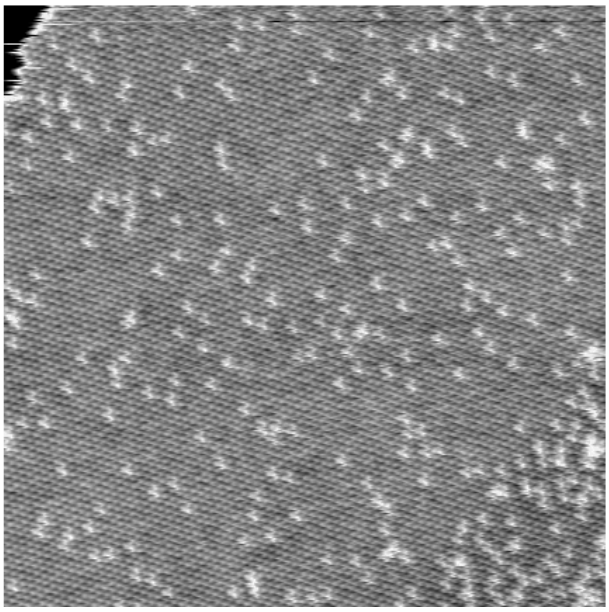

Figure 4.18: STM image of 1.2 ML Au deposited at 550 K; image size: 210 Å × 220 Å, $I_t = 10$ nA, $U_t = +1$ mV.

small. As expected from the brightness modulations observed in the previous figure, a rather inhomogeneous surface composition has been found by comparing the different STM images. The Pd concentrations vary between 12.8% and 28.9% in the first adlayer and between 3.5% and 6.3% Pd in the second adlayer. The statistical uncertainties of these numbers are below 1%. These numbers show that the activation barrier for the exchange process between single Au adatoms and Pd terrace atoms is such, that at 550 K up to one third of the adatoms are being exchanged on their migration across the terrace. If such experiments were repeated at different temperatures, an estimate for the difference between the energy barriers for adatom diffusion and for adatom – substrate atom exchange could be obtained.

It would be interesting to examine the reactivity of AuPd(111) surfaces with smoothly varying composition. It might well be, that for a given reaction each of the reaction steps requires a different surface composition for an optimum reaction rate. Therefore, surfaces as the one shown in figs. 4.17 and 4.18 possibly exhibit an exceptionally high activity for certain reactions. However, the detailed analysis of reactions on such inhomogeneous surfaces requires many different measurements. For the adsorption and reaction studies presented in part III no such complicated surfaces were used.

4.4 Distribution of Au and Pd atoms in the surface layer

The equilibrium element distribution within a bimetallic surface composed of species A and species B atoms belongs to one of the following four classes:

1. Random distribution. The interaction energy between atoms of different kind is identical to the interaction between atoms of the same kind. The distribution is then given by the maximum entropy distribution, which is the one with the lowest possible degree of order. The pure form of this behaviour is unlikely to be encountered in real systems, because at least a small asymmetry in the interaction strength should be expected. However, the deviations from a completely random distribution might be only small and therefore might be difficult to detect experimentally.

2. Phase separation. If atoms of type A prefer to be surrounded by A atoms and the same is true for atoms of type B, then areas consisting of pure A and areas consisting of pure B will coexist on the surface. The size of these areas might be limited by the strain in the surface layer that could build up with increasing domain sizes. Example: Ag/Pt(111) [86].

3. Enhanced mixing. For systems that have a negative mixing energy in the surface plane, a mixed composition is expected that deviates from the random distribution. As equivalent description of this situation a repulsive interaction between neighbours of the same kind can be stated. Smaller clusters of one species will be preferred over larger clusters because of the tendency to increase the number of neighbours of the other type. Example: Pd/Cu(111) [22].

4. Ordering. If the negative mixing energy in the surface plane is large enough, it might lead to the formation of ordered phases. For instance in an fcc(111) surface, up to $\frac{1}{3}$ ML of type B atoms can be accommodated in a $(\sqrt{3} \times \sqrt{3})R30°$ superstructure, where the formation of B–B neighbour pairs is completely avoided. This class forms a subset of the former class. Examples: Pd/Cu(100) [75] and Pd/Au(111) [97].

While ordered structures are easily detectable experimentally either by diffraction methods (LEED) or by real-space methods (STM), the other three cases are more difficult to be distinguished. For this purpose, STM measurements seem to be best suited, because they are capable of exactly determining the element distribution in the surface layer. With the help of atomically resolved images, where the two components of the bimetallic surface can be identified, the formation of domains consisting solely of one element (i. e., phase separation) should be detectable at

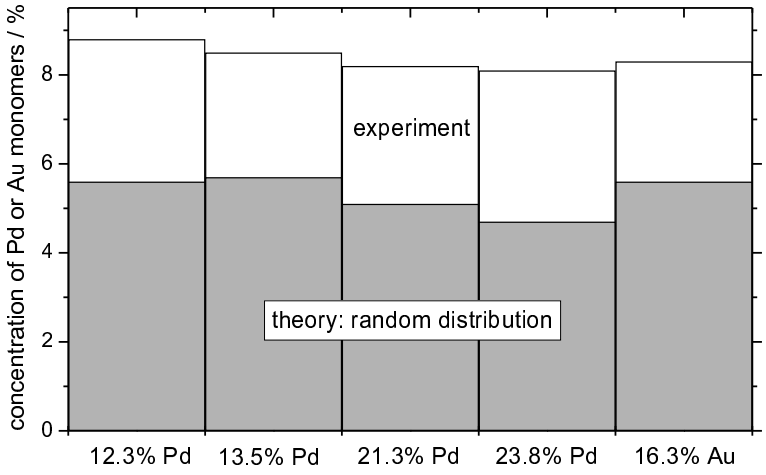

Figure 4.19: Statistical analysis of Pd and Au monomers on different AuPd(111) surface alloys. The (higher) experimental values are marked by white boxes, and the (lower) theoretical predictions are marked by grey boxes. The preparation parameters for the different surfaces are given in table 4.4.

first sight. If neither an ordered structure nor phase separation is detected, it still has to be clarified, to what extent the element distribution deviates from a completely random distribution. In the following this problem will be examined for AuPd(111) surface alloys.

Although the mixing energy in general depends on the surface composition, it is likely that the general trend — i. e., whether phase separation or enhanced mixing occurs — is constant for a given system. For qualitative statements it is therefore sufficient to evaluate concentrations with either a surplus of Au or of Pd atoms in the surface layer. The results obtained on three different films are displayed in fig. 4.19, and the preparation parameters are given in table 4.4. In the figure only the amount of Pd (or Au) monomers are shown, because these numbers demonstrate already that the atoms are not randomly distributed. For a completely random distribution the following value for the concentration of monomers of type A in an A_xB_{1-x} surface can be calculated:

$$c_{mono} = x\,(1-x)^6 \tag{4.1}$$

As can be seen in table 4.4, the deviation from a random distribution seems to be largely independent of the preparation conditions and of the local film thickness. Also it is found for both cases that were analysed: large Pd surplus and large Au surplus in the surface, respectively.

This behaviour is not surprising for two reasons. First, it is well known, that on the inverse system (Pd-Au(111)) an ordered alloy phase exists, which exhibits a $(\sqrt{3}\times\sqrt{3})R30°$ superstructure [97] and corresponds to the bulk Pd_2Au phase. This indicates that in principle the mixing energy is negative on (111)

Pd(**Au**) conc./%	initial Θ_{Au}/ML	annealing parameters	local Θ_{Au}/ML
12.3	2.7	2 min; 700 K	3
13.5			2
21.3	1.4	30 s; 775 K	2
23.8			1
16.3	0.8	30 s; 1000 K	-

Table 4.4: Preparations parameters for the AuPd(111) surface alloys used for the evaluation that is shown in fig. 4.19.

oriented AuPd surfaces[6]. The fact that on AuPd(111) no long-range order has been detected, can be attributed to a somewhat smaller mixing energy compared to the inverse system. Or to express it in other words: For AuPd(111), the repulsion between next-nearest Au (or Pd) atoms is not strong enough to lead to a complete absence of Au or Pd dimers and of larger clusters consisting of only one species. Secondly, the mixing tendency within AuPd(111) surfaces is also predicted by self-consistent calculations based on the density-functional theory. Christensen et al. report phase diagrams of surface alloys for all combinations of the transition and nobel metals [98]. In their model, pseudomorphic overlayers of A_xB_{1-x} composition are put onto the close packed surface of a pure B crystal. According to their model two numbers describe the essential features of such an surface alloy. First, a segregation energy for impurities of type A in a host B is calculated. If a negative value is found then the system A_xB_{1-x}/B tends to be stable against bulk diffusion and vice versa. Second, a surface mixing energy provides an estimate for the tendency of intermixing between the two components in the surface layer. For the present considerations the latter quantity is of interest for the AuPd(111) system. Christensen et al. calculate a negative mixing energy of -0.22 eV/atom for this system. This number by itself does not say much, but if it is compared to the corresponding number for PdAu(111) (-0.73 eV/atom) it becomes clear that the mixing tendency and hence the ordering tendency is less pronounced for AuPd(111) compared to PdAu(111). Also for other systems where ordering is observed experimentally the absolute value of the mixing energy is considerably higher than for the AuPd(111) system (e. g., for PdCu(100) a mixing energy of -0.85 eV/atom is calculated).

At the end of this section an example of the element distribution in a AuPd(111) surface alloy with intermediate Pd concentration (42%) will be discussed. This case is instructive in so far as it demonstrates the tendency of the human perception to overestimate the degree of order in random structures. An STM image of this film is shown in fig. 4.13(c). At first sight, it seems that the Au and

[6]In a recent combined experimental (STM) and theoretical (DFT) study Sadigh et al. found a clear tendency of the Au-Pd alloying system towards enhanced mixing also in the case of pseudomorphic monolayer thick Au-Pd alloy films on a Ru(0001) substrate [96].

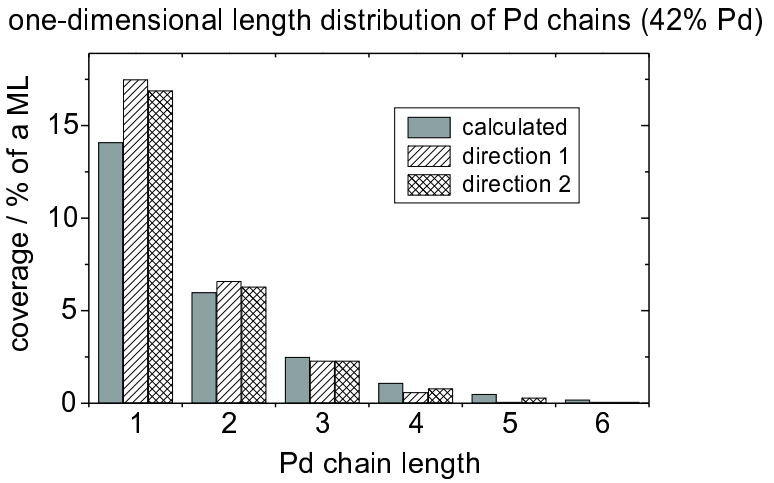

Figure 4.20: Statistical analysis of the Pd chain lengths in a AuPd(111) surface alloy with 42% Pd in the surface layer (see fig. 4.13(c)). From an STM image with $\sim$ 3000 atoms the chain length distribution has been evaluated in two of the three equivalent close-packed directions. They are compared to the calculated values for a random Pd distribution.

the Pd atoms form larger continuous structures than expected for a random distribution. Therefore, one feels inclined to propose a significant deviation from the above mentioned behaviour of Au and Pd to exhibit enhanced mixing in the surface layer. Especially, the abundance of one-dimensional Pd chains containing three and more atoms seems to be larger than intuitively expected for a random distribution. The latter point has been checked by a statistical evaluation of an STM image of the same film as fig. 4.13(c) that contains $\sim$ 3000 atoms. For two of the three equivalent close-packed directions of the surface the length distribution of continuous Pd chains has been evaluated. The result is shown in fig. 4.20. It is evident that also in this film *smaller* Pd structures are preferred over larger Pd structures as compared to a completely random distribution. Hence, also here a clear tendency towards enhanced mixing is detected, which is in complete agreement to the above evaluations and discussions for AuPd(111) surface alloys with either a low Pd or a low Au concentration. On the other hand, the visual expression is shown to be misleading in this case. While the eye suggests larger Pd structures to be preferred, the opposite is demonstrated to be true by a careful analysis. It can be concluded that the judgement about the degree of order in an atom distribution can not be done by merely looking at STM images.

4.5 Interdiffusion kinetics analyzed by AES and numerical integration of rate equations

As it was shown above, the local composition of the surface layer of bimetallic substrates can be determined exactly with the help of atomically and chemically resolved STM images. Therefore, information on alloying processes that involve mainly surface atoms is readily accessible. On the other hand, the interdiffusion of metals in the bulk can be studied on a macroscopic scale. These processes have been investigated for many years and a large database is available on the diffusion parameters for binary and even for ternary alloy systems (see for example [99] for an overview over the database and for a short introduction to the employed experimental methods). However, between the surface and the bulk an intermediate region exists that might exhibit transport properties which are considerably different from the behaviour in the volume. One way to study diffusion processes in this subsurface region consists in the analysis of temperature and time dependent changes of near-surface concentration profiles. Of course it is difficult to obtain these profiles experimentally. While for diffusion processes in the bulk the typical length scales are in the range of a few micrometers and concentration gradients can be measured by macroscopic methods, for the present case the sample composition has to be measured on atomic length scales. Even with surface sensitive tools like AES the signal is integrated over several atomic layers and therefore from peak intensities alone no precise information can be inferred regarding the local chemical composition. However, if a diffusion experiment is performed in a way, where the starting situation is completely determined, the connection between AES intensities and concentration profiles might be provided by physical models describing the evolution of the system. The details of this approach will be explained below for the example of Au-Pd interdiffusion in the near-surface region of Pd(111).

Epitaxial layers of Au on Pd(111) were prepared by Au deposition around room temperature, where interdiffusion is negligible. Therefore, well-defined concentration profiles serve as starting points for the alloying experiments. The description of the alloying processes at elevated temperatures still contains many free parameters. Hence, further approximations are necessary and the experimental data set has to be large enough to determine some of the parameters. By annealing the sample at different temperatures in front of the AES analyzer and by continuously monitoring the Au(NVV) and the Pd(MNN) peaks it is possible to gain a data set that is sufficiently large for a detailed analysis. Two sets of experiments are displayed in figs. 4.21 and 4.22 (curves a) for 0.9 ML and 2.7 ML Au, respectively. Since Au and Pd are completely miscible in the bulk, these AES experiments are monitoring the evolution of the system from a highly non-equilibrium situation (pure Au layers ontop of a pure Pd crystal) towards thermodynamic equilibrium. The latter would be characterized by a homogeneous

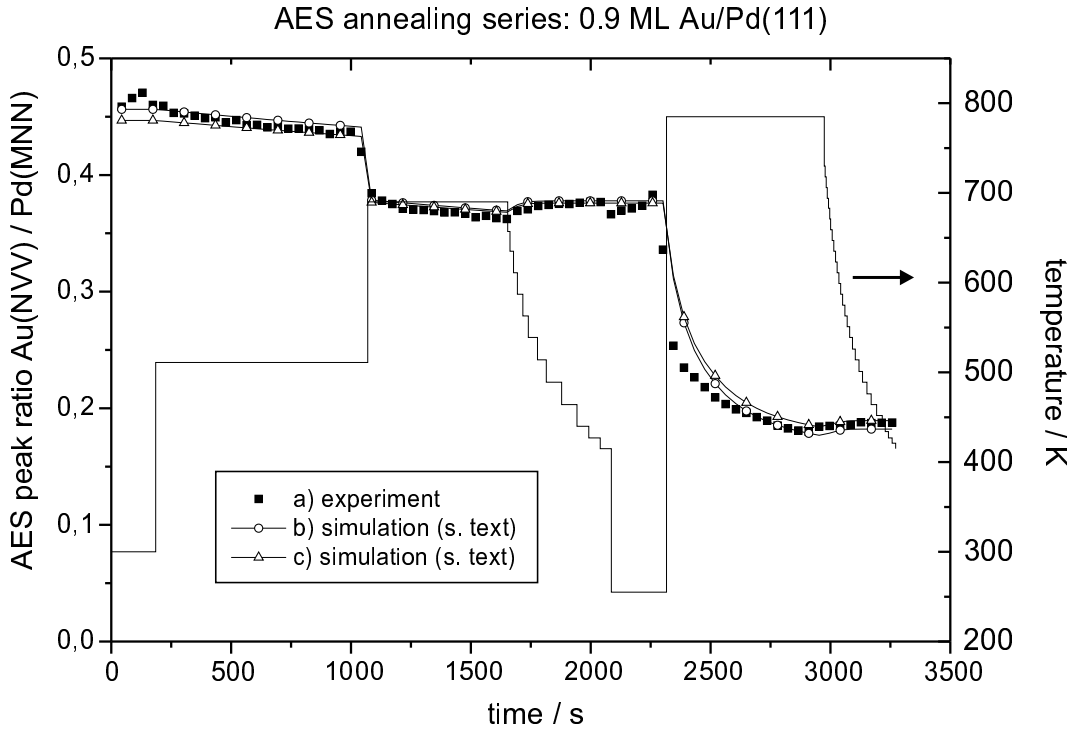

Figure 4.21: Au-Pd(111) interdiffusion monitored by AES (0.9 ML Au). The parameters for the simulations are explained in the text and are listed in table 4.5. The temperature curve represents the temperatures that were used for the simulations. These are derived from the temperatures measured during the AES experiment.

distribution of Au in the Pd crystal with an enhanced surface Au concentration due to segregation. For the temperatures that were applied in these experiments the atoms can not overcome the energy barriers of the equilibration process fast enough to approach equilibrium on the experimental time scale. The kinetics of this process is describable by rate equations for the Au concentrations of the different layers. The change of the Au concentration (c_i) in layer i per time is determined by the concentration of the layer itself and of the neighbouring layers $i-1$ and $i+1$ and by the exchange rates between these layers ($r_{k\to l}$)[7]:

$$\begin{aligned}\frac{\mathrm{d}}{\mathrm{dt}}c_i = \dot{c_i} \;\; = \;\; & r_{(i-1)\to i}\cdot c_{i-1}\cdot(1-c_i) - r_{i\to(i-1)}\cdot c_i\cdot(1-c_{i-1}) \\ & + r_{(i+1)\to i}\cdot c_{i+1}\cdot(1-c_i) - r_{i\to(i+1)}\cdot c_i\cdot(1-c_{i+1}), \qquad (4.2)\end{aligned}$$

for $i \geq 1$ and $(i = 0)$ = surface layer.

[7]In this description it is assumed that the Au atoms are distributed homogeneously within each layer. The possible dependence of the exchange rate on the *local* layer composition is neglected

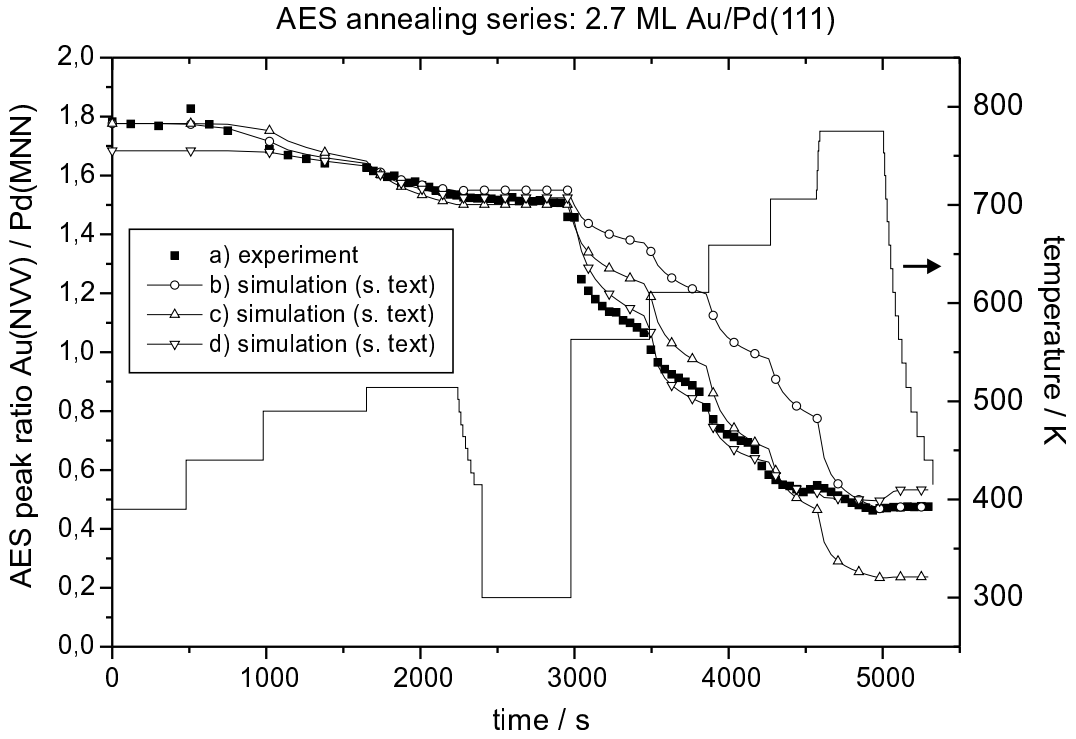

Figure 4.22: Au-Pd(111) interdiffusion monitored by AES (2.7 ML Au). The parameters for the simulations are explained in the text and are listed in tables 4.5 and 4.6. The temperature curve represents the temperatures that were used for the simulations. These are derived from the temperatures measured during the AES experiment.

It should be noted that the above formula follows immediately if direct atom exchange processes are considered. However, the diffusion mechanism that is commonly found in metallic systems is vacancy mediated diffusion. As long as the concentration of vacancies is small, equation 4.2 is valid also in this case. The exchange rate $r_{k\to l}$ can be written as product of a preexponential or frequency factor ν and an exponential function:

$$\begin{aligned} r_{k\to l} &= \nu_{k\to l} \cdot e^{-\frac{E_{k\to l}}{kT}} \\ \nu_{k\to l} &= \nu_{k\to l}(k, l, c_k, c_l, T) \\ E_{k\to l} &= E_{k\to l}(k, l, c_k, c_l) \end{aligned} \tag{4.3}$$

In a first approximation the preexponential factor is assumed to be constant. $\nu = 4 \cdot 10^{14}\mathrm{s}^{-1}$, which is the measured value for Pd self diffusion [99], will be employed in the calculations presented below. The following discussion concentrates on the information that can be derived concerning the energy barriers $E_{k\to l}$ encountered by atoms that migrate from layer k to layer l. First, a model developed by Gleich

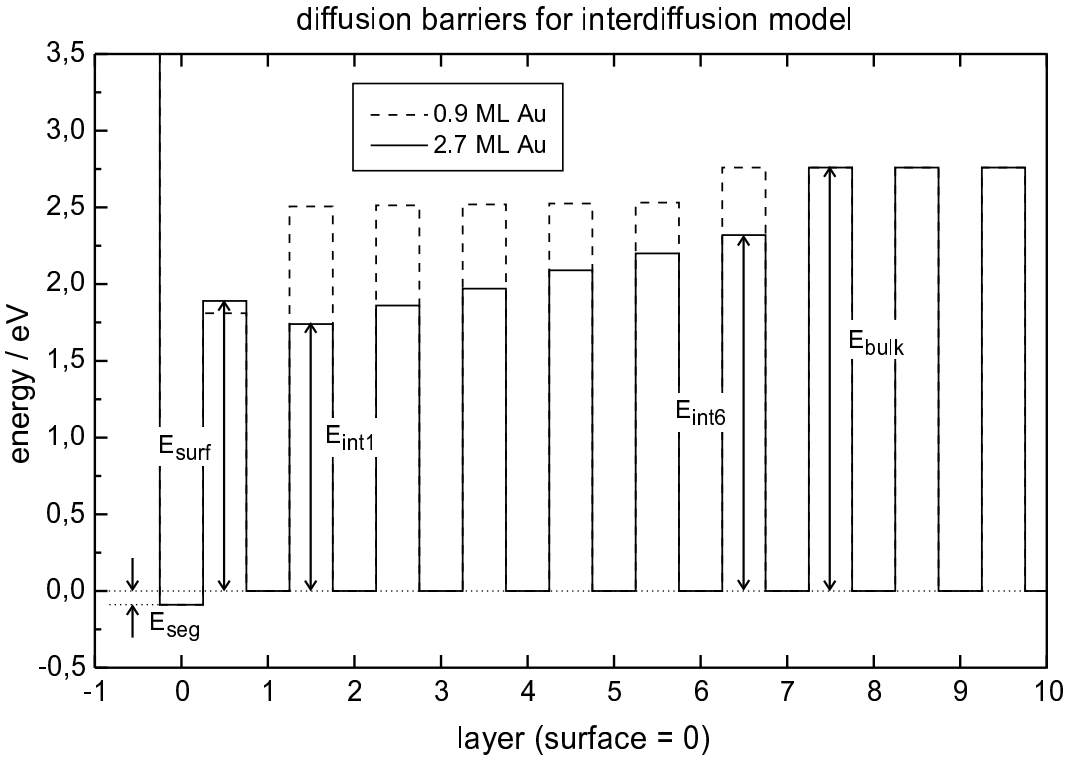

Figure 4.23: Scheme of the diffusion barriers used for the simulations.

for the analysis of the same data sets as shown in figs. 4.21 and 4.22 will be explained [38]. As second step, some generalizations of this model, that were explored in this work, will be presented. Gleich attempted to fit the measured AES intensity ratios with a model that contains as few free parameters as possible. Therefore, he introduced the following approximations and assumptions:

- The diffusion barriers are independent of the local Au concentrations.
- The negative Au-Pd mixing enthalpy is neglected.
- A Au segregation energy has to be introduced in the surface layer to fit the data.
- As a consequence of the two above points, the chemical potential for Au and Pd atoms is assumed to be constant for all layers except of the surface layer, where μ_{Au} is higher than in the other layers.
- The diffusion barrier for atom migration between deeper layers is fixed at the value for Pd self diffusion (2.76 eV [99]; the diffusion barrier of Au tracer diffusion in Pd has not been reported so far).

- For the diffusion between several intermediate layers, that are located near the surface, the energy barriers are reduced compared to the bulk value. While the barrier between the surface and the subsurface layer is adjusted independently, a linear relationship between $E_{k\to l}$ and k is considered for these intermediate layers.

- The inelastic mean free paths of the Auger electrons are held constant at 4.5 Å for Au(NVV) electrons with 69 eV kinetic energy (λ(Au)) and at 6.4 Å for Pd(MNN) electrons (330 eV, λ(Pd)) [100], i. e., the matrix dependence of λ is neglected.

As a result of these assumptions four parameters to adjust the diffusion barriers and one normalization factor for the relative AES sensitivities remain as fit parameters. In fig. 4.23 these parameters are illustrated: The segregation energy E_{seg} determines the slight increase of the Au AES signal that is observed upon cooling the sample from temperatures around 700 K to room temperature (see fig. 4.21 at 1700 s and at 3000 s). The relatively low diffusion barrier between the surface and the subsurface layer (E_{surf}) is responsible for the slight decrease of the relative Au AES intensity observed for annealing temperatures up to 500 K (if $\Theta_{\mathrm{Au}} < 2$ ML). At higher annealing temperatures the decrease of the AES signal can be reproduced by adjusting the diffusion barriers of several intermediate layers. In the example shown in fig. 4.23 six intermediate layers are used. The heights of these intermediate barriers are not varied independently but a linear increase of the energy from E_{int1} to E_{int6} is assumed.

The resulting model can be expressed by the following system of simplified rate equations (the surface is taken as layer 0 and $\beta = \frac{1}{kT}$):

$$\begin{aligned}
\dot{c_0} &= \nu\left(c_1(1-c_0)e^{-\beta E_{surf}} - c_0(1-c_1)e^{-\beta(E_{surf}+E_{seg})}\right)\\
\dot{c_1} &= \nu\left(c_0(1-c_1)e^{-\beta(E_{surf}+E_{seg})} + (c_2-c_1)e^{-\beta E_{int1}}\right)\\
\dot{c_2} &= \nu\left((c_1-c_2)e^{-\beta E_{int1}} + (c_3-c_2)e^{-\beta E_{int2}}\right)\\
&\vdots\\
\dot{c_7} &= \nu\left((c_6-c_7)e^{-\beta E_{int6}} + (c_8-c_7)e^{-\beta E_{bulk}}\right)\\
\dot{c_{i\geq 8}} &= \nu(c_{i-1}+c_{i+1}-2c_i)e^{-\beta E_{bulk}}.
\end{aligned} \tag{4.4}$$

A numerical integration of these differential equations yields the Au concentrations in the different crystal layers for arbitrary annealing procedures of Au/Pd(111) films. For fractional Au coverages like 2.7 ML the initial conditions are chosen as $c_0 = c_1 = 1$, $c_2 = 0.7$, $c_{n>2} = 0$, i. e., the influence of surface steps is neglected. The relative Au(NVV)/Pd(MNN) AES intensities follow immediately from the c_i by:

$$\frac{I_{Au(NVV)}}{I_{Pd(MNN)}} = N\frac{\sum_{i=0}^{\infty} c_i e^{-\alpha_i(Au)}}{\sum_{i=0}^{\infty}(1-c_i)e^{-\alpha_i(Pd)}} \tag{4.5}$$

and

$$\alpha_i(X) = \frac{i\,d}{\lambda(X)\,cos\theta} = \frac{i}{\lambda^*(X)} \quad , X = Au, Pd \tag{4.6}$$

with

N	ratio of the sensitivity factors for Au(NVV) and Pd(MNN) Auger electrons,
α_i(Au) [α_i(Pd)]	attenuation factor of electrons with 69 eV [330 eV] kinetic energy emitted in layer i,
d	interlayer distance (2.25 Å for Pd(111)),
θ	polar angle of the direction to the electron analyzer (42°),
λ^*(Au) [λ^*(Pd)]	modified inelastic mean free paths of 69 eV [330 eV] electrons: $\lambda^* = \lambda\,cos\theta/d$.

As has been shown by Gleich and as will be illustrated below, this model is capable of an accurate description of the AES annealing series with initial Au coverages of 0.9 ML (fig. 4.21) and of 2.7 ML (fig. 4.22). However, the fitting parameters had to be chosen differently for the low and for the high Au coverage film, respectively. Hence, the interesting question arises, whether it is possible to define a more general model that is able to describe both experiments with an identical set of parameters. Before this shall be attempted, it will be tested, how strongly the choice of the λ values influences the other parameters. Then, an explicit dependence of the diffusion barriers on the local alloy composition will be included into the model.

Variation of λ(Au) and λ(Pd). As a first modification of the calculations by Gleich, the matrix dependence of the inelastic mean free paths of the Auger electrons is introduced into the model. The different contributions to the sum for

Θ_{Au}	0.9 ML (fig. 4.21)		0.8 ML[a] [38]	2.7 ML (fig. 4.22)	2.3 ML[a] [38]
E_{seg}/eV	0.09				
E_{surf}/eV	1.81		1.80	1.89	1.80
n	5			6	5
E_1/eV	2.51		2.48	1.74	1.80
E_n/eV	2.59		2.68	2.31	2.35
E_{bulk}/eV	2.76				
$\lambda^*_{Au/Pd}$(Au)	2.0/1.7[b]		1.5/1.5	2.0/1.7[b]	1.5/1.5
$\lambda^*_{Au/Pd}$(Pd)	2.3/3.0[b]	3.0/4.0	2.1/2.1	-12.3/3.0[b]	2.1/2.1
N	1.33	1.9		1.09	
curve	b	c		d	

[a]The discrepancies between the Au coverages given by Gleich and those used for the present calculations are due to a new AES coverage calibration, that is improved because of the inclusion of additional combined AES-STM experiments.

[b]Values taken from [100].

Table 4.5: Parameters for fitting the AES annealing series for 0.9 ML and 2.7 ML Au/Pd(111). The values used by Gleich for the simulation of the same experimental data sets are included for comparison.

the Au and Pd intensities in equation 4.5 have to be rewritten:

$$c_i e^{-\alpha_i(Au)} \rightarrow c_i \prod_{j=0}^{i-1} \epsilon_j(Au) \tag{4.7}$$

$$(1-c_i) e^{-\alpha_i(Pd)} \rightarrow (1-c_i) \prod_{j=0}^{i-1} \epsilon_j(Pd) \tag{4.8}$$

$$\begin{aligned} \epsilon_j(Au) &= c_j e^{-\frac{1}{\lambda^*_{Au}(Au)}} + (1-c_j) e^{-\frac{1}{\lambda^*_{Pd}(Au)}} \\ \epsilon_j(Pd) &= c_j e^{-\frac{1}{\lambda^*_{Au}(Pd)}} + (1-c_j) e^{-\frac{1}{\lambda^*_{Pd}(Pd)}} \end{aligned}$$

with $\lambda^*_{Au[Pd]}$(Au/Pd) being the modified inelastic mean free paths for Au(NVV, 69 eV)/Pd(MNN, 330 eV) Auger electrons in Au[Pd]. The values for $\lambda^*_{Au[Pd]}$ (Au/Pd) are taken from calculations by Tanuma, Powell, and Penn [100]. This modification of the model calculations results in only minor changes of the fitted parameters, which is shown in table 4.5, where the parameter used by Gleich and those from this work are compared. For both films, calculations have been performed with strongly altered λ values, but even for unrealisticly high or low values no better agreement between the parameters for the two films could be achieved. One example for the 0.9 ML Au film is included in fig. 4.21 and in table 4.5, which shows that the kinetic parameters do not have to be changed if $\lambda^*_{Au[Pd]}$(Pd) is considerably increased. It can be concluded that the deviation between the parameter sets for 0.9 ML Au and for 2.7 ML Au is not an artefact that is caused by an erronenous choice of the Auger electron attenuation parameters.

curve	b	c
dependence $E_{i\leftrightarrow i\pm1}(c_i, c_{i\pm1})$	linear (eq. 4.9)	square root (eq. 4.10)
E_{bulk}/eV	2.76	
E_{Au}/eV	1.56	1.66
E_{seg}/eV	0.09	
E_{low}/eV	0.06	

Table 4.6: Parameters for fitting the AES annealing series for 2.7 ML Au/Pd(111) using concentration dependent diffusion barriers. The barriers follow from equations 4.9 and 4.10 with E_{low} giving the additional lowering of $E_{0\rightarrow1}$ and $E_{1\rightarrow0}$.

Concentration dependence of the diffusion barriers. Au-Pd interdiffusion in bulk alloys exhibits a strong dependence on the alloy composition [101], with Pd diffusion in Au rich alloys being considerably faster than Au diffusion in Pd rich alloys. This was inferred from the analysis of the concentration profile across a polycrystalline Au-Pd interface that had been annealed at 1173 K. Therefore, it is not surprising that the simple model introduced by Gleich, where the concentration dependence of the diffusion barriers is neglected, is not general enough to provide a unique set of parameters for different experimental situations. In the following, several attempts to obtain such a generally applicable description will be discussed. It should be mentioned beforehand, that these efforts have not reached their aim and that they were even less successful in fitting the two experiments separately than the previous model. It is sufficient to discuss the problems that are encountered, if the Au concentration dependence is introduced, for the case of 2.7 ML Au.

The concept of several near-surface layers (intermediate layers) with enhanced atom exchange rates is given up in the following calculations because the number of free parameters in a combined model (concentration *and* layer dependence of the diffusion barriers) would be too high to allow the derivation of meaningful results. Only the lowering of the energy barrier between the surface and the subsurface layer by E_{low} and the segregation energy E_{seg} are included in the new model as additional parameters. Next, the functional relationship between $E_{i\leftrightarrow i\pm1}$ (diffusion barrier between layer i and layer $i\pm1$)) and the $c_i, c_{i\pm1}$ has to be chosen. Two different functions have been tested, both of which require only one additional fitting parameter, namely the Pd diffusion barrier in pure Au (E_{Au}):

1. It is always a good idea to start with the simplest possible function if the true dependency is unknown. Therefore, a linear relationship between the energy barrier and the Au concentrations was used in the first calculations:

$$E_{i\leftrightarrow i\pm1} = E_{Au} + (1 - \overline{c_{i,i\pm1}})\Delta E \qquad i \geq 2^8 \tag{4.9}$$

with $\Delta E = E_{bulk} - E_{Au}$. Two possibilities to define the local Au concentration were investigated:

(a) $\overline{c_{i,i\pm1}} = 0.5\,(c_i + c_{i\pm1})$

(b) $\overline{c_{i,i+1}} = c_i \qquad$ and $\qquad \overline{c_{i,i-1}} = c_{i-1}$.

While the former seems to be a natural choice, the latter was included for reasons that will be explained below. Typical results for the linear dependence are included as curve b in fig. 4.22. The parameters for this calculation are given in table 4.6. Here, the second version (b) for calculating the $\overline{c_{i,i\pm1}}$ was used, but there is no significant difference in the shape of the curve if the first version (a) is applied. While the initial and the final parts of the curves could be reproduced statisfactorily by adjusting E_{Au}, the intermediate sections of the calculated curves were always found to be considerably too high. This is also true for the first choice of the $\overline{c_{i,i\pm1}}$. The reason for these deviations is that at intermediate temperatures (550 K–700 K) the Au atoms propagate too slowly into deeper layers. This was the motivation to use version (b), where the $\overline{c_{i,i\pm1}}$ are determined as the concentrations of the layer which is closer to the surface and which contains more Au. It was expected that for these $\overline{c_{i,i\pm1}}$ the intermediate region could be fitted more successfully, but it turned out that the effect of changing the calculation method for $\overline{c_{i,i\pm1}}$ is very small (therefore only one of the possibilities is included in fig. 4.22).

2. A square root dependence of the energy barrier on the Au concentration was chosen as one possibility to enhance the Au diffusion in the "frontier layers", where only few Au atoms are present and where the above discussed linear model resulted in atom mobilities that were too low to reproduce the AES data. The diffusion barriers for this square root model were calculated using the following equation:

$$E_{i\leftrightarrow i\pm1} = E_{Au} + (1 - \sqrt{\overline{c_{i,i\pm1}}})\Delta E \qquad i \geq 2^{8} \tag{4.10}$$

As an example for this type of calculations curve c is shown in fig. 4.22. For the parameters used in the calculations for the displayed curve see table 4.6. Again different possibilities to determine the values for $\overline{c_{i,i\pm1}}$ were tested, but no significant differences were noticed. Curve c in fig. 4.22 was obtained by method (b). In short, the assumption of a square root dependence $E_{i\leftrightarrow i\pm1}(c_i, c_{i\pm1})$ resulted generally in an even poorer agreement between the simulated and the measured data points compared to the linear model. From the example shown in fig. 4.22 only the initial part of curve c exhibits

[8] For $E_{0\rightarrow1}$ and $E_{1\rightarrow0}$ the lowering of the first layer barrier by E_{low} and the segregation energy E_{seg} have to be accounted for.

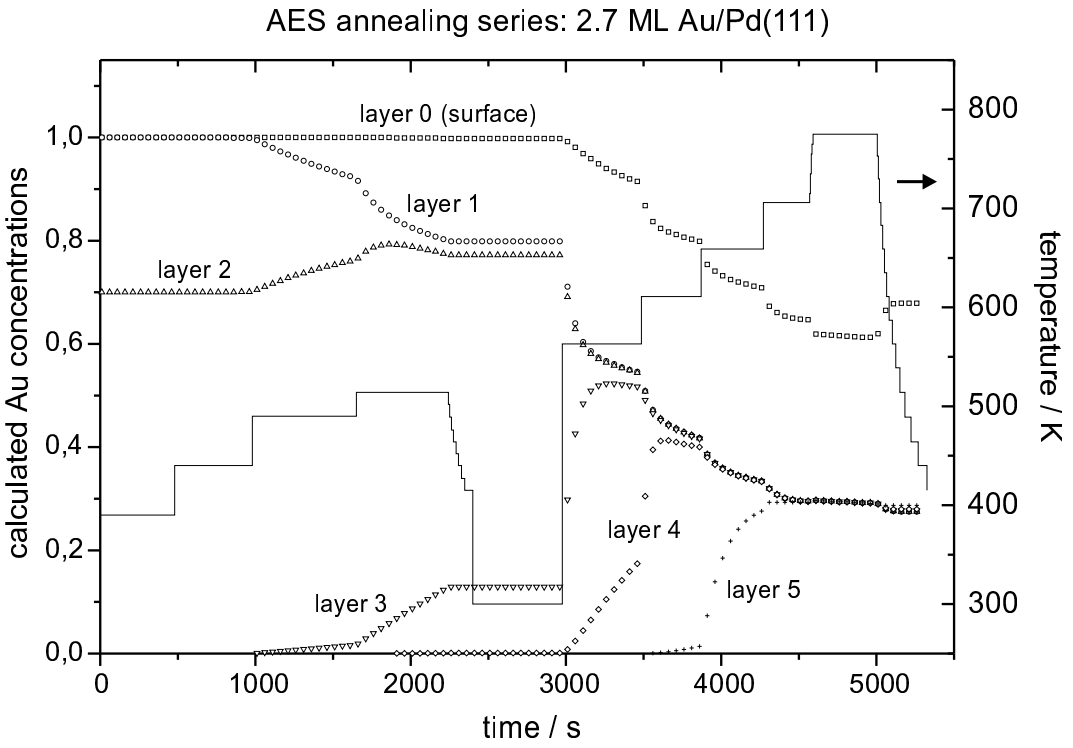

Figure 4.24: Calculated Au concentrations in the near-surface region of AuPd(111). The values correspond to the results obtained in the simulation run that is displayed as curve d in fig. 4.22.

good agreement with the experimental points. In the intermediate region systematic deviations are obvious and in the final section of the curve it is seen that the square root dependence results in exaggerated Au diffusion into deeper layers. Of course it is possible to fit the calculations to the final section of the curve, but then similar discrepancies are observed for the initial and the intermediate sections.

Two other ideas were explored by additional model calculations, but they were also not successful and will therefore only be mentioned in passing. An "interface energy" can be included either to lower or to enhance the diffusion barrier. For this a term that is proportional to $|c_i - c_{i\pm1}|$ is subtracted (added) from (to) the respective energy barrier. Also, a concentration dependent chemical potential can be introduced to account for the negative mixing enthalpy of the Au-Pd system. This results in asymmetric diffusion barriers similarly to the barrier shown in fig. 4.23 between the surface and the first sub-surface layer. With realistic values for the mixing enthalpies (~ 0.1 eV per atom) no significant changes of the interdiffusion kinetics were observed in the calculations.

As a conclusion from these calculations, it has to be stated that it was not

possible to develop a model for the interdiffusion processes of Au and Pd in the near-surface layers of AuPd(111) surface alloys that is able to explain all experimental observations. The best agreement between calculated and measured AES intensities could be obtained by adjusting concentration independent energy barriers for several sub-surface layers as proposed by Gleich [38]. At this stage, it is certainly not allowed to conclude that the experiments in principle can not be explained by an unified model — unified in the sense of applicable to arbitrary initial Au coverages — that exclusively relies on the concentration dependence of the diffusion barriers. However, it seems to be likely that only combined models, that on the one hand postulate intermediate layers with reduced diffusion barriers and that on the other hand also include a dependence on the local alloy composition, will be able to provide an adequate description of the problem. Since such models contain more adjustable parameters than the models that were presented above, additional experiments with different initial Au coverages are required to test these models and to determine the free parameters.

Despite of the fact that no physical reason is provided for the assumption of a linear decrease of the diffusion barrier as the surface is approached and that this assumption is only justified empirically, it is producing very good agreement between calculated and measured AES intensities. Therefore, it can be used to extract some additional information about the interdiffusion process. For example, the time evolution of the concentration profile in the near-surface region can be monitored by integrating the differential equations of the model. It is instructive to examine the changes of the Au concentrations that were calculated for the 2.7 ML film shown in fig. 4.24. According to these values, the initial slight decrease of the relative Au AES intensity ($T \leq 500\,K$) is solely caused by the interchange of atoms from the first and the second subsurface layers. With increasing temperatures additional layers are populated by Au atoms and a homogeneous distribution of the Au atoms among the subsurface layers is reached shortly after a new layer has started to be included in the exchange processes. The relatively small Au segregation energy of 0.09 eV is sufficient to result in a significantly enhanced surface Au concentration throughout the experiment.

4.6 Conclusions: AuPd(111) surface alloy formation

It has been shown in this chapter that by STM and AES measurements many different aspects of the surface alloying process could be revealed. In this concluding section these results will first be summarized and then they will be put into a broader perspective by a comparison with the structurally related systems PbCu(111) and PdCu(111). The following findings for the AuPd(111) alloying system have been demonstrated in the above sections:

- The alloy formation process starting from Au/Pd(111) overlayers strongly depends on the initial Au coverage.
- For low Θ_{Au}, where the Pd(111) substrate is not covered completely by the deposited Au layer, a complicated interplay between different diffusion and exchange processes has to be postulated in order to explain the structure of the experimentally observed surface alloys:
  - Au atoms evaporate from step edges and form a twodimensional lattice gas. The exchange between Au adatoms and Pd terrace atoms leads to an evenly distributed incorporation of Au atoms into the terraces. These processes have been observed for $T \geq 550\,K$.
  - At the same temperature a second alloying mechanism is gaining importance. The diffusion of Au atoms along island or step edges is accompanied by occasional exchange processes with Pd substrate atoms. These processes result in imprints on the terraces, the shape of which resemble the initial shapes of Au structures (islands and aggregations at steps).
  - At 650 K also a direct interlayer atom exchange process has to be assumed in order to explain the appearance of Pd atoms within larger Au islands.
  - It can be excluded that vacancy mediated intralayer diffusion processes occur with a substantial rate at $T \leq 600\,K$, because this would not be compatible with the observed sharp division lines between areas of different composition.
  - The island shapes change continuously from the initial dendritic and triangular shapes towards round shapes. The latter constitute the equilibrium island shapes on AuPd(111) surface alloys at an estimated temperature of about 600 K, where island edge diffusion processes become too slow to change the island shapes during cooling. Round shapes can be explained by a low kink formation energy on AuPd(111) surface alloys and the tendency to minimize the island edge length. Also, the higher configurational entropy of round islands as compared to hexagonal or triangular islands contributes to the preference of round shapes at higher temperatures.
  - Short (30 s) annealing at $T \approx 780\,K$ was determined to be sufficient for the formation of a homogeneous AuPd(111) surface alloy from submonolayer Au films. With these annealing parameters only about 10%–20% of the Au atoms are lost into subsurface layers.
- The interdiffusion phenomena of Au and Pd in multilayer Au/Pd(111) films are shown to be explainable by a much simpler mechanism. Only a single

type of interlayer Au–Pd exchange processes is necessary to account for the observed accumulation of Pd atoms in the surface layer by annealing. The exact nature of this exchange mechanism could not be revealed. Step edges and the stress relief pattern in the second and higher adlayers do not influence the alloying process.

- Au deposition at elevated temperatures (550 K and 600 K) leads to the formation of different alloy structures than obtained by room temperature Au deposition followed by annealing. These inhomogeneous surfaces might be applicable in future reaction experiments.

- The distribution of the atoms within homogeneous parts of the surface shows a pronounced preference of smaller clusters. Specifically, a considerable enhancement of the monomer density has been found for Pd and Au concentrations between 12% and 24% of the respective minority species. Also for 42% Pd, the preference of small structures (here: one-dimensional Pd chains) has been confirmed.

- The interdiffusion kinetics of Au and Pd in subsurface layers can be simulated using a model that accounts for a lowered diffusion barrier within several subsurface layers. The limitations of this model are demonstrated to consist in the failure to explain different experiments with an unique set of parameters.

As has been mentioned in the introduction to this chapter, the present investigations might be compared to recent STM studies on the Pb-Cu(111) [12] and the Pd-Cu(111) [22] alloying systems, which belong to the same class of surface alloys as Au-Pd(111) as defined in the introduction to this chapter (see table 4.1). Since Pb and Cu are immiscible in the bulk and because of the considerably lower surface energy of Pb compared to Cu (0.5 J/m^2 vs. 1.96 J/m^2) it is not expected that these two element should form surface alloys. However, STM measurements by Nagl et al. showed that even on the close-packed Cu(111) surfaces the incorporation of Pb atoms is possible [12]. Room temperature deposition of Pb leads to the formation of disordered Pb-Cu alloy stripes in the vicinity of downward step edges. Only few Pb atoms are found within the Cu terraces. For low Pb coverages (0.02 ML) most of the evaporated atoms are not visible in the STM images and are assumed to form a mobile adatom gas. Specifically no Pb islands or aggregations at step edges are detectable. Annealing at 573 K is sufficient for all Pb atoms from the adatom gas to become incorporated into the substrate layer. Nagl et al. determined the maximum amount of Pb atoms that can be accommodated in the former Cu(111) surface layer to be 0.22 ML. The enhanced Pb concentration in the vicinity of downward steps that is observed upon room temperature deposition is suggested to be due to a process, where the Pb atoms

are able to push several Cu atoms one atom spacing towards the step. The alloy formation process for Pb-Cu(111) appears to proceed via considerably different processes compared to Au-Pd(111). Only the exchange of adatoms and terrace atoms seems to be similar. The alloy formation in the vicinity of substrate steps is not comparable because in the case of Au-Pd(111) the Au aggregations at the steps play a decisive role while in the case of Pb-Cu(111) no such aggregations exist. The great differences between these two systems might be largely due to the immiscibility of Pb and Cu and to the large misfit between the Pb and the Cu crystal lattices.

A higher degree of common features can be expected if the present system is compared to the formation of PdCu(111) surface alloys, because these metals are also miscible in the bulk (like Au and Pd) and since the misfit between Pd and Cu is similar to the misfit of the Au-Pd system. Pd growth on Cu(111) at different temperatures has been investigated by Aaen et al. [22]. They find first indications of surface alloy formation already at room temperature, where highly disordered aggregations ("brims") are found to stretch out from former Cu step edges onto the lower terraces. Annealing at 453 K of Pd films that have been deposited at room temperature leads to a partial Cu capping of the brims accompanied by Cu erosion, which leaves one ML deep depressions in some of the terraces. Upon Pd deposition at elevated temperatures (523 K) broad PdCu alloy bands are visible in the terrace regions that are directly adjacent to a downward step. These bands exhibit a rather homogeneous composition and there exists a relatively sharp transition to almost Pd free areas in the centre of the terraces. Also the bands are found to be rather stable against further diffusion of the incorporated Pd atoms onto the pure Cu terraces. These observations are explained by Aaen et al. assuming an initial diffusion of Pd atoms to upward step edges followed by incorporation into the upper terrace and vacancy mediated diffusion over a certain distance. Finally, a favourable composition of the Pd rich bands is reached preventing any further diffusion into the inner parts of the terraces. Interestingly, it can be excluded that exchange processes between Pd adatoms and Cu terrace atoms occur frequently, because large Pd free areas are visible even after Pd deposition at 523 K. At this temperature also the incorporation of Pd atoms into the subsurface layer have been observed directly by STM with favourable tip conditions.

This short overview over the results obtained by Aaen et al. on the PdCu(111) surface alloy formation clearly demonstrates that there exist many qualitative differences also between this alloying system and the AuPd(111) system, even though in both cases complete miscibility of the components in the bulk exists and both studies were performed using the same crystal orientation. A qualitative explanation of the main differences can be found in the fact that the substrate atoms on Cu(111) are less strongly bound than on Pd(111), which can be inferred from the considerably lower melting point of Cu (1357 K) compared to Pd

(1828 K). Hence, at temperatures between 300 K and 600 K, where a comparison between the experiments on these two alloying systems is possible, larger fluctuations of Cu(111) step edges and also a higher rate of vacancy formation at these steps can be expected compared to Pd(111). This could explain the strong tendency for Pd incorporation into Cu steps and the formation of the broad PdCu alloy bands. Another factor that influences the alloy formation process is the diffusion rate of adatoms on the respective surfaces. Pd appears to be very mobile on Cu(111), because at room temperature islands are only formed on terraces with a minimum size of 1000 Å, whereas the critical terrace width for Au island formation on Pd(111) is around 400 Å at room temperature. The difference between the energy barrier for adatom diffusion and the energy barrier for the exchange between an adatom and a terrace atom determines the probability of an adsorbed atom to become incorporated into the terrace on its way to the next step or island edge. Hence, if the energy barrier for exchange was similar in both cases, the lack of Pd incorporation into the Cu(111) terraces could still be explained by the faster diffusion of the Pd adatoms on the Cu(111) terraces compared to the slower diffusion of Au on Pd(111). However, in order to show that this argument is correct the height of the diffusion barrier for Pd on Cu(111) is needed.

From the comparison of the two alloying systems it can be concluded, that even in systems with several common properties a completely different mixing behaviour in the surface might be encountered, because of subtle differences in the balance between the competing atomic processes on the surface (adatom diffusion, adatom exchange, step fluctuation, vacancy formation, etc.). Therefore, great care has to be employed if results from one system are analogized to other cases.

Part III

Adsorption and reaction on Au-Pd surfaces

Chapter 5

CO adsorption on bimetallic Au-Pd surfaces

The adsorption of CO has been chosen as starting point of these investigations on the local chemical properties of Au-Pd surfaces. Since the interaction of metal surfaces with CO is relatively well-understood, CO was considered to be the ideal probe molecule to reveal the basic chemical features of bimetallic Au-Pd surfaces.

5.1 Earlier results for CO adsorption

Without doubt, CO adsorption on metal surfaces is among the most extensively discussed topics in the surface science literature. A review has been given, for instance, by Campuzano in [102]. The reason for this might be found in an unique combination of technological relevance and experimental advantages. CO adsorption processes play a crucial role in many economically important applications of heterogeneous catalysts, e. g., the catalytic cleaning of car exhaust fumes, the selective oxidation of CO to reduce the CO concentration in the gas feed for low-temperature fuel cells gained from reformation of hydrocarbons [103], and catalytic synthesis of hydrocarbons in the chemical industry (Fischer-Tropsch synthesis). The practical advantages of CO for experimental studies are manifold. First it is easy to handle in UHV systems. Second, it is on the one hand reactive enough to stick to the surfaces of many metals even at room temperature and, on the other hand, it is relatively stable and can be found molecularly adsorbed on most of the late transition metals and on noble metals. Third, in the molecularly adsorbed form, CO is well suited for vibrational spectroscopic experiments because of its large dynamic dipole moment.

5.1.1 Theory: The nature of the metal–CO bond

The interaction between CO and metal surfaces has been in the focus of many theoretical studies. While several features of the metal–CO bond have been already qualitatively explained by the simple molecular orbital model of Blyholder [104], state of the art quantum chemical calculations have recently arrived at relatively accurate results for different CO-adsorption systems and provide a general understanding for trends in the reactivity towards CO adsorption across the periodic table [105]. Even for bimetallic surfaces, concepts have been developed to allow certain predictions for the effects of alloying or of depositing a thin metal overlayer on a second metal [106]. Also the structure sensitivity of CO adsorption has been successfully examined for selected Pt surfaces [107]. Here, a brief outline of the theoretical view on the CO–metal interaction should provide the basis for later discussions of the experimental results on CO adsorption properties of different Au-Pd surfaces. Since the language used to convey the calculated results is still based on the concepts of molecular orbital theory and the basic features of the so-called "Blyholder model" continue to be applied in modern investigations, it is appropriate to put some emphasis on the explanation of this model and to add the additional insight, that is provided by more accurate modern calculations, in the course of the presentation.

Blyholder developed his molecular orbital model for the chemisorption of CO on metal surfaces mainly to explain different vibrational spectroscopic observations that were available at that time [104]. In the pioneering work of Eischens, Francis, and Pliskin [108, 109] the C–O stretching vibrations had been recorded for silica-supported Cu, Ni, Pd, and Pt. Generally, a positive shift of the vibrational bands with increasing CO coverage was found. Other investigations were concerned with the influence of coadsorbates (O_2 and H_2 [110]), of alloying ($Ni_{90}Cu_{10}$ [111]), and of isotopic effects ($C^{12}O/C^{13}O$ [109]). In the framework of molecular orbital theory, the 10 valence electrons available in the CO molecule are distributed over five molecular orbitals, three of which are located in the region between the C and the O atoms constituting a triple bond. One lone pair of electrons is left at each of the two atoms, where on the C side the molecular orbital is mainly composed of an sp_z hybrid orbital of the C atom (if the z-axis is taken as the molecular axis). This orbital is able to form a σ bond together with a suitable acceptor orbital from a metal atom. The negative charge on the metal atom is reduced by a backflow of electron density from the metal d orbital to the lowest unoccupied orbital of the molecule. In other words, only two orbitals of the CO molecule are considered to participate in the metal–CO bond formation, namely the highest occupied molecular orbital (HOMO, 5σ) and the lowest unoccupied molecular orbital (LUMO, $2\pi^*$). From the former charge is transferred to metal orbitals ("donation"), whereas the latter receives electron density from the metal ("back-donation"). This picture has been confirmed in

modern first-principle studies, e. g., by Aizawa and Tsuneyuki for the case of CO/Pt(111) [112].

Blyholder assumes the effect of the donation to be constant and discusses only variations in the degree of back-donation from the metal d orbitals (or d bands in the case of bulk metals) to the $2\pi^*$ orbital for different metal–CO adsorption systems. Since the $2\pi^*$ orbital is antibonding with respect to the C–O bond, the back-donation leads to a weakening of the C–O bond, which manifests itself in a decreased C–O stretching frequency readily observable by IR spectroscopy. This argument can be applied both for metal CO complexes and for CO chemisorbed on metal surfaces. If in the latter case only linear bonded CO is considered (i. e., the CO molecule is located directly above a surface metal atom) the metal atom to which the CO molecule is bonded can be considered as the centre atom of a complex, where the CO molecule and the surrounding metal atoms constitute the ligands. The degree of back-donation to the CO $2\pi^*$ orbital is determined by the availablity of metal d electrons, which in turn is given by the number and the nature of the other ligands.

Using this simple argumentation, Blyholder discussed several spectroscopic observations:

- The different C–O stretching bands that are usually observed for CO adsorption on Ni surfaces are explained by adsorption of CO on Ni atoms with different coordination number. Undercoordinated metal atoms, that can be found at defect sites like surface steps, have less ligands to compete for d electrons, and therefore the back-donation is larger on these sites compared to regular terrace sites. Consequently, the higher frequencies would be ascribed to CO on terrace sites, while the lower frequencies originate from CO on defect sites. According to Blyholder, this could also explain the differences found in vibrational spectra for CO adsorbed on differently prepared supported metal particles, where the ratio of defect sites to terrace sites should determine the positions and relative intensities of the C–O stretching bands.

- The generally observed positive shift of the C–O stretching frequency with increasing CO coverage is explained by initial adsorption at undercoordinated defect sites (step edge and corner atoms) and subsequent filling of terrace sites.

- If other molecules are added to a CO adsorbate layer an upward shift of ν_{C-O} is expected for electron accepting coadsorbates and a negative shift should occur for donor coadsorbates. Both effects are observed for oxygen and hydrogen as coadsorbates, respectively [110].

- On alloys the band positions are also largely determined by the availability of d electrons. In the example of adding Cu to Ni ($Ni_{90}Cu_{10}$ [111]), Eischens

observed indeed a lowering of the C–O stretching frequency compared to CO on pure Ni. Cu with a filled d band is expected to provide additional d electrons and to increase the degree of back-donation.

Not all of the examples given by Blyholder can be considered to be sufficiently explained by his simple model. Here is not the place to discuss these cases in detail, but it should be emphasized that also in the more sophisticated approaches, that will be presented in the following, the basic idea of tracing changes in metal reactivity back to differences in the interaction between the metal d bands and the CO $2\pi^*$ and 5σ orbitals is found as a central thread.

Density functional theory (DFT) calculations[1] using the general gradient approximation (GGA) have been applied by Hammer, Morikawa, and Nørskov (HMN) to produce a database for the adsorption energy of CO on several close-packed metal surfaces. The latter were modeled with the atoms fixed at truncated bulk positions and no relaxations have been taken into account. Also only linearly bonded CO molecules were assumed with a coverage of $\frac{1}{4}$ ML. These calculations can be judged as computer experiments because of the idealization of the adsorption systems, that might not necessarily correspond to the experimental situations. According to the authors, the general trends observable in the calculated results for adsorption energies should not be altered by the simplifications. On the other hand, keeping the geometries fixed provides the advantage to be able to concentrate on the purely electronic effects vs. the structural effects that might additionally occur, e. g., by changing the adsorption site or by relaxations. As an example, the adsorption energy for CO on Pd(111) in an assumed on-top position at $\theta_{CO} = \frac{1}{4}$ ML is determined by the calculations to 1.30 eV compared to the experimental value for CO in fcc threefold hollow sites of 1.47 eV [114]. In other cases where the direct comparison with experimental data is possible, the deviations are of the order of 0.2 eV. On the one hand, this means that theoretical results are still not accurate enough to allow, for example, predictions about the rates of catalytic reactions on surfaces. On the other hand, the general trends found in the calculated adsorption energies should be reliable. This is exploited by HMN to correlate CO adsorption energies obtained from DFT calculations on several metallic and bimetallic systems to predictions from a simple model, that gives insight into the physical background behind the reactivity of metal surfaces. In this model the CO adsorption process is devided into two steps. In a first step the interaction of the frontier adsorbate states (5σ and $2\pi^*$) with the metal sp bands leads to a lowering and broadening of the adsorbate states. This step occurs both on simple metals, where no d bands are available, and on transition and noble metals with partially or completely filled d bands. Using

[1] An introduction into the basic consepts of the DFT and examples for its application in adsorption/surface reaction studies have been given, for instance, by Hammer and Nørskov in [113].

cluster calculations, Bagus and Pacchioni found that the interaction with the metal sp bands contributes a significant fraction of the CO adsorption energy on Cu and might be sufficient for a weak CO chemisorption on Li and Na, which has still to be verified experimentally [115].

In the following only CO adsorption on late transition metals and on noble metals will be discussed. These systems exhibit very similar half occupied s bands and therefore it is assumed by HMN that the first step, the renormalization of the adsorbate states, is identical for all metals under consideration. As a second step for the CO adsorption on transition and noble metals, the interaction of the already renormalized adsorbate states with the metal d band gives an additional contribution to the adsorption energy. In the limit of small S (overlap between adsorbate states and metal d states) and small V (coupling matrix element between adsorbate and metal states) compared to the energy separation between the two states, the following expression is a good approximation of the adsorbate – metal d band contribution to the CO adsorption energy on transition metal surfaces:

$$E_{d-hyb} \simeq -4\left\{f\frac{V_\pi^2}{\epsilon_{2\pi}-\epsilon_d}+fS_\pi V_\pi\right\}-2\left\{(1-f)\frac{V_\sigma^2}{\epsilon_d-\epsilon_{5\sigma}}+(1+f)S_\sigma V_\sigma\right\} \tag{5.1}$$

with

V_π, V_σ	coupling matrix elements of adsorbate states to metal d states
S_π, S_σ	overlap integral between adsorbate states and metal d states
f	fractional filling factor of the metal d bands
$\epsilon_{2\pi}, \epsilon_{5\sigma}$	energy position of the (renormalized) adsorbate states
ϵ_d	centre of metal d band.

The important idea of the model proposed by HMN is to assume the parameters f, $V_{\pi,\sigma}$, and $S_{\pi,\sigma}$ to depend exclusively on the atomic number of the respective metal and to consider the influence of the environment only by possible changes in the position of the d band centre ϵ_d prior to CO adsorption. Since the latter parameter is obtainable both experimentally (either directly by valence band photoemission experiments or indirectly by evaluation of surface core-level shifts (SCLS) that are found to be coupled to ϵ_d for the late transition metals [116]) and theoretically, certain predictions for CO adsorption energies on a broad variety of metal surfaces (ranging from pure metals via overlayer systems to alloys) become possible based on a single number, namely ϵ_d. The CO adsorption energies determined by this model, where the values for ϵ_d are derived from a DFT based treatment of the metal electronic structure, are compared by HMN to the respective energies of the above mentioned database gained from self consistent DFT calculations. By

adjusting two parameters to describe the coupling matrix elements and the overlap integrals for the different substrate elements a close correlation between the model and the DFT values is achieved for the following metal surfaces (the overlayers are always taken as pseudomorphic 1 ML thick films): Ag(111), Au(111), Cu(111), Ni(111), Pd(111), Pt(111), Cu/Pt(111), Ni/Ru(0001), Pd/Ru(0001), NiCu(111) surface alloy with 25% Ni, and $Cu_3Pt(111)$.

An immediate consequence of these considerations is, that the model is able to account for the experimentally observed correlation between CO adsorption energies and SCLSs for several metals and metal overlayers [116,117]. The identification of the physical properties of metal surfaces that determine the interaction with adsorbates — the arguments given for CO adsorption can be generalized to other molecules and to atoms — allows for certain predictions about adsorption energies for almost arbitrary combinations of transition and noble metals if the centre of the metal d band (ϵ_d) is either measured or calculated. Values for ϵ_d have been computed by Ruban et al. for a large variety of bimetallic systems using the "linear muffin-tin orbitals" (LMTO) method within the atomic sphere approximation (ASA) [106]. General trends in the variation of ϵ_d are observed for the cases where a metal is put as an overlayer on another metal and for cases where metal atoms are alloyed into a different host metal. These trends can be rationalized using a simple argumentation. Ruban et al. emphasize that the main trends observable in the self-consistently calculated values for ϵ_d are already captured by the simpler approach of effective medium theory (EMT) which considers variations in the electron density to be the only effect if the environment of an atom is changed. The electron densities depend in turn largely on size effects, i. e., if the Wigner-Seitz radius s of a metal is enlarged, the atoms will experience a lower embedding electron density. For transition and noble metals this leads to a decreased local band width of the d bands. Since changes in the d band filling factors f are strongly disfavoured, the position of the d band with respect to the Fermi level changes with the band width in order to keep f constant. Following this argument, $\frac{d\epsilon_d}{ds}$ has to be positive for the late transition metals ($f \geq 0.5$) and negative for the early transition metals ($f \leq 0.5$), which is confirmed by independent calculations [118]. Although for noble metals the idealized filling factor of the d band is 1 and the simple argument of $f \stackrel{!}{=} const.$ can not be used in this case, they are found to behave qualitatively similar to the late transition metals. For late transition metals it is found, that the core-levels are influenced by changes in the embedding electron density in the same manner as the valence-bands and therefore changes in the SCLS may be used as indicators for $\Delta\epsilon_d$ [116].

The results of Ruban et al. that are relevant for the Au-Pd system are given in table 5.1 as a reference for the discussion of the experimental results in the later sections of this thesis. The values for metal overlayers are calculated assuming a pseudomorphic monolayer of the deposited metal without accounting for lattice relaxations due to the overlayer. For the alloy systems 1at% of the impurity

system	ϵ_d / eV	$\Delta\epsilon_d$ / eV
Au(111)	-3.56	
Au overlayer on Pd(111)		-0.14
Au impurity atom in Pd(111)		0.17
Pd(111)	-1.83	
Pd overlayer on Au(111)		0.35
Pd impurity atom in Au(111)		0.17

Table 5.1: Calculated d band centres and shifts in the d band centres of surface impurities and pseudomorphic overlayers relative to the clean metal values. The values are taken from [106].

element is put into the host assuming a completely random alloy. Only the most close-packed surfaces of the host elements are considered. Concerning the effects of lattice relaxations, that were neglected in these calculations, Ruban et al. state that they are generally found to reduce the magnitude of the d band shifts without changing the observable trends and the sign of the shifts. Since the extreme values for $|\Delta\epsilon_d|$ calculated by Ruban et al. reach up to $\sim 2\,\mathrm{eV}$ (e. g., for Au overlayers on Fe, Co, Ni or Cu), it can be stated that the effects in the case of Au-Pd are relatively small.

For the adsorption of CO on different Au-Pd surfaces, the values given in table 5.1 allow the following general predictions:

- If a pseudomorphic monolayer of Au is put on Pd(111) the reactivity of the Au atoms should be decreased compared to a hypothetical bulk truncated Au(111) surface. However, the experimentally observable effect should be rather small, because the reactivity of a herring-bone reconstructed Au(111) surface with a reduced Wigner-Seitz radius in the surface layer should already be lower compared to the bulk truncated Au(111) surface used as the reference state by Ruban et al..

- Au atoms in a dilute Au-Pd(111) alloy surface should have a higher reactivity than Au atoms in the Au(111) surface. Here, the "real" effect might be even larger than predicted based on the same argument as given in the preceeding point (reconstructed vs. non-reconstructed Au(111) reference surface).

- Pd overlayers on Au should be more reactive towards CO adsorption than the Pd(111) surface. This effect should be relatively strong with $\Delta\epsilon_d = 0.35$ being the largest shift calculated for the Au-Pd system.

- Pd impurity atoms in a Au(111) matrix should exhibit a slightly higher reactivity compared to Pd(111) surface atoms.

It should be emphasized again that in this theoretical argumentation only electronic effects are considered and for example CO adsorption in higher coordinated sites (bridge/hollow sites) is not captured by the model. Therefore, a direct comparision with experimental data might not be possible in certain cases. It has to be discussed below, to what extent the presented experimental results for CO adsorption on Au-Pd(111) surfaces can be related to the above outlined calculations.

Besides reactivity modifications, that occur by adding a second metallic component to the substrate (either as overlayer or as alloy), changes are also observed if the local structure of an atom in a single component system is varied. These effects are subsumed under the label "structure sensitivity" of a reaction. DFT calculations have also been performed to study this aspect. Hammer, Nielsen, and Nørskov (HNN) report investigations on different stepped and reconstructed Pt surfaces [107]. As in the case of metallic overlayers and alloys, they found a close correlation between calculated adsorption energies on different Pt sites and the local centre of the metal d band. With increasing coordination number of the Pt atom a lowering of the CO adsorption energy was calculated. The overall effect was as large as $\sim 1\,\mathrm{eV}$, if kink sites on a Pt(11 8 5) surface are compared with terraces sites on the Pt(100)-hex(1×5) reconstructed surface, where the density of Pt surface atoms is even higher than on the Pt(111) crystal face. Also, a lowering of the C–O stretching frequencies is generally determined for undersaturated sites, which is in complete agreement with the expectations of Blyholder [104]. The variations of ϵ_d is again explained by changes in the width of the d band and the tendency to keep the d band filling factor constant. Therefore, the electronic effects of changing the local coordination of a metal atom can be described in a similar way as the changes by adding a second metallic component to the system. The key parameter that determines to a large extent the interaction with CO adsorbates is the centre of the d band, which correlates strongly with the d band width. Unfortunately, calculations for the d band positions of different Pd or Au sites have not been reported so far, but the general arguments should also be applicable to other elements than Pt.

5.1.2 Earlier experimental studies

A rough overview over the recent literature dealing with experimental studies of CO adsorption on metals reveals, that certainly Pt has most frequently been examined, but Pd surfaces are also well characterized concerning their CO adsorption properties. CO adsorption on more inert metals, like Au or Ag, has to be studied at low temperatures (or relatively high pressures) and is therefore not as thouroughly discussed in the literature as CO adsorption on transition metals. As it comes to bimetallic surfaces, the efforts to investigate CO adsorption on these more complicated systems have increased during the last years, such that

even for the very special system Au-Pd a number of studies have been published.

Basically all available experimental tools of surface science have been applied for investigations of CO adsorption on the various low index single crystal planes of Pd. Here is not the place to give a complete review on all of this work, but only the results which are relevant for the following presentations and discussions are summarized with strong emphasis on the system CO/Pd(111). Comparing differently oriented crystal planes of one metal with respect to a given reaction gives some insight into the so-called "structure sensitivity" of a reaction. Therefore, also the most important features of CO adsorption on Pd(100) and on Pd(110) will be mentioned. The effect of high step densities will be illustrated using the two examples Pd(112) and Pd(510). As will be seen in the course of this work, a discussion of the influence of coadsorbed residual gas species is required to rationalize some CO/Pd(111) TPD data and to explain striking discrepancies in published experiments on low temperature CO adsorption on Pd(111). Hydrogen constitutes by far the most abundant residual gas component — under typical low temperature conditions in the experiments of the present work the partial pressure of H_2 was a factor of 50 higher than that of the next frequent molecule besides CO. Therefore, some findings concerning the adsorption of H_2 on Pd(111) at low temperatures and the coadsorption of H_2 and CO will be added to this review chapter.

CO/Pd(111)

Almost 30 years ago, Ertl and Koch determined the main characteristics of the CO/Pd(111) adsorption system for temperatures equal and higher than room temperature [119]. By measuring adsorption isotherms via the determination of work function changes they found a constant adsorption energy of 142 kJ/mole up to a third of a monolayer followed by a sharp drop of about 8 kJ/mole within a few percent of a monolayer coverage. Then the adsorption energy decreases more gradually until at about 0.5 ML again a sharp drop occurs corresponding to CO saturation of the surface. At $\theta_{CO} = \frac{1}{3}$ ML Ertl and Koch observed a sharp $(\sqrt{3} \times \sqrt{3})R30°$ LEED pattern. With increasing CO coverage the superstructure spots split due to a compression of the adsorbate structure. In a further publication [114] the same authors together with Conrad and Latta point out, that already at relatively low coverages a sharp $(\sqrt{3} \times \sqrt{3})R30°$ pattern is observed, which indicates the formation of ordered CO islands due to attractive CO–CO interactions. Coverages above 0.5 ML can be achieved in UHV by lowering the sample temperature below 300 K. At 190 K - 200 K Conrad observed a $c(4 \times 2)$ structure with 0.5 ML CO and a subsequent continuous shift of the LEED reflexes with increasing CO dosis [120]. At a stationary CO pressure of $\sim 7 \times 10^{-6}$ mbar a (2×2) structure was obtained (200 K).

Indirect evidence for the respective adsorption sites of CO at different cov-

erages was found using Infrared Reflection-Absorption Spectroscopy (IRAS) by comparing the C–O stretching frequencies of the adsorbate with infrared spectra of carbonyl complexes with known structure [121–123]. At room temperature [121] only a single absorption band was found for all CO coverages under UHV conditions. For low exposures it is located at 226 meV and it shifts only slightly to 228 meV for 0.30 ML CO. From the low value of the C–O stretching frequency it was inferred that up to 0.3 ML CO adsorbs in threefold hollow sites of the Pd(111) surface. Between 0.30 ML and 0.43 ML a considerable broadening together with a large shift (to 238 meV) of the band occurs. This was interpreted as indication for a change in the CO adsorption sites from threefold hollow to twofold bridge sites. Consequently, in the structural model proposed by Hoffmann [123] for the $c(4 \times 2)$ structure at 0.5 ML all molecules occupy twofold bridge sites — a site assignment, which was later found to be incorrect by a structure determination using photoelectron diffraction (vide infra). At lower temperatures (90 K), CO coverages up to 0.75 ML were found to be stable in UHV [122, 123]. With increasing coverage a sequence of complex LEED patterns appears until at CO saturation a (2×2) pattern is observed. Also the IR spectra become more sophisticated at higher coverages ($\theta_{CO} > 0.6$ ML) with bands at 235 meV, 242 meV, 248 meV, and 260 meV.

Goodman and coworkers have largely increased the temperature and pressure range for IRAS measurements on CO/Pd(111) and CO/Pd(100) by employing a combined UHV and "high pressure" surface analysis system [124, 125], which could be operated at temperatures up to 1000 K and pressures up to 13 mbar. For CO/Pd(111) they found three different types of IR spectra. In the high temperature/low coverage limit, spectra with a single peak at 226 meV are recorded, which are attributed to CO on threefold hollow sites. By lowering the temperature at a given constant CO pressure a second regime is observed with a peak around 242 meV corresponding to bridge bonded CO molecules [2] according to the authors. This transition from the hollow to the bridge regime is not as abrupt as the next transition at even lower temperatures (or higher pressures) to the coexistence of linearly bonded CO (261 meV) with molecules on threefold hollow sites (235 meV). These two transitions are observed in the entire accessible pressure range (1.3×10^{-7}mbar – 13mbar) and obviously they occur at higher temperatures if the pressure is increased. They could be correlated to similar transitions observed in UHV experiments at low temperatures and with variable CO coverage. However, comparing the low temperature data of Kuhn et al. [124] with the work of Ortega [122] a striking discrepancy can be noticed. While in the first case it was not possible to populate on-top sites by CO adsorption at

[2] Here the assignment of the authors is used in order to be consistent in the nomenclature with the cited publications even though it will be seen later, that a new structure determination by photoelectron diffraction [126] determined the CO adsorption sites at 0.5 ML CO to be a mixture of fcc and hcp threefold hollow sites.

90 K, Ortega found a IR peak at 260 K after only 1.8 L CO at the same temperature. It will be shown later (section 5.2.1), that this deviation of the data most likely can be attributed to coadsorption of residual gas at low temperatures and is not characteristic for the CO/Pd(111) system itself. Kuhn et al. suggest as explanation for the discrepancy with the earlier studies, that CO adsorption at 90 K leads to a frozen non-equilibrium adsorbate structure, which of course would depend on the employed CO pressure and therefore could vary between different experiments without being an artefact. Another remarkable observation of Kuhn et al. is the detection of a C–O stretching frequency at 267.5 meV, which is considerably *above* the gas phase value of 265.7 meV. This high frequency peak was observed after annealing the surface in 1×10^{-6} mbar CO from 90 K to 200 K and recooling again in the CO atmosphere to 90 K. As possible explanation for this peak CO adsorption at surface defects (e. g., step edges) is suggested.

While in the above mentioned investigations the determination of CO adsorption sites was only arrived at indirectly by comparing IR data of the adsorption system with metallorganic complexes, also truely structure sensitive methods have been applied to study CO/Pd(111). Ohtani, van Hove, and Somorjai report a LEED intensity analysis for the $(\sqrt{3} \times \sqrt{3})R30°$ structure at $\theta_{\mathrm{CO}} = \frac{1}{3}$ ML [127]. They found, that the CO molecules indeed occupy threefold hollow sites as suggested by the vibrational spectra. Additionally, it was determined that the fcc type hollow sites are preferred over the hcp sites. In a recent photoelectron diffraction (XPD) study of Gießel et al. [126] these findings were confirmed. But also for the $c(4 \times 2)$ structure at 0.5 ML CO the occupation of threefold hollow sites (a 1:1 mixture of fcc and hcp sites) gave the best agreement with the photoelectron diffraction data. This is in contrast to the earlier indirect assignment to bridge bonded molecules based on the C–O stretching frequency at ~ 238 meV. Recent DFT calculations by Loffreda, Simon, and Sautet are in complete agreement with the structure determination by XPD [128]. The authors could explain the relatively large frequency shift from 226 meV (small CO coverages) to 238 meV (0.5 ML) by a combination of static and dynamic adsorbate–adsorbate interactions without changing the adsorption sites from threefold hollow to bridge.

Extensive TPD measurements for CO/Pd(111) are reported by Guo and Yates [129]. By employing the "threshold" TPD method (for an explanation see section 5.2.4 on page 163) they could independently determine the preexponential factor (ν) and the activation energy for desorption (E_a) for different CO coverages. While for small CO coverages the kinetic parameters for desorption from adsorbate layers, which were prepared at 87 K, are identical to those measured after adsorption at 200 K[3], for coverages above 0.27 ML CO a clear dependence of the desorption kinetics on the adsorption temperature is observed.

[3]In the limit $\theta_{\mathrm{CO}} \to 0$ the activation energy is determined to 148 kJ/mole, which is quite close to the value obtained for the adsorption energy of this system under equilibrium conditions by Ertl and Koch [119] of 142 kJ/mole and the preexponential factor is found to be $10^{15.3}\mathrm{s}^{-1}$.

Specifically, for the adsorption temperature of 87 K a continuous decrease of the activation energy is found between 0.27 ML and 0.47 ML CO from 119 kJ/mole to 29 kJ/mole. No further change is observed up to saturation coverage (0.75 ML). In the case of adsorption at 200 K a more complex behaviour is detected: There is also an overall decrease of E_a but there are two plateaus at 0.33 ML and at 0.5 ML, respectively, and an astonishing, small *increase* in E_a occurs between 0.60 ML and 0.66 ML. Generally, above 0.27 ML CO adsorption at 200 K results in larger values of E_a than adsorption at 87 K. At 0.5 ML the difference amounts to about 43 kJ/mole. It is attributed to a non-equilibrium effect. This means that at the temperature where desorption occurs the adsorbate structure has not adopted its lowest free energy configuration. Guo and Yates mention that even an 1800 s anneal at 200 K following adsorption of 0.5 ML at 87 K does not result in desorption kinetics equivalent to adsorption at 200 K, whereas cooling down of an adsorbate layer prepared at 200 K does not influence the desorption spectrum. Again, a striking deviation of the low temperature CO adsorption behaviour between the work of Guo and Yates and the publication of Kuhn et al. [124] has to be noted: While in the latter case no CO desorption below 290 K was detected even for a saturated adsorbate layer obtained by exposing the crystal at 90 K to 1.3×10^{-6} mbar, the TPD spectra of Guo and Yates clearly show a broad desorption feature starting at about 180 K (adsorption temperature 87 K).

The non-equilibrium effects found for CO adsorption on Pd(111) at low temperatures, which have been pointed out by Guo and Yates [129] and by Kuhn, Szanyi, and Goodman [124], have been studied recently in more detail by Bourguignon et al. [130]. They employed sum frequency generation (SFG) and IRAS to characterize the vibrational properties of the CO/Pd(111) system for different adsorption conditions. A fully ordered adsorbate layer with only two peaks at 258.2 meV and 242.4 meV, respectively could be obtained by annealing and recooling the surface from 170 K to 330 K in a CO atmosphere of 10^{-7} mbar. Up to four "extra peaks" were found, if the sample was held at low temperatures during the experiment. They were located at 234.3 meV, 240.5 meV, 259.5 meV, and 267.5 meV. The latter value is *above* the gas phase value for the C–O stretching vibration (265.7 meV) and was already assigned to CO adsorption on defect sites by Kuhn et al. [124](vide supra). However, Bourguignon et al. prefer to explain this peak by a weakly chemisorbed state within an environment of high local CO coverage at domain boundaries, because it appears reproducibly and exhibits considerable intensity. The extra peaks vanish by annealing the surface to 230 K and reappear, if the sample is cooled again under a CO pressure of 10^{-7} mbar. Annealing to 330 K in the presence of CO causes the sites, which are responsible for these peaks to be eliminated because in this case no extra peaks are observed after recooling in CO. In short, the authors interprete these experimental results as evidence for the formation of small antiphase domains during low temperature CO adsorption, where the metastable extra adsorption sites are found at

the domain boundaries. Annealing to 330 K causes the domains to rearrange, until only very large domains remain with a negligible amount of sites at domain boundaries. Guo and Yates explained the adsorption temperature dependence of the CO desorption kinetics also by the formation of antiphase domains. But in contrast to Bourguignon et al., they suggest, that at lower temperatures *larger* domains are formed. As experimental evidence for this explanation, they point out, that both IR bands and LEED reflexes are reported to be much sharper in the case of low temperature (90 K) adsorption as compared to room temperature adsorption [123]. Unfortunately, in the work of Bourguignon et al. no LEED experiments are reported, which could serve as direct evidence for differently sized domains at different temperatures. It is obvious, that there are still many uncertainties concering the non-equilibrium phenomena observed in the CO/Pd(111) adsorption system at $T \leq 230\,K$.

As final aspect of the CO/Pd(111) system in this overview, adsorbate diffusion parameters determined by photoemission electron microscopy (PEEM) should be mentioned. Šnabl et al. were imaging the broadening of a $\sim 100\mu$m wide CO adsorbate stripe on the Pd(111) surface [131]. They observed that this broadening occurs inhomogeneously, i. e., at certain locations a much faster migration of CO into the initially CO free areas is detected compared to the average CO spreading. These quasi-one-dimentional fast propagation channels of the CO concentration profile are called "streamers". The streamers appeared reproducibly at the same locations of the surface and were attributed to CO migration on elongated, almost defect-free terraces, that are confined by steps or step bunches. By measuring the propagation velocity of various streamers in the temperature range 160 K – 260 K, Šnabl et al. deduced the energy barrier for CO diffusion on Pd(111) terraces and the corresponding prefactor to be (175 ± 12) meV and $2.2 \times 10^{3\pm0.3}\,cm^2s^{-1}$, respectively. A significantly higher diffusion barrier is expected for CO migration across step edges, because a measurable propagation of the concentration profiles in the "slow" directions, which are expected to be perpendicular to the locally preferred step directions, is observed in the time scale of the PEEM experiment only at temperatures above 270 K.

Coadsorption of CO and H_2 on Pd(111) and low temperature adsorption of H_2

As was already mentioned above, large discrepancies in the CO adsorption behaviour on Pd(111) at low temperatures ($T \leq 150\,K$) can be found by comparing the work of different groups [122, 124, 129]. As will be shown later (in section 5.2.1), in the present work it was observed, that the CO saturation coverages at these temperatures are very sensitive to the time the sample is kept at low temperatures prior to CO dosing. These findings could be easily explained by a strong influence of coadsorbed molecules from the residual gas on the subsequent

CO adsorption. In this work it was determined that H_2 was by far the most abundant species in the residual gas during the TPD experiments. Its partial pressure exceeded the partial pressure of the next important gas component H_2O (besides CO, which can be neglected in the present context) by a factor of about 50. Therefore, coadsoption of H_2 was found to have considerable influence on the CO adsorption measurements and an overview on results for this coadsorption system is required for the later discussions.

Even though it is principally not possible to study "pure" CO adsorption in conventional UHV systems (the partial pressure of H_2 in the residual gas is certainly not negligible), in almost none of the available publications on CO adsorption on Pd(111) this coadsorption problem is discussed, and only very few experiments are reported, where the coadsorption of CO with H_2 on Pd(111) was explicitly studied. For the present purpose of interpreting the influence of preadsorbed hydrogen on the subsequent CO adsorption, it is sufficient to concentrate on this adsorption sequence. Conrad mentions in his PhD thesis [120], that preadsorbed hydrogen inhibits the formation of the $(\sqrt{3} \times \sqrt{3})R30°$ LEED pattern at 200 K but the superstructures found for $\theta_{CO} \geq 0.5$ ML — e. g., the $c(4 \times 2)$ structure — were not influenced by hydrogen. Besides a reduction of the CO sticking coefficient for adsorption temperatures around 200 K, he did not notice any hydrogen induced changes in CO TPD spectra. On the other hand, a CO predosis of 3 L corresponding to a coverage of $\sim$0.5 ML was sufficient to completely suppress H_2 desorption in the temperature range below 350 K, where chemisorbed hydrogen on clean Pd(111) would be observed. Only a small desorption feature at 400 K remained. The reversed adsorption sequence (CO adsoption on a hydrogen precovered surface, $T_{ads} \approx 200$K) resulted in similar changes in the H_2 TPD spectra. A CO postdosis of 6 L again completely suppressed the "clean" H_2 desorption peak around 300 K and gave rise to a new feature around 400 K. The intensity of this high temperature peak was only slightly smaller than the total intensity measured in the pure H_2 adsorption experiment. From this it follows, that at 200 K CO adsorption does not cause predosed hydrogen to desorb from the crystal but rather to migrate to a different, possibly sub-surface, adsorption site. Conrad interprets his observations in terms of a speculative formation of a "H_2 - CO" surface complex.

Kiskinova and Bliznakov studied the $H_2 + CO$ coadsorption on Pd(111) using TPD and electron stimulated desorption (ESD) measurements for $T \geq 250$ K [132]. Qualitatively, they found the same CO induced changes in H_2 TPD spectra as Conrad. Their additional EDS experiments showed a large increase in H^+ yield by coadsorption of up to 0.3 ML CO. This was attributed to a CO induced enhancement of the H ionization cross section and/or a reduction of the neutralization probability of the desorbing H^+ ions by CO in close contact to H on the surface. However, they point out that the hydrogen species, which gives rise to the H^+ ESD signal, is not identical to the species responsible for the high

temperature desorption peak. Therefore, they conclude that coadsorption of CO and H_2 at 250 K has at least two effects: Small CO coverages lead to the formation of a mixed adsorption phase on the surface (high H^+ signal), while higher CO coverages result in the population of subsurface sites by H atoms. In a combined LEED, AES, and TPD study of $H_2 + CO$ coadsorption on Pd(111) at $T \geq 220$ K Kok, Noordermeer, and Nieuwenhuys reported similar results, which point also to the formation of subsurface hydrogen by postdosing of CO [133].

Since there are no reports on the CO + H_2 coadsorption on Pd(111) at temperatures below 190 K, which is the interesting temperature range for interpreting the deviations in the CO data observed for adsorption below 120 K, it might be useful to summarize the low temperature adsorption behaviour of H_2 itself. Eberhardt and coworkers found by angle-resolved photoelectron spectroscopy that at low temperatures ($T \leq 250$ K) H atoms form an ordered (1×1) structure on Pd(111) [134]. Heating above 250 K causes the hydrogen to become invisible in the photoemission spectra, but it remains localized near the surface which is concluded from the still observable changes in the work function of the surface. At temperatures below 100 K Felter and Stulen detected two ordered H/Pd(111) phases by LEED [135, 136]. Both exhibit a $(\sqrt{3} \times \sqrt{3})R30°$ diffraction pattern, and occur at coverages of $\frac{1}{3}$ ML and $\frac{2}{3}$ ML and contain 1 or 2 H atoms per unit cell, respectively. A LEED intensity analysis of the latter structure [137], referred to as $(\sqrt{3} \times \sqrt{3})R30°$-2H structure, gave the best agreement between experimental and calculated I(V) curves for either all H atoms in fcc hollow sites or for a mixture of H atoms on these sites and on octahedral sites between the first and second crystal layers, i. e., directly below the fcc hollow sites. These subsurface sites are also favoured by calculations using the embedded atom method (EAM) [136]. Occupation of subsurface sites at low temperatures is also suggested by ESD measurments of Kubiak and Stulen [138]. They found in a temperature dependent ESD measurement an initial increase of the H^+ signal between 100 K and 200 K and a subsequent continuous decrease until the background level is reached at about 450 K, which corresponds to the high temperature limit of the H_2 TPD peak. Therefore, a qualitatively different behaviour of the H_2 and hence also of the $CO + H_2$ adsorption systems on Pd(111) can be expected at 100 K as compared to $T \geq 200$ K.

CO adsorption on other low index Pd surfaces

CO/Pd(110) The system CO/Pd(110) was one of the first reported examples of a surface reconstruction induced by adsorbed *molecules* (vs. atoms). Throughout a wide coverage range ($0.3\,\text{ML} \leq \Theta_{CO} \leq 0.75\,\text{ML}$) a (4×2) superstructure is observed by LEED at room temperature [114, 139]. Based on a LEED I(V) analysis of this superstructure, Hu et al. showed that the corresponding surface consists of a (1×2) missing row reconstructed substrate covered by a poorly or-

dered CO superlattice, which gives rise to diffuse fourth order reflexes [140]. As driving force for the reconstruction, Raval et al. determined an *increase* of the integral heat of adsorption in the coverage region, where the reconstruction is formed, from 134 kJ/mole (0.1 ML) to 183 kJ/mole (0.75 ML) [139]. This finding is at variance with an earlier determination of the coverage dependent isosteric heat of adsorption carried out by Conrad et al., who report an initial heat of adsorption of 167 kJ/mole and a continuous *decrease* with coverage [114]. The reason for this deviation might be found in the fact, that the two groups used different indicators for the constance of the CO coverage (IR band positions and intensities were used by Raval et al., while Conrad et al. monitored the work function changes). Considering the very complex interplay between adsorbate coverage, temperature, and surface reconstruction in the case of CO/Pd(110), it might well be that for this system neither IR absorption properties nor the work function are functions with the CO coverage as the only independent variable. At temperatures below 250 K no (4×2) LEED pattern can be detected [139], which is attributed to the fact, that for the formation of the (1×2) missing row reconstruction the Pd atoms have to overcome a relatively high energy barrier, which is only possible if sufficient thermal energy is available. Instead, at intermediate coverages and a surface temperature of 180 K only (2×1) and (4×1) structures are observed, respectively. Heating of these surfaces to 250 K in UHV results in the irreversible formation of the (4×2) structure. On the other hand, if the latter structure is formed at 300 K and the surface is cooled down to 180 K and covered with additional CO, a completely different behaviour results compared to the "normal" low temperature adsorption sequence. Therefore, also for lifting the (1×2) missing row reconstruction the thermal energy of the surface Pd atoms has to exceed a critial value, which corresponds to a surface temperature of about 250 K. At coverages above 0.75 ML a $(2 \times 1)p2mg$ pattern appears at low temperatures (130 K) and the coexistence of the (4×2) and the $(2 \times 1)p2mg$ structures is found at higher temperatures (285 K) [141]. The $(2 \times 1)p2mg$ structure has been analyzed by photoelectron diffraction with the result, that the CO molecules are located in the short bridge sites of the unreconstructed Pd(110) surface and that they are tilted by 24° with respect to the surface normal [142]. These findings imply that for temperatures above 250 K the missing row reconstruction is lifted between 0.75 ML — (4×2) — and 1 ML — $(2 \times 1)p2mg$. It should be noted that an earlier tensor LEED structural analysis by Wander, Hu, and King came to the result, that in the $(2 \times 1)p2mg$ structure the CO molecules occupy on-top sites [143]. This result was judged to be rather surprising because of the C–O stretching frequency (248 meV [139]) being very low for linearly bonded CO. Therefore, the occupation of short bridge sites as determined by photoelectron diffraction seems to be more plausible. The reconstruction of the surface also takes place if it is saturated with CO at low temperatures and then heated in a TPD experiment. A sharp peak at 338 K (heating rate 5 K/s) was attributed by

He and Norton to the formation of the surface reconstruction [141].

The vibrational properties of this system have been investigated by Chesters et al. using HREELS [144] and by Raval et al. using reflection-absorption infrared spectroscopy (RAIRS) [139]. In the HREELS experiments the Pd–CO stretching frequency is detected at 45 meV – 47 meV, almost independent of surface temperature and coverage. For the C–O stretching frequency the more accurate IR data can be referred to. At room temperature the coverage dependent behaviour of the spectra is found to be very complex. At low coverages a single band at 237 meV is detected, while for coverages, where the (4×2) structure exists (0.3 ML – 0.75 ML) a broad band with 5 features (231 meV, 236 meV, 242 meV, 247 meV, and 257 meV) is found. This variety of frequencies is explained by the coexistence of unreconstructed areas and areas, that have already undergone the missing row reconstruction. At the border of these differently structured patches adsorption sites exist, which are not found in neither of the two coexisting structures themselves. At 0.75 ML CO, where the entire surface is reconstructed, a simpler IR spectrum consisting of only 2 bands at 237 meV and 245 meV is recorded. A further increase of the CO coverage to 1 ML ($\rightarrow (2\times1)p2mg$) is accompanied by the emergence of a single and sharp IR band at 249 meV. The sequence of IR spectra recorded at 110 K appears to be much less complex. Depending on CO coverage, one or two bands are found with a final position of the band again at 249 meV for saturation coverage. In a very recent publication by Kato, Kawai, and Yoshinobu, the tilted geometry of the CO molecules is confirmed by measuring the hindered rotational vibrations using HREELS [145]. They found that the molecules are first adsorbed in an upright geometry (up to 0.4 ML), then a tilt along the close-packed atom rows occurs, and finally the molecules are tilted perpendicular to the close-packed rows (above 0.7 ML). For all coverages only bridge-bonded CO molecules are observed.

CO/Pd(100) For the adsorption system CO on Pd(100) rather simple vibrational spectra consisting of only one band are recorded both for low temperature (80 K) and for room temperature adsorption [121,146,147]. The frequency of this single C–O stretching vibration shifts gradually from 235 meV at the lowest coverages (0.06 ML) to 243 meV (242 meV) at 0.5 ML and 80 K (300 K) and to 248 meV at the highest coverage accessible in UHV at 80 K (0.81 ML) [147]. By IR absorption measurements with $^{12}CO/^{13}CO$ isotopic mixtures Ortega, Hoffman, and Bradshaw determined, that about 4 meV of the total frequency shift of 13 meV is caused by vibrational coupling between the adsorbates, the rest beeing due to static adsorbate–adsorbate interactions. At 0.5 ML a $c(2\sqrt{2}\times\sqrt{2})R45°$ LEED structure was detected by Park and Madden [148]. Their structural model of all CO molecules sitting in bridge sites at this coverage was confirmed by a LEED I(V) analysis carried out by Behm et al. [146]. Upon increasing the coverage above 0.5 ML, only a small fraction of the CO molecules can remain in twofold

bridge sites. A uniaxial compression of the $c(2\sqrt{2} \times \sqrt{2})R45°$ structure was observed by Tracy and Palmberg [149] and was interpreted as a commensurate-incommensurate transition at 0.5 ML. Since no strong shift in the IR spectra takes place during this transition, which would be indicative of a change in the adsorption geometry, e. g., from bridge to on-top sites, Ortega et al. concluded that during the uniaxial compression all CO molecules remain on a path, which connects the geometric bridge sites [147]. Along this path the changes in potential energy are only small and therefore a twofold bonding of the CO molecules to the substrate can be maintained even in positions, which are geometrically not exactly bridge sites. By recent calorimetric measurements Yeo, Vattuone, and King determined an initial heat of adsorption of 165 kJ/mole and a continuous decrease of this quantity with increasing CO coverage, where this decrease becomes more abrupt upon exceeding 0.5 ML [150]. The value for $\theta_{CO} \to 0$ is in good agreement to isosteric heats of adsorption reported previously by monitoring work function changes [151, 152] or infrared absorption intensities [125]. Only the coverage dependence of the heat of adsorption varies somehow between the different publications.

A non-equilibrium phenomenon called "fast compression" was reported by Bradshaw and Hoffmann for this adsorption system [121]. Exposing the crystal to a sudden CO pressure rise to $\sim 10^{-7}$ mbar at room temperature leads to a second IR band at 260 meV, which is attributed to the occupation of unfavourable on-top sites by CO. This peak disappears on heating to 400 K and recooling to 300 K in a CO atmosphere. It follows that the occupation of on-top sites by CO/Pd(100) at not too high CO pressures is only possible in a non-equilibrium situation. This finding was confirmed by Szanyi, Kuhn, and Goodman, who detected in isobaric IRAS experiments by cooling the sample in different CO pressures even in the presence of 1.3 mbar CO and at low temperatures (162 K) only one IR feature at 248 meV. They attributed this to a highly compressed CO overlayer situated in twofold coordinated sites. TPD spectra of the same authors show a main desorption peak at $\sim$ 500 K for all coverages and a second peak at $\sim$ 370 K for $\theta_{CO} \geq 0.5$ ML. Considering the above mentioned stabilization of a non-equilibrium adsorbate structure due to a "fast compression" of the CO/Pd(100) adsorbed layer even at 300 K, it is very surprising that Szanyi et al. explicitly did not find a dependence of either the IR data nor the TPD spectra on the surface temperature during the initial CO adsorption. This is in contrast to their results on CO/Pd(111), where TPD and IRAS spectra of low temperature adsorbate layers are quite different depending on the adsorption procedure, i. e., for CO/Pd(111) it makes a difference if the CO adsorption was started at higher temperatures and the surface was cooled down in a CO background or if CO was adsorbed only at low temperatures.

CO adsorption on stepped Pd surfaces

As was already pointed out by Conrad et al., the adsorption energy of CO does not depend significantly on the presence of steps by comparing a vicinal Pd(S)[9(111) × (111)][4] surface with the Pd(111) surface [114]. However, in this case the orientation of the microfacet found at the steps was identical to the terrace orientation. By comparing two more recent investigation on Pd(112) and on Pd(510), respectively, it can be shown, that the chemical properties of surface steps depend sensitively on the orientation of both the terraces and the step-microfacets.

CO/Pd(112) The Pd(112) surface consists of three atom wide (111) terraces separated by (001) oriented steps (alternative notation: Pd(S)[3(111) × (001)]). Ramsier, Lee, and Yates have studied its CO adsorption properties by thermal (TPD) and electron stimulated desorption (Electron Stimulated Desorption Ion Angular Distribution – ESDIAD) experiments at 300 K [153]. The analysis of the leading edge of the TPD spectra (TTPD method, see section 5.2.4 on page 163) yields a continuously decreasing activation energy for desorption from 143 kJ/mole at low coverages to 40 kJ/mole at saturation coverage. The frequency factor decreases simultaneously from $10^{15}\,s^{-1}$ to $10^{3}\,s^{-1}$, which is attributed to a compensation effect arising from strong adsorbate–adsorbate interactions. At no CO coverage any CO induced superstructures are observed by LEED. Only an increased background intensity is noticed upon CO dosing. ESDIAD patterns of the ions — presumably O^+ leaving the surface during electron (600 eV) bombardment — clearly show, that initially only desorption in a direction perpendicular to the orientation of the step-microfacets occurs. After higher CO exposures also a desorption feature directed in the direction of the terrace normal is observed. This is interpreted in terms of preferential adsorption of CO at step edge sites on Pd(112).

CO/Pd(510) Unlike to the previous example, CO adsorption on Pd(510) — three atom wide (100) terraces separated by kinked (110) like steps — does not seem to occur preferentially at step edge sites. In the low coverage limit, Svensson et al. did not find any significant deviations in HREEL spectra recorded on Pd(510) from the behaviour of the flat Pd(100) surface [154]. Also the ordering of the adsorbate layer did not appear to be changed by the high step density for coverages up to 0.5 ML, where a $c(2\sqrt{2} \times \sqrt{2})R45°$ LEED pattern is observed. For higher CO coverages the influence of the steps become obvious both in the HREEL spectra and in the LEED patterns. The latter show no sharp diffraction spots for $\theta_{CO} \geq 0.5$ML indicating the inhibition of adsorbate ordering across the steps. An additional peak at 264 meV appears in the HREEL spectra for the same

[4] Nine atom wide (111) oriented terraces are separated by (111) oriented steps.

coverages. Since no peak in this frequency range is observed in the CO/Pd(100) system, Svensson et al. conclude that at high CO coverages also on-top step edge sites are occupied by CO.

As a conclusion, it can be stated that for the adsorption system CO/Pd there is no clear preference of step site occupation. It seems that the argument for an increased adsorption energy at step edges (see page 120 and [107]), which basically relies on the changes in electronic structure of the step atoms due to the loss of neighbour atoms, generally does not hold in the case of Pd. The example of Pd(112), where indeed step edge sites are found to be preferred, can also be explained by the fact, that the step-microfacets are (100)oriented, while the terraces have (111) orientation. Pd(100) exhibits a significantly higher adsorption energy compared to Pd(111) [114,150] and it can be concluded that bridge bonded CO molecules on Pd(100) facets are more stable than CO molecules on three fold hollow sites within (111) crystal faces.

CO adsorption on Au surfaces

Since CO adsorption on Au surfaces can only be studied at relatively low temperatures and/or at high CO pressures, not many surface science investigations have been carried out on this system. They concern mainly CO adsorption on dispersed Au particles or on polycrystalline Au films. Some of this work will be included in this short review, because it is interesting to compare measurements on single crystals with a deliberately chosen high defect density to these studies on less well-defined Au surfaces.

In an early RAIRS study Kottke, Greenler, and Tompkins investigated the adsorption of CO on evaporated and annealed Au films at $T \geq 300\,K$ [155]. At room temperature they found an IR absorption band centered at 262.8 meV for 0.013 mbar CO. Upon increasing the CO pressure a small *negative* shift was detected to 262.2 meV at $p_{CO} = 26\,mbar$. They determined an isosteric heat of adsorption of 56 kJ/mole, but there is a large scatter of the data points in their adsorption isosteres, such that this value might be not very accurate (constant CO coverages were inferred from constant IR peak areas). However, the IR band position matches well with an earlier measurement of Bradshaw and Pritchard [156], who found by IR transmission experiments for CO adsorption on evaporated Au films ($T_{dep} = 110\,K$) an IR absorption band at 262.8 meV and also a negative shift with increasing CO coverage. There is also a close agreement to an IR study of Yates on silica-supported Au [157]. In this case, an infrared active vibration was found at the same position (262.8 meV) and exhibited again a negative frequency shift. An interesting conclusion on the nature of the CO adsorption sites on Au surfaces can be drawn from the work of Dumas, Tobin, and Richards [158]. They compared the CO adsorption properties of differently prepared Au films. If the Au

film was evaporated onto a sapphire substrate at temperatures above 290 K, no CO chemisorption was detected, whereas low temperature Au deposition yielded surfaces with active sites for CO chemisorption. Therefore, it is suggested that the CO adsorption energy is largely increased on surfaces with many structural defects like step edges and kinks (low temperature Au deposition) compared to smoother surfaces (room temperature Au deposition). Hence, CO chemisorption seems to be more favourable on Au step edge and kink atoms than on Au terrace atoms. In vacuum, CO desorbs from these defect sites at temperatures around 170 K. The frequency of the C–O stretching vibration was found at 263.5 meV, which is somehow above the value determined by the above mentioned authors. This small deviation can be explained by the fact that Dumas and coworkers used very low sample temperatures (4 K) and small CO doses for their infrared measurements, instead of a constant CO background preasure and higher temperatures. A similar value for the low coverage C–O stretching vibration was reported by France and Hollins [159]. On silica-supported Au particles they detected an IR band at 263.9 meV (room temperature, $p_{CO} = 1.3 \times 10^{-3}$ mbar). Using $^{12}CO/^{13}CO$ isotopic mixtures they could interprete the negative frequency shift, that is typical for CO/Au, to be due to the combination of a large negative static (or chemical) shift and a smaller positive shift because of dynamic dipol-dipol interactions. The same conclusion was already arrived at by Dumas et al. in their non-equilibrium CO adsorption study on Au films at 2 K–4 K [158].

Au single crystal surfaces have been studied to a lesser extent than the dispersed or polycrystalline Au systems. On Au(110) CO oxidation was investigated by Outka and Madix [160]. They did not find CO stable adsorbed on the Au(110) surface at 125 K. Sandell et al. report a photoelectron emission study for CO adsorption on the same surface [161]. At 77 K they could detect CO chemisorption both by UPS and by XPS. Even at 117 K CO chemisorption on Au(110) was detected by Dückers and Bonzel using photoelectron spectroscopy with Y Mζ radiation [162]. On the Au(111) surface a very low sticking coefficient (2×10^{-6}) of CO at 135 K has been estimated from a He scattering experiment [163]. The adsorption system CO/Au(100) has been studied by McElhiney and Pritchard in the temperature range 81.5 K – 260 K and with CO pressures up to 10^{-3} mbar [164]. No ordered structures could be detected by LEED indicating a rather low CO coverage. By monitoring the work function changes in a series of isobaric annealing experiments McElhiney and Pritchard determined the isosteric heat of adsorption to decrease continuously with increasing CO coverage starting at an initial value of 58 kJ/mole.

Extensive investigations upon CO adsorption on the stepped Au(332) surface are reported by Ruggiero and Hollins [165] based on a variety of experimental methods (LEED, work function measurements, RAIRS, TPD). They found an initial isosteric enthalpy of adsorption of 55 kJ/mole derived from monitoring the isobaric decrease of the work function with increasing temperature. The coverage

dependence of the adsorption enthalpy was not explicitly measured (because of the lack of a cross-calibration of the work function changes to the surface coverages), but it is evident that there exists a plateau of this quantity at low CO coverages. Neither at 92 K nor at 105 K could any CO derived superstructures be detected by LEED. IR spectra were recorded also at 92 K and 105 K. A single band was detected, which starts for low coverages at 263.5 meV for both temperatures and shifts to lower frequencies with increasing coverage. With $C^{16}O/C^{18}O$ isotopic mixtures Ruggiero and Hollins could resolve up to 4 features in the IR spectra at dynamic CO pressures of 1×10^{-5} mbar and at T = 105 K, three of which they attributed to CO adsorbed on Au kink sites, Au step edge sites, and Au terrace sites. The origin of the fourth component is not clear. TPD spectra (heating rate: 1.5 K/s) following CO adsorption at 92 K and at 105 K display two major components at 185 K and at 140 K, where the low temperature peak is more pronounced at the lower adsorption temperature and develops a low temperature shoulder. From the position of the high temperature peak (185 K) an activation energy for CO desorption of 55 kJ/mole is derived by employing the Redhead formula (see equation 5.3 in section 5.2.4, [166]) assuming a frequency factor of 10^{15} s. This value agrees well with the above mentioned equilibrium value for the isosteric heat of adsorption in the low coverage limit. By a questionable comparison with infrared frequency shifts observed in the CO/Cu(111) system, Ruggiero and Hollins estimated the CO saturation coverage on Au(332) under UHV conditions to be 0.17 ML at 92 K.

CO adsorption on bimetallic Au-Pd surfaces

Polycrystalline Au-Pd alloys Eley and Moore used TPD to study the adsorption and oxidation of CO on Au-Pd alloy wires [167]. From changes in the temperature of the maximum desorption rates they deduced a fall in CO adsorption energy from 127 kJ/mole for pure Pd wires over 112 kJ/mole for 83% Pd, 84 kJ/mole for 60% Pd to 67 kJ/mole for a pure Au wire. However, these values are derived from the CO saturated samples at different temperatures, which makes the comparison not very meaningful. On the other hand, a comparison of the TPD data in the limit of low CO coverage — i. e., high desorption temperature — seems to be also not reliable, because even on pure Au wires a small desorption peak around 380 K was detected, which is far above desorption temperatures expected for pure Au adsorption sites. Therefore, the possibility of small amounts of impurities dominating the low coverage TPD curves has to be considered. A tremendous decrease in CO saturation coverage with increasing bulk Au content of the alloy wires (with 17% Au only about 8% of the CO coverage for the pure Pd wire was obtained) suggests, that in the Au-Pd alloy wires strong Au segregation leads to an enhanced Au content in the surface layer.

Au/Pd(110) CO adsorption experiments on bimetallic Au-Pd single crystalline systems have been reported for (110) and for (111) oriented surfaces. To begin with the former case, Schmitz et al. studied the CO adsorption properties of Au films on Pd(110). They employed AES, LEED, and TPD to characterize the system. Au deposition was carried out at low surface temperatures (130 K), where at least up to 7 ML only (1×1) patterns were observed by LEED. Annealing to temperatures above 300 K led to the formation of (1×2) and (1×3) LEED patterns depending on Au coverage. CO adsorption experiments are only reported for the unannealed and therefore non-reconstructed films. With increasing Au coverage, the Pd related TPD features (desorption above 300 K) are suppressed, and they have vanished completely at an AES calibrated Au coverage of about 1 ML. Instead, two low temperature CO desorption states are populated at 225 K (α state) and at 190 K (β state), respectively. The α state is observed already at very low Au coverages and has gained maximum intensity for a Au coverage between 1.0 ML and 1.5 ML. At 3 ML Au it is not visible anymore. The β state starts to grow at ~ 1 ML, passes through a maximum at ~ 2 ML, and slowly loses intensity with further increased Θ_{Au}. At the highest Au coverages studied by Schmitz et al. (5 ML), this desorption peak still retains about half of its maximum intensity. The authors interpret their TPD findings in terms of CO adsorption on first (α state) and second layer (β state) Au atoms.

Pd/Au(111) The relationship between the electronic structure and the CO adsorption properties of thin Pd films on Au(111) have been studied by different groups. While Shen and coworkers concluded from UPS and HREELS measurements, that a 1 ML Pd film deposited at room temperature onto a Au(111) substrate is relatively inert towards CO chemisorption at room temperature [168,169], Sellidj and Koel came to the contrary result [170]. They inferred from UPS, HREELS, and TPD measurements that a 1 ML Pd film on Au(111) closely resembles the Pd(111) surface with respect to CO chemisorption, even though UPS valence band spectra show considerable differences in the electronic structures of these two surfaces. While the former group made statements about CO coverages based on UPS and HREELS measurements alone, the latter group presented TPD data, which allows an accurate determination of CO coverages and a relatively reliable estimation of CO adsorption energies. Therefore, their conclusions seem to rest on sounder grounds. For a comparison with results from the present work, some of their HREELS and TPD experiments will be summarized in the following. After the deposition of various amounts of Pd (0.5 ML – 5 ML) at 125 K, Sellidj and Koel recorded TPD spectra, which show CO desorption in a broad temperature range, that is almost identical for all Pd coverages. An increase in the Pd coverage from 0.5 ML to 1 ML is accompanied by an increase in the total amount of desorbed CO, which is mainly due to a stronger desorption in the high temperature region (400 K – 500 K). On 2 ML Pd a distinct peak

around 500 K dominates the TPD spectrum, while a further increase of Θ_{Pd} to 5 ML leads to the evolution of two additional strong peaks at about 250 K and 380 K, respectively. Qualitatively, the TPD spectrum for 2 ML Pd closely resembles CO TPD data on Pd(111) [129] and the two distinct low temperature features on the thicker Pd film seems to be caused by surface roughening due to the low deposition temperature. Pd deposition and subsequent CO adsorption at room temperature show similar Pd coverage dependent changes in the high temperature region of the TPD spectra with the difference that for 5 ML Pd the peak at 380 K is reduced to a small shoulder indicating a smoother film growth under these conditions. HREEL spectra recorded at 125 K on a 1 ML Pd film show one or two peaks in the C–O stretching region depending on CO exposure. After low exposures (0.1 L) a single peak at 230 meV is observed. With increasing exposure it shifts to 236 meV and is accompanied by a second peak at 259 meV for 1 L CO. Annealing the CO covered surface to 300 K is sufficient to eliminate the high frequency peak.

Au/Pd(111) In the group of Lambert, the system Au-Pd has been studied quite extensively due to its interesting catalytic properties. The activity for the catalytical coupling of acetylene to benzene on Pd(111) was found to be considerably enhanced by the presence of Au atoms in the surface layer. In order to gain insight into the reaction mechanism, a combined LEED, TPD, AES, and HREELS study was performed by Baddeley et al. on the Au/Pd(111) system [171]. Au films with different coverages were deposited at room temperature and annealed to subsequently higher temperatures. The results concerning the growth and intermixing behaviour of this system have already been summarized in chapter 3 on page 34. CO was used as a molecular probe for the chemical properties of the surface. The CO saturated surfaces (30 L at 150 K) were characterized by TPD (heating rate: 10 K/s) and by HREELS after each annealing step (9.4 eV incident beam energy; 10 meV FWHM of the elastic peak; only the C–O stretching vibrations are reported). TPD data are presented for a 1.3 ML and a 4.5 ML Au film, respectively. Up to four desorption states can be distinguished in the spectra. Generally, the thicker Au film has to be annealed to higher temperatures in order to exhibit a qualitatively similar TPD behaviour compared to the 1.3 ML film. A peak at $\sim$ 300 K is detected after annealing the 4.5 ML Au film at 510 K for 5 min. Two high temperature desorption states centered at 350 K and at 445 K appear after annealing the higher coverage film at $\sim$ 650 K and at $\sim$ 760 K, respectively. This film shows an additional feature at 220 K, which gains maximum intensity after annealing at 760 K and which does not appear in the 1.3 ML case. A HREELS analysis of CO adsorbed on similarly prepared surfaces (1.3 ML and 6 ML Au films deposited at 300 K and annealed to temperatures up to 1090 K) revealed the existence of two distinguishable CO species. After annealing of the 1.3 ML (6 ML) film to 660 K (760 K) a

weak peak is detected around 260 meV. It gains maximum intensity after annealing at 760 K (830 K). A second peak appears at about 240 meV after heating to 760 K (910 K) and grows with increasing annealing temperature. Simultaneously, the 260 meV peak shrinks, until after annealing at 1020 K (1090 K) the HREEL spectrum looks similar to the spectrum recorded from pure Pd(111). From these findings Baddeley et al. conclude, that with increasing annealing temperature, the concentration of Pd atoms in the surface layer increases more and more due to thermal intermixing of Au and Pd in the surface region, until an almost pure Pd surface results after annealing at temperatures above 1000 K. Since no ordered structures are observed by LEED, the authors assume that in the mixed Au-Pd surface layer the different elements are more or less randomly distributed. From this they infer, that first single Pd atoms appear on the surface, which constitute adsorption sites for linearly bonded CO (TPD peak at 300 K and C–O stretching vibration at 260 meV), followed by Pd dimers, on which bridge bonded CO can be accommodated (350 K; 240 meV). Finally, threefold hollow sites consisting of only Pd atoms give rise to a TPD peak at 445 K. In the HREEL spectra this species could not be distinguished from the bridge bonded molecules.

5.2 TPD results for CO adsorption on Au-Pd(111) surfaces

CO TPD measurements have been performed both on layered Au/Pd(111) surfaces, where each crystal layer is composed of only one element, and on intermixed Au-Pd(111) surfaces (i. e., AuPd(111) surface alloys), where the topmost crystal layers consist of a mixture of Pd and Au atoms. Since CO TPD from pure Pd(111) has been widely studied by different groups in the past (for an overview on their results see section 5.1.2 on page 121 and following pages), not much emphasis has been put on this adsorption system in the present work. Nevertheless, it is useful to present some results for pure Pd(111) in order to allow for a direct comparison with the bimetallic Au-Pd surfaces under the same experimental conditions.

The experimental TPD results will be presented in three different subsections, beginning with CO TPD from pure Pd(111), followed by two subsections on the results from the two different types of Au-Pd(111) surfaces that are mentioned above. TPD spectra contain information on many thermodynamic and kinetic properties of the adsorption system. Only in the simplest cases (homogeneous surface, negligible adsorbate-adsorbate interaction) can these be extracted from the spectra merely by the determination of integral features, e. g., the position of the desorption peak maximum or the parameters that describe the peak shape. On heterogeneous surfaces a more sophisticated data analysis is required to obtain an adequate picture of the physical processes occuring during thermal desorption experiments. Therefore, some simulations by numerical integration of

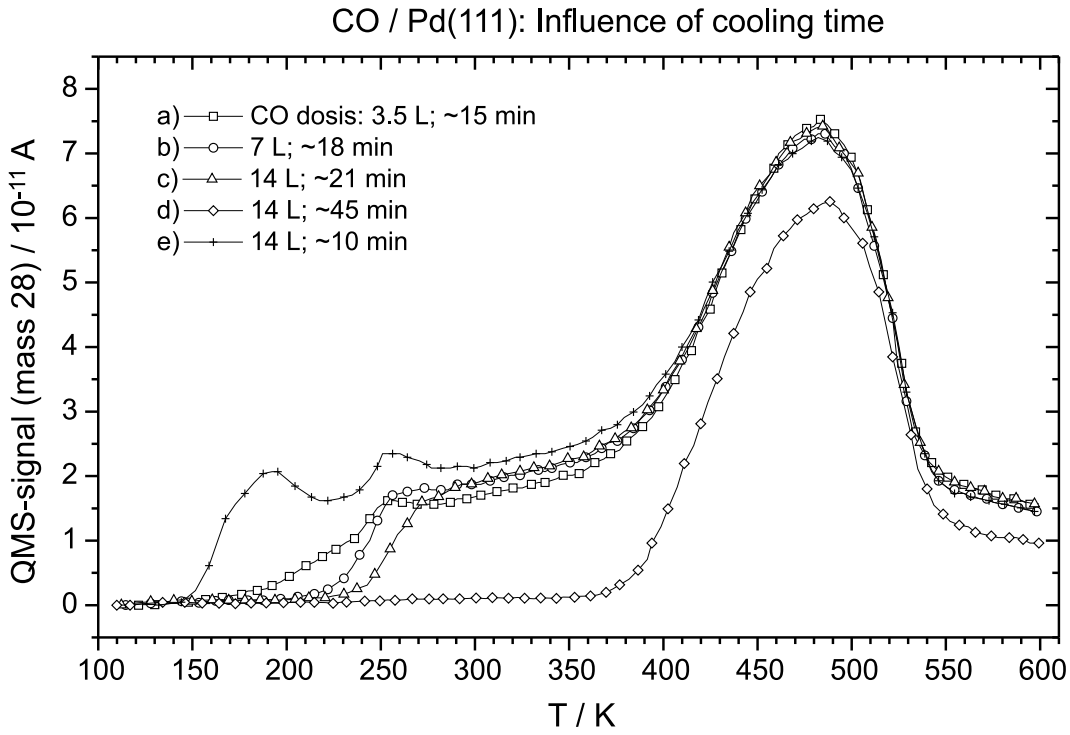

Figure 5.1: CO TPD spectra from Pd(111). The CO doses and the time between two consecutive spectra are given in the legend.

rate equations have been performed for the TPD measurements from AuPd(111) surface alloys. They will be presented in the fourth subsection subsequent to the experimental results.

5.2.1 CO adsorption on Pd(111)

CO TPD experiments on the pure Pd(111) surface were mainly performed to ensure, that the QMS setup used for TPD spectroscopy is working properly. Also, since the CO saturation coverages on Pd(111) are well-known from literature, these experiments provide the possibility for an absolute CO coverage calibration. In short, the overall shape of the TPD spectra is in good agreement to the spectra recorded by Guo and Yates [129]. In the course of the experiments presented below it was found, however, that at temperatures below 150 K great care has to be devoted in order to prepare a "clean" CO adsorbate layer. It will be shown in the following that residual gas adsorption has a significant influence on the CO TPD spectra. Even at a relatively low background pressure of $\sim 2 \times 10^{-10}$ mbar (ionization gauge reading during the cooling phases of the TPD experiments) the low temperature CO desorption features were found to be affected by preadsorption of residual gas on the time scale of a few minutes.

The influence of the residual gas becomes apparent in the TPD spectra displayed in fig. 5.1. This sequence was first intended as part of a coverage dependent TPD series, where higher CO saturation coverages were expected to be obtained at lower adsorption temperatures, which was shown to be the case in the work of Guo and Yates at least in the temperature range 87 K – 200 K [129]. It was surprising to find the opposite effect by comparing spectra a and b. For the latter spectrum twice the CO exposure ($\sim$7 L) and a lower adsorption temperature (114 K instead of 123 K) were used with the consequence that the onset temperature for CO desorption shifted by about 40 K to *higher* temperatures. An additional shift of about 20 K was found in the next spectrum (c), which shows the situation after again doubling the exposure of the previous TPD run but keeping the adsorption temperature constant. Obviously, adsorption temperature and CO exposure are not the only factors which determine the appearance of the TPD spectra. The only parameter, which has not been taken into account so far, is the exposure of the surface to residual gas. The time between two consecutive TPD heating cycles can be considered as a rough measure of this exposure. Spectra a, b, and c have been taken 15 min, 18 min, and 21 min, respectively, after the previous spectrum. The time between the begin of CO exposure and the start of the heating ramp was about 3 min in each case. The heating ramp itself and the time that the crystal needed for recooling to 400 K, which is an estimate of the critical temperature for residual gas adsorption, amount to approximately 1 min. Therefore, an offset of $\sim$4min has to be subtracted from the values given above to obtain a realistic measure for the residual gas exposure at low crystal temperatures. Up to spectrum c, the differences in the total CO coverages were not very large and it could be argued that some kind of non-equilibrium effect was responsible for the deviations in the spectra. Spectrum d, which was recorded 45 min after spectrum c (corrected exposure time to residual gas: 41 min) with the same CO exposure and at an almost identical adsorption temperature (112 K vs. 114 K), clearly shows that indeed the exposure to the residual gas, which is almost 3 times larger for spectrum d than for spectrum c is a decisive factor for the subsequent adsorption of CO. Consequently, spectrum e, which was recorded with the shortest possible time for cooling the sample ($T_{ads} = 142$ K) shows CO desorption starting already at 150 K and the intergrated area under spectrum e is 80% larger than the area of the single peak in spectrum d.

Up to now, it has been made clear that some coadsorbate from the residual gas strongly inhibits the adsorption of CO at low temperature. The question remains, which component of the residual gas is responsible for this effect. Of course, the CO contribution to the residual gas can be neglected in the present considerations. A QMS analysis of the residual gas during the TPD measurements revealed that at a total pressure of 2×10^{-10} mbar (ionization gauge reading) H_2 was by far the most abundant gas species. Its partial pressure was about 50 times larger than the partial pressure of H_2O, which was the next important component

(besides CO). Correcting for the lower ionization cross-section of H_2 compared to the heavier gas molecules, it follows that the H_2 partial pressure during the CO TPD experiments was about 4×10^{-10} mbar. From this, it can be calculated that in spectrum d of fig. 5.1 the CO adsorption was carried out after an H_2 exposure of about 0.7 L. Assuming a sticking coefficient of 1 and dissociative adsorption, a maximum H atom coverage of 2 ML (!) is possible for spectrum d. On the other hand the surface coverages of other residual gas components can be estimated to be not larger than 2% of a ML. As already mentioned in section 5.1.2 on page 125, no studies of CO + H_2 coadsorption on Pd(111) at T $\approx$ 100 K have been reported so far.

On Pd(100) Nyberg and Westerlund have studied CO adsorption on the hydrogen precovered surface by LEED, TPD, and HREELS in the temperature range 20 K – 250 K [172, 173]. At the lowest temperatures CO occupies on-top sites in the presence of 1 ML H atoms. Annealing to 80 K is sufficient to irreversibly transfer the CO molecules into bridge sites, which correspond to the CO adsorption sites on the clean Pd(100) surface. Adsorption of 2 L CO on the p(1 × 1)Pd(100)-H surface at 80 K results in a disordered adlayer, which transforms upon annealing at 200 K into a $(2\sqrt{2} \times 2\sqrt{2})$R45° structure, which is not found in the respective single-component adsorption systems. An intense Pd–H stretching peak is detected in HREEL spectra at 56 meV. This is about 7 meV below the Pd–H stretching frequency of the pure p(1 × 1)Pd(100)-H surface. Therefore, a mixed CO + H adsorbate layer is proposed by Nyberg and Westerlund to exist on Pd(100) at 200 K. From an additional high temperature H_2 desorption peak in TPD spectra of this system they conclude that part of the hydrogen is located in subsurface sites. Even though it has been made clear by the authors that preadsorbed hydrogen has considerable influence on the ordering behaviour and on the vibrational properties of postdosed CO, they make no statement about changes of the CO saturation coverages at different temperatures and various H precoverages.

Information about the latter topic is available for the close-packed faces of Ru, Rh, Ni, and Pt. On Ru(0001) Peebles, Schreifels, and White found an almost linear decrease of the CO saturation coverage with increasing D precoverage at 100 K [174]. By saturating the Ru(0001) surface with deuterium the CO saturation coverage is decreased to $\sim$20% (!). Williams et al. report that on Rh(111) preadorption of D_2 leads to a reduction of both the initial CO sticking coefficient and the CO saturation coverage [175]. The latter amounts on the D saturated surface to only one fifth of the corresponding value on the clean surface. The same trend is observed for Ni(111) (reduction of θ_{CO}^{sat} to 45% [176]) and for Pt(111) (reduction of θ_{CO}^{sat} to 34% [177]). Therefore, it seems to be plausible that also on Pd(111) CO adsorption might be blocked by preadsorbed hydrogen at temperatures around 100 K. The fact, that this effect is not observed at higher temperatures (see section 5.1.2 and [120,132,133]), can be explained by a different

interlayer mobility of H atoms at the different temperatures. If they have enough thermal energy to overcome the migration barriers for occupation of sites below the surface, their influence on CO adsorption *on* the surface layer is certainly reduced. It has already been pointed out in section 5.1.2, that subsurface sites might be already populated at T $\approx$ 100 K [137], but the entire complexity of the potential energy space for H atoms in the topmost crystal layers of Pd(111) has not yet been understood. Specifically, the penetration depth of adsorbed H atoms into the Pd(111) subsurface-region at different temperatures is not known. Additionally, desorption of H_2 might be induced by a destabilization of adsorbed hydrogen caused by CO coadsorption.

As already has been pointed out in the review-section on literature results for CO/Pd(111) (section 5.1.2), there exist striking discrepancies between published TPD data for this adsorption system. While Guo and Yates observed the onset of CO desorption from saturated adsorbate layers ($T_{ads} = 87$ K) at around 180 K [129], in the work of Kuhn, Szanyi, and Goodman CO desorption is only detected at temperatures above 290 K — even after prolonged exposure of the crystal to 1.3×10^{-6} mbar CO at 90 K. A comparison of the TPD spectra taken from the different publications with the spectra collected in fig. 5.1 clearly shows that the mentioned deviations among the published results can be explained by the influence of different amounts of residual gas adsorbed before CO was dosed. Since H_2 is an ubiquituous residual gas species, it is likely to be the decisive factor in this contamination effect.

As a conlusion, it can be stated that there is convincing evidence for hydrogen from the residual gas being responsible for a partial inhibition of CO adsorption at low temperatures. However, in the following discussions the more general expression "residual gas" will still be employed to make clear that up to now no direct proof for the H_2-hypothesis has been presented, e. g., by a systematic $H_2 + CO$ coadsorption study at 100 K, and that the effects have to be judged as unintended artefacts.

5.2.2 CO adsorption on layered Au/Pd(111) surfaces

The influence of Au defect sites (step atoms, kink atoms) upon the CO adsorption on Au/Pd(111) overlayers has been studied by TPD on metastable Au films with high defect densities. These were prepared by low temperature Au deposition (T $\leq$ 130 K). The temperature ranges of the TPD heating cycles were chosen such that the effect of Pd-Au intermixing was negligible and that the Au film morphology changed gradually to more stable structures over several consecutive TPD runs. Relating morphological changes, which were observed by STM, to changes in the TPD spectra allows for the assignment of the different desorption states to structural elements of the surface and consequently to atomically defined adsorption sites.

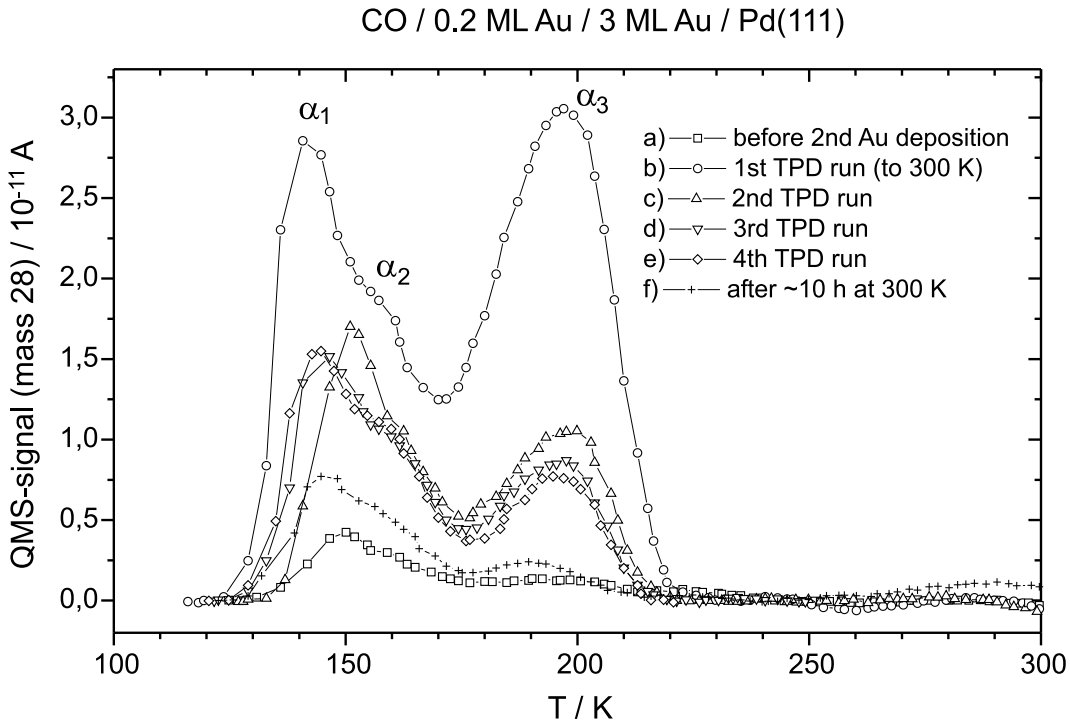

Figure 5.2: CO TPD spectra from completely Au covered Pd(111). All spectra were recorded after CO saturation of the surface. The first spectrum (a) was measured after the first Au deposition step (3 ML at 300 K); the subsequent spectra were recorded after a second Au deposition step (0.2 ML at 120 K).

In principle, the chemical properties of Au surface atoms depend on their environment. Therefore, the Au film thickness might be an important parameter for adsorption experiments. It will be shown that there is indeed a significant difference in CO TPD spectra recorded from submonolayer Au films compared to those recorded from multilayer ($\Theta_{Au} \geq 3$ ML) Au films. However, as will be discussed later, this change is not necessarily due to a qualitative difference in the Au reactivity for various film thicknesses and therefore the influence of the Au film thickness has not been studied systematically. Here, TPD measurements for CO saturation coverages on a 3 ML Au film (fig. 5.2), where no Pd atoms are exposed to the gas phase, will be compared to experiments on only partially Au covered Pd(111) surfaces (Θ_{Au}=0.25/0.5 ML, figs. 5.4/5.5). Because of the coexistence of CO on Au sites with CO on Pd sites in the latter case, the interpretation of these data is more complicated than in the former case. Therefore, the TPD spectra from the completely Au covered Pd(111) surface are presented first.

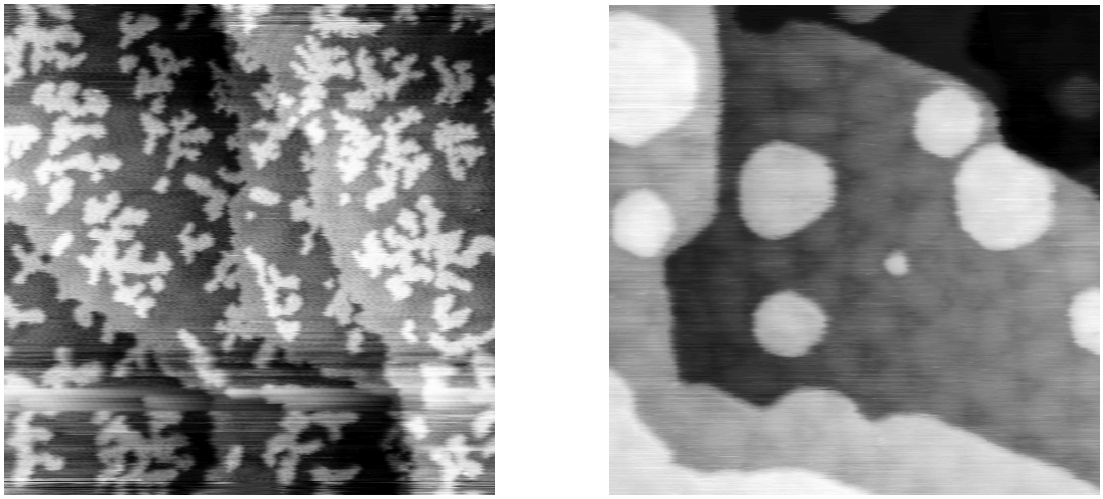

(a) directly after Au deposition

(b) after warming up ($\sim$ 10 h at 300 K)

Figure 5.3: STM images of 0.2 ML Au on Pd(111) precovered with 3 ML Au ($T_{dep} = 120$ K, image sizes: 800 Å $\times$ 800 Å).

CO adsorption on completely Au covered Pd(111)

The spectra displayed in fig. 5.2 constitute a continuous series of CO TPD experiments on a completely Au covered Pd(111) surface. As will be explained in detail below, these experiments were performed using constant CO exposures on a Au film that gradually changes its structure from TPD run to TPD run. A linear background was subtracted from all spectra, but no additional normalization of the QMS intensities was performed. Generally, the QMS intensities were reproducible in different experiments with an error of less than 20%. Spectrum a was recorded after the first Au deposition step, which was carried out at a substrate temperature of $\sim$300 K. After this TPD heating-cooling cycle additional 0.2 ML Au were deposited at low substrate temperature ($T \approx 110$ K, spectra b - f). The temperature ramp was stopped at 300 K in order to minimize the morphological and compositional changes of the surface during the TPD measurements. In independent TPD and HREELS experiments it was confirmed that this temperature range is sufficient for a complete desorption of CO from the surface. STM images of the surface after the second Au deposition step are displayed in fig. 5.3. They show the surface morphology both directly after low temperature Au deposition (before spectrum b was recorded) and after warming up to 300 K for about 10 h (before spectrum f).

Three desorption features can be distiguished in fig. 5.2: Two peaks at $\sim$ 140 K (α_1) and at $\sim$ 195 K (α_3), respectively, and a shoulder of the low temperature

peak at $\sim$160 K (α_2). Between each consecutive spectrum a significant difference in both, the absolute and the relative peak intensities can be noticed. While in spectrum a the observed desorption rates are small and for the α_3 peak even at the detection limit, the subsequent spectrum (b) exhibits the highest desorption rates over the whole temperature range. This can easily be explained by the creation of additional CO adsorption sites at Au island edges during the second Au deposition step. The following spectra (c - f) show by continuously decreasing peak intensities that these sites are thermally unstable. However, with the difference between spectrum d and spectrum e being only small, it can be stated, that already after two TPD heating cycles to 300 K the surface is stable enough to resist major changes during the short TPD temperature ramp (T $\geq$ 200 K for only $\sim$20 s). The peak shapes do not change markedly with the exception of peak α_1 in spectra a and c, where the low temperature side of the peak seems to be decreased. This can presumably be attributed to small changes in the sample temperature during CO adsorption, which varied between 116 K (spectrum b) and 127 K (spectrum c). After recording spectrum e the sample was slowly warmed up to room temperature by stopping the liquid nitrogen flow. The next spectrum (f) was recorded after leaving the sample for about 10 h at this temperature. Again, a drastic decrease of the overall CO-desorption signal can be observed, but the integrated QMS signal is still considerably larger compared to the spectrum taken before the second Au deposition step (a).

Up to now, only the global changes of the TPD spectra were described. A more detailed description of the relative peak intensities should give further insight into the nature of the different desorption features. First, it has to be stated, that in this experimental temperature range (T > 100 K) and under UHV conditions CO is not stable on Au terrace sites of the Au/Pd(111) surface. This can already be concluded from the fact that all observed CO desorption features from the island rich surfaces (spectra b - f) in fig. 5.2 are decreasing during the TPD sequence. If there was a peak originating from CO adsorbed on Au terrace sites, this peak should increase rather than decrease by a thermal equilibration of the surface. Therefore, at least three different types of Au defect sites have to be present on the surface to account for the observed TPD features [5].

Second, the "high" temperature peak α_3 (at $\sim$ 195 K) exhibits the larges intensity variations throughout the TPD cycle. While in spectrum A it is hardly visible, it is the strongest peak in spectrum B, and in spectrum F it is shrunk again to a small fraction of the total CO desorption signal. Correlating this behaviour with the structural changes of the surface observed by STM imaging directly after the low temperature Au deposition step (fig. 5.3(a)) and after the 10 h

[5] The possibility to explain two desorption features with only one type of adsorption site by the assumption of a superstructure, which is stabilized by adsorbate – adsorbate interactions, can practically be excluded, because here CO adsorption is taking place on irregular defect sites.

equilibration period at 300 K (fig. 5.3(b)), respectively, it can be concluded that this desorption peak is caused by CO adsorbed on sites, which are very frequent at irregularly shaped, branched islands and which are only scarce in compact hexagonal islands with rather straight island edges. Obviously, these are the Au kink sites. Besides this direct argument, which is based on the observation of morphological differences in the various surfaces, there are at least two indirect arguments for the same assignment. The first argument is based on the fact, that generally the diffusion barrier for atom diffusion along island edges is considerably smaller than the barrier for the detachment of an island edge atom. From this it follows that by mild annealing of irregularly shaped islands the smoothening of the island edges, which is accompanied by a decrease in kink density, is a faster process than the Ostwald ripening of the islands, which is accompanied by a decrease in total island edge length. The second argument considers the dependence of the chemical activity of metal atoms on their coordination. As has already been mentioned in section 5.1.1, transition and noble metal atoms with lower coordination number are expected to exhibit a narrower d band compared to regular surface atoms. For late transition metals and for noble metals this causes an upward shift of the d band. Hence, the degree of metal to CO back-donation increases. Therefore, the atoms with lowest coordination number should constitute the most stable CO adsorption sites and should be responsible for the highest temperature desorption peak.

Third, having assigned peak α_3 to Au kink sites, there remain different types of regular step sites to account for the two low temperature features. The edges of hexagonally shaped island on fcc(111) surfaces are structurally not equivalent. Three sides of the hexagon expose microfacets with (111) orientation ("B steps") and the other three sides consist of (100) oriented microfacets ("A steps", see fig. 3.2). This fact, together with the STM observation, that at 300 K the Au island shape is indeed hexagonal rather than triangular, could explain the two distinct low desorption features as originating from the two differently oriented Au island edges. This is, however, not the only possible assignment. If the difference in adsorption energy for both step types was negligible, there remains the possibility that both linear and bridge bonded CO molecules could exist at Au island edges. From the TPD data displayed in fig. 5.2 it is not possible to decide this question. In section 5.3.2 it will be shown that in HREEL spectra of CO adsorbed on a similar surface only one C–O stretching peak around 263 meV is observed, which is a typical value for linearly bonded CO. Therefore, the occurence of bridge bonded CO at Au island edges seems to be unlikely and the two peaks α_1 and α_2 have to be explained by CO adsorbed linearly on Au atoms, which are chemically not equivalent. Although an exact evaluation of the peak areas of α_1 and α_2 is not possible due to their small separation by only about 20 K, it is obvious that α_1 is considerably stronger than α_2. In principle, one could use the intensity ratio of the peaks to assign the stronger peak to the dom-

inating step type. Unfortunately, the available STM images of this surface are not sufficient to determine which step type is more abundant. Nevertheless, if the above argumentation is correct, it can be stated that the more stable step type, i. e. the dominating step type, is slightly less active towards CO adsorption compared to the less stable step type. This would fit well in the general trend, that the higher the binding energy of a Au atom to the substrate the lower the ability to form a chemical bond to CO.

The CO TPD results obtained on the Au/Pd(111) surface can be compared with TPD data from an (332) oriented bulk Au crystal reported by Ruggiero and Hollins [165]. Using a low heating rate of 1.5 K/s and adsorption temperatures of 92 K and 105 K, respectively, they found two major TPD peaks (140 K and 185 K) and a low temperature shoulder at $\sim$ 120 K for the 92 K experiments. Considering the different heating rates used in both cases, the agreement between the CO desorption temperatures on Au(332) and on 3 ML Au/Pd(111) is very good. The system CO/Au(332) has also been analysed by infrared spectroscopy [165]. In the spectral region of linearly bonded CO, Ruggiero and Hollins found four components of the absorption band, three of which they assigned to CO bonded to kink sites, regular step edge sites, and terrace sites, respectively. For the remaining spectral feature they could not present a convincing assignment. The detection of CO adsorbed on Au(332) terrace sites, which are structurally equivalent to Au(111) terrace sites, is not in contradiction to the above statement, that CO cannot be found on these sites under UHV conditions, because in the work on Au(332) a dynamic CO pressure of up to 1×10^{-5} mbar is necessary to populate all of the above described states.

CO adsorption on partially Au covered Pd(111)

In fig. 5.4 a sequence of four TPD spectra of saturation CO exposures on a 0.25 ML Au/Pd(111) film is displayed. As has been already mentioned, the QMS-intensities could generally be reproduced very well from day to day. Therefore, the QMS-signals of the different spectra presented in this chapter can be directly compared with each other. The first spectrum (a) was recorded after the low temperature Au deposition and the subsequent CO dosage. The temperature ramp for spectra a and b was stopped at 350 K, while for spectra c and d the sample was heated up to 400 K.

As has been already pointed out in section 5.2.1, residual gas adsorption has a significant influence on subsequent CO adsorption. Specifically in CO TPD spectra the low temperature desorption states diminish with increasing time, that the sample was exposed to residual gas at low temperature ($T \leq 200$ K). In fig. 5.4 this effect is obvious for spectrum a, where the sample had stayed at temperatures between 110 K and 120 K for the time necessary to deposit Au, to determine the Au coverage by XPS, to set the aperture down onto the sample holder, and to

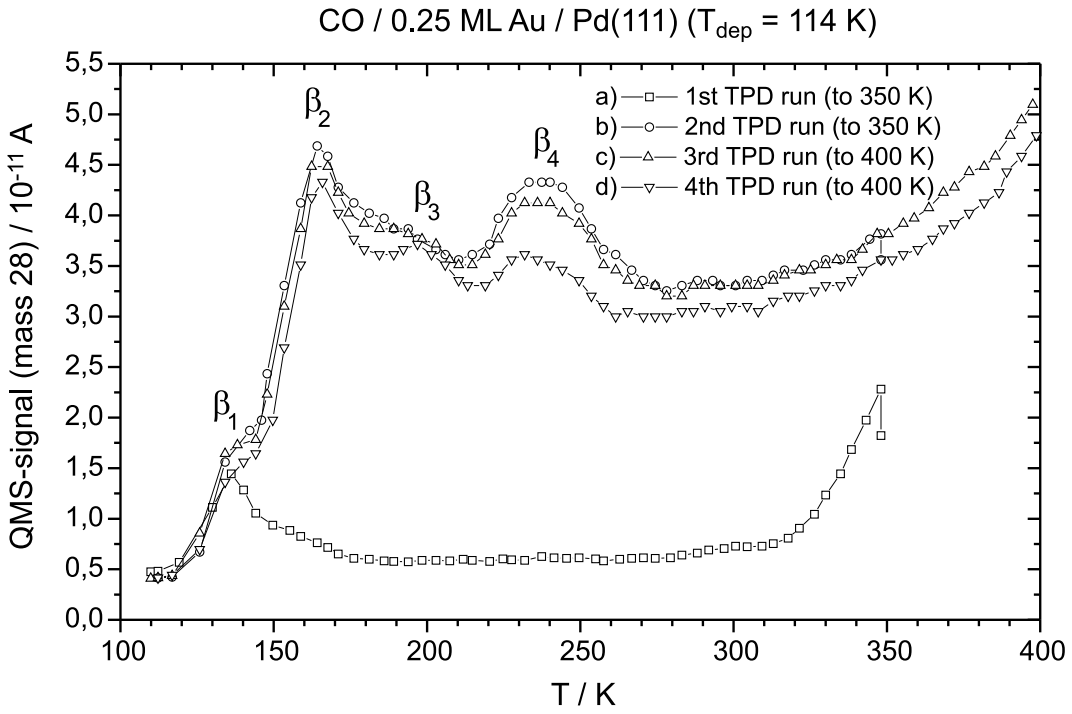

Figure 5.4: CO TPD spectra from partially Au (0.25 ML) covered Pd(111). All spectra were recorded after CO saturation of the surface. The first spectrum (a) was measured directly after Au deposition at 114 K and subsequent CO dosing.

move the sample to the dosing position, which amounts to ∼90 min. Therefore, this spectrum does not contain much useful information and is only included in fig. 5.4 to be consistent with the previous figure, where also a continuous series of TPD spectra is displayed starting directly after the low temperature Au deposition step. Since in the case of completely Au covered Pd(111) no effect of residual gas adsorption was found, it should be expected that also in the case of submonolayer Au films CO adsorption sites on Au atoms are not blocked by residual gas molecules. In spectrum a no CO desorption is detected between 170 K and 310 K. In subsequent TPD runs Au derived features are observed also in this temperature region. Although it cannot be ruled out, that in contradiction to the above mentioned expectation also Au sites are affected by residual gas adsorption, a second and more likely explanation is, that the desorption of residual gas molecules from the open Pd patches starts at the beginning of the temperature ramp and that therefore additional free sites become available for CO, which can be filled by molecules diffusing from Au sites to the more stable Pd sites. The small CO feature at the beginning of the temperature ramp (120 K – 170 K) could then be attributed to CO desorbing from Au sites prior to a redistribution of the CO molecules on the surface. On first sight, this feature could also be ascribed to CO desorption from the aperture. However, in other TPD spectra, e. g., from

the pure Pd(111) surface, it does not show up. Therefore it is most likely related to Au sites.

In total, 4 desorption features can be distinguished in the spectra shown in fig. 5.4. First, the low temperature peak in spectrum a (β_1), which was already mentioned above. It can be also identified in spectra b – d as a low temperature shoulder of the steep increase in the desorption rate, which passes a first local maximum at $\sim 165\,\mathrm{K}$ (β_2). The next small feature (β_3) is located at around 200 K, and only in spectrum d it is clearly visible. Finally, a prominent and broad peak at $\sim 235\,\mathrm{K}$ (β_4) is seen in all spectra but spectrum a. The origin of the different peaks can be discussed using similar arguments as in the above section on CO desorption from completely Au covered Pd(111): The TPD peak which decreases most rapidly within the TPD sequence can be attributed to Au sites that are thermally most unstable, i. e., to Au kink sites. As the information of the peak intensities in the very first spectrum (a) is missing, the decision about the desorption peak from Au kink sites is not as unequivocal as in the case of the thicker Au film. However, by comparing spectrum c with spectrum d the changes that are induced by the first heating cycle to 400 K (vs. 350 K in the previous spectra) can be identified. Generally, the low temperature CO desorption is decreased after the anneal to 400 K. The largest effect is seen in the region of β_4. From this observation and from the fact that β_4 corresponds to the most stable CO species on Au sites that are present on the 0.25 ML Au film, the assignment of β_4 to desorption from Au kink sites can be inferred. This interpretation is supported by TPD experiments on another submonolayer Au film, that will be discussed in the following.

Fig. 5.5 shows TPD spectra, which were obtained during the first 5 heating cycles on a 0.5 ML Au film. In this case, the sample was saturated with CO before Au deposition. By this procedure, adsorption of hydrogen from the residual gas could be prevented. Another effect of preadsorbed CO is to lower the mobility of the deposited Au atoms which leads to an increased island density and consequently to a higher proportion of Au island edge and Au kink atoms. The resultant TPD spectra from this surface are displayed in fig. 5.5. As expected, strong low temperature CO desoption is detected even in the first spectrum of this sequence (a), which is in distinct contrast to the almost complete absence of low temperature CO desorption in spectrum a of fig. 5.4. Since in spectrum a it is not possible to subtract a background signal, only a rough estimate for the amount of the desorbing CO molecules can be given. Integration of the spectrum yields an area that corresponds to 94% of the area under under the TPD spectrum for CO saturation on Pd(111) (spectrum e in fig. 5.1). Taking into account that above 300 K additional CO desorption is likely to occur also for 0.5 ML Au/Pd(111), it can be stated that on this surface at least the same amount of CO can be adsorbed at 110 K as on the clean Pd(111) surface. The almost featureless contour of spectrum a hints to a disordered surface, where presumably very small

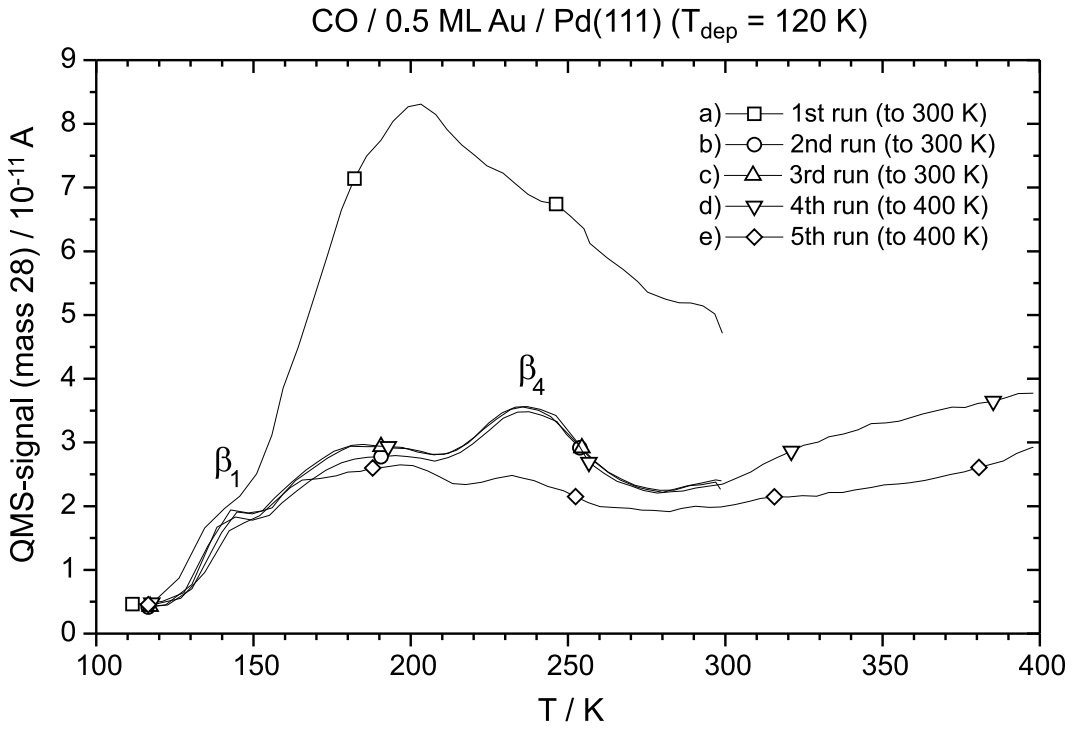

Figure 5.5: CO TPD spectra from partially (0.5 ML) Au covered Pd(111). All spectra were recorded after CO saturation of the surface. The first spectrum (a) was measured directly after Au deposition at 120 K, which was carried out after an initial CO saturation of the Pd(111) surface.

Au island are spread across the substrate. Since the Au coverage is relatively high (0.5 ML) also most of the remaining Pd adsorption sites are likely to be affected by Au islands in their immediate vicinity. Therefore, no clear distinction can be made in spectrum a between CO which desorbs from Au sites and CO originating from Pd sites that are affected by neighbouring Au. The situation becomes clearer in the next spectrum (b). It shows a shape similar to the shape of the spectra for 0.25 ML Au/Pd(111) (fig. 5.4). The partial equilibration of the surface during the first TPD heating cycle to 300 K obviously resulted in the coalescence of Au islands. Consequently, the surface morphology changed to the coexistence of larger Au islands with larger Au free Pd patches as compared to the situation directly after Au deposition. The effect of this structural change for CO desorption is clearly seen in spectrum b, where again more or less well defined desorption states can be distinguished. The most prominent peak is detected at $\sim$237 K. Two additional heating cycles to 300 K have almost no influence on the subsequent CO TPD spectra, while a drastic change is observed after the first heating to 400 K (spectrum e). Similar to the observation in fig. 5.4, the most significant decrease of the desorption rate is observed at temperatures around

240 K. Even though an STM characterization of the surface has not been carried out for this TPD experiment, it can be assumed that short annealing at 300 K is not sufficient for the formation of compact hexagonal Au islands. Therefore, the amount of Au kink atoms is likely to be still significant up to spectrum d. The strongly reduced intensity of peak β_4 in spectrum e can then be attributed to the partial equilibration of the Au island shapes and the concomitant decrease in the kink density along the Au island edges.

In order to explain the remaining structures in the spectra of figs. 5.4 and 5.5, also CO desorption from Pd sites has to be considered. The assignment of the remaining peaks is further complicated by the lack of significant changes in the peak intensities during the TPD series. On clean Pd(111) (s. fig. 5.1) two relatively small peaks are found at 190 K and 255 K, respectively. The feature, which was labeled β_3 in fig. 5.4, is the only one, which seems to be stable during the TPD series. Consequently, it is likely to be a remainder of the 190 K peak for Pd(111). The other Pd(111) derived feature at 255 K is not seen in the spectra from submonolayer Au film. Possibly it is covered by the larger contribution from the Au kink sites. Returning to the assignment of the low temperature structures β_1 and β_2 in fig. 5.4, the following observations have to be considered: First, β_1 is clearly detected also in the spectra from the 0.5 ML Au film (fig. 5.5). Second, the sharp peak β_2 is not visible in fig. 5.5. Third, both features do not change significantly after annealing the surface shortly at 400 K. A comparison with the TPD peaks observed from the completely Au covered Pd(111) surface (fig. 5.2), would suggest to assign the β_2 peak to desorption from regular Au step sites. However, the fact that for the 0.5 ML Au film no such feature is observed and that it is not shrinking during the TPD series, queries this assignment. Also the origin of the shoulder β_1 remains an open question, because its desorption temperature is certainly too high for CO on Au terrace sites (s. section on HREELS measurements, 5.3.2), and its intensity is too stable to be likely to be related to Au step edge sites.

5.2.3 CO adsorption on AuPd(111) surface alloys

TPD spectra have been measured from a broad variety of different AuPd(111) surface alloys. These were prepared by Au deposition on the Pd(111) crystal ($\Theta_{Au} \geq 2$ ML) around room temperature and subsequent annealing at temperatures above 600 K[6]. For most of the resulting intermixed Au-Pd surfaces, atomically and chemically resolved STM images were obtained partly before and partly

[6]In chapter 4 it has been shown that in the case of multilayer Au films annealing temperatures around 600 K are sufficient for the preparation of homogeneous surface alloys with high Au concentrations, while in the case of submonolayer Au films temperatures $\geq$ 780 K have to be used in order to eliminate the inhomogenities that are induced by the coexistence of open Pd terrace areas with Au islands and Au aggregations at step edges.

after the TPD experiments. This allowed for the quantitative determination of the Au and Pd concentrations in the surface layer. The heating ramp of the TPD runs was restricted to temperatures well below the respective initial annealing temperature to ensure that during the TPD cycles the changes in surface composition and morphology were negligible. TPD spectra from CO saturated alloy surfaces are displayed in figs. 5.6 ($c_{Pd} \leq 24\,\%$) and 5.7 (overview over the complete range of surface compositions). A constant background has been subtracted from the spectra, such that they all start at 0. Since the size of the aperture between the sample and the ionization chamber of the QMS has been changed during the course of these measurements, some of the spectra have been multiplied by a correction factor. The Pd surface concentrations are given in the legend. A few numbers are marked by an "$*$" to indicate that they are only estimates of the Pd content. These are either derived from the TPD spectra (CO saturation coverages and peak positions) or from the preparation conditions. In most cases, however, it was possible to evaluate the surface composition directly from STM images. The following presentation of this complex set of data begins with the simpler cases, which are the surfaces with low Pd content. Then, by passing to higher and higher Pd concentrations, also more sophisticated spectra will be explained at least qualitatively.

Spectra a – j in fig. 5.6 cover the range from $\sim$ 1% Pd to 24% Pd. Only a single desorption peak around 300 K is detected on the surfaces with the lowest Pd concentrations ($c_{Pd} \leq 5\%$). A comparison between the CO saturation coverages calculated from the TPD peak areas of these spectra and the number of Pd atoms per surface area reveals that within the experimental accuracy, one CO molecule can be accommodated per Pd atom. A typical sequence showing the CO coverage dependence of this type of TPD spectra is displayed in fig. 5.8 for $\sim$ 2% Pd. It should be mentioned in passing, that in the low temperature region (140 K – 230 K) of the spectrum with saturation CO coverage, small desorption features from Au kink and Au step edge sites can be detected. In STM images of AuPd(111) surface alloys with a Pd concentration below 5%, almost exclusively Pd monomers are detected. A comparison of the STM derived size distribution of Pd clusters with a statistical model showed a significant preference of Pd monomer formation, i. e., the number of monomers was determined to be considerably higher than expected from an entirely statistical distribution (see fig. 4.19). From these observations it can be concluded that the CO desorption peak at $\sim$300 K originates from molecules which have been adsorbed on Pd monomers. Obviously, no direct information on the exact nature of these adsoption sites has been presented so far, but to come to the point, HREELS experiments which will be presented below (in section 5.3.3), demonstrate that CO is linearly bonded to the Pd monomers. In fig. 5.8 a vertical line has been drawn at the position of the saturated monomer peak in order to draw the attention to the small, but significant, negative peak shift.

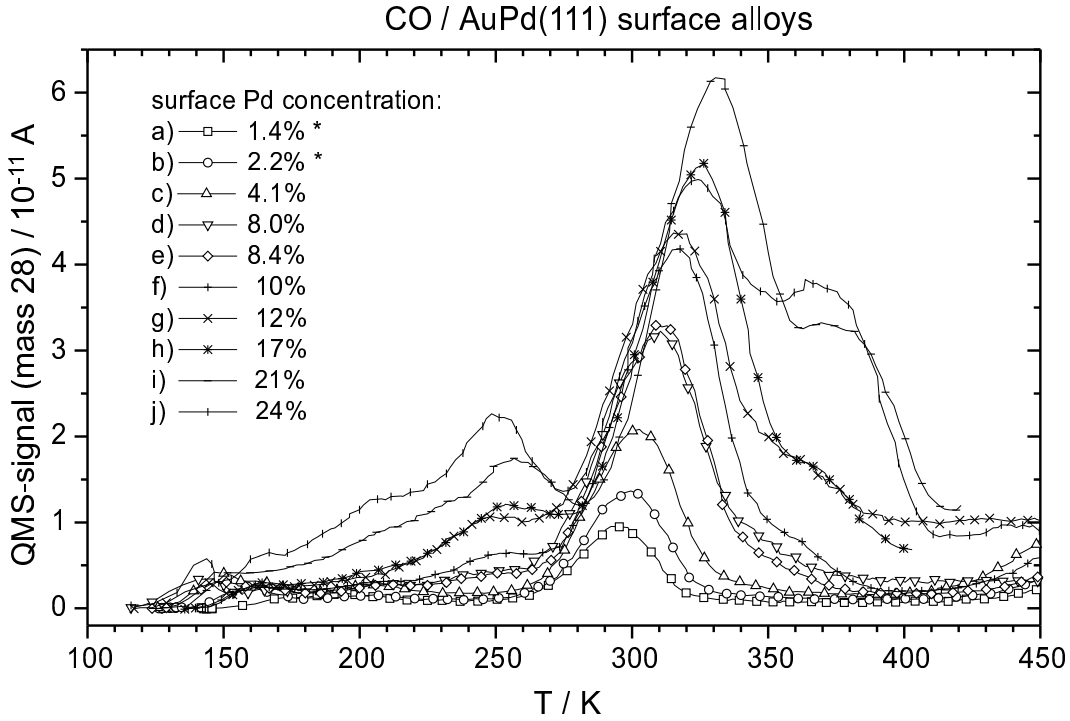

Figure 5.6: CO TPD spectra from AuPd(111) surface alloys with Pd concentrations between 1% and 24%, that were mostly determined from atomically resolved STM images. The numbers marked by an "*" are only estimates of c_{Pd}. The spectra were recorded after CO saturation of the surfaces. A constant background has been subtracted from each spectrum.

On surface alloys with $\sim 8\%$ Pd, about 0.5% ML Pd dimers are found in STM images. This is already above the detection limit of the TPD system used for this work. Consequently, in spectra d and e of fig. 5.6 two new features appear at $\sim 250\,K$ and at $\sim 350\,K$, respectively. They grow significantly with increasing Pd concentration. Therefore, *two* different CO adsorption sites have to be identified on Pd dimers. Based on the available information on CO adsorption on the different low index planes of Pd (see section 5.1.2), it should be expected that the bridge site between two Pd atoms is energetically more favourable for CO adsorption than the on-top sites on Pd monomers. Hence, the new feature on the high temperature side of the Pd monomer peak is to be assigned to CO desorbing from the bridge sites between two neighbouring Pd atoms[7]. If on the

[7]From TPD alone it can not be decided if the first CO molecule per Pd dimer is adsorbed "on-top" of one of the Pd atoms or at the Pd bridge site. However, from HREELS experiments that will be presented below (section 5.3.3) for 23% Pd it can be concluded that the bridge sites in one-dimensional Pd structures (dimers and linear trimers) within a Au matrix are populated at low CO exposures, while on the CO saturated alloys with low c_{Pd} almost all molecules are linearly bonded.

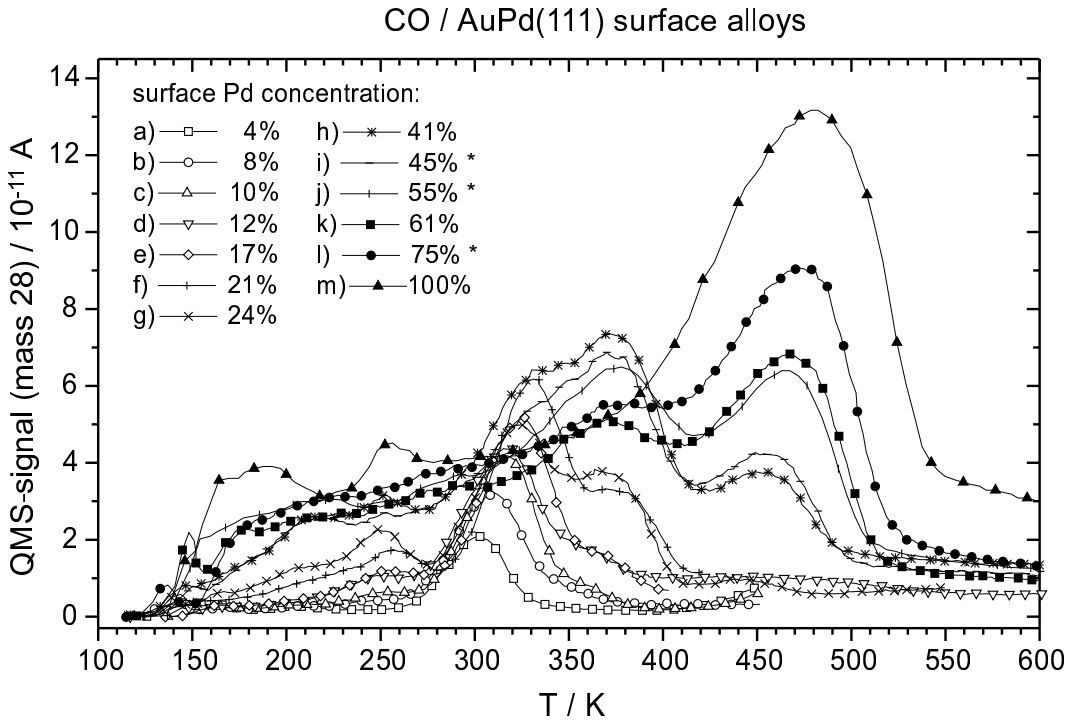

Figure 5.7: CO TPD spectra from AuPd(111) surface alloys with Pd concentrations between 4% and 75%, that were mostly determined from atomically resolved STM images. The numbers marked by an "*" are only estimates of c_{Pd}. Additionally, a spectrum from the clean Pd(111) surface is shown. The spectra were recorded after CO saturation of the surfaces. A constant background has been subtracted from each spectrum.

CO saturated sample these bridge sites were occupied, then no adsorption would be possible on-top of either of the Pd atoms and only one CO molecule could be accommodated on a Pd dimer. This is in contradiction to the observation of a second additional desorption state at the low temperature side of the Pd monomer peak. It follows, that for "high" CO coverages the molecules on the bridge sites are shifted to one of the on-top sites over a Pd atom, which makes the occupation of the other on-top site in the Pd dimer by a second CO molecule possible. A more direct evidence for this scenario is obtained by vibrational spectroscopy and will be given below (5.3.3). During the thermal desorption process the adsorption sequence is reversed, i. e., first a CO molecule from one of the on-top sites desorbs enabling the remaining CO molecule to shift to the more stable bridge site and to desorb at a considerably higher temperature. For simplicity, the two new types of CO adsorption sites (desorption peaks) provided by Pd dimers will be termed "dimer-bridge site (peak)" and "dimer-on-top site (peak)". The temperature difference between the monomer peak and the dimer-on-top peak is a

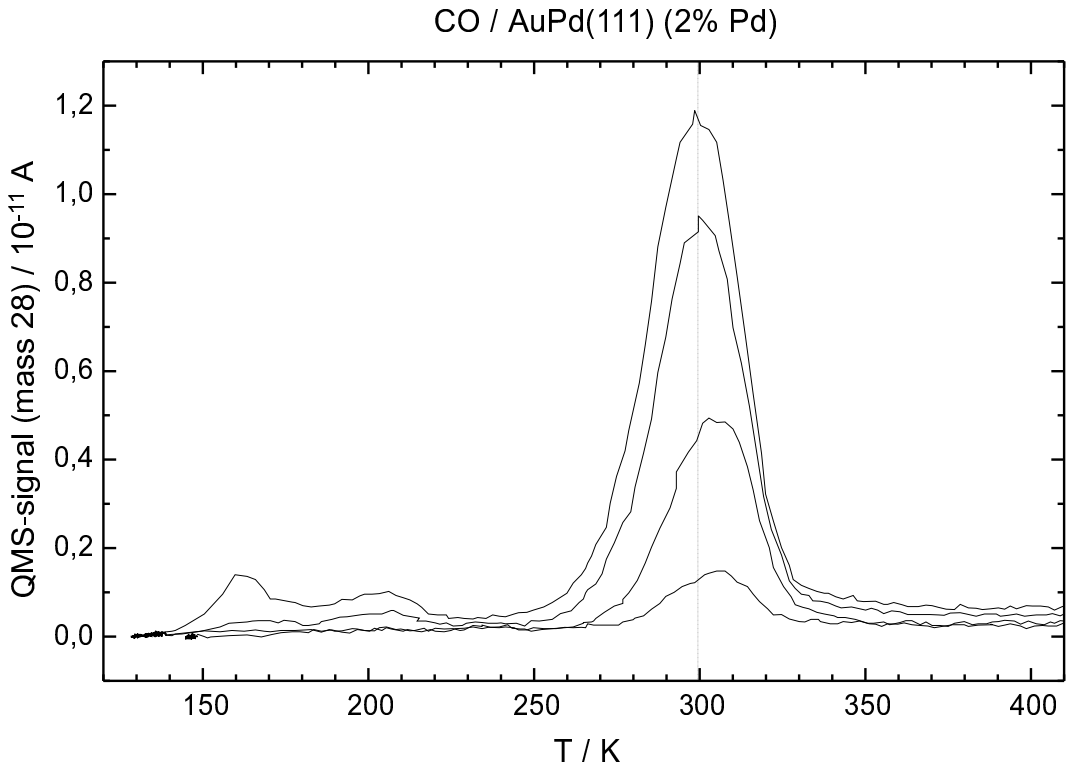

Figure 5.8: CO coverage dependent TPD spectra from a AuPd(111) surface alloy with about 2% Pd in the surface layer. A constant background has been subtracted from each spectrum. For the two low coverage spectra the sample was exposed to the residual gas for a few minutes; the CO doses for the two high coverage spectra were 0.09 L and 0.19 L, respectively.

consequence of the CO–CO repulsion, which has to be expected for the small distance between the two molecules on the Pd dimer. It is quite obvious that this repulsion causes the molecules to be tilted away from each other and even to be displaced somehow from the direct on-top positions to positions, that might be even close to a geometric bridging position between a Pd atom and a Au atom. However, the chemical signature of this site remains that of an on-top site (see section 5.3.3).

A CO coverage dependent TPD series is shown in fig. 5.9 for a surface containing 12% Pd. At very low CO coverages, only desorption from the dimer-bridge sites is observed, while the dimer-on-top sites are only observed for CO coverages close to saturation. The peak areas of the two Pd dimer related features cannot be evaluated exactly because of the overlap with the broad monomer desorption peak. Judging by eye, these features seem to be of more or less the same intensity as expected from the above developed model. It should be noted, that the monomer peak exhibits a small, but still significant shift to lower temperatures for

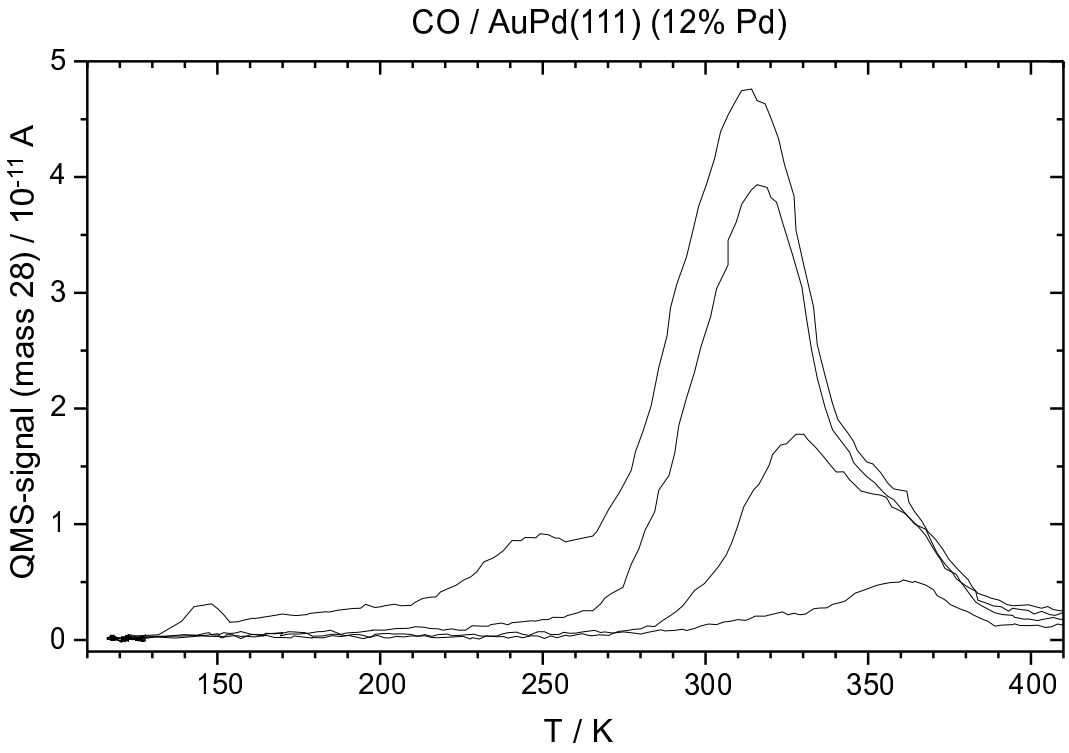

Figure 5.9: CO coverage dependent TPD spectra from an AuPd(111) surface alloy with 12% Pd in the surface layer. A constant background has been subtracted from each spectrum. CO doses: Residual gas, 0.19 L, 0.38 L, and $\sim$ 1 L (using doser).

increasing CO coverages. STM images of this surface show 0.06 ML monomers, 0.02 ML dimers, and less than 10^{-4} ML three-fold sites, i. e., the latter clearly have no influence on the TPD spectra.

With increasing Pd concentration the contributions from Pd dimers is growing and on a surface with 21% Pd (spectrum i in fig. 5.6) the two dimer related shoulders have developed to relatively strong peaks, that can be resolved from the still stronger monomer peak. While up to 21% Pd the monomer peak is continuously gaining intensity with increasing Pd content, this trend is reversed as the Pd concentration is increased to 24%. In this spectrum (j in fig. 5.6 and g in fig. 5.7), the monomer peak is diminished compared to 21% Pd. In STM images of the two surfaces the same trend is observed: The coverage of Pd monomers decreases from 0.087 ML for 21%Pd to 0.083 ML for 24% Pd. However, accounting for statistical errors and for possible inhomogenities across the surface, this small decrease of about 5% is not significant. On this surface (24% Pd) again a new high temperature desorption feature is observed at around 440 K (fig. 5.10). The next type of CO adsorption site, that is becoming available upon increasing the surface Pd content, is the threefold hollow site. For example a compact Pd trimer would

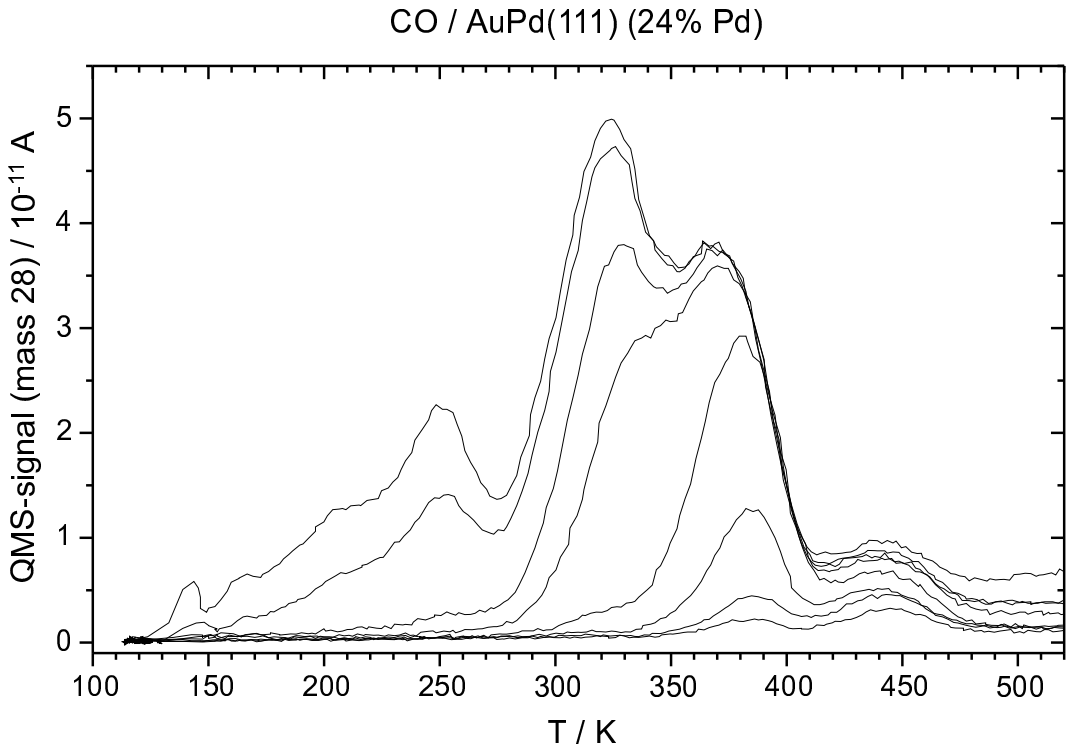

Figure 5.10: CO coverage dependent TPD spectra from an AuPd(111) surface alloy with 24% Pd in the surface layer. A constant background has been subtracted from each spectrum. Approximate CO doses (using doser): 0.02 L (background dosing), 0.05 L (background dosing), 0.15 L, 0.3 L, 0.9 L, 1.1 L, 1.4 L, and 5 L.

provide one threefold hollow site. On the surface with 24% Pd, 0.7% ML threefold Pd sites are identified in the STM images. Since this surface concentration of threefold sites agrees well with the intensity of the small peak at 440 K, this peak is unambiguously demonstrated to originate from CO molecules in threefold Pd sites. In the case of the Pd dimers, also a low temperature counterpart of the dimer bridge-peak was identified. On a CO saturated AuPd(111) surface alloy with compact Pd trimers it is plausible that not only one CO molecule is adsorbed per trimer. While it seems to be unlikely that all three bridge sites could be occupied by CO, there are a number of other possibilities that cannot be excluded a priori. For instance, one bridge site between two of the three Pd atoms and the on-top site on the third Pd atom could be occupied at the same time; or alternatively, CO molecules could be adsorbed on all three on-top sites of the trimer. However, since the TPD spectra exhibit already a large variety of strong features in the range where desorption from these additional Pd trimer sites should be expected, they are not visible as new peaks in the spectra of fig. 5.10. Consequently, from these TPD spectra only the new peak appearing in

the low CO coverage/high temperature limit allows for a definite statement on the respective CO adsorption site.

Another observation, that can be made in this TPD sequence is, that now the so-called dimer-bridge peak is much stronger than the dimer-on-top peak. This can be explained by the fact, that on larger linear Pd chains (linear trimers etc.) the ratio between the number of on-top sites and the number of bridge-sites approaches one. Therefore, the energetic advantage for the on-top site occupation in the case of Pd dimers, which is the simple fact, that more on-top sites are available than bridge-sites, is gradually lost with increasing Pd chain length. Therefore, the bridge peak at $\sim$375 K, which should not be called "*dimer*-bridge peak" anymore, contains intensity also from bridge bonded CO on larger Pd clusters, whereas the peak around 250 K is caused only by on-top bonded CO from smaller Pd clusters. It should be expected that on a hypothetical infinite Pd chain in a Au matrix only bridge sites are occupied. This configuration would be similar to the close-packed rows on the Pd(110) surface, where indeed the bridge sites have been determined to be the energetically most favourable sites [142]. For linear Pd chains of intermediate size, it is difficult to make a statement about the CO adsorption sites. Since it is not possible to prepare a surface with only one type of larger Pd clusters (e. g., with only linear Pd trimers) and since the TPD signal from the high number of Pd monomers and Pd dimers is overlapping with, for instance, a hypothetical trimer-on-top peak, the question about the CO adsorption sites on chains containing three and more Pd atoms cannot be decided solely based on the TPD data.

With increasing Pd content, the average size of the Pd clusters grows and also the size distribution becomes broader. Therefore, the elegant assigment of the two dimer related TPD peaks and of the three-fold hollow peak cannot be repeated for larger Pd clusters. The development of the TPD spectra with increasing Pd concentration will be described only qualitatively for $c_{Pd} \geq 24\%$ (see fig. 5.7). The high temperature desorption peak, that is associated with threefold bonded CO molecules, is continuously growing, and it shifts to higher temperatures. For $c_{Pd} \geq 60\%$ it becomes the dominating feature. At the same time, an increased desorption rate in the low temperature region ($T \leq 300$ K) of the spectra can be observed. Also, the peaks correlated with Pd monomers and with Pd bridge sites are losing intensity, until at $c_{Pd} \approx 60\%$ they have disappeared. Only a small hump around 370 K might be interpreted as a remainder of the bridge peak. In general, there are two limiting cases of TPD spectra for CO saturated AuPd(111) surface alloys:

- First the spectra on surfaces with low Pd concentrations, which were discussed extensively above. These are characterized by a clear fingerprint of the adsorption sites, that are available on the surface. The features in the spectra are directly correlated with specific structures on the surface.

- Second the spectra on Pd-rich surfaces, which are dominated by an almost featureless low temperature CO desorption region and a relatively strong high temperature peak. Here, CO-CO interactions dominate the spectrum and the potential energy surface of the substrate itself is not as important as in the other case. Only for low CO coverages, some information on the energetics of the most favourable adsorption site (the fcc threefold hollow site, [127]) can be gained from TPD spectra.

In the next section a detailed discussion on the further evaluation of CO TPD spectra from AuPd(111) surface alloys will be presented. Three important general observations from the experiments should be summarized at this point as basis for the following quantitative analysis:

1. For increasing CO coverages on a given AuPd(111) surface alloy, a small shift of the peak position to lower temperatures is observed (see figs. 5.8–5.10).

2. If TPD spectra from CO saturated surfaces with different Pd concentrations are compared (see figs. 5.6 and 5.7), distinct positive shifts of the monomer and the threefold hollow peak positions with increasing c_{Pd} are apparent.

3. The CO doses that are required to saturate different AuPd(111) surface alloys (see figs. 5.8–5.10) clearly depend on the alloy composition with only very small saturation doses needed in the case of the lowest Pd concentrations; e. g., the surface with 2% Pd is saturated after dosing 0.19 L CO.

5.2.4 Quantitative evaluation of the TPD spectra

In the literature on the evaluation of TPD measurements, many different approaches have been suggested. Since TPD was only one of several powerful experimental methods used in this work, it should not be attempted to give an extensive review on all available evaluation methods. The aim of the following introductory remarks is merely to justify the model that will be outlined below. The maximum information from TPD spectra can certainly be extracted, if computer simulations are performed to verify the employed model and its numerical parameters. But generally, the level of sophistication of the data analysis has to be adapted to the achieved level of accuracy in the acquired data. For example, state of the art simulations of TPD spectra, that are based on the solution of lattice gas models with the tools of statistical mechanics (see for example [178]), are only useful if the corresponding experimental spectra are free from artefacts like significant background signals and if the characterization of the substrate is almost perfect, e. g., if the experiment is carried out on a clean single crystal surface. Although in this study the substrate being a bimetallic surface is

a rather complicated system by itself, the latter condition is fulfilled at least in those experiments where a sufficient number of well resolved STM images could be obtained. The former condition, however, is hard to be met at the same time because of the difficulties which arise if several different experimental methods are combined in one apparatus.

In this section, a relatively simple model for the desoption kinetics on a bimetallic alloy, like Au-Pd, where one component (Pd) is considerable more active towards molecular chemisorption than the other (Au), will be developed. It will be applied first to evaluate the kinetic parameters of CO desorption from AuPd(111) surface alloys with low surface Pd content and secondly to simulate CO TPD spectra from surfaces, where only one type of strong adsorption sites exists, namely the Pd monomers. It has been pointed out in the previous section, that for higher Pd concentrations the exact adsorption sites are difficult to be decided on. In this case, only a statistical model would be promising, because a broad variety of possible configurations has to be considered. However, this approach is far beyound the scope of this work, and the TPD spectra are not perfect enough to reveal all the details of CO desorption from Au-Pd(111) surfaces with too many possible adsorption configurations.

The quantitative discussion of TPD spectra commonly starts at the Polanyi-Wigner differential equation [166], which relates the temperature and coverage dependent desorption rate to an expression consisting of a temperature independent preexponential factor ν, which is a questionable assumption (vide infra), a exponential function containing the activation energy for desorption E_d and the temperature T, and the momentary coverage on the surface raised to a certain power n (desorption order):

$$\frac{d}{dt}\,\theta\,(\theta, T) = \nu(\theta)\theta^n e^{-\frac{E_d}{kT}} \tag{5.2}$$

with

θ	fractional adsorbate coverage
T	temperature
ν	preexponential factor
n	desorption order
E_d	activation energy for desorption
k	Boltzmann's constant.

In the general case, i. e., if adsorbate–adsorbate interactions are taken into account, both ν and E_d are coverage dependent. The intuitive picture behind this formalism is that of an adsorbate particle attempting to cross the activation barrier with a certain frequency ν, that is commonly related to the vibrational frequency of the adsorbate. The probability to overcome the barrier is given by

$e^{-E_d/kT}$. In many cases, where both quantities (ν and E_d) can be determined experimentally, it is found that they obey a simple law of the form

$$ln\,\nu(\theta) = bE(\theta) + c,$$

which is referred to as "compensation effect" [179]. This observation points to the fact that the above-described picture is certainly oversimplified. It has to be mentioned, that in some cases the observation of a compensation effect might be due to an erroneous analysis of the TPD data [180, 181]. A possible limitation of approaches based on the Polanyi-Wigner equation (5.2) is the explicit temperature-dependence of ν itself, which has been emphasized for example by Ibach, Erley, and Wagner [182]. They derive expressions for $\frac{d}{dt}\theta\,(\theta, T)$ from equilibrium considerations and find that the preexponential factor in general is temperature-dependent. It also strongly depends on the nature of the adsorption site and the respective vibrational partition function of the adsorbate. Finally, they point out that the commonly assumed value of $\nu = 10^{13}s^{-1}$ is too low in many cases. For example, Ibach et al. calculated for the CO/Ni(111) system $\nu = 9.2\ 10^{16}s^{-1}$ for T = 300 K [182]. They conclude, that the identification of ν as some kind of vibrational frequency is conceptually wrong.

By using the most primitive approach to estimate E_d from TPD spectra, one could employ a formula derived by Redhead for first order desorption [166], which makes use of the peak temperature T_p as the only parameter taken from experiment:

$$\frac{E_d}{RT_p} = ln\frac{\nu T_p}{\beta} - 3.64 \tag{5.3}$$

with

R	gas constant
β	heating rate.

This formula is only justified under very special conditions:

- The quantities ν and E_d have to be coverage-independent, i. e., lateral interactions between the adsorbed molecules[8] are neglected.
- Desorption occurs directly from the chemisorbed state and not via a mobile precursor.
- The preexponential factor is assumed not to depend on the substrate temperature, which was already mentioned above to be generally wrong [182].

[8]It is sufficient to restrict the present discussion to the case of non-dissociative molecular adsorption/desorption.

- A reliable estimate for ν has to be provided as input for (5.3). In principle, this could be obtained from TPD experiments with varied β.

It is obvious that only in a limited number of adsorption systems these conditions are met to a sufficient extent. In the case of CO/AuPd(111) several features of the TPD spectra cannot be reconciled with the approach of Redhead. The following discussion is restricted to the relatively simple situation of small Pd concentrations ($\leq 5\%$), because then only one type of adsorption sites (Pd monomers) has to be considered. First, by comparing spectra from surfaces with different Pd concentrations a positive shift of T_p with increasing c_{Pd} is observed (see fig. 5.6). Second, for a given Pd concentration a θ_{CO} dependent negative shift occurs (see figs. 5.8, 5.9). This effect is small but still significant. Third, the peaks are much broader compared to calculated spectra using (5.3) with any pair of reasonable values for ν and E_d, and they are rather symmetric in contrast to the asymmetric calculated peaks. Now the question arises, which of the conditions mentioned above is violated and is thus responsible for the observed discrepancies between the experimental TPD spectra and the simple Redhead approach. The temperature-dependence of ν might result in some changes of the peak shapes but cannot explain the observed coverage dependent peak shifts. These are often ascribed to adsorbate–adsorbate interactions. The latter are likely to play only a minor role in the present case, because the average CO–CO distance is rather large due to the low Pd concentrations and the concomitant small CO saturation coverages at T $\geq$ 110 K. Even if the small negative θ_{CO} dependent shift was explained by CO–CO interactions, the reason for the larger c_{Pd} dependent shift in the opposite direction would still be unclear. One could postulate that the reactivity of single Pd atoms is increasing with the Pd concentration in the surface layer by electronic interactions between the surface atoms. But only the immediate environment of the individual surface atoms is likely to influence their chemical behaviour and therefore a change in the peak shape rather than a peak shift could be the consequence of varying the global surface composition. On the other hand, it is reasonable to expect, that both shifts can be explained by the existence of a mobile precursor state. Before this hypothesis will be justified below by applying the precursor state model to the evaluation and simulation of the TPD spectra, a more qualitative argument will be given in the following. At low temperatures, the CO molecules are certainly localized on the stable Pd monomer adsorption sites. With increasing temperature they start to populate the mobile precursor state[9], and eventually they desorb. A molecule in the precursor state has a certain probability to be trapped again in a potential well over a free Pd atom. Therefore, the environment of an occupied site has a certain influence on the desorption kinetics. From the perspective of the individual adsorbate molecules, the average desorption temperature shifts to higher temper-

[9] Here, the precursor state is most likely a weakly chemisorbed state on Au terrace sites.

atures if more free Pd sites are available on the surface simply because then the re-trapping of the molecules occurs more frequently. This applies now to both types of observed peak shifts:

1. If the same initial CO coverage[10] is considered on surfaces with different Pd concentrations, the average number of free Pd sites during the desorption process is larger for higher c_{Pd}.

2. On the other hand, if the initial CO coverage is varied on the same surface, the average number of free Pd sites decreases with increasing θ_{CO}.

From these considerations it follows, that the concept of a mobile precursor is able to explain the observed peak shifts at least qualitatively. The existence of such a precursor state can also be inferred directly from experiment. If the CO doses for TPD spectra from various AuPd(111) surface alloys are compared (see figs. 5.8–5.10) it is obvious that for low Pd concentrations also only low CO doses are needed to saturate the surface, i. e., the sticking coefficient of CO on AuPd(111) surface alloys stays quite high, until CO saturation is reached. This is a clear indication for the existence of a weakly bonded precursor state on the Au terrace sites of the surface.

Before the kinetic model for CO desorption from AuPd(111) surface alloys will be outlined, the possibility to apply other common TPD evaluation methods to this system should be discussed very briefly. The already mentioned Redhead analysis is an example for a so-called "integral method" that uses only integral features of the TPD spectra like T_p or parameters describing the peak shape. Chan, Aris and Weinberg (CAW) propose a formalism, where besides T_p also the width of the desorption peak is taken into account and consequently not only E_d but also ν can be estimated [183]. However, the common disadvantage of all integral methods is the fact that in the case of coverage dependent peak shifts, they can only make statements about the dependence of the kinetic parameters on the *initial* adsorbate coverage, which is — in a physical sense — a quite meaningless parameter. If E_d or ν are coverage dependent then the *actual* coverage has to be considered, which, of course, changes continuously during a single TPD run.

In this sense, the so-called "differential approaches" can be expected to produce more meaningful results. Among these the "complete analysis" method described by King [184] uses the largest set of input data from experiment and therefore contains the maximum information that is available within the Polanyi-Wigner framework. In short, the TPD spectra are integrated to obtain θ vs. T curves. Then by combining values taken from spectra with different initial coverages a set of r_d $(= \frac{d}{dt}\theta)$ vs. T values can be extracted for constant actual coverages θ_i. From an Arrhenius plot of these data pairs the activation energy $E_d(\theta_i)$ is

[10] This argument holds for absolute coverages and also for coverages that are measured relative to the amount of Pd atoms.

given by the slope $(-E_d/k)$ and the preexponential factor $\nu(\theta_i)$ follows from the intercept $(ln\,\nu(\theta_i) + n\,ln\,\theta_i)$ if the desorption order n is known. As a practical disadvantage of this procedure it has to be noted that it only makes sense if many different initial coverages were measured on the same system. Unfortunately, for most of the Au-Pd(111) surfaces the number of spectra with different initial CO coverages is rather small and therefore the complete analysis cannot be applied in this case.

The requirement of a large data set can be avoided by a method proposed by Habenschaden and Küppers [180]. They argue that if only the initial part of the TPD spectra is considered, the variation of θ is small and therefore also E_d and ν should be practically constant. This method is called "threshold TPD" (TTPD) analysis. Therefore, in an Arrhenius plot of $ln(r_d/\theta^n)$ vs. $1/T$ up to a temperature which corresponds to desorption of only a small fraction of the adsorbate, E_d and ν should follow from the slope and the intercept, respectively. Here, the obvious disadvantage is found in the fact, that this method relies on the accuracy of the measurement in the region of low desorption rates. Furthermore, if the kinetic parameters vary strongly with θ, then only a very small temperature window can be used from each spectrum. Habenschaden and Küppers mention that it might be necessary to restrict the analysis to the desorption of less than one percent of the initial coverage. Miller et al. [181] emphasize that, on the one hand, in systems which show a compensation effect the threshold region, that can be used as input for the TTPD analysis, is quite large. On the other hand, if the TTPD method is applied outside of the range of its validity then the TPD data might be forced to show erroneously a compensation effect. The difficulties that are encountered if the TTPD method is applied to the CO desorption from AuPd(111) surface alloys are mainly due to a continuously increasing background signal. Only in the cases of small CO doses and hence also small CO coverages the background was found to be sufficiently small to allow the application of the TTPD method. It will be shown below, that the presence of a precursor state introduces an additional effective coverage dependence of ν, which is strongest for CO coverages near saturation. However, for low CO coverages the TTPD method should still be applicable. Only the value for ν has to be reinterpreted based on the precursor model. Therefore, before some results from the TTPD evaluation of CO on AuPd(111) surface alloys will be presented, the generalization of the Polanyi-Wigner approach to a system with a mobile precursor state has to be discussed. It will be shown, that the interpretation of the kinetic parameters, which are obtained from any of the differential methods described above, critically depend on the kinetic desorption model, i. e., if precursor states are taken into account or not.

The concept of precursor-mediated surface reactions has been introduced by Taylor and Langmuir [185] to explain an almost constant sticking probability close to one for Cs adsorption on W. A review on this topic has been given for ex-

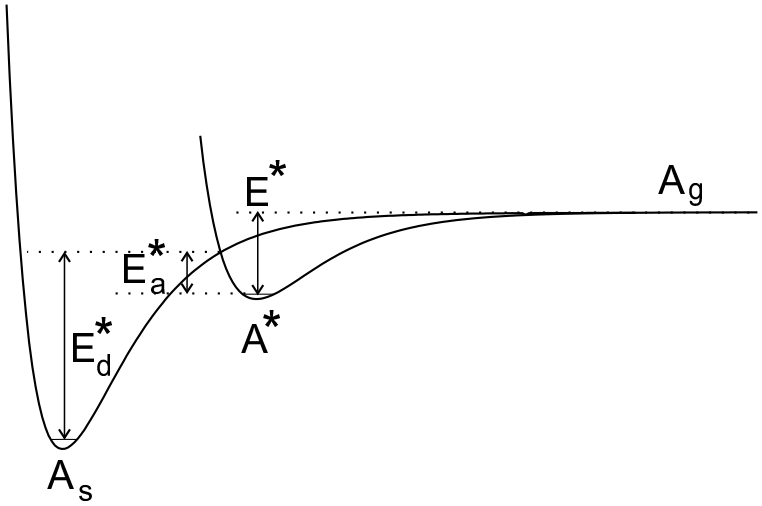

Figure 5.11: One-dimensional potential energy diagram for precursor mediated adsorption/desorption. The heat of adsorption (E_d) can be expressed by $E_d = E_d^* + E^* - E_a^*$. It should be noted that in the case of an intrinsic precursor state the two energy minima are situated at different locations of the surface (here: A_s: Pd atom, A^*: Au atom).

ample by Weinberg in [186]. The consequences of a precursor state for desorption processes was discussed by King [187] and by Gorte and Schmidt [188]. In the following, some basic ideas are taken from the latter reference and are adapted to the AuPd(111) system. In general, two types of precursors are distinguished: *Intrinsic* precursor states, which exist over unoccupied surface states and *extrinsic* precursor states over sites, that are already occupied by a chemisorbed species. As was already mentioned above, in the case of inhomogeneous surfaces as the AuPd(111) surface alloys, where the components are very different in their chemisorption behaviour, the weakly bonded chemisorbed state over the less reactive surface species can be considered as mobile precursor state in the temperature range where desorption from the chemically more active component occurs. Therefore, only the case of an intrinsic precursor will be discussed in the following. In fig. 5.11 an one-dimensional potential energy diagram for a non-dissociative chemisorption system with a single precursor state is shown. The symbols that are introduced in this figure are

A_s	chemisorbed state
A^*	precursor state
A_g	gas phase
E_a^*	activation energy for $A^* \rightarrow A_s$
E_d^*	activation energy for $A_s \rightarrow A^*$
E^*	activation energy for $A^* \rightarrow A_g$.

Desorption from the chemisorbed state A_s proceeds through the precursor state and can be described by

$$A_s \underset{k_a^*}{\overset{k_d^*}{\rightleftharpoons}} A^* \overset{k^*}{\rightharpoonup} A_g, \tag{5.4}$$

where k_d^*, k_a^*, and k^* denote the different rate coefficients, which can be written as

$$k_d^* = k_0^d \, e^{-\frac{E_d^*}{kT}} \tag{5.5}$$

$$k_a^* = k_0^a \, e^{-\frac{E_a^*}{kT}} \tag{5.6}$$

$$k^* = k_0^* \, e^{-\frac{E^*}{kT}} \; . \tag{5.7}$$

In the steady state approximation of θ^* (fractional coverage of molecules in the precursor state) being constant ($\frac{d\theta^*}{dt} = 0$) and small, which can be justified if k_a^* is sufficiently large, i. e., if $E_a^* \ll E_d^*$, and for a homogeneous chemisorption system with an intrinsic precursor state it follows for the desorption rate

$$r_d = \frac{k^* k_d^* \theta}{k^* + k_a^*(1-\theta)} \; .$$

The rate of re-trapping of molecules from the precursor state into the more strongly bonded chemisorbed state, is given by $k_a^*(1-\theta)$. In the case of the AuPd(111) surface alloys, where only the Pd sites are available for strong chemisorption, this expression has to be changed to $k_a^*(c_{Pd} - \theta)$ and the desorption rate results in

$$r_d = \frac{k^* k_d^* \theta}{k^* + k_a^*(c_{Pd} - \theta)} \tag{5.8}$$

with

c_{Pd}	concentration of Pd atoms in the surface layer

and

$\theta \leq c_{Pd}$	because CO is only stable on the Pd sites.

With the assumption of $k_a^* \, (c_{Pd} - \theta) \gg k^*$, equation 5.8 can be rewritten as

$$r_d = \frac{k^* k_d^*}{k_a^*} \, \frac{\theta}{c_{Pd} - \theta} \; . \tag{5.9}$$

It is obvious that this approximation fails in the limit of $\theta \rightarrow c_{Pd}$, which means that in TPD spectra from saturated CO layers equation 5.9 can only be applied after partial desorption of CO. By inserting the rate coefficients it follows from (5.9)

$$r_d = \frac{k_0^* k_0^d}{k_0^a} \, \frac{\theta}{c_{Pd} - \theta} \, e^{-\frac{E_d^* - E_a^* + E^*}{kT}} \; . \tag{5.10}$$

If this result is compared to the Polanyi-Wigner equation (5.2) the kinetic parameters $\tilde{\nu}$[11] and E_d can be identified as

$$\tilde{\nu} = \frac{k_0^* k_0^d}{k_0^a} \frac{1}{c_{Pd} - \theta} = \nu \frac{1}{c_{Pd} - \theta} \quad (5.11)$$

$$E_d = E_d^* - E_a^* + E^* \ . \quad (5.12)$$

The activation energy of the precursor mediated desorption process corresponds to the heat of adsorption, i. e., it is the same activation energy as in the case if no precursor state was present. The deviation from the standard Polanyi-Wigner approach manifests itself in a modified preexponential factor. The application of the TTPD method could still be justified, if only small initial coverages are taken into account, because then $\frac{1}{c_{Pd}-\theta}$ will be almost constant during the desorption of only a few percent of the molecules. However, the observed preexponential factor has to be reinterpreted as the product of three different preexponential factors, which belong to different processes, and the additional factor $\frac{1}{c_{Pd}-\theta}$ has to be accounted for.

Equation 5.10 together with (5.11) and (5.12) can readily be applied to extract the kinetic parameters ν and E_d from TPD spectra. For this purpose a computer program (EVALPREC.exe) was developed to convert the TPD raw data into an Arrhenius form. I. e., 1/T and $ln(r_d \cdot \frac{c_{Pd}-\theta}{\theta})$ are calculated at each point of the spectrum after subtraction of a linear background. If equation 5.10 was exactly valid, then the plot of $ln(r_d \cdot \frac{c_{Pd}-\theta}{\theta})$ vs. 1/T should give a straight line with slope $-E_d/k$ and intercept $ln(\nu)$. Due to the approximation step from (5.8) to (5.9) significant deviations from a straight line have to be expected for initial coverages close to saturation ($\theta_{\mathrm{CO}} \approx c_{Pd}$). In fig. 5.12 an example of the evaluation based on the precursor model is shown for a AuPd(111) surface alloy with ~2% Pd. Between 260 K and 310 K, all six curves with initial CO coverages below saturation are indeed reduced to a single straight line. This indicates that the applied method is valid in this temperature region. As expected, the evaluation based on the precursor model of a TPD spectrum that was taken from the saturated surface (curve g in fig. 5.12) leads to a strong deviation from the uniform course of the other data points. Also, for higher temperatures (T $\geq$ 310 K) a large scatter of the points has to be noticed. Since there is no correlation between the CO coverage and the direction of the latter deviations, this effect is probably due to a slightly incorrect determination of the actual coverage on the surface. For $\theta_{\mathrm{CO}} \rightarrow 0$ even small errors in θ_{CO} cause significant changes in $ln(r_d \cdot \frac{c_{Pd}-\theta}{\theta})$. Similar data sets as shown in fig. 5.12 have been obtained for surfaces with 4% and with 8% Pd, respectively. By linear regression of the straight sections of the plots values for ν and E_d have been derived. The results are collected in tab. 5.2.

[11]Here a differentation between the frequency factor as it appears in the Polanyi-Wigner equation ($\tilde{\nu}$) and the "real" frequency factor (ν) has to be introduced.

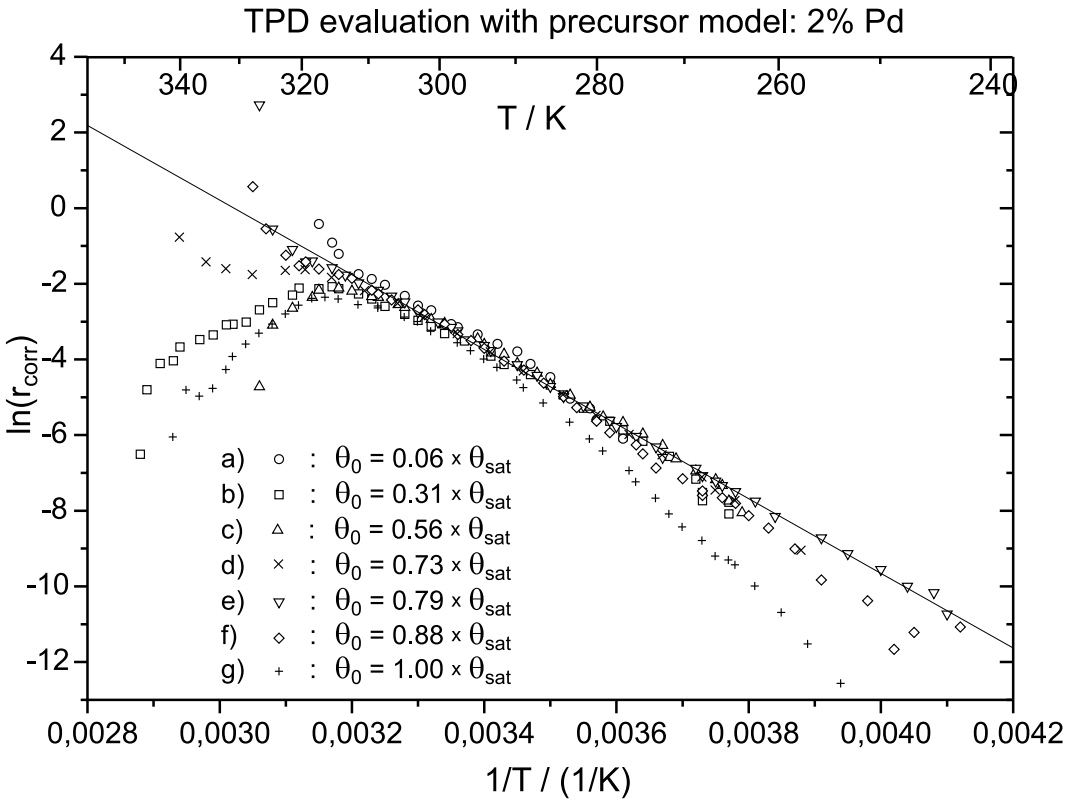

Figure 5.12: Example for the analysis of CO TPD spectra from an AuPd(111) surface alloy with $c_{Pd} \approx 2\%$ employing the precursor model. The corrected desorption rate r_{corr} was calculated by $r_{corr} = r_d \cdot \frac{c_{Pd}-\theta}{\theta}$ The line shows the result of a linear regression of the data points for $\theta_0 = 0.79 \cdot \theta_{sat}$.

The agreement between the different values for E_d and for $ln(\nu)$ is good ($\frac{\Delta E_d}{E_d} \leq 3\%; \frac{\Delta ln(\nu)}{ln(\nu)} \leq 4\%$), which is a necessary condition for the employed model to be correct. Since the comparison of data that were taken from different surface compositions and with different CO coverages shows this nice agreement, it can be inferred that the precursor model is able to account for the observed TPD peak shifts. To demonstrate this directly and to show the influence of the approximations that were made to derive the simple formula (5.10) for data evaluation, computer simulations have been performed using both the simple model (equation 5.9) and the more exact model (equation 5.8; for simplicity, this will be termed "exact model", which, of course, is not correct in a strict sense). The exact model contains the complete information on the desorption kinetics via an intrinsic precursor state and therefore four additional kinetic parameters have to

[13]It should be noted, that in these evaluations and in the following simulations the energies are given per molecule and not per mole in order to be consistent with the microscopy approach of the precursor model.

c_{Pd}	$E_d/10^{-19}$J	ν/s
2	1.36	$8.9 \cdot 10^{12}$
4	1.39	$1.4 \cdot 10^{13}$
8	1.40	$4.5 \cdot 10^{12}$

Table 5.2: Kinetic parameters for CO desorption from AuPd(111) surface alloys[13]. The values have been determined by evaluation of TPD spectra based on the precursor model. For details see text.

$E_d/10^{-19}$J	1.38
$E_d^*/10^{-19}$J	1.18
$E^*/10^{-19}$J	0.3
$E_a^*/10^{-19}$J	0.1
ν	$6.5 \cdot 10^{12} s^{-1}$

Table 5.3: Kinetic parameters for the CO TPD simulation shown in figs. 5.13 and 5.14 ("standard parameter set"). From the four energies only three can be varied independently, because of equation 5.12.

be inserted into the differential equation. At this stage, it is necessary to reduce the dimensionality of the parameter space. This can be achieved by setting the two preexponential factors that belong to CO molecules in the precursor state (k_0^* and k_0^a) to be equal, which seems to be a reasonable assumption. As a consequence, k_0^* can be factored out in the denominator of (5.8) and the expression can then be reduced by k_0^*. Therefore, only the preexponential factor that belongs to the strongly chemisorbed state remains. With these conversions, the differential equation for the exact model (5.8) can be rewritten as

$$r_d = k_0^d \, \frac{\theta \; e^{-\frac{E_d^* + E^*}{kT}}}{e^{-\frac{E^*}{kT}} + (c_{Pd} - \theta) \, e^{-\frac{E_a^*}{kT}}} \; . \tag{5.13}$$

Results of the simulations using the exact model are shown in fig. 5.13 for a AuPd(111) surface alloy with 2% Pd and in fig. 5.14 for Pd concentrations between 1% and 9%. The circles in the latter figure are examples of spectra that have been calculated based on the simple model. The input parameters for the exact model are listed in table 5.3. For the simple model the same E_d and ν values have been applied. The heat of adsorption, which is identical to E_d in the simple model, has been fixed at $1.38 \cdot 10^{-19}$ J for all simulations, since this value was experimentally determined (see table 5.2). Because of equation 5.12 only two of the three additional energy parameters of the exact model remain as independent quantities. The heat of adsorption on the Au terraces sites (E^*) has been estimated to one third of the value, that is reported for the CO adsorption energy at Au step edge sites ($\sim 0.9 \cdot 10^{-19}$ J; from the initial heat of

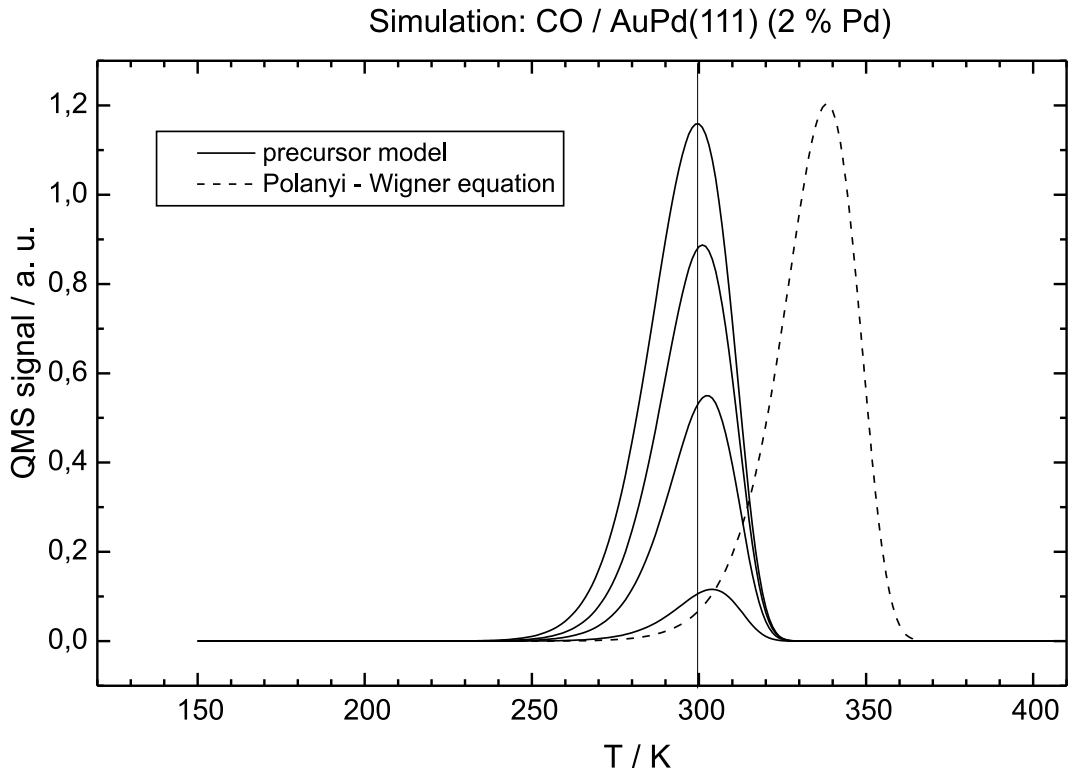

Figure 5.13: Simulation of CO TPD from a AuPd(111) surface alloy with $c_{Pd} = 2\%$. The initial CO coverages are 0.005 ML, 0.01 ML, 0.015 ML, and 0.02 ML. The vertical line at T=298 K is drawn to make the small θ_{CO} dependent peak shift more apparent. The kinetic parameters used for the simulations are listed in table 5.3. The spectrum drawn with a dashed line was calculated by inserting the same kinetic parameters into the Polanyi-Wigner equation (5.2).

adsorption measured by Ruggiero and Hollins for CO/Au(332)). The activation barrier for the transition from an Au site to a neighbouring Pd site (E_a^*) has to be selected with even less support from experiment. The value of $0.1 \cdot 10^{-19}$ J corresponds to about one third of the value, that was reported for CO diffusion on Pd(111) terraces [131]. The preexponential factor could have been taken from the experimental results. However, since these give values differing by a factor of three, which makes a difference in the peak temperature of about 7 K, the value of $6.5 \cdot 10^{12}\ s^{-1}$ has been determined to give the best accordance with experiment for an 4% Pd surface alloy[14] and was selected for the simulations. Since the choice of the values for E^* and E_a^* is based on crude estimates, the consequences of choosing an alternative set of activation energies have to be checked. For this purpose, simulations have been performed where one of the parameters E^* and

[14] Here, the surface with 4% Pd has been preferred as reference, because the STM characterization of this surface alloy is more reliable than the estimation of c_{Pd} for the 2% Pd surface.

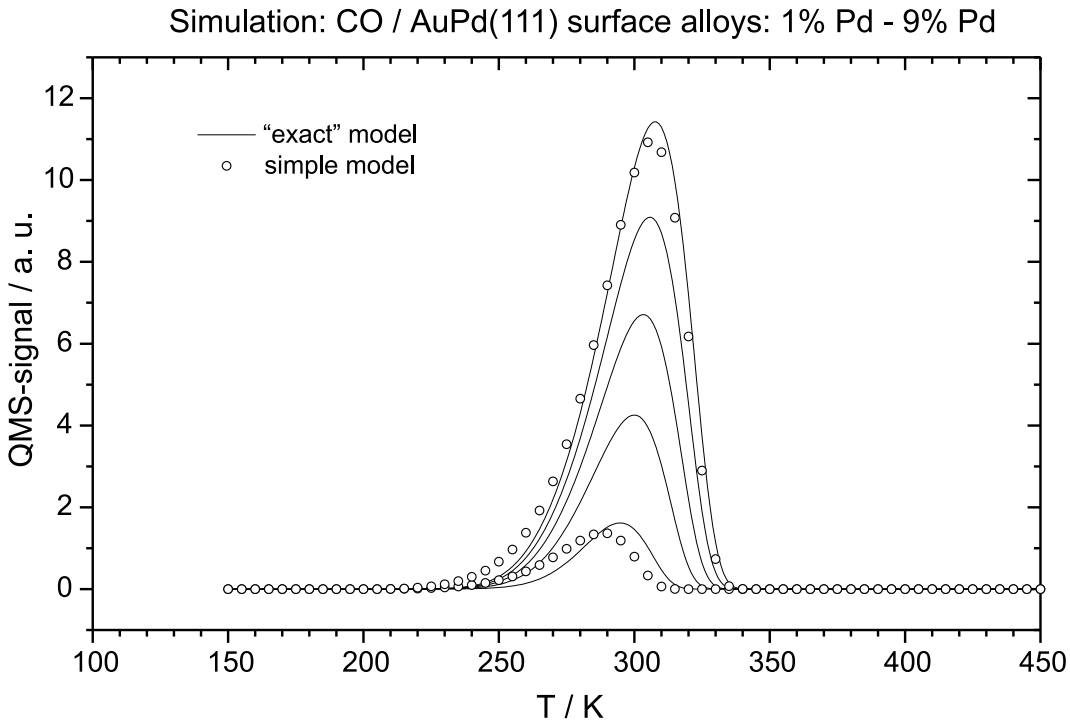

Figure 5.14: Simulation of CO TPD from CO saturated AuPd(111) surface alloys with c_{Pd} = 1%, 3%, 5%, 7%, and 9%. Two examples of TPD simulations using the simple model (5.10) are included in the figure. The kinetic parameters used for the simulations are listed in table 5.3.

E_a^* has been varied compared to the standard parameter set (see table 5.3). As result from this set of simulations, the peak positions of TPD spectra from CO saturated surfaces with varying Pd concentration have been evaluated, and they are displayed in fig. 5.15. The main purpose of this plot is to show, how the c_{Pd} dependent peak shift changes with varying activation energies. For the sake of clarity, only one parameter has been varied for each set of spectra with the consequence, that the absolute values of the peak positions are a few K off the experimental data points. This could have been corrected for by using an adjusted value for ν. Since a slight variation of ν was found not to change the magnitude of the peak shifts, it was preferred to hold ν constant during the simulations.

The results of the simulations can be summarized in the following points:

1. By comparing figs. 5.8 and 5.13 it is obvious that the precursor model is able to yield a negative θ_{CO} dependent peak shift of the correct magnitude. In the simulated spectra a shift of -4.5 K occurs between 0.5% ML and 2.0% ML CO, whereas in the experiment a shift of -5 K is observed between 0.7% ML and 2.2% ML[15].

[15]From the CO saturation coverage the Pd concentration of this surface was determined to

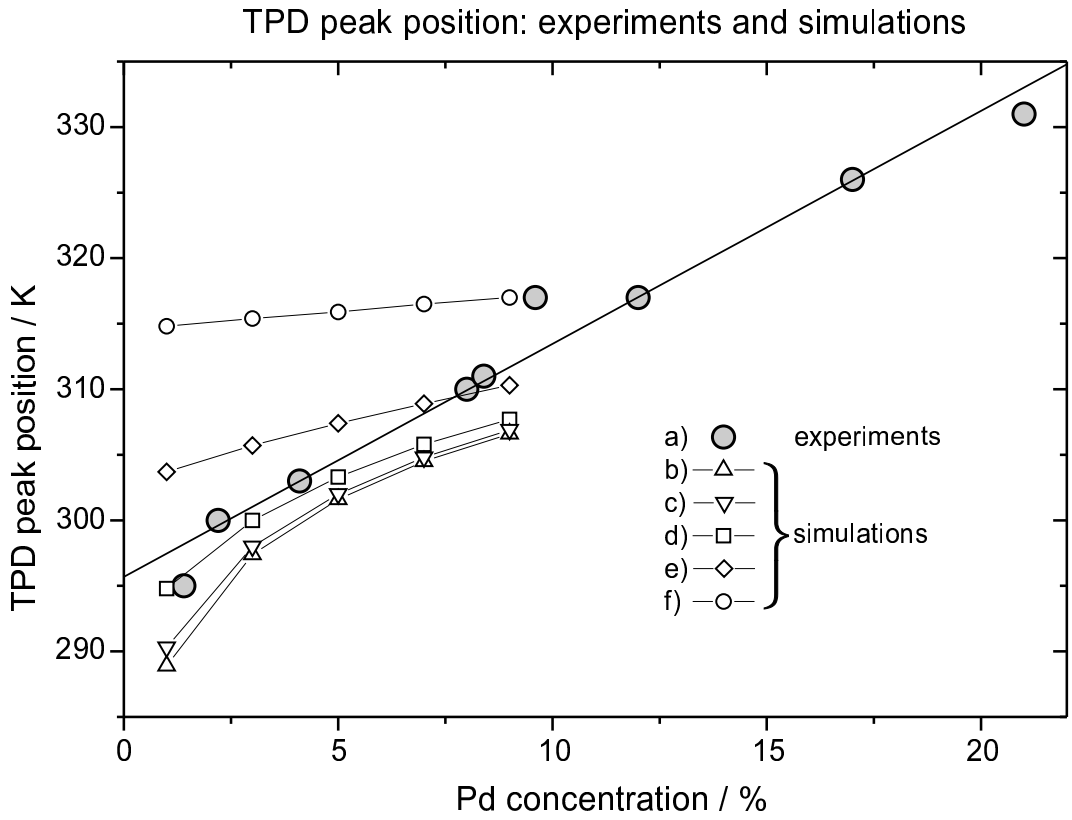

Figure 5.15: Comparison between simulations and experimental TPD peak positions from CO saturated AuPd(111) surface alloys with different Pd concentrations. The lines are merely drawn as guides for the eye. The kinetic parameters are given in table 5.4. Curve d corresponds to the results using the standard parameter set (table 5.3).

2. Also the c_{Pd} dependent peak shift is reproduced quite well if the standard set of kinetic parameters (table 5.3) is employed in the simulations (see curve d in fig. 5.15).

3. If the different activation energies of the exact model are varied around the standard values, both the peak positions and the magnitude of the c_{Pd} dependent peak shift change significantly (see fig. 5.15).

4. For relatively small deviations from the standard values for E^* and E_a^* (e. g., for the values displayed in table 5.4) it has been found that only the difference between these activation energies determines the appearance of the calculated spectra. This is equivalent to the statement, that for not too

be 2.2%, where the value of 2.0% is within the error bar. Therefore, this surface is referred to as surface alloy with 2% Pd.

curve in fig. 5.15	b	c	d	e	f
$E_d/10^{-19}$J	1.38				
$E_d^*/10^{-19}$J	1.08	1.13	1.18	1.23	1.28
$E^*/10^{-19}$J	0.4	0.3	0.3	0.3	0.2
$E_a^*/10^{-19}$J	0.1	0.05	0.1	0.15	0.1
ν	$6.5 \cdot 10^{12} s^{-1}$				

Table 5.4: Kinetic parameters for the simulations using variable activation energies. The value for E_d^* follows from the choice of the other three activation energies. The column for spectrum d contains the standard parameters.

exotic values of the kinetic parameters and for fixed E_d only the activation energy E_d^* for diffusion of CO from a Pd site to a neighbouring Au site is decisive for the desorption kinetics and not the adsorption energy on the Au sites itself. This is a consequence of the assumption of a negligibly small population of the precursor state, that has been made on page 165 (steady state assumption).

5. The experimentally observed c_{Pd} dependent TPD peak shift suggests a nearly linear correlation between the Pd concentration and the CO TPD peak position (fig. 5.15). However, it has to be noted that in the experiment already at $\sim 8\%$ Pd two additional types of CO adsorption sites are provided by Pd dimers. Hence, from the experimental data points in fig. 5.15 a linear dependence of T_p on the concentration of Pd *monomers* can not be inferred and the apparent discrepancy between the non-linearity of the simulated data points and the values taken from experiment might be due to the influence of larger Pd clusters.

6. If the standard kinetic parameters are employed for both models, the TPD peaks calculated for the simple model are shifted downward by a few K.

7. As saturation coverage is approached[16], the peak shape derived from the simple model changes markedly from rather symmetric to extremely asymmetric with a pronounced low temperature tail (see fig. 5.14). This discontinuity in peak shape is neither observed in the exact simulations nor in the experimental spectra. Obviously, it is an artefact that is caused by applying the simple model outside of its range of validity.

8. If E_d^* is chosen too large ($\geq 1.23 \cdot 10^{-19}$J), the magnitude of the peak shift becomes significantly smaller than the experimentally observed shifts. This behaviour can be explained qualitatively by the fact, that for $E_d^* \rightarrow E_d$ the

[16]Since equation 5.10 is not defined for $\theta_{\mathrm{CO}} = c_{Pd}$ the CO saturation coverage has been chosen as $0.999\, c_{Pd}$.

direct desorption from Pd sites becomes more important and the kinetic effects of the mobile precursor (e. g., the peak shifts) are diminished.

9. An increase in E^* to $0.4 \cdot 10^{-19}$ J ($E_a^* = const.$), which is equivalent to a decrease of E_d^* to $1.08 \cdot 10^{-19}$ J, is sufficient to eliminate the differences between calculations based on the simple model and calculations using the exact model. By inspection of equations 5.8 (exact model) and 5.9 (simple model) it becomes obvious that for small k^*, i. e., for relatively high values of E^*, the two models should yield nearly identical results. Since the peak shapes of the simple model were found not to agree with the measured spectra for CO coverages near saturation, it can be concluded that $E_d^* \geq 1.08 \cdot 10^{-19}$ J.

10. The peak widths (FWHM) of the simulated spectra agree quite well with experimental values, but the peak shapes of the simulations are somewhat too asymmetric. E. g., for the CO saturated surface with 2% Pd the FWHM of the measured TPD spectrum is 36 K (19 K on the low temperature side of the maximum and 17 K on the high temperature side) compared to 37 K (23 K / 14 K) from the simulations.The finite pumping speed inside of the QMS could be one reason for these deviations.

11. The presence of a mobile precursor state for desorption effectively lowers the desorption temperature. This effect is largest for low Pd concentrations and for 2% Pd it was found to amount to about 40 K (see fig. 5.13).

Based on the above listed observations it should now be discussed, what kind of additional information has been gained by the simulations. The finding that the precursor model is able to account for the observed peak shifts could be already inferred from the fact that an evaluation based on the precursor model can be applied successfully for different surface compositions and CO coverages. The justification for the usefulness of the simulations has to be sought in the possibility to gain some insight into the idealized one-dimensional potential energy curve (as sketched in fig. 5.11) for the CO/AuPd(111) system by employing the exact model in the calculations. From points 4 and 8 the value of $1.23 \cdot 10^{-19}$ J follows as upper limit for E_d^* (activation barrier for diffusion from a Pd monomer site to a neighbouring Au site). If E_d is set to $1.38 \cdot 10^{-19}$ J a lower limit of $0.15 \cdot 10^{-19}$ J (9 kJ mole^{-1}) — corresponding to a vanishingly small activation energy E_a^* for diffusion from a Au site to a Pd site — can then be deduced for the desorption activation energy from Au sites. On the other hand, a lower limit of $1.08 \cdot 10^{-19}$ J for E_d^* was determined from the observed changes in peak shape of the simulated spectra with decreasing E_d^* (point 9). If the CO diffusion barrier on Pd(111) ($0.28 \cdot 10^{-19}$ J) is taken as upper limit for E_a^*, it follows that $E^* \leq 0.58 \cdot 10^{-19}$ J (35 kJ mole^{-1}). In short, with E_d fixed at $1.38 \cdot 10^{-19}$ J, the following ranges for

E_d^* and E^* could be determined by the simulations:

$$\begin{aligned} 1.08 \cdot 10^{-19}\,\mathrm{J} &\leq E_d^* \leq 1.23 \cdot 10^{-19}\,\mathrm{J} \\ 0.15 \cdot 10^{-19}\,\mathrm{J} &\leq E^* \leq 0.58 \cdot 10^{-19}\,\mathrm{J} \end{aligned}$$

The simulations show also, that the employed precursor model is not able to reproduce all relevant features of the measured spectra. Especially the peak shapes do not fit very well. However, taking into account that certain simplifications have been made in the derivation of the rate equations for the precursor model, it cannot be expected to account perfectly for all observations. For instance, in the precursor model (fig. 5.11) it is assumed that a CO molecule after leaving a Pd site immediately encounters an "average environment" which is described by the Pd concentration and the actual CO coverage. In reality, it is possible for the CO molecule to return to the same Pd site, which of course increases the average probability of the CO molecules to be retrapped. This effect depends critically upon the exact potential energy surface around the Pd atoms. Since there is no information available about the latter, it was not attempted to account for these effects.

Up to now, the discussion of the CO desorption kinetics from AuPd(111) surface alloys was restricted to the simple case of a single type of relatively strong CO chemisorption sites, namely well-separated Pd monomers in a Au matrix. This situation is encountered in experiments on surfaces with less than 5% Pd atoms. For higher Pd concentrations first Pd dimer sites, then Pd trimer sites, and finally a broad variety of different Pd ensemble types have to be taken into account. As the preexponential factor generally depends on the nature of the adsorption site, the assumption of a single value for ν, which has been necessary for the derivation of the simple rate equations for the precursor model, can no longer be justified. A further complication arises from the fact that on Au-rich surfaces the CO saturation coverage increases almost linearly with the Pd content and therefore above a certain value of c_{Pd} also adsorbat–adsorbate interactions might play a role and could give rise to additional peak shifts in the TPD spectra. For these reasons, it was not attempted to evaluate or simulate spectra with features other than the Pd monomer peak ($T_p \approx 300\,\mathrm{K}$) within the framework of the precursor model. However, as has already been pointed out above, the TTPD method should give reliable results also on more complex surfaces, as long as only small initial CO coverages are considered. If $\theta_{CO} \ll c_{Pd}$, small changes in θ_{CO} will not have a large influence on the desorption rate (equation 5.10), which will be approximately proportional to the temperature dependent exponential function. Therefore, in an Arrhenius plot of TTPD data the slope should correspond to the activation energy for desorption from the energetically most favourable site.

In fig. 5.16 the results for E_d from a TTPD evaluation of low CO coverages on various AuPd(111) surface alloys are displayed. Since the dosing procedure was not exactly reproduced for each experiment, the CO coverages vary somehow

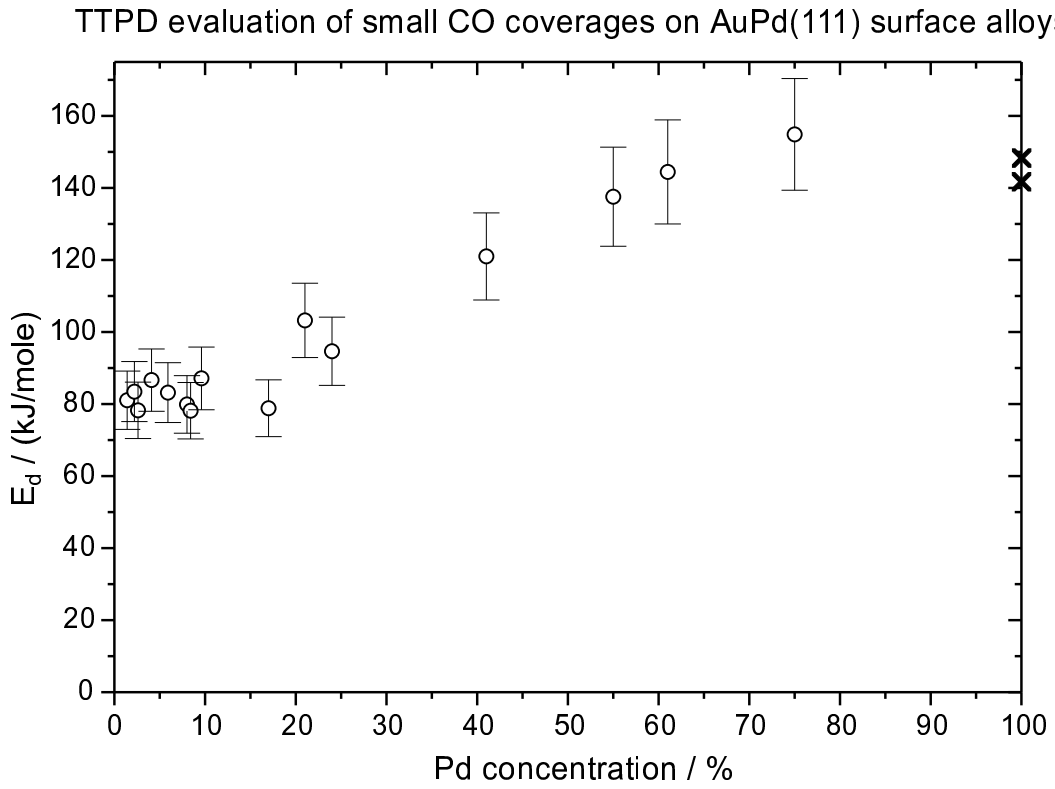

Figure 5.16: E_d for CO/AuPd(111) surface alloys evaluated by the TTPD method. The two crosses on the right y-axis are results for CO/Pd(111) from Ertl and Koch (isosteric heat of adsorption: 142 kJ/mole) and from Guo and Yates (148 kJ/mole by TTPD). An error bar of $\pm 10\%$ was determined to be adequate for the observed statistical deviations between different measurements.

across the data set of fig. 5.16. Also the subtraction of a linear background is a possible source of a statistical error. As a consequence of these deviations the threshold CO coverage, up to that the data points were included in the analysis, had to be determined individually for each spectrum. This was done by taking the set of data points from each spectrum that gave the best agreement with the expected straight line in an Arrhenius plot. In some cases it was possible to include values up to a temperature corresponding to desorption of 15% of the initial coverage in the analysis, but sometimes already after 3% desorption a significant deviation from linearity occured. A computer program (EVALTTPD.exe) was developed for the complete TTPD evaluation procedure including background subtraction and linear regression of the Arrhenius plots. A relatively large scatter of the data points was found for the TTPD determination of the preexponential factor. Since the latter is derived from the y-intercept of an Arrhenius plot, it is quite sensitive to possible errors caused by incorrect background subtraction. As a further complication, it has been found in the derivation of the precursor model

that the preexponential factor determined by a TTPD evaluation from a system with mobile precursor has to be interpreted with great care. For these reasons, the values for ν are not presented here.

The following results can be extracted from the collection of the TTPD evaluations (fig. 5.16):

1. Up to about 15% Pd the TTPD evaluation yields within the statistical scatter of the data points a constant activation energy for desorption of $(82 \pm 6)\,\mathrm{kJ\,mole^{-1}}$, which is identical to the value obtained by the analysis based on the precursor model for small Pd concentrations.

2. At $\sim 20\%$ Pd a first distinct increase of E_d to $(99 \pm 8)\,\mathrm{kJ\,mole^{-1}}$ is observed.

3. A further continuous increase of E_d occurs for Pd concentrations exceeding 20% and at $c_{Pd} \approx 75\%$ the value for pure Pd(111) has been reached[17].

As conclusion of this section on the quantitative evaluation of CO TPD spectra from AuPd(111) surface alloys, the above observations will shortly be discussed. As was anticipated already in the discussion of the precursor model on page 166, there is good agreement between the activation energies for desorption derived from an evaluation based on the precursor model and the values found by a TTPD analysis of small CO coverages. From the inspection of the TPD spectra that correspond to the data points in fig. 5.16 the CO species that is desorbing in the threshold region used for the TTPD evaluation can be identified. Up to 17% Pd, the dimer peak is sufficiently small to be saturated even for the lowest CO coverages that were used in these measurements. Hence, in the threshold region of the spectra only desorption of CO from monomer sites is to be expected. The initial plateau in fig. 5.16 shows that the adsorption energy of CO on Pd monomers does not depend significantly on the exact surface compositon. In other words, as long as Pd monomers are present on the surface, the CO–Pd monomer interaction is constant within the experimental accuracy and no evidence for any long range interactions, e. g., between CO and next nearest neighbour Pd atoms nor for an influence of second layer atoms is detected. The data points for 21% and 24% Pd are derived from spectra, where the Pd dimer peak has not been saturated. Therefore, the CO adsorption energy on the bridge site of the Pd dimers can be determined to be $(99 \pm 8)\,\mathrm{kJ\,mole^{-1}}$. The reason for the continuous increase of E_d above 24% Pd is less clear. While on the 41% Pd containing surface some desorption from dimer sites could still influence the TTPD evaluation and lead to a reduction of E_d compared to the value for trimer sites, for the higher Pd

[17] Unfortunately, relatively high CO coverages have been used in this work for TPD measurements on the pure Pd(111) surface. For $\theta_{\mathrm{CO}} = 0.16\,\mathrm{ML}$ E_d was determined to $128\,\mathrm{kJ\,mole^{-1}}$, which is significantly below the value measured for 75% Pd ($155\,\mathrm{kJ\,mole^{-1}}$), and might be already distorted by adsorbate–adsorbate interactions. Therefore, it is not included in the present considerations.

concentrations the Pd trimer peak is clearly not saturated at the low CO coverages used to derive the values of fig. 5.16. Consequently, these activation energies for desorption should correspond to the same type of adsorption site, i. e., to the Pd threefold hollow site, and should be more or less constant for $c_{Pd} \geq 50\%$. Two effects can be mentioned as possible reasons for the observed rather gradual approach of the E_d value for pure Pd(111). First, the TTPD evaluation is not exactly valid on AuPd(111) surface alloys due to the presence of a mobile precursor state, that has been discussed quite extensively above. Even though the influence of the precursor state can be assumed to be quite small in the threshold region of spectra obtained from small initial CO coverages, it can not be excluded that it is responsible for the relatively low E_d determined for intermediate Pd concentrations. Secondly, the above statement of the localized character of the CO–surface bond in the case of adsorption on Pd monomers could fail for adsorption in threefold hollow sites, because here atoms in the second layer clearly play a role — on pure Pd(111) only fcc sites, i. e., sites with no Pd atom directly underneath the threefold hollow site, are occupied at low CO coverages. On AuPd(111) alloys there are at least three different types of threefold hollow sites, even if only pure Pd surface ensembles are considered:

- Fcc sites, that correspond to the most favourable CO adsorption site on the pure Pd(111) surface. In this case, one can assume the influence of the three second layer atoms that are underneath the surface trimer to be very small due to the relatively large separation of the adsorbate from these atoms. If the second layer atoms played a role also for fcc sites, four additional types of ensembles could be distinguished with none, one, two, or three Pd atoms below the Pd surface trimer.

- Hcp sites with a Pd atom in the second layer directly below the threefold hollow site.

- Hcp sites with a Au atom in the second layer.

In the TPD spectra there is no indication for a significant difference in CO adsorption energy on these different types of threefold hollow sites. However, the TTPD evaluation might be more sensitive to small energy differences and could result in the observed lower E_d values for the bimetallic surfaces compared to the clean Pd(111) crystal due to a continuously changing mixture of the above mentioned different types of threefold hollow sites.

Concluding this section, the activation energies for desorption from three different CO adsorption sites on AuPd(111) surface alloys are summarized in the following table:

adsorption site	$E_d/10^{-19}$J	E_d/kJ mole^{-1}
Pd monomer	1.36 ± 0.1	82 ± 6
Pd dimer	1.64 ± 0.13	99 ± 8
Pd trimer (fcc)	2.41 ± 0.08	145 ± 5

Table 5.5: Activation energies for CO desorption from different Pd sites on AuPd(111) surface alloys. The Pd monomer value is obtained both by a TTPD analysis and by the analysis using the precursor model (vide supra). For Pd dimers only the TTPD method could be applied. The value for Pd trimers is taken from the literature on CO adsorption on Pd(111) [119, 129]. These results are only valid for small CO coverages.

5.3 HREELS results for CO adsorption on Au-Pd(111) surfaces

HREELS measurements on the CO/Au-Pd(111) adsorbate system have been performed using similar preparation procedures of the bimetallic surfaces as for the TPD experiments (vide supra). Hence, it is appropriate to devide this section into the same subsections as in the case of the TPD measurements. These subsections treat CO adsorption first on the pure Pd(111) surface, second on layered Au/Pd(111) surfaces, and third on AuPd(111) surface alloys. It should be noted that the TPD experiments were only possible in the last part of the experimental work for this thesis and therefore the vibrational spectroscopic investigations were performed prior to the TPD measurements, although in this presentation of the experimental data, the TPD results preceed this part on HREELS measurements. For this reason, some HREELS experiments might have been performed differently, if the TPD results had been known earlier.

5.3.1 CO adsorption on Pd(111)

The vibrational properties of the CO/Pd(111) adsorption system have already been characterized quite extensively by infrared spectroscopy (IRAS, [122–125, 130] and by sum frequency generation (SFG, [130]). Since the optical techniques allow higher resolutions than HREELS and are therefore better suited for detailed investigations of peak positions and shapes, not much emphasis has been put in this work on CO adsorption measurements on the pure Pd(111) surface. The main purpose of the following experiments was to provide reference data for the subsequently performed measurements on bimetallic Au-Pd(111) surfaces. As was pointed out in the above section on CO-TPD measurements on Pd(111), H_2 coadsorption from the residual gas might influence the CO adsorption properties tremendously. Therefore, it is necessary to compare the HREEL spectra of the bimetallic surfaces with reference spectra of the pure Pd surface, that were taken

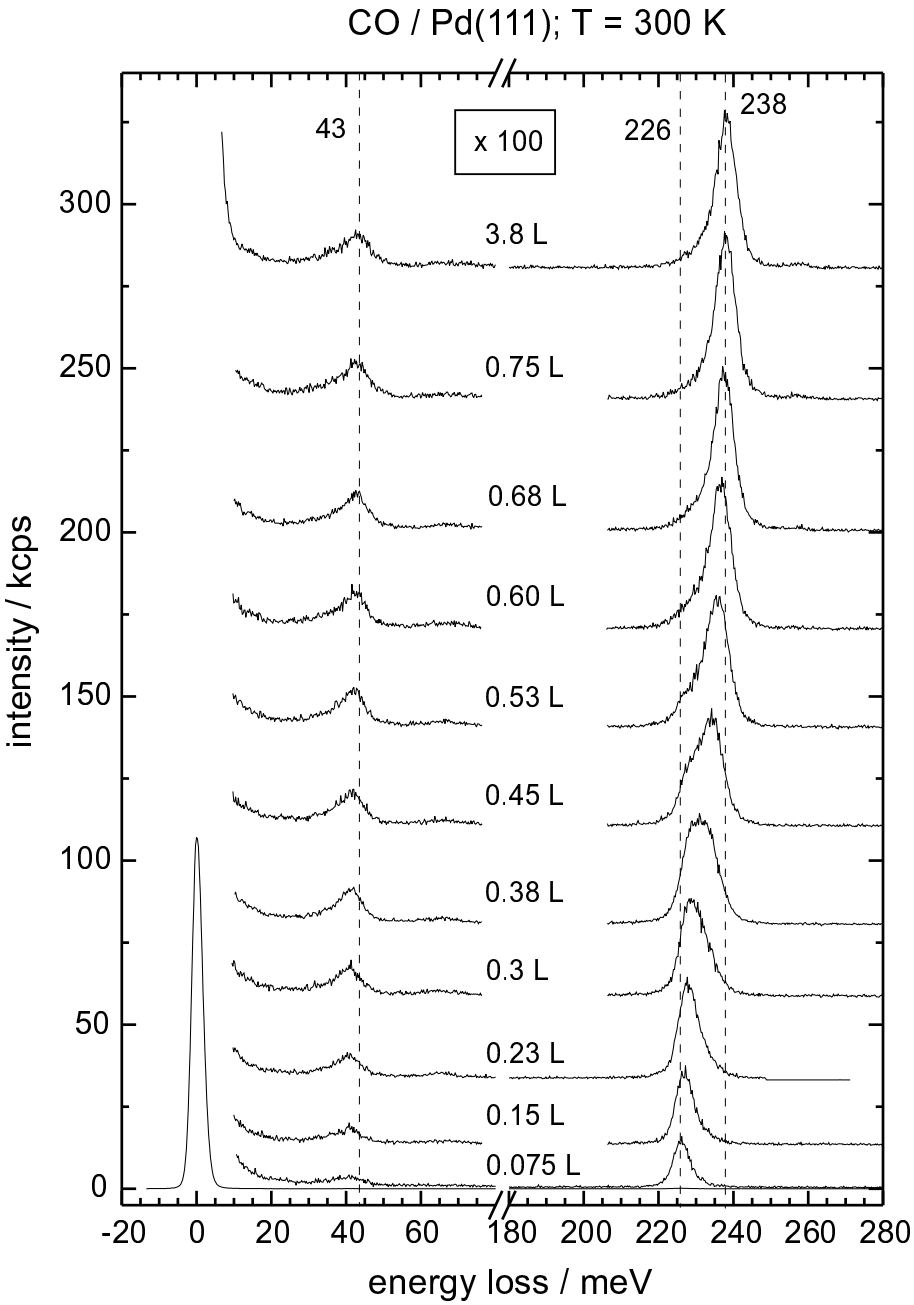

Figure 5.17: HREEL spectra of CO adsorbed on Pd(111) at 300 K. The CO doses are given in the figure. All spectra are normalized to equal height of the elastic peak; $E_p = 6\,eV$.

as far as possible under identical experimental conditions.

In figs. 5.17 and 5.18 HREELS results for CO adsorption on Pd(111) at 300 K and 100 K, respectively, are displayed. CO was accumulated on the surface and the total doses are given in the figures. Since at low temperatures this procedure inevitably leads to coadsorption of H_2 and to partial inhibition of CO adsorption, spectrum h has been included in fig. 5.18 to show a truely CO saturated Pd(111) surface. The dosing procedure for this spectrum will be explained below. In the spectra taken at 300 K two peaks can be distinguished: the Pd–CO stretching peak around 40 meV and the C–O stretching peak in the region around 230 meV. Both peaks shift to higher energies with increasing CO coverage. While for the C–O stretching peak this shift is quite substantial (from 226 meV to 238 meV), in the case of the low energy peak only a small shift of about 3 meV is observed. Above a CO dose of 0.68 L no further changes are observed in the spectra upon increasing the dosage. Both the C–O stretching peak positions and the broadening of this peak for intermediate CO doses correspond well with IR spectra reported by Bradshaw and Hoffmann [121] at 300 K. They determined the CO saturation coverage on Pd(111) at 300 K to be 0.5 ML under UHV conditions. Although at 300 K no sharp LEED pattern is obtained for this coverage, the local CO structure most likely corresponds to a $c(4 \times 2)$ superstructure, that is observed more clearly at a somewhat lower substrate temperature (200 K [126]). A structure determination of this CO structure by photoelectron diffraction showed, that the CO molecules occupy a 1:1 mixture of fcc and hcp threefold hollow sites. From this it follows that the CO coverage dependent peak shift observed in fig. 5.17 is due to adsorbate–adsorbate interactions rather than to a change of the bonding configuration from threefold-hollow sites to bridge sites, as was assumed in earlier publications [121, 124]. In a recent theoretical study using a coverage-dependent periodic DFT approach, Loffreda et al. have shown that the observed frequency shift between 0.33 ML and 0.5 ML is fully compatible with the occupation of only hollow sites [128].

CO adsorption at 100 K results in spectra with additional features. For low CO doses, the behaviour is essentially identical to CO adsorption at 300 K. For CO doses above 0.3 L the C–O stretching peak is split into two components, where the higher energy component shifts to 240 meV for 0.75 L. Two very small peaks can be recognized at 259 meV and at 267 meV, respectively, for a CO dose exceeding 0.6 L. The nature of the CO species giving rise to the latter frequency, that is significantly *above* the gas phase value of 265.7 meV, will be discussed below. After a short flash to 300 K (spectrum g) a spectrum is obtained that is almost identical to the spectrum for CO saturation coverages at 300 K and the two small high energy features at 259 meV and at 267 meV have disappeared. It was already mentioned above that the gradual accumulation of CO on the surface and the concomitant relatively long exposure of the sample to the residual gas might result in partial inhibition of CO adsorption due to hydrogen preadsorption.

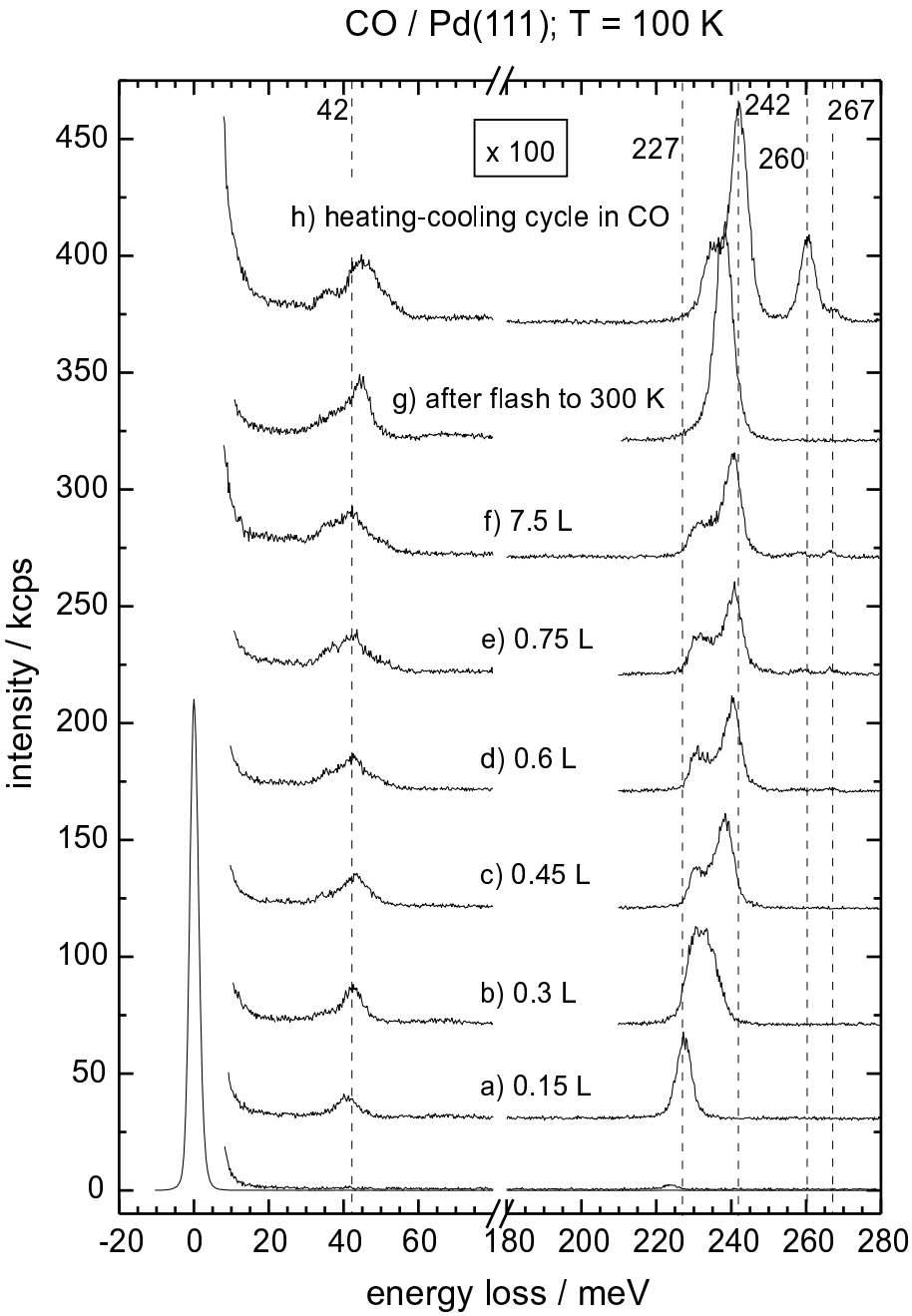

Figure 5.18: HREEL spectra of CO adsorbed on Pd(111) at 100 K. The total CO doses are given in the figure. All spectra are normalized to equal height of the elastic peak; $E_p = 6\,eV$.

In order to avoid this distortion of the CO adsorption properties, spectrum h was recorded after a heating-cooling cycle (100 K → 300 K → 150 K) of the surface in the presence of $2 \cdot 10^{-8}$ mbar CO. This procedure ensures that hydrogen atoms that are possibly adsorbed on the surface are removed — probably by diffusion to subsurface sites — and the complete surface area is available for CO adsorption. The resulting HREEL spectrum shows the following differences compared to direct adsorption at 100 K:

- The peak intensities are increased for both the Pd–CO stretching peaks and the C–O stretching peaks.
- The major component of the Pd–CO peak is shifted from 42 meV to 45 meV.
- The two strong features in the C–O region show also a small positive shift of about 2 meV.
- An additional strong peak at 260 meV appears.
- The peak at 260 meV exhibits a distinct shoulder at 267 meV.

Kuhn et al. report similar changes in IR spectra for CO/Pd(111) if low temperature adsorption is compared with adsorption during an annealing-recooling cycle (90 K → 200 K → 90 K) in $1.33 \cdot 10^{-6}$ mbar CO [124]. In the first case they observed a single broad band centered at about 237 meV. This band splits into two components at 235 meV and at 241 meV after heating to 200 K and recooling in the CO atmosphere. The latter procedure gives rise to two additional high energy components at 261.6 meV and at 267.5 meV, respectively. The small deviations in the peak positions if the results of Kuhn et al. are compared with the HREELS measurement shown in fig. 5.18 can be explained by differences in the adsorption conditions (90 K vs. 100 K and the presence of gas phase CO during the IR measurements). Interestingly, Kuhn et al. report also TPD measurement following both adsorption conditions. In the case of direct adsorption at 90 K there is a similar depletion of low temperature CO desorption states as was observed in the TPD measurements discussed in section 5.2.1. Here, it was shown that coadsorption of H_2 from the residual gas is able to inhibit CO adsorption at low temperatures. It is most likely that Kuhn et al. suffered the same H_2 coadsorption effect. The alternative explanation that they give — namely the formation of a highly disordered adsorbate structure at 90 K with a significantly reduced CO saturation coverage — can already be disproved by their own measurements. If a CO saturation exposure at 90 K gives rise to TPD desorption states only above 290 K even though in principle lower temperature desorption states are available on the surface, it is necessary either to assume the coadsorption of a species that desorbes already at the initial temperature increase of the TPD heating ramp or to suppose a thermal equilibration process starting at temperatures only a few

K above the adsorption temperature (90 K). Since the latter possibility has to be excluded based on the observation of Kuhn et al. that annealing in UHV of a CO covered surface to 200 K does *not* result in significant changes of the IR spectra [124], only the explanation based on coadsorption from the residual gas remains. Another, independent argument against the equilibration model can be derived from a comparison with TPD data for CO adsorption on Pd(111) at 87 K reported by Guo and Yates [129], because they find an onset temperature of CO desorption for the saturated surface that is about 100 K below the value observed by Kuhn et al.. Such discrepancies have to be expected in the case of a considerable influence of coadsorption from the residual gas, because the H_2 partial pressure and the time for cooling the sample certainly deviate substantially between different laboratories. Finally, it should be noted that in earlier IRAS measurements by Ortega on CO/Pd(111) at 90 K four features are detected in the presence of $1.33 \cdot 10^{-8}$ mbar CO [122]: 235 meV, 243 meV, 247 meV, and 260 meV. I. e., there is again a significant deviation from the spectra reported by Kuhn et al.. Since the spectra in the work of Ortega are only reported for vibrational energies below 266 meV no statement is possible on the occurence of the high energy component at 267 meV. The comparison of IR spectra for identical CO coverages at different adsorption temperatures reported by Ortega is of higher relevance for the present discussion. In short, he notices a continuous broadening of the band if the temperature is increased from 90 K via 200 K to 300 K. This can be explained by assuming *better* ordering at *lower* temperatures, which is corroborated by the observation of sharper LEED patterns at lower temperatures. It is obvious that the latter observations cannot be reconciled with the assumption of a highly disordered and therefore less densely packed CO layer at 90 K as proposed by Kuhn et al..

Having shown, that CO adsorption measurements on Pd(111) at $T \leq 150$ K have to be interpreted with great care, it can be stated that for CO adsorption at 200 K or during a heating-cooling cycle to $T \geq 200$ K the influence of coadsorption from the residual gas seems to be negligible. This is supported by the above mentioned close agreement between vibrational spectra from different laboratories for similarly annealed Pd(111) surfaces. Therefore, the surprising observation of a C–O stretching frequency at 267 meV, that is above the value observed for gaseous CO (265.7 meV), cannot be considered a priori to be an artefact caused by the residual gas. Bourguignon et al. proposed in a recent IRAS study a model, where this peak is caused by CO molecules adsorbed at domain boundaries that exhibit a high local CO coverage [130]. In this model, small domains of CO are formed at low substrate temperatures and an appreciable amount of adsorption sites at the domain boundaries are available. In a two step annealing-cooling experiment in CO atmosphere (190 K $\rightarrow$ 230 K $\rightarrow$ 195 K $\rightarrow$ 330 K $\rightarrow$ 205 K in 10^{-7} mbar CO) they observed partial desorption from these sites at temperatures above 205 K and their repopulation during the first recooling step. After heating

the CO covered sample to 330 K the sites themselves have been eliminated and no high energy peak appears upon recooling in CO to 205 K. The latter fact can be explained by reordering and coalescence of antiphase domains at temperatures above 300 K and the elimination of domain boundaries. Again, the explanation is based on the assumption of poorer adsorbate ordering at lower temperatures, which seems to be quite questionable if the IR and LEED observations of Ortega are taken into account [122]. Therefore, also in this case an influence of a hydrogen coadsorbate, possibly on subsurface sites, has to be considered as an alternative explanation.

Even though the HREELS measurements displayed in fig. 5.18 can certainly not resolve the open questions regarding the low temperature CO adsorption on Pd(111), it has been found necessary to discuss the obvious discrepancies that are encountered if measurements of different groups are compared and to emphasize the possible influence of H_2 coadsorption. It should be pointed out, that a systematic investigation on the role of H_2 seems to be a prerequisite for a further understanding of CO adsorption on Pd(111) below 200 K and possibly also on other Pd surfaces.

5.3.2 CO adsorption on layered Au/Pd(111) surfaces

In this section, HREELS experiments will be presented, that are performed on layered Au/Pd(111) surfaces, i. e., on surfaces, where each crystal layer consists of only one element. These are prepared by Au deposition below 400 K, in order to avoid Au-Pd intermixing. Since for submonolayer Au coverages CO adsorption on free Pd sites is giving rise to additional peaks in the HREEL spectra compared to spectra from completely Au covered surfaces, the former case will be discussed after the straightforward interpretation of the vibrational properties of CO that is exclusively adsorbed on Au sites.

CO adsorption on completely Au covered Pd(111)

In order to investigate the role of Au defect sites (step edges, kinks) for CO adsorption, completely Au covered surfaces have been prepared with different morphologies. In a first set of experiments, 1.5 ML Au have been deposited at 320 K resulting in the surface structure shown in the STM image of fig. 5.19(a). Second layer Au islands are the dominant structural features of this surface. The island edges are rather straight and the diameter of the islands vary between 50 Å and 500 Å. Approximately 2% of the surface is covered by third layer Au atoms and the proportion of uncovered Pd(111) can be estimated to be below 1%. Due to the relatively large island sizes and the straight island edges, the fraction of Au island edge atoms is small ($\sim$ 1%). In a second deposition step, 0.25 ML Au have been added to this surface at 110 K. An STM image of the drastically

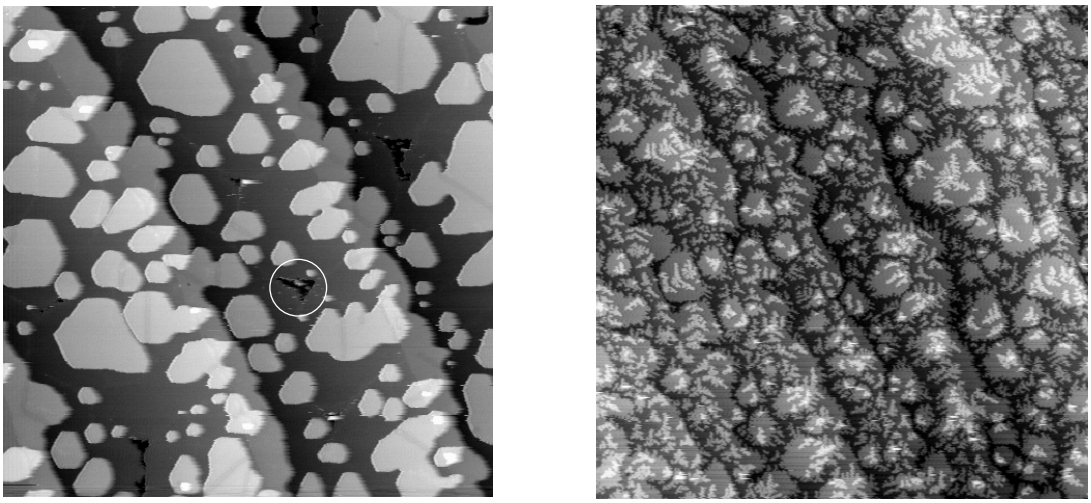

(a) after the first Au deposition step

(b) after the second Au deposition step

Figure 5.19: STM images of 1.3 ML Au deposited at 320 K on Pd(111) (a) and of additional 0.25 ML deposited at 110 K on the same surface (b). The white circle in (a) marks a hole in the first Au layer. Image sizes: 3400 Å × 3400 Å.

changed surface morphology is displayed in fig. 5.19(b). The previously rather smooth Au-covered surface now exhibits a large number of ramified second and third layer Au islands, with an average diameter of 80 Å and an average branch thickness below 30 Å, together with Au arms growing off the Au island edges that stem from the first deposition step. From both the increase in island density and the ramified shape of the low-temperature-grown island and arm structures, the density of island edge atoms increased significantly, and can be estimated to amount to $\sim 5\%$ of the total surface atoms.

Low temperature CO adsorption after each Au deposition step has been characterized by HREELS. The results are displayed in fig. 5.20. Spectra a and b were recorded on the surface covered by 1.5 ML Au prior to the STM measurements (STM: fig. 5.19(a)). On the clean bimetallic surface, before CO exposure, the HREEL spectrum (spectrum a in fig. 5.20) shows no significant loss signal, indicating that this surface is free of adsorbates. The surface, however, is not completely inert towards CO adsorption, which can be seen from the two peaks at 35 meV and at 263 meV after a CO dose of 0.7 L. These peaks arise from the Au–CO and the C–O stretching vibrations, respectively. After the second Au deposition step, the C–O peak intensity is approximately doubled because of CO adsorption from the residual gas. Assuming that after the first CO dose the surface was saturated (spectrum b), this implies that the activity for CO adsorption

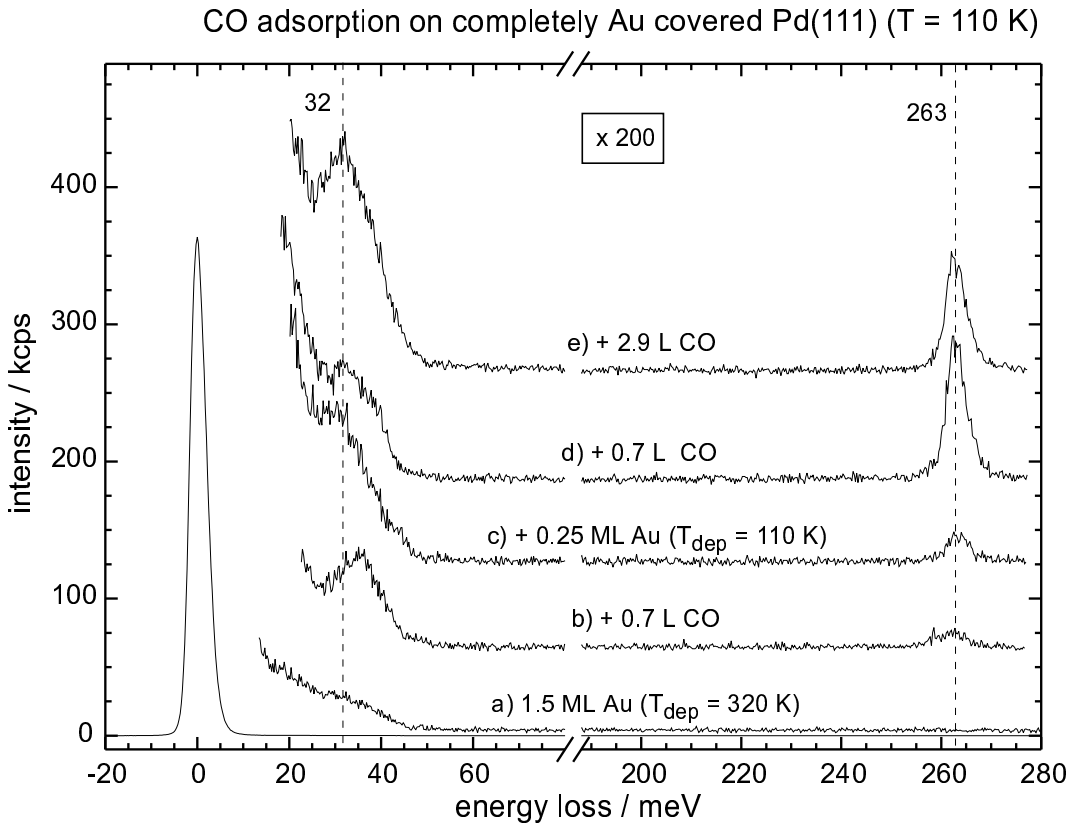

Figure 5.20: HREEL spectra of CO adsorbed on completely Au covered Pd(111) at 110 K. The film preparation and dosing sequence is indicated in the figure. STM images from the two Au films are shown in fig. 5.19. All spectra are normalized to equal height of the elastic peak; $E_p = 6\,eV$.

is increased by the second Au evaporation step. This idea is confirmed by the next CO exposure of 0.7 L (spectrum d), which leads to a strong increase in the intensity of the 263 meV peak, by about a factor of 10. Hence, the number of sites allowing CO adsorption at 110 K must have been drastically increased by adding 0.25 ML of Au at low temperatures to the Au covered Pd(111) surface. The constant frequency of this peak furthermore indicates that the nature of the adsorption complex was not altered by the second Au deposition. From these results and from the fact that the only major morphological difference between the two surfaces in question consists in different amounts of Au island edge atoms, it can be inferred that the CO molecules giving rise to the peak at 263 meV are bound to Au atoms at second and third layer island edges. After 0.7 L the surface is practically saturated and further CO exposure (2.9 L, spectrum e) causes no significant changes. It should be noted that the intensity of the Au–CO stretching peak exhibits no clear correlation neither with the intensity of the C–O peak

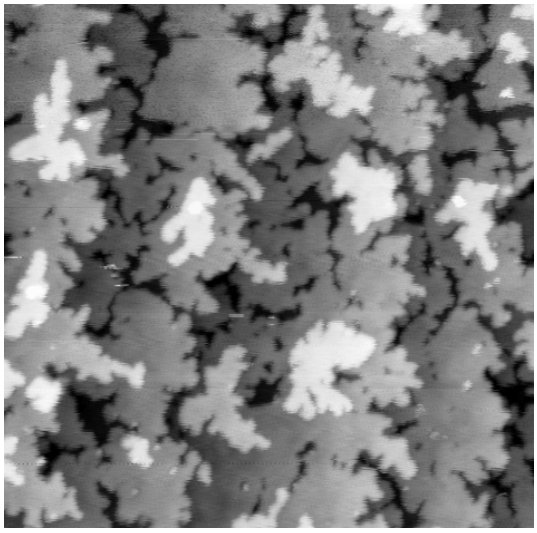

Figure 5.21: STM image of 4.2 ML Au deposited at 166 K on Pd(111). Image size: 845 Å × 845 Å.

nor with the preparation conditions. This might be due to the overlapping of the former peak with the tail of the elastic peak, that was rather asymmetric during these measurements.

A second combined STM and HREELS experiment on a thicker Au film (4.2 ML deposited at 166 K) is documented by figs. 5.21 (STM) and 5.22 (HREELS). At a Au film thickness of more than 4 layers, the influence of the Pd(111) substrate should be further reduced compared to the above experiments. The deposition temperature of 166 K was chosen in order to ensure a relatively flat surface morphology together with a high amount of Au edge sites. An inspection of the STM image in fig. 5.21 reveals that only three Au layers are exposed. These correspond to local Au film thicknesses of 3 to 5 ML[18]. Also the island edges are found to be irregularly shaped, which results in a relatively large ratio of Au edge atoms to Au terrace atoms. HREELS measurements on this surface are shown in fig. 5.22. Due to a large high energy tail of the elastic peak, that might be the consequence of the rough surface morphology, the Au–CO stretching vibration is not detectable in these spectra. A distinct C–O peak is found at 263 meV, which is, within the experimental accuracy, the same position as observed on the Au film with only 1.75 ML total Au coverage, where it was shown to be caused by CO on Au edge sites. Therefore, it seems to be plausible to explain this feature also by CO adsorbed on Au edge sites. A successive increase of the total CO dose shows that already after 0.14 L saturation is achieved. Therefore, the CO sticking coefficient is not proportional to the available adsorption sites, which is a

[18] Some tiny sixth layer island can also be detected but their total area is too small to play a role in the area integrating adsorption experiments.

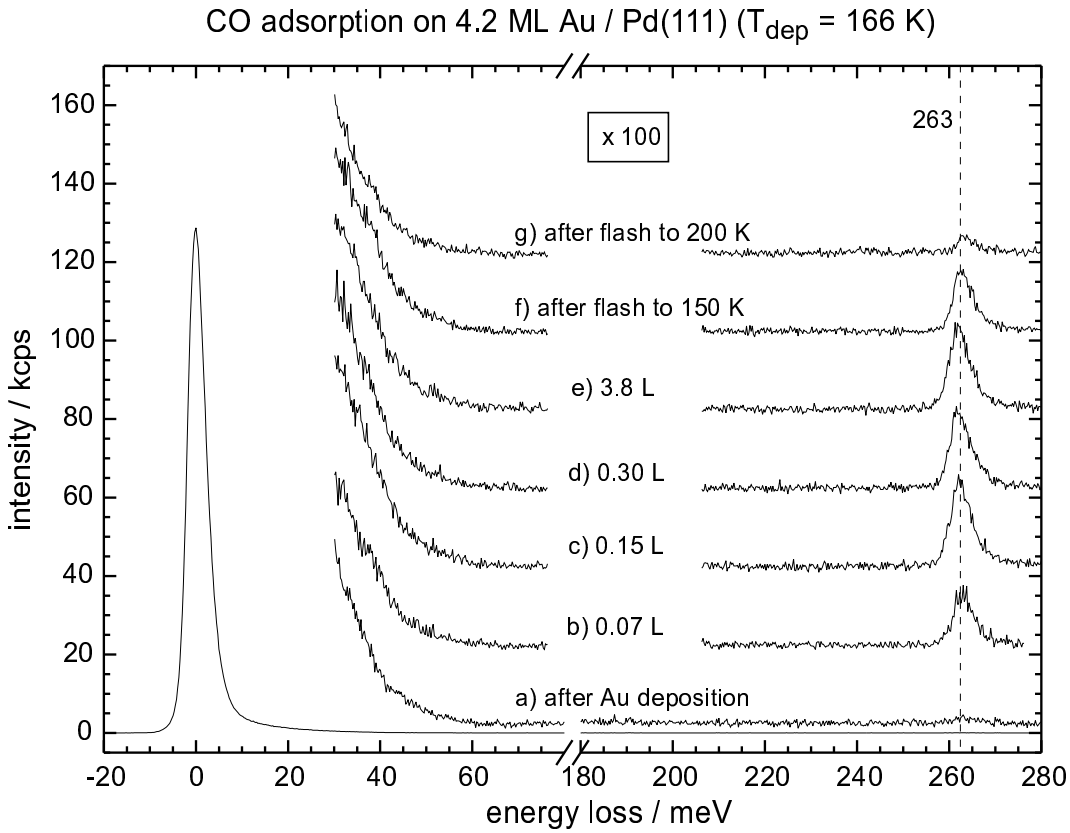

Figure 5.22: HREEL spectra of CO adsorbed on 4.2 ML Au/Pd(111) (T_{dep} = 166 K): (a – e) increasing CO exposures at 110 K with the total exposures given in the labels; (f, g) spectra after short annealing to the indicated temperatures and subsequent recooling to ∼110 K. All spectra are normalized to equal height of the elastic peak; E_p = 6 eV.

clear indication for the presence of a mobile CO precursor state on the Au terrace sites. The thermal stability of the CO species at Au edge sites has been tested by shortly annealing the CO covered surface at 150 K and at 200 K, respectively. Already after the first heating step an appreciable decrease of the C–O peak intensity is observed and almost complete desorption of CO occurs during the second heating step. In the latter case not only CO desorption from the Au edge sites has to be considered but also irreversible changes in the surface morphology, because 200 K is above the film preparation temperature (166 K).

In section 5.1.2 a review on previous investigations of CO adsorption on different Au surfaces has been presented. Several examples for IR studies on the CO/Au adsorption system have been cited. It is interesting to note that in all of these experiments the C–O stretching frequency was reported in the range from 262.2 meV for evaporated Au films and relatively high CO pressures [155] to

263.9 meV for silica-supported Au particles [159]. Since the C–O peak positions detected by HREELS in figs. 5.20 and 5.22 fall within this range, it can be concluded that only the immediate environment of the surface Au atoms (e. g., the number of nearest neighbour metal atoms) influence the vibrational properties of the CO-Au surface complex and longer range interactions, e. g., with the support in the case of dispersed Au particles or with the Pd(111) substrate in the present case play no significant role.

Concerning the HREELS results from CO adsorbed on completely Au covered Pd(111) the following points can be concluded:

- A comparison of experiments on Au covered Pd(111) surfaces with different proportions of Au edge sites gives clear evidence for the occupation of Au step edge sites by CO at T $\approx$ 110 K.
- The frequency of the C–O stretching vibration for molecules adsorbed at Au step edges is found at 263 meV, while the Au–CO stretching vibration is located around 35 meV.
- From the high vibrational energy of the C–O stretching vibration it can be inferred that the molecules are bonded in a linear ("on-top") configuration to the Au step edge atoms.
- There is close agreement in the C–O stretching frequencies if different CO-Au adsorption systems are compared. All of these vibrational energies are located in an intervall of only 2 meV around the value observed for the CO/Au/Pd(111) system.
- The local Au film thickness has no measurable effect on the C–O peak position.
- CO adsorbed on Au step edges is weakly bonded and desorbes below 200 K.

CO adsorption on partially Au covered Pd(111)

Having demonstrated that on Au/Pd(111) surfaces, where the topmost crystal layer consists of only Au atoms, Au step edge atoms are active sites for CO adsorption, we now turn to the situation, where a second chemical component (i. e., Pd substrate atoms) is present on the surface. Here again a comparison of surfaces with different well-characterized structures is employed to interpret the CO adsorption behaviour. In fig. 5.23 HREELS measurements on six different Au/Pd(111) and Pd(111) surfaces are displayed. Concering the CO doses for the different spectra in fig. 5.23 it should be noted that they were chosen such that no significant change in the spectra was observed upon further CO dosing. As was pointed out above, in the sections on TPD and HREELS measurements for

CO adsorption on Pd(111) at low temperatures, the maximum CO coverage on Pd(111) depends sensitively on the dosing procedure, i. e., on the extent of H_2 coadsorption from the residual gas. Especially for spectrum d, where between Au deposition and CO adsorption the sample could not be annealed above the film preparation temperature to remove possible coadsorbates, it has to be taken into account that an appreciable amount of H_2 is coadsorbed on the free Pd areas. Therefore, the HREELS peak positions and peak shapes of CO adsorbed on Pd sites might deviate from the respective values on a clean Pd(111) surface without being caused by the presence of Au islands. However, an influence of this coadsorbate on the CO adsorption properties of Au sites seems to be unlikely and no indication for such an effect was provided by the experiments.

Besides a reference spectrum for CO adsorbed on Pd(111) after the standard crystal preparation procedure (spectrum a) an additional spectrum (f) on pure Pd(111) is included in fig. 5.23, where the surface has been mildly sputtered by Ar^+ ions (1 keV, dosis: $3.9 \cdot 10^{14}$ ions cm^{-2}, 300 K) in order to investigate the influence of Pd step edges on the vibrational spectrum of adsorbed CO. An STM image of the sputtered surface is shown in fig. 5.24. It can be seen that after the above described sputter step four crystal layers are open on former flat terraces. The hole and island structures have a typical size of about 30 Å. If the average terrace width is assumed to be in the range of a few hundred Å, it can be estimated that the number of Pd step edge atoms is enlarged by about an order of magnitude due to the sputtering process. Approximately 10% of the surface atoms are located at step edges on the sputtered surface displayed in fig. 5.24.

The Au/Pd(111) surfaces, that were used as substrates for the HREELS CO adsorption measurements in fig. 5.23 can be devided into two classes:

1. Surfaces prepared by Au deposition around room temperature: spectra b (0.2 ML Au) and c (0.6 ML Au).

2. Surfaces prepared by low temperature Au deposition: spectra d (0.2 ML on clean Pd(111)) and e (0.2 ML Au on CO precovered Pd(111)).

As has already been shown in chapter 3, a large variation in the Au island density and hence in the relative amount of Au step edge sites can be achieved by choosing different substrate temperatures during Au deposition. For example, Au deposition on Pd(111) at 300 K (Θ_{Au}=0.2 ML, flux: 0.8 ML/min) leads to an island density of $6.1 \cdot 10^{10}$ cm^{-2} whereas the island density is increased by more than two orders of magnitude to $9.1 \cdot 10^{12}$ cm^{-2}, if the experiment is carried out at 110 K. A rough estimate of the concomitant differences in the amount of Au island edge atoms yields 5% (45%) of the Au atoms for the deposition temperature of 300 K (110 K). Hence about 0.01 ML and 0.09 ML of Au edge atoms are present on the respective surfaces. A further increase of the Au island density to $1.3 \cdot 10^{13}$ cm^{-2} could be achieved by precovering the Pd surface with CO, which leads to reduced

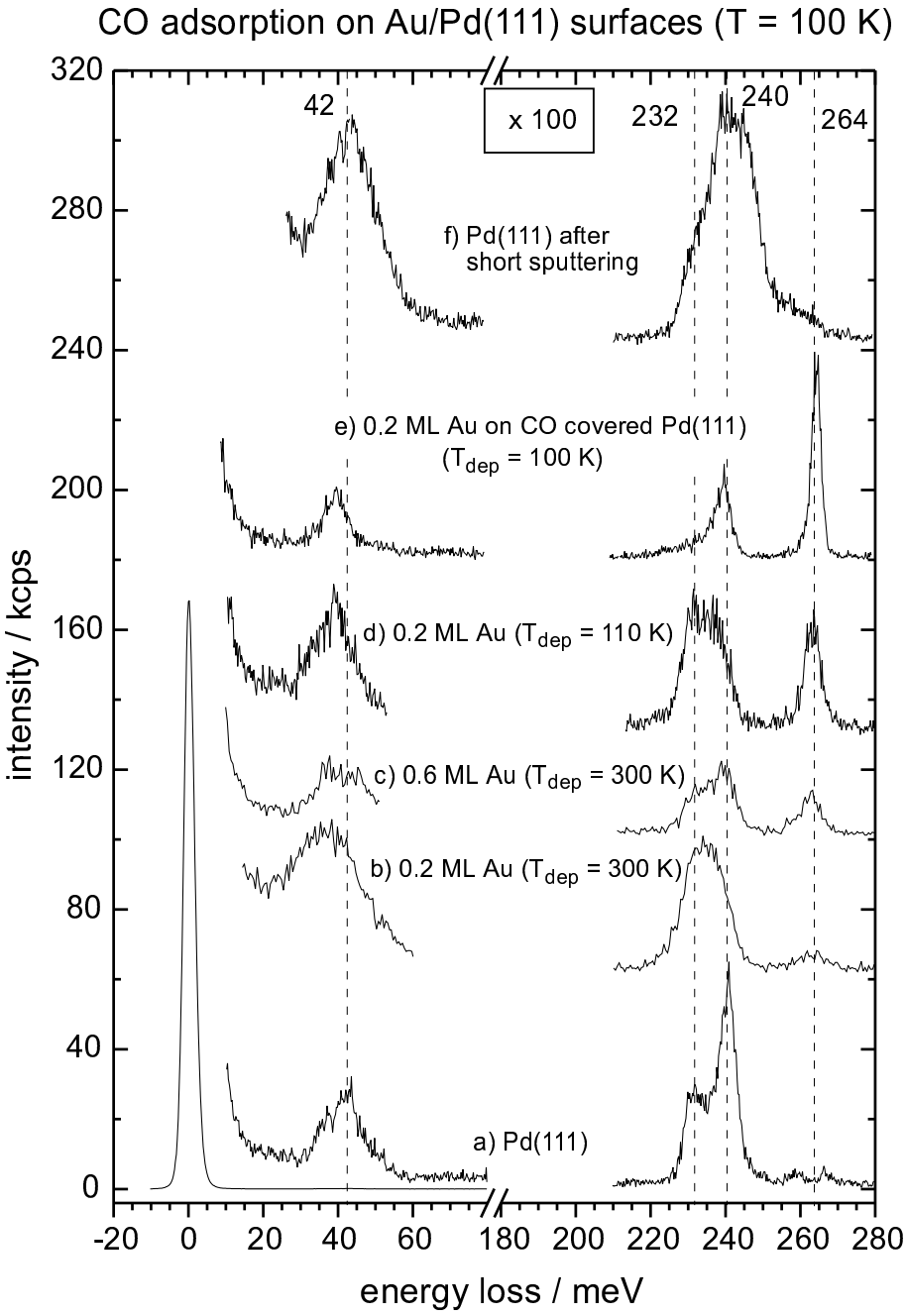

Figure 5.23: HREEL spectra of CO adsorbed on partially Au covered Pd(111) at $\sim$110 K. All spectra are normalized to equal height of the elastic peak; E_p = 4 eV.

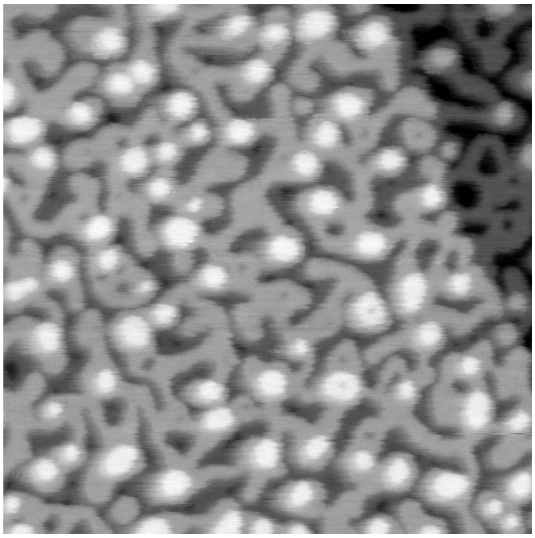

Figure 5.24: STM image of mildly Ar^+ sputtered Pd(111) (1 keV, dosis: $3.9 \cdot 10^{14}$ ions cm^{-2}, 300 K). Image size: 800 Å × 800 Å.

mobility of the Au atoms on the surface. HREEL spectra for CO adsorbed on submonolayer Au films on Pd(111) (fig. 5.23) exhibit two distinct features in the C–O stretching region. The lower energy compontent, that is found to be rather broad, is situated between 230 meV and 245 meV. The sharper high-energy component is detected at 262 meV – 265 meV. The low energy vibration of the metal–CO stretching mode gives rise to broad features around 40 meV with no clearly distinguishable structures. The observations that can be derived from the spectra in fig. 5.23 are summarized in the following list:

1. On pure Pd(111) surfaces only two strong C–O bands at 232 meV and 240 meV and two very weak structures at 260 meV and at 267 meV are observed, but no feature at 263 meV, irrespective of the abundance of Pd step atoms (spectra a and f).

2. If CO is adsorbed on Au films with the same Au coverage, but with different morphologies caused by Au deposition at different temperatures (spectra b and d), the peak around 263 meV is much more pronounced in the case of low temperature Au deposition and high Au island density.

3. Increasing the Au island density by precovering the surface with CO (spectrum e) leads to an additional growth of the 263 meV peak.

4. A variation of Au coverage at 300 K shows that the 263 meV component is growing with increasing Θ_{Au}.

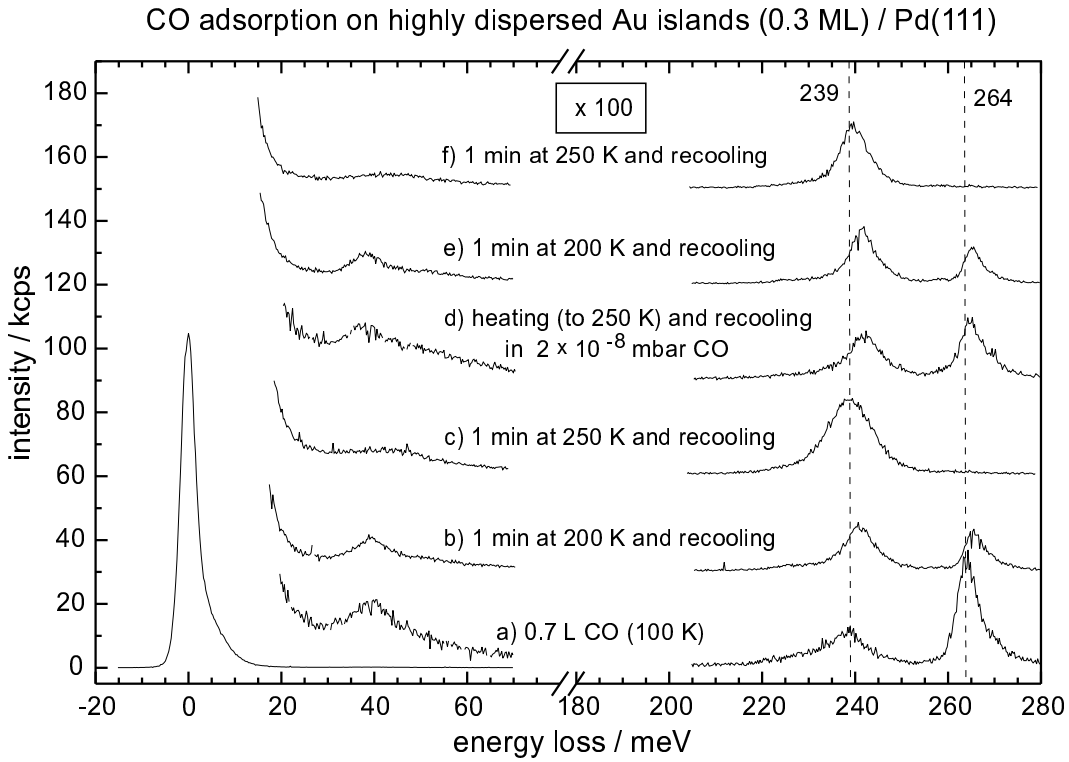

Figure 5.25: HREEL spectra of CO adsorbed on 0.3 ML Au/Pd(111). Au was deposited at 100 K on the CO precovered Pd(111) surface. All spectra are normalized to equal height of the elastic peak; $E_p = 6$ eV.

5. No clear correlation between the position and shape of the metal–CO stretching peak around 40 meV and the preparation conditions of the Au films can be inferred from the spectra in fig. 5.23

From these findings it follows that first layer Au step edge sites are active for CO adsorption at ~ 100 K. The C–O stretching frequency of the resulting adsorption complex is located in the narrow intervall between 262 meV and 265 meV. Considering the observation of a similar stretching frequency for CO adsorped at Au step edges on completely Au covered Pd(111) surfaces (see the previous section) and the fact that generally all vibrational studies on CO-Au adsorbate systems reported C–O stretching frequencies within the above mentioned range, it can be decided that CO is adsorbed on Au atoms at the upper step edges. From the measurements for partially Au covered surfaces alone, also Pd sites in the immediate vicinity of Au step edges would be possible candidates for the additional CO species.

In a final experiment to CO adsorption on layered Au/Pd(111) surfaces the thermal stability of CO adsorbed on highly dispersed Au islands has been investigated by HREELS. The Au film was prepared by depositing 0.3 ML Au at

100 K on a CO precovered Pd(111) surface. Spectrum a in fig. 5.25 was recorded after an additional CO dose of 0.7 L on the Au/Pd(111) surface. It is very similar to spectrum e in fig. 5.23. After annealing for 1 min at 200 K and subsequent recooling to ∼110 K the Au edge peak (264 meV) is reduced to less than 50% of its initial intensity (spectrum b). After an additional annealing cycle to 250 K (spectrum c), the Au edge peak has disappeared completely. These findings are in good agreement to the TPD results that were obtained on similar submonolayer Au/Pd(111) films (section 5.2.2). It was shown that CO desorption from the most stable Au sites (the Au kink sites) occurs around 240 K. The thermally induced loss of CO from the Au edge sites might be caused by several different effects: CO desorption from these sites; CO diffusion from the Au step sites to free Pd terrace sites; Ostwald ripening of the Au islands and changes in the island shapes causing a decrease of the amount of Au step atoms available for CO adsorption. The latter effect was probed by the next spectrum (d), where the surface was again saturated with CO during an annealing–cooling cycle in $2 \cdot 10^{-8}$ mbar CO. This procedure ensures that eventually coadsorbed hydrogen is removed from the surface and the maximum amount of CO is adsorbed (see the discussion in section 5.2.1). It is obvious that the number of Au edge sites has decreased significantly during the two annealing cycles to 250 K. But on the other hand, the remaining Au step edges give still rise to an intense peak at 265 meV.

In this context it is interesting to mention the results of related STM measurements concerning the influence of mild annealing on the density and shape of Au islands (s. figs. 3.1(a) and 3.4). It was found that the island density observed after 0.1 ML Au had been deposited at 99 K using a Au flux of 0.6 ML/min ($9.7 \cdot 10^{12}\,\mathrm{cm}^{-2}$) is reduced to about one third ($3.0 \cdot 10^{12}\,\mathrm{cm}^{-2}$) upon prolonged annealing at 300 K. This is still about a factor of 50 more than the value for direct Au deposition at 300 K. The effect of short annealing at 250 K should be even less pronounced and the reduced peak intensity in spectrum d agrees well with the expectations from the mentioned STM results. The anneal to 300 K was also found by STM to result in rather compact hexagonal Au islands, where the amount of Au kink and corner atoms is relatively low compared to the very small and irregularly shaped islands observed at low temperatures. If CO adsorbed on Au kink and corner atoms exhibited different vibrational properties than CO on regular Au step edge sites, a corresponding change in the Au edge peak would be observed by comparing spectra a and d. However, only a small shift from 264 meV to 265 meV is detectable, which might also be due to different local CO coverages. Therefore, the C–O stretching frequency seems to differ by less than 1 meV between molecules on regular Au step edge sites and molecules on Au kink and corner sites.

If spectrum d of fig. 5.25 is compared to the spectrum of a CO adsorbate layer on Pd(111) that was prepared using the same conditions (spectrum h in fig. 5.18) it is obvious that the spectrum of the partially Au covered surface

cannot be composed by a mere superposition of a spectrum from pure Pd(111) and a spectrum from the completely Au covered surface (e. g., spectrum d in fig. 5.20). The main difference is a missing significant component at 260 meV on the Au film. As the mean distance between two neighbouring Au island can be estimated to be below 60 Å[19] in the case of the annealed Au film, it is likely that the CO domain structure is significantly changed by the presence of the Au islands. On the other hand, the very high energy component at 267 meV is also found on the surface with Au islands (spectrum d, fig. 5.25) and therefore seems to be not as sensitive to a reduction of the size of continuous CO/Pd(111) domains as the 260 meV peak. This is in accordance with the proposed origin of the 267 meV peak as being caused by CO on domain boundaries of a metastable CO adsorbate structure [130].

Finally, the thermal stability of CO on the already annealed Au film was tested by two additional heating–recooling cycles to 200 K and 250 K (spectra e and f), respectively. No significant differences can be detected compared to the previous annealing steps (spectra b and c), i. e., desorption from the Au step edges starts already at temperatures below 200 K. These experiments are closely related to corresponding TPD experiments and a discussion of the correlations between the HREELS and TPD measurements will be given in the concluding section of this chapter.

5.3.3 CO adsorption on AuPd(111) surface alloys

Whereas for Au overlayers on Pd(111) the number of different local atom configurations is quite limited, in the case of random AuPd(111) surface alloys a large variety of possible arrangements of the two components is possible. In a first HREELS experiment, which is basically a reproduction of an earlier experiment by Baddeley et al. [171], it was attempted to gain a qualitative picture for the dependence of the CO adsorption behaviour on the Pd concentration in the surface layer: starting with a completely Au covered surface (Θ_{Au}=1.3 ML) the surface was saturated with CO at 100 K and a HREEL spectrum was recorded. The low temperature CO dosing and HREELS measuring cycle was repeated after several annealing steps to subsequently increased temperatures. Even without taking STM images after each annealing step, it is save to suppose that the concentration of Pd atoms in the surface layer is continuously increasing during the experiment, because the thermodynamically stable state of a system consisting of a Pd crystal and a very small amount of Au atoms is a dilute Au-Pd alloy. This equilibration process is monitored by Baddeley et al. using LEED and AES [171]. The reasons for repeating this experiment were first to find the preparation parameters for producing certain types of CO/AuPd(111) HREELS

[19] This estimate is based on the assumption that during annealing at 250 K the island density is reduced from $\sim 9 \cdot 10^{12}\,\mathrm{cm}^{-2}$ to about one third.

spectra for future, more detailed investigations. Secondly, STM imaging of the alloy surface after the last annealing step should put the interpretation of the spectra on sounder grounds; and finally an improved resolution and signal to noise ratio of the HREEL spectra presented below should provide a more precise determination of the peak positions. Also the metal–CO stretching peak for this system has not been reported before.

The results of this conceptually very simple experiment are displayed in fig. 5.26. The annealing temperatures (annealing time: 5 min) is given in the figure labels. Spectrum a was recorded directly after Au deposition and shows only a very small feature at ~ 260 meV, which might be due to CO adsorbed on Au step edges. The absence of any peaks in the region around 240 meV demonstrates that essentially all of the substrate surface is covered by Au. The first annealing step (450 K) does not produce any remarkable changes in the spectrum, but after annealing at 550 K two pronounced peaks can be observed at 47 meV and at 259 meV, respectively. The former is caused by the metal–CO stretching mode and the latter by the C–O stretching mode. These two peaks have gained intensity after the next annealing step (625 K). A second component in the C–O stretching region grows in at about 235 meV and a shoulder is found at the low energy side of the 47 meV peak. The next significant change in the spectra occurs after annealing at 775 K. The relative intensities of the two initial peaks (47 meV and 259 meV) is decreased, while the two respective low energy counterparts have gained intensity. This tendency is observed also after the next two annealing steps (825 K and 925 K). The final surface composition was investigated by STM and a Pd concentration of 83% was determined. The corresponding spectrum h is already very similar to a spectrum from the pure Pd(111) surface, especially if it is compared to a truely saturated CO layer (spectrum h in fig. 5.18).

A comparison of the CO-HREEL spectra on the AuPd(111) surface alloys with spectra from pure Pd shows that all peaks observed on the alloys are also found on Pd(111). The striking difference between the two types of spectra is the occurence of a single C–O stretching peak at 259 K in the case of the alloys for $T_{anneal} \leq 625$ K without a concomitant feature in the region around 240 meV. On Pd(111) the high energy component of the C–O vibration is only observed for high CO coverages that could be achieved by cooling the sample in a CO atmosphere. In this case also a strong peak at lower vibrational energies is detected. Baddeley et al. interpreted this finding as indication for CO adsorbed on-top of Pd monomers in a Au environment. However, even on the surface with only 17% Au atoms left in the surface layer ($T_{anneal} = 925$ K) the peak at 259 meV exhibits much higher intensity compared to pure Pd(111) for the same CO dosing conditions (see spectrum e in fig. 5.18). Since on that surface the amount of Pd monomers is negligibly small, it can be excluded that only CO on Pd monomers contributes to this peak. In the following a series of HREELS experiments on well-defined AuPd(111) surface alloys will be presented, which

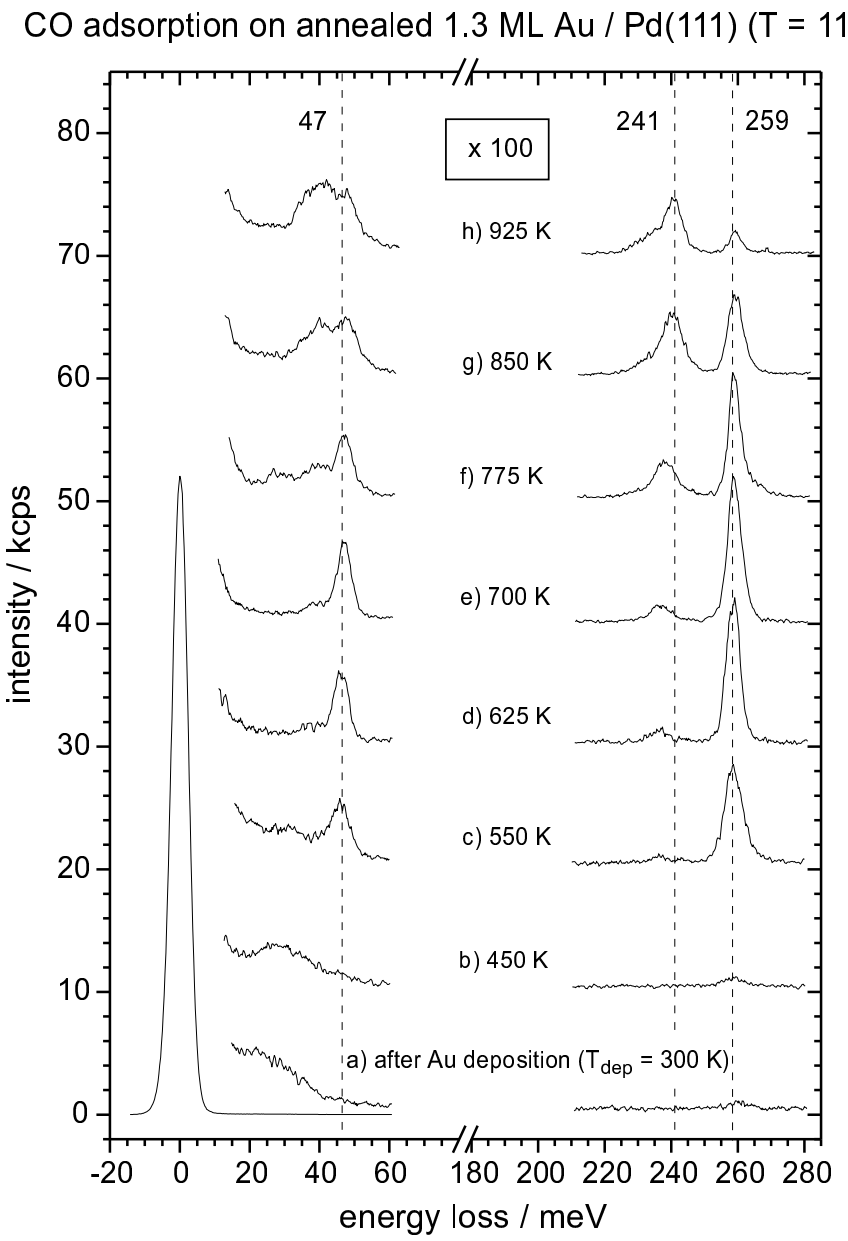

Figure 5.26: HREEL spectra of CO adsorbed on AuPd(111) surface alloys prepared by successive annealing of 1.3 ML Au/Pd(111) at the indicated temperatures. All spectra are normalized to equal height of the elastic peak; E_p = 4 eV.

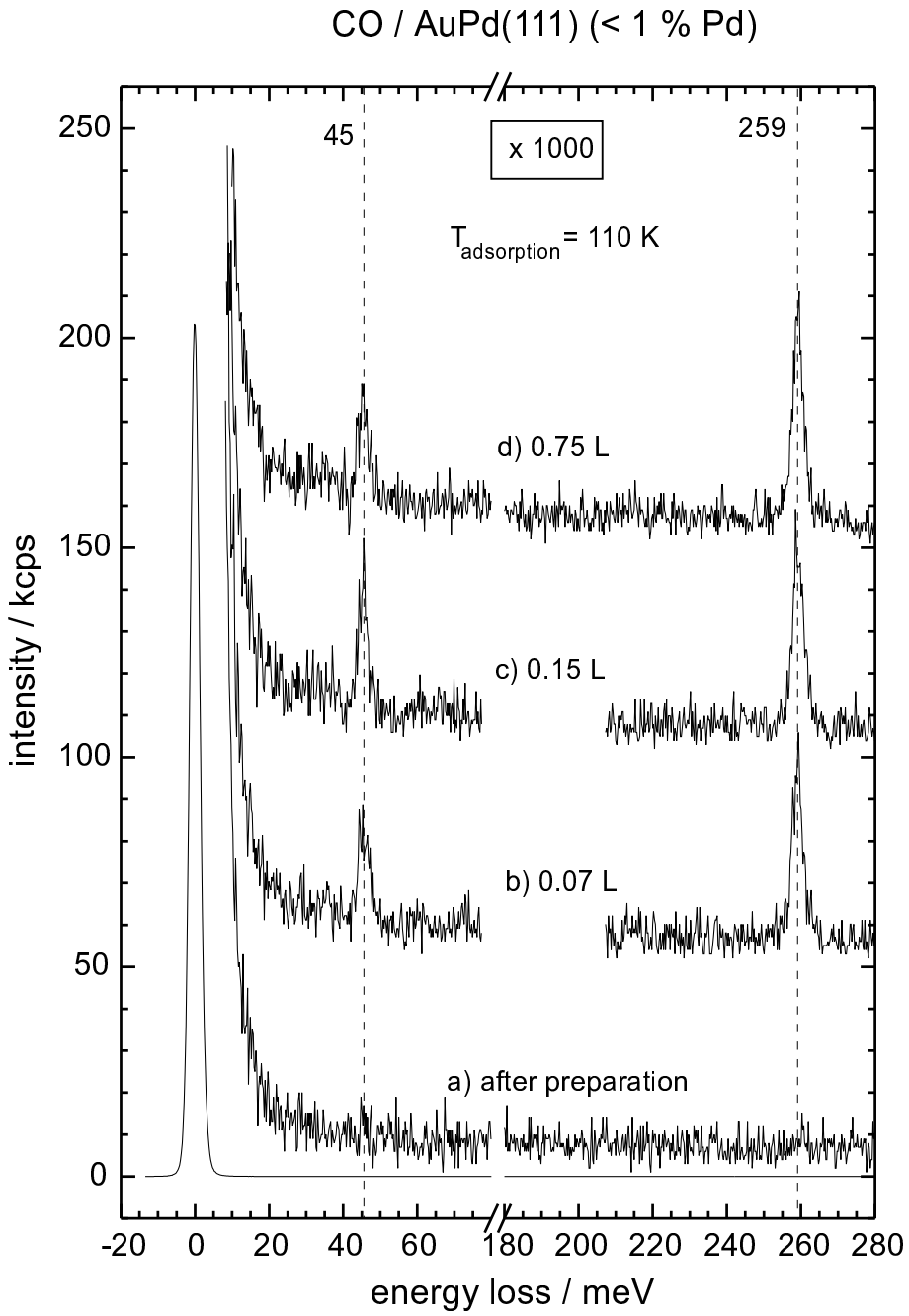

Figure 5.27: HREEL spectra of CO adsorbed on a AuPd(111) surface alloy with $c_{Pd} < 1\%$. All spectra are normalized to equal height of the elastic peak; $E_p = 6\,eV$.

allow to gain deeper insight into the factors that govern the adsorption of CO on such heterogeneous surfaces. Together with the TPD measurements that were presented above a consistent picture of this adsorption system will emerge and will be discussed in the concluding section of this chapter.

First, HREELS experiments will be presented for CO adsorption on the simplest possible surface configuration, namely on an alloy surface with a Pd concentration below 1% (determined by STM) and consequently with only Pd monomers as possible CO adsorption sites on the crystal terraces. This surface was prepared by annealing 1.6 ML Au for 5 min at 550 K and should exhibit a similar composition as the surface used for spectrum c in fig. 5.26. In fig. 5.27 four spectra for different CO doses are displayed. The quality of the reflected electron beam in these spectra is considerably improved (higher count rates at better resolution: $\sim$3 meV FWHM instead of $\sim$5 meV FWHM) compared to the series shown in fig. 5.26 and therefore the determination of peak positions is more accurate in this case. Two peaks are clearly visible already after a small dose of 0.07 L CO at 45 meV and at 259 meV, respectively. They grow only slightly upon an additional dose of 0.07 L and are found to be saturated after the total dose of 0.14 L. This is significantly below the doses that had to be used for saturating the pure Pd(111) surface or Pd-rich AuPd(111) surface alloys. This observation is an additional indication for the presence of a weakly adsorbed, mobile precursor state of CO on the Au covered terraces which has been discussed in the section on the quantitative evaluation of TPD spectra from AuPd(111) surface alloys (section 5.2.4). This precursor state allows the CO molecules to diffuse on the surface and to eventually encounter a more favourable Pd adsorption site. The main conclusion that can be drawn from the spectra in fig. 5.27 is that CO undoubtedly adsorbs at 110 K on Pd monomers within a Au matrix and that this adsorbate complex gives rise to a Pd–CO stretching peak at 45 meV and to a C–O stretching peak at 259 meV. This is a typical value for linearly bonded CO and in a DFT study by Loffreda et al. 257 meV have been calculated as the C–O stretching frequency for a hypothetical on-top configuration of CO on Pd(111) [128].

In fig. 5.28 a set of spectra is combined to show the results of HREELS measurements for CO saturation coverages on five AuPd(111) surface alloys, that were characterized on the atomic scale by STM. Therefore, more specific statements can be derived from these experiments compared to the qualitative measurements in fig. 5.26. The preparation conditions for the different surface compositions are summarized in table 5.6. Since the following discussion will be concentrated on the surfaces with low Pd concentrations, two STM images for the surfaces with 12% Pd and with 23% Pd are presented in figs. 5.29 and 5.30, respectively. As an example for a Pd-rich surface alloy the 83% Pd surface (spectrum e) is shown in fig. 5.31. The results of a statistical analysis of several STM images for each of the Au-rich surfaces is given in table 5.7 and is visualized in fig. 5.32. The numbers for twofold and threefold sites are obtained from Pd dimers (1 twofold site

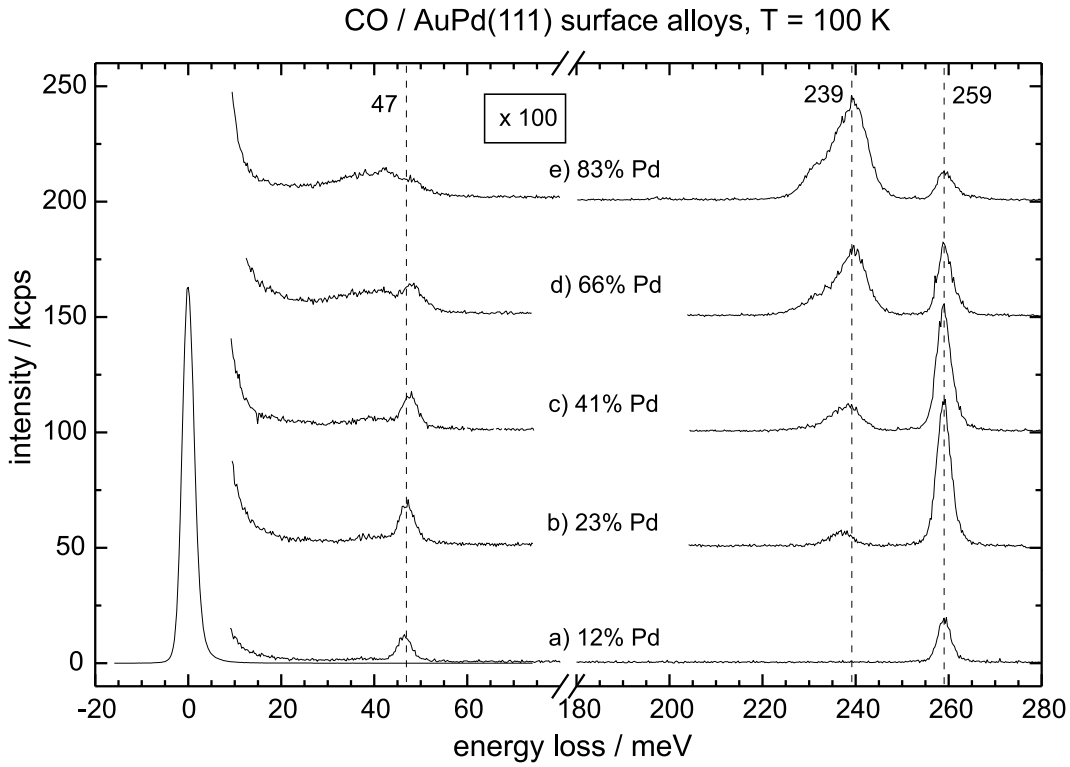

Figure 5.28: HREEL spectra of CO adsorbed on AuPd(111) surface alloys with different Pd concentrations in the surface layer. The latter have been determined from atomically and chemically resolved STM images of the surfaces (see for instance figs. 5.29–5.31). All spectra are normalized to equal height of the elastic peak; $E_p = 6\,eV$.

per dimer) and from larger Pd clusters by determining first all pure Pd threefold hollow sites and then counting the remaining twofold sites, where it was assumed that one threefold site blocks the directly adjacent three twofold sites.

In spectrum a of fig. 5.28 only a single peak is visible in the metal–CO region (around 47 meV) and in the C–O region (259 meV). Following a simple argumentation, one could assume that on the corresponding AuPd(111) surface with 12% Pd only Pd monomers should be available as adsorption sites for linearly bonded CO. However, figs. 5.29 and 5.32 together with table 5.7 clearly show that the number of twofold sites on this surface is high enough (0.02 ML vs. 0.09 ML of Pd monomers) to give rise to a detectable signal in the HREEL spectrum. From this it has to be concluded that in the case of CO saturation the CO molecules are bonded to Pd dimers in a similar configuration as to Pd monomers, i. e., "on-top" of a Pd atom and not at the bridge site between the two dimer atoms. Taking into account that on all low index Pd single crystal surfaces the occupation of on-top sites is only observed for high CO coverages and that therefore the bridge

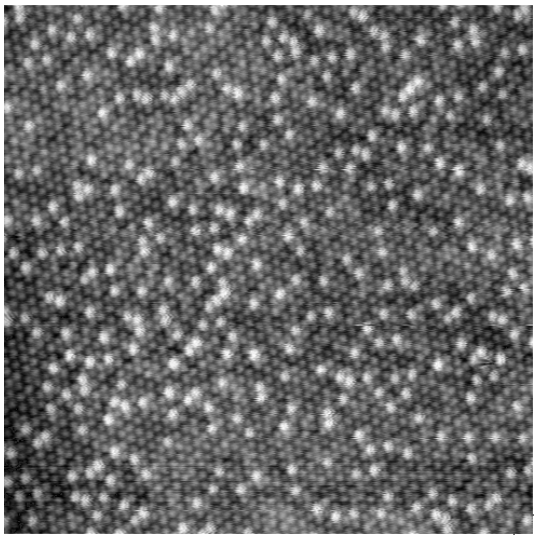

Figure 5.29: STM image of a AuPd(111) surface alloy with 12% Pd. Pd atoms appear brighter than Au atoms. The preparation parameters are given in table 5.6. A statistical analysis of the Pd cluster size distribution is presented in table 5.7 and in fig. 5.32. Image size: 135 Å × 135 Å.

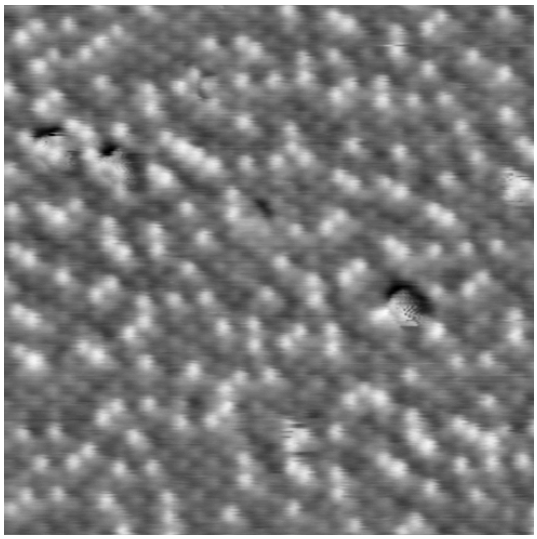

Figure 5.30: STM image of a AuPd(111) surface alloy with 23% Pd. Pd atoms appear brighter than Au atoms. The preparation parameters are given in table 5.6. A statistical analysis of the Pd cluster size distribution is presented in table 5.7 and in fig. 5.32. Image size: 83 Å × 83 Å.

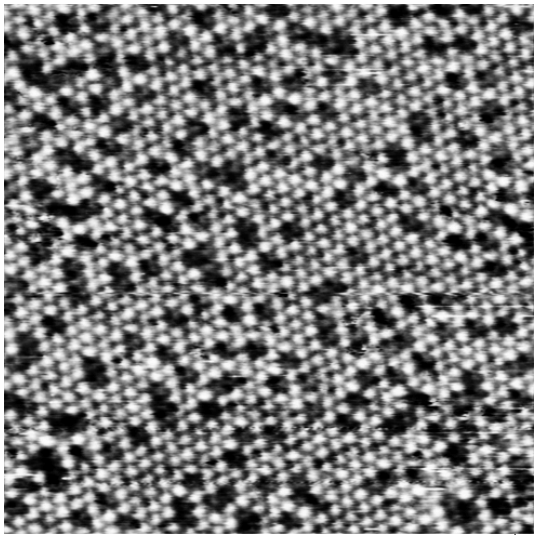

Figure 5.31: STM image of a AuPd(111) surface alloy with 83% Pd. Pd atoms appear brighter than Au atoms. The preparation parameters are given in table 5.6. Image size: 83 Å × 83 Å.

spectrum	c_{Pd}/%	Θ_{Au}/ML	t_{anneal}	T_{anneal}/K
a	12	2.7	2 min	700
b	23	1.4	30 s	775
c	41	0.8	30 s	775
d	66	0.8	30 s	925
e	83	0.8	30 s	1000

Table 5.6: Preparation parameters for the AuPd(111) surface alloys used for the HREELS measurements in fig. 5.28.

sites seem to be energetically more favourable, it can be assumed that the driving force for the on-top site occupation is the possibility to accommodate *two* CO molecules per Pd dimer. This is in good agreement with the TPD results and a further discussion of this phenomenon will be given in the concluding section of this chapter on CO adsorption. From the values given in table 5.7 it can be calculated that about 0.008 ML of twofold sites should be available from Pd clusters other than dimers, i. e., mainly from linear Pd trimers. Even this should be enough to produce a small feature in spectrum a. Although in this case the evidence is not as clear as in the case of the dimers, it seems to be likely that for saturation coverages also on linear Pd trimers CO is not occupying the two bridge sites of the trimer but rather the on-top sites. Consequently three CO molecules might be bonded to a Pd trimer. From the values given in table 5.7 it can also be seen that threefold Pd sites are too rare to play any role in the present discussion.

c_{Pd} in %	Pd monomers in % of a ML	Pd dimers in % of a ML	2fold Pd sites in % of a ML	3fold Pd sites in % of a ML
12	8.7	1.3	2.1	< 0.1
23	8.2	3.2	8.6	0.4

Table 5.7: Statistical analysis of STM images from AuPd(111) surface alloys. For Pd clusters of a larger size than 2 atoms, first the available pure Pd threefold sites have been determined and then the remaining twofold sites consisting of only Pd atoms have been counted.

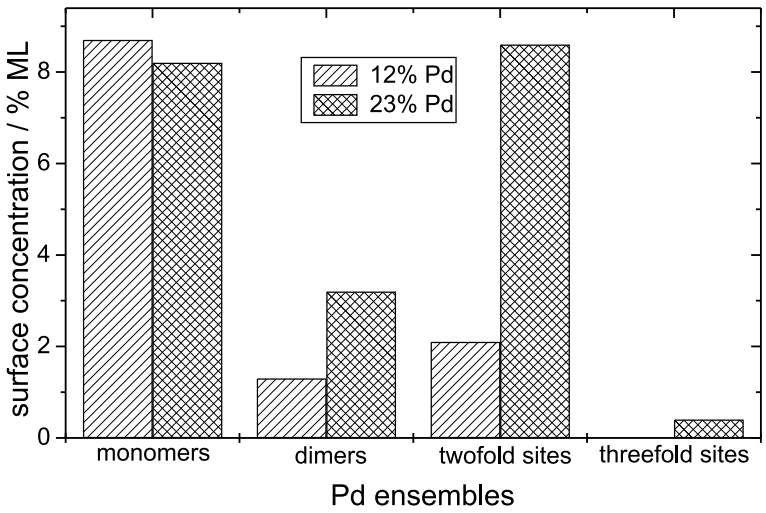

Figure 5.32: Size distribution of Pd ensembles on AuPd(111) surfaces with 12% and 23% Pd in the surface layer, respectively; the values are given in table 5.7.

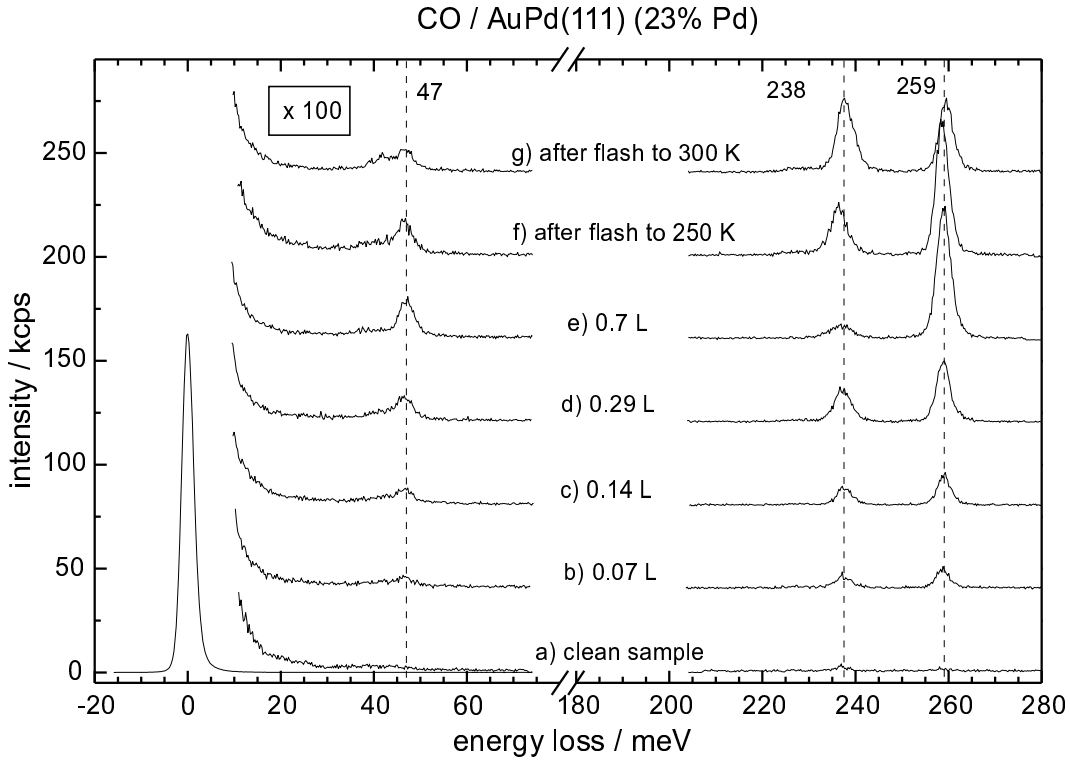

Figure 5.33: HREEL spectra of CO adsorbed on a AuPd(111) surface alloy with $c_{Pd} = 23\%$. Spectrum e is identical to spectrum b in fig. 5.28. An STM image of the surface is shown in fig. 5.30. All spectra are normalized to equal height of the elastic peak; $E_p = 6\,eV$.

It is quite remarkable, that on the surface with 23% Pd (spectrum b), the C–O stretching peak at 259 meV is still about an order of magnitude more intense than the peak at 238 meV, which corresponds to bridge bonded CO (as will be shown below). An inspection of table 5.7 shows that on this surface there are already more twofold sites available than Pd monomers, which corroborates the statements in the above paragraph. However, since HREELS is not a quantitative method in the sense that peak intensities do not necessarily depend linearly on adsorbate coverages, it is not possible to determine the amount of CO that is bonded on bridge sites from spectrum b. In order to gain more information on the relative occupancy of linear and bridging sites for this surface, a sequence of CO coverage dependent HREELS spectra was recorded (see fig. 5.33). For low CO doses ($\leq$ 0.29 L) the intensity of the peak at 238 meV is only about a factor of 2 smaller than the intensity of the peak at 259 meV. Between 0.29 L and 0.7 L a growth of the higher energy peak at the expense of the lower energy peak can be observed. After short annealing at 250 K (f) the 238 meV peak has gained intensity, while the height of the 259 meV peak remains almost constant.

Annealing at 300 K results in a spectrum (f) that is similar to spectra for low CO doses, i. e., the low energy peak grows while the high energy peak is diminished. If spectrum g is compared to spectrum e it is quite obvious that in the case of a CO saturated adsorbate layer, only a small fraction of the available bridge sites is occupied by CO.

Before we turn to the final set of HREEL spectra shown in fig. 5.34 for a AuPd(111) surface alloy with 57% Pd, some additional remarks are necessary about the origin of the C–O stretching peak around 238 meV. From the vibrational energy alone no unambiguous assignment of the corresponding adsorption site is possible, because threefold bonded CO on Pd(111) exhibits a large positive energy shift (to energies of up to 238 meV) with increasing coverage. On the other hand, on Pd(100) twofold bonded CO gives rise to a peak at 235 meV for low coverages. From the STM evaluation of the 23% Pd surface it is known that the amount of threefold hollow Pd sites is too small to explain the strong peak at 238 meV. The only possibility to explain the HREEL spectra with threefold bonded CO would be to assume that CO adsorbs on a mixed Au-Pd threefold site. Since from our measurements no indication for such an "exotic" adsorption site can be derived and since all experimental findings can be consistently explained by the intuitive proposition of bridge bonded CO giving rise to the 238 meV peak, the latter is judged to be the best explanation for the HREEL spectra. It is important to note that on the 23% Pd surface no significant CO coverage dependent peak shift is noticed and hence the value of 238 meV can be taken as vibrational energy for an isolated CO molecule adsorbed on the bridge site of a Pd dimer. CO coverages up to ~ 0.1 ML (occupation of all bridge sites of the 23% Pd surface plus some monomer sites) apparently do not influence the peak positions, which is an important observation with respect to the interpretation of HREEL spectra from surfaces with higher Pd concentrations. These findings are supported by recent DFT based calculations reported by Loffreda et al. [128], where the vibrational frequency of a hypothetical isolated bridge-bonded CO molecule on Pd(111) is determined to be 235 meV.

The Pd surface concentration of 57% that belongs to the spectra shown in fig. 5.34 is already too high to allow a simple statistical analysis of the available CO adsorption sites, because it is not clear a priori how the CO molecules could be arranged on "large" Pd clusters. Nevertheless, this sequence of HREELS experiments provides some additional information. In spectrum a, which was recorded after a very low CO dose (0.07 L), two low-energy C–O stretching peaks are resolved. The peak at 237 meV has been already observed on surfaces with lower Pd concentrations and was determined to originate from bridge bonded CO molecules[20], while the peak at 227 meV is not observed for $c_{Pd} \leq 23\%$. On

[20] In principle, also threefold bonded CO molecules are able to produce a C–O stretching peak around 237 meV. However, on Pd(111) this is only found for high CO coverages (> 0.3 ML [122]). Also the occurence of a distinct low energy peak (227 meV) is in contradiction to the assignment

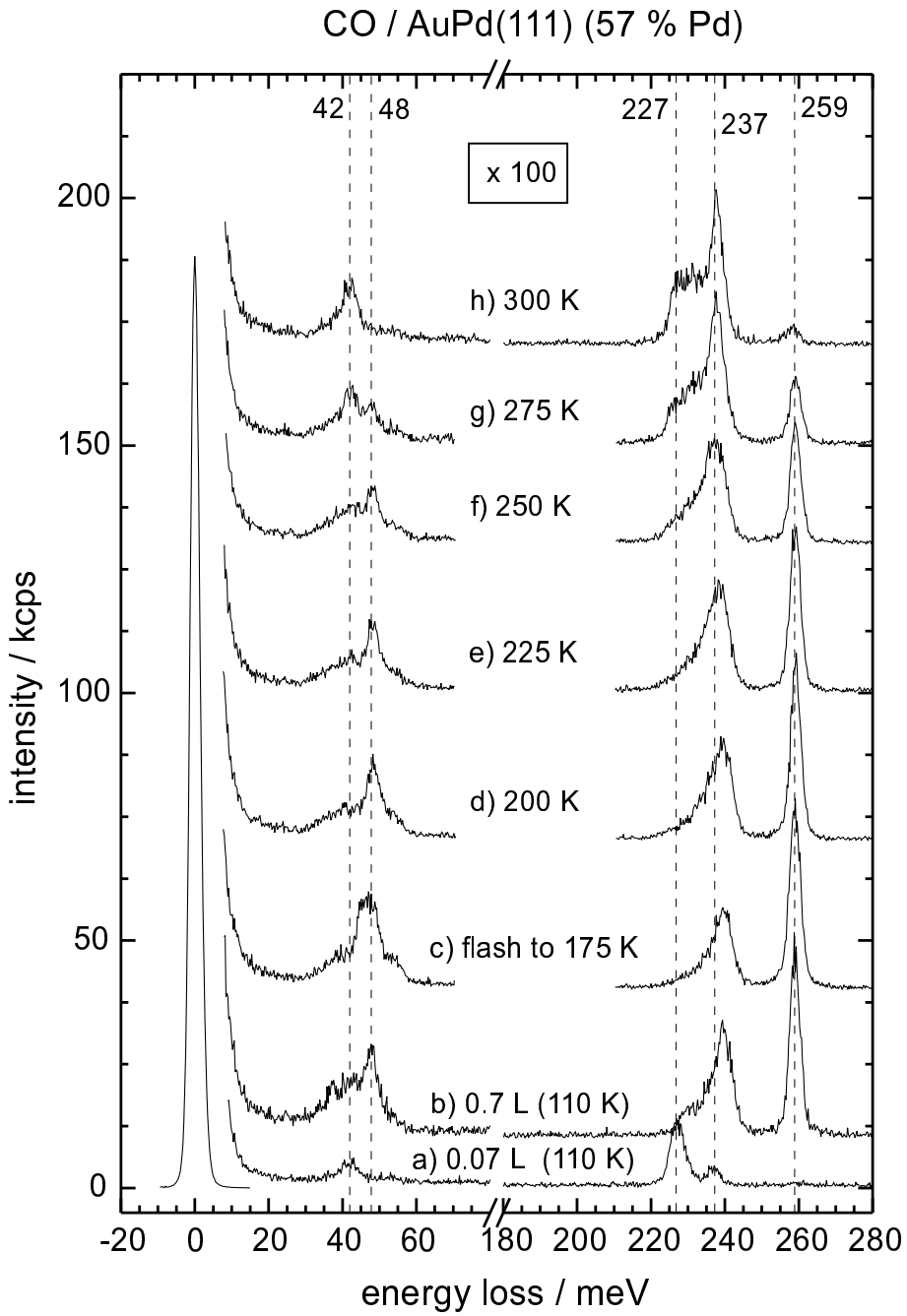

Figure 5.34: HREEL spectra of CO adsorbed an AuPd(111) surface alloy with $c_{Pd} = 57\%$. All spectra are normalized to equal height of the elastic peak; $E_p = 4\,eV$.

the other hand, the position of the latter peak corresponds well with the peak position observed on pure Pd(111) for low CO coverages. It can be concluded that this peak is caused by CO molecules in threefold hollow sites. Since on Pd(111) for $\theta_{CO} \leq 0.33$ ML only one type of threefold hollow sites is occupied [126, 127], namely those that correspond to fcc stacking and that do not have a second layer atom directly underneath the hollow site, fcc and hcp sites are not equivalent concerning the activity towards CO adsorption. However, the difference in CO adsorption energy on these sites is relatively small, because it is known that the sites to be occupied upon increasing θ_{CO} above 0.33 ML are the hcp sites [126] and that bridge or on-top sites are populated only for CO coverages exceeding 0.5 ML. On the surface with 57% Pd atoms, there are certainly enough hcp threefold sites available to be detected by HREELS. From these findings and from the fact that in spectrum a of fig. 5.34 only two components (227 meV and 237 meV) are resolved, it follows that the C–O stretching frequency of molecules on fcc and on hcp threefold sites are not distinguishable by HREELS. The width of the peak at 227 meV is enlarged compared to the elastic peak (from a FWHM of 3.1 meV to 4.5 meV) and also compared to the peak of the linearly bonded CO species at 259 meV (3.5 meV). Since the locations of the CO molecules are given by the local composition of the bimetallic surface, it can be excluded that the molecules form CO island as in the case of pure Pd(111). Therefore, the influence of vibrational coupling between the molecules should be small for low CO doses and the broadening of the peak at 227 meV could be ascribed to the presence of two different components, namely fcc and hcp hollow sites. If this is correct then the difference in vibrational energy between these two sites will amount to only about 1 meV. A definite statement on this issue clearly requires additional vibrational data that are recorded with high resolution.

An additional observation that can be made from the spectra in fig. 5.34 concerns the annealing behaviour of the CO saturated surface. It was pointed out above that on a surface with only 23% Pd a major redistribution of the CO molecules between the different adsorption sites is observed upon annealing the surface to temperatures above 200 K. The annealing sequence shown in fig. 5.34 demonstrates that on a surface with 57% Pd atoms only minor changes in the intensity of the lower energy components of the C–O stretching mode occur if the sample is heated, whereas the peak corresponding to linearly bonded molecules is significantly diminished after annealing at 250 K.

Up to now, the presentation of the HREELS measurements has concentrated on the C–O stretching peaks. Some observations concerning the low energy metal–CO stretching vibrations should be added to this section. On pure Pd(111) (figs. 5.17 and 5.18) this mode is observed at 40 meV for low CO coverages, and for the highest coverages (spectrum h in fig. 5.18) it is split into two components

of the 237 meV peak to threefold bonded CO.

CO adsorption site	metal–CO /meV	C–O / meV	reference figure (spectrum)
threefold hollow/Pd(111)	40	227	5.18(a)
threefold hollow/AuPd(111)	42	227	5.34(a)
bridge/AuPd(111)	-	238	5.33(d,g)
on-top/Pd(111)	-	260	5.18(h)
on-top/Au-edges	~ 35	263	5.20(e)
on-top/Pd monomers	45	259	5.27(c)
on-top/larger Pd clusters	~ 48	259	5.28(c)

Table 5.8: Collection of vibrational energies for CO adsorbed on different well-defined sites on Au-Pd(111) surfaces. Where possible, only values for small CO coverages have been included to minimize the influence of adsorbate–adsorbate interactions.

centered at 35 meV and at 45 meV, respectively. The corresponding energy for the CO species at Au edge sites is not so easy to determine, because on the surfaces with high Au island densities the elastic beam usually exhibited a strong high energy tail and therefore the metal–CO vibration was not easy to detect. However, in fig. 5.20 a broad peak for the Au–CO vibration can be found around 35 meV. On the AuPd(111) surface alloys, the elastic peak was sufficiently narrow for the Au–CO stretching vibration to be well resolved. On a surface with only Pd monomers the corresponding peak from linearly bonded CO is located at 45 meV – 46 meV fig. 5.27. In the figures which show spectra from different AuPd(111) surface alloys (figs. 5.26 and 5.28) this peak can also be identified. Besides the evolution of lower energy features, that correspond to CO molecules on bridge and on hollow sites, a small positive shift of the Pd–CO peak for linearly bonded CO is observable for increasing c_{Pd}. E. g., for 66% Pd (spectrum d in fig. 5.28) the peak is located at 48 meV. Spectrum a in the same figure shows that already for 12% Pd the Pd–CO stretching peak is shifted by at least 1 meV compared to the surface with only Pd monomers. On the other hand, the C–O stretching peak for linearly bonded CO does not shift significantly if the Pd concentration is varied (see figs. 5.28 and 5.28). Therefore, it seems that the metal–CO vibration is more sensitive to the local environment of the adsorption site than the C–O vibration. Consequently, the metal–CO peak can be used as an indicator to distinguish linearly bonded CO molecules on Pd monomers (45 meV) and linearly bonded CO molecules on larger Pd clusters (47 meV–48 meV) — dimers and possibly also linear Pd trimers —, where the CO molecules have a very high local density. Finally, it should be emphasized that no simple correlation between the position of the C–O stretching peaks and the positions of the metal–CO stretching peaks exists. The respective values for different CO species are collected in table 5.8.

5.4 HREELS results for CO adsorption on Pd-Au(110) surfaces

Besides the extensive measurements on differently prepared Au-Pd(111) surfaces, also some HREELS experiments concerning the adsorption of CO on Pd precovered Au(110) surfaces have been carried out. The HREEL spectra for CO/Pd-Au(110) were the first HREELS measurements preformed in the UHV system described in section 2.1 and several components still had to be optimized:

- Due to severe heat leaks to the support of the sample holder the lowest possible sample temperature was $\sim$150 K.
- The Au(110) crystal was too small (only a circle with 4 mm diameter was visible for the electron beam) to allow for a good preformance of the HREEL spectrometer because the electron beam had to pass the Mo ring, that surrounds the sample, at a small distance. Therefore, the elastic beam was rather broad with a FWHM mostly above 10 meV.
- No atomically resolved STM images with chemical contrast between Pd and Au atoms could be obtained on this system.

Most of the results on Pd-Au(110) were already presented in [38] and therefore only a brief overview is given in the following. A short description of the growth and alloying behaviour of Pd on Au(110), that has been studied by STM and AES, will be presented first. The (110) face of Au is (1×2) reconstructed under the experimental conditions used in this work for Pd deposition. An STM analysis of the Au(110)-(1×2) surface structure showed that this reconstruction is of the missing row type, which means that every other close-packed atom row of the fcc(110) surface is removed leaving a highly corrugated surface [189, 190]. A hard sphere model of the surface is displayed in fig. 5.36(a). Metal growth on Au(110)(1×2) has attracted some attention in the past, because alloying occurs already at relatively low temperatures on this open surface and because of the pronounced anisotropy of the surface which yields interesting growth phenomena[21].

A sequence of STM images from a Pd-Au(110) surface with 0.1 ML Pd is shown in figure 5.35. Pd deposition was carried out at 165 K and STM images were obtained directly after the low temperature deposition (a) and after subsequent annealing steps at 293 K (b), 393 K (c), and 493 K (d), respectively. In fig. 5.35(a) it can be seen that the additional atoms are mainly located in the troughs of the missing row structure upon low temperature deposition and that only few second layer islands exist. It can not be excluded that already at this

[21] The following metal adsorbates have been studied on Au(110) in the past: Au [32], Ni [20, 37, 69], and Cu [16, 70].

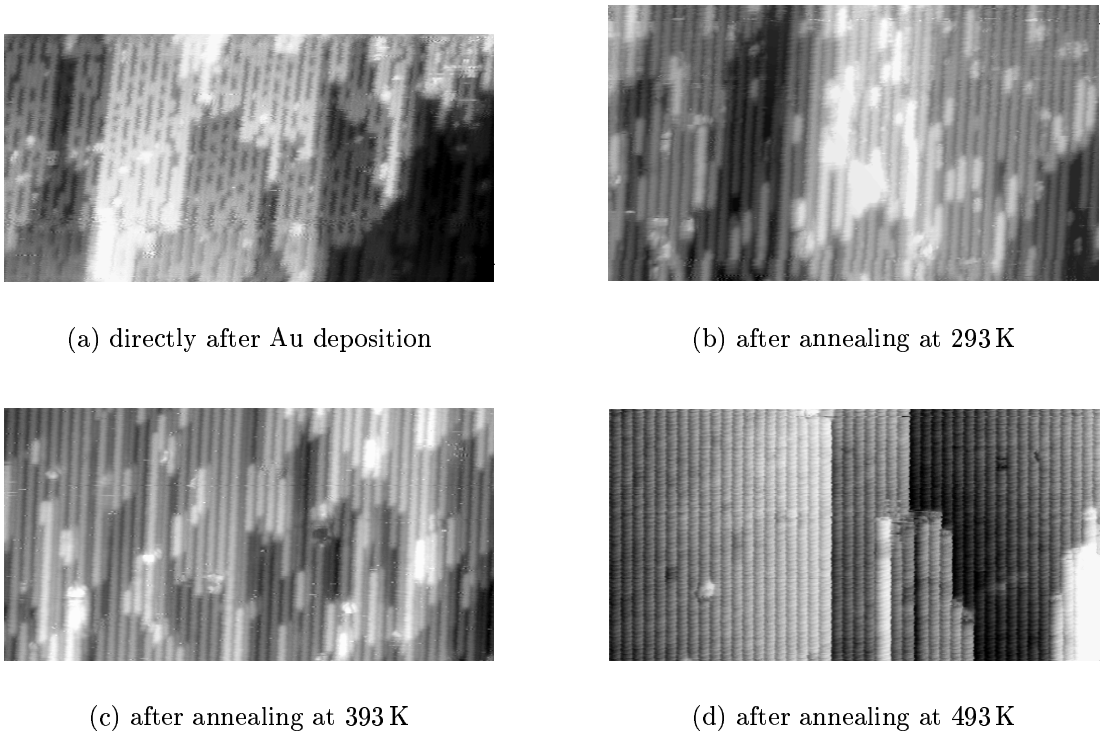

(a) directly after Au deposition

(b) after annealing at 293 K

(c) after annealing at 393 K

(d) after annealing at 493 K

Figure 5.35: STM images of 0.1 ML Pd on Au(110) (T_{dep}=165 K) after annealing at different temperatures.

stage Pd–Au exchange processes occur leading to an intermixed surface layer of a local (1 × 1) structure. A hard sphere model of this morphology is displayed in fig. 5.36(b). After heating to room temperature (fig. 5.35(b)) the dominating Pd derived structural elements are so-called "double rows", where an additional atom row is situated above a filled trough (model see fig. 5.36(c)). Considerable interlayer mass transport is required to form this surface structure. In the case of Cu/Au(110) a similar transition was observed around 250 K [16]. Using ISS it was shown that in this case the formation of the double rows is accompanied by Cu–Au exchange processes resulting in an almost pure Au surface layer. For Pd/Au(110) no direct evidence for the chemical composition of the double rows is available. However, taking into account that in Pd-Au alloys or surface alloys Au tends to segregate to the topmost layer, it is likely that also for Pd/Au(110) the Pd atoms are at least partly covered by Au after the double row formation. The typical lengths of the double row islands after heating to 293 K are still small ($\sim 20\,\text{Å} - 50\,\text{Å}$). Annealing at 393 K (fig. 5.35(c)) causes the smaller islands to vanish and only longer double rows survive. They are partly attached to former step edges of the Au(110) surface. After annealing at 493 K (fig. 5.35(d)) the original (110)(1 × 2) structure is almost completely restored apart from some

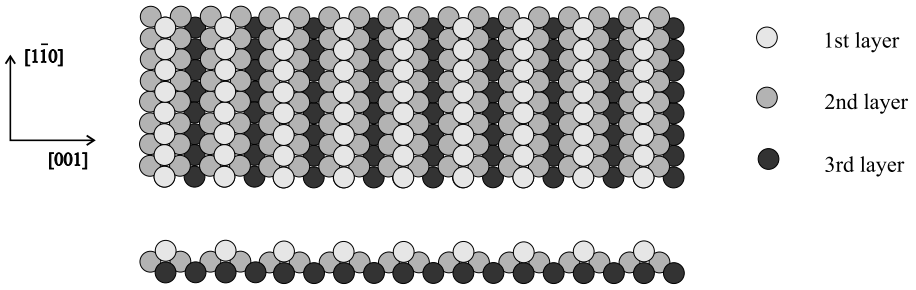

(a) fcc(110)(1 × 2) missing row reconstruction

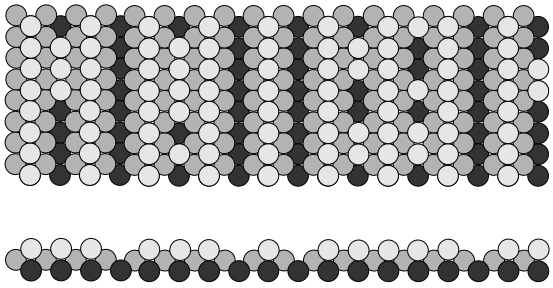

(b) filling of the missing row troughs at low sample temperatures

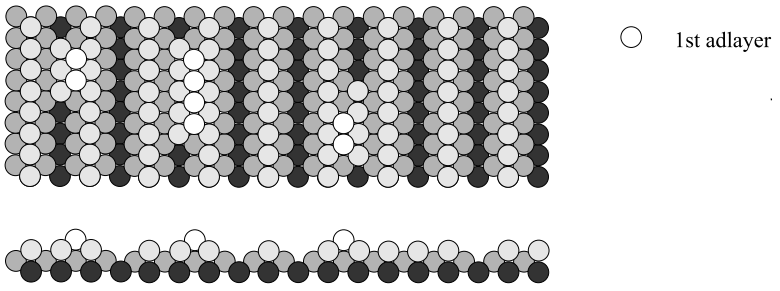

(c) formation of "double-rows" at room temperature

Figure 5.36: Hard sphere models for metal growth on Au(110)(1 × 2).

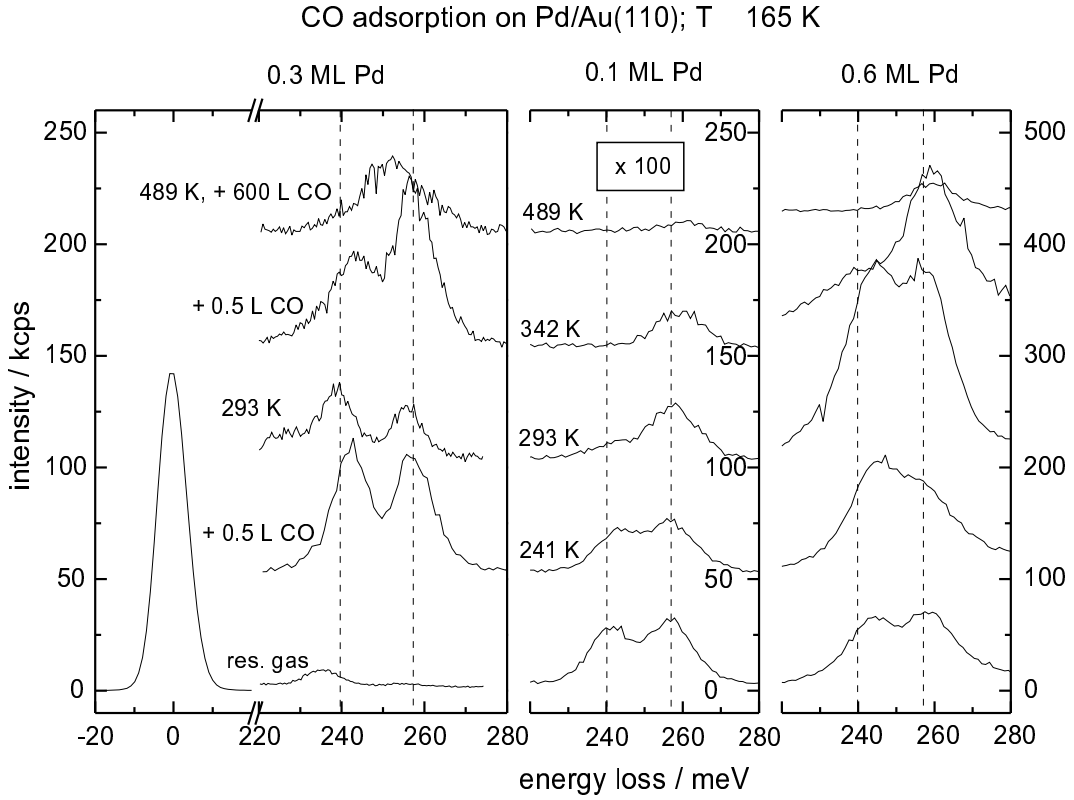

Figure 5.37: HREEL spectra of CO on Pd-Au(110) surfaces. These were prepared by deposition of 0.3 ML, 0.1 ML, and 0.6 ML Pd on the Au(110) crystal at T $\approx$ 165 K. The experimental procedure for the 0.1 ML and the 0.6 ML surfaces were identical: after Pd deposition the surfaces were exposed to a saturation dose of CO and a HREEL spectrum was recorded. This was repeated after annealing the sample for five minutes at the temperatures given in the figure and after recooling to $\sim$165 K. On the 0.3 ML surface, the first spectrum was recorded before dosing CO. Also after annealing at 293 K, a spectrum is included that was recorded prior to the CO dose. For each set of spectra two vertical lines are drawn at 240 meV and at 257 meV, respectively. All spectra are normalized to equal height of the elastic peak; $E_p = 4$ eV.

structural defects caused by the deposited Pd atoms. As has been pointed out above, no statement about the surface composition could be derived from the STM images. From a comparison of AES peak ratios (Pd(MVV) at 330 eV to Au(NVV) at 69 eV) measured for Pd deposition at low temperatures and at room temperature, respectively, it can be concluded that deposition at room temperature leads already to a lowered Pd concentration in the surface layer [38]. AES annealing experiments after 0.2 ML Pd deposition at 300 K show that the peak ratio is almost constant up to 350 K and starts to decrease slowly at that temperature. Above 550 K a steeper decrease of the Pd(MVV) peak intensity is observed.

HREEL spectra of CO adsorbed on differently prepared Pd-Au(110) surfaces are collected in fig. 5.37. 0.1 ML, 0.3 ML, and 0.6 ML Pd have been deposited around 165 K on the Au sample. The experimental procedure for the 0.1 ML and the 0.6 ML films were identical, namely annealing the surface for 5 minutes at 241 K, 293 K, 342 K, and 489 K, respectively, with a low temperature CO adsorption and HREELS measuring step after each annealing cycle. On the 0.3 ML Pd film only annealing at 293 K and at 489 K was investigated. The following observations can be derived from the spectra in fig. 5.37:

- For all investigated Pd films (0.1 ML – 0.6 ML) deposited at low sample temperatures, two C–O stretching features are discernible on the CO saturated surfaces. They are located around 242 meV and 257 meV, respectively.
- The intensity ratio of these peaks does not depend strongly on the Pd coverage, at least not in the low coverage regime ($\Theta_{Pd} \leq 0.6$ ML).
- The lower energy peak is populated first, as seen from the first spectrum for 0.3 ML Pd, which indicates that it is caused by the adsorbate state which is more strongly bonded to the surface.
- Annealing the surfaces at 293 K and subsequent low temperature CO adsorption results in a significantly decreased peak intensity at 242 meV for the two lower Pd coverages. For $\Theta_{Pd} = 0.6$ ML this annealing temperature has almost no effect on the relative peak intensities.
- Annealing at 342 K is sufficient to eliminate the adsorption sites that give rise to the lower energy C–O stretching component for very small Pd coverages (here: 0.1 ML), whereas for larger Θ_{Pd} a low energy shoulder of the 257 meV peak can still be distinguished.
- For Θ_{Pd}=0.1 ML almost no C–O stretching signal is observed after annealing at 489 K. For higher Pd coverages there remains some intensity around 250 meV (0.3 ML Pd, very high CO dose!) and around 260 meV (0.6 ML Pd, 0.5 L CO), respectively.

Taking into account the above, unfortunately rather incomplete, information about Pd growth and alloying on Au(110) certain consequences can be derived for the interpretation of the HREEL spectra.

1. From the HREEL spectra that were recorded on the non-annealed surfaces it can be concluded, that on the patches with a local (1×1) structure that are caused by adsorbed Pd atoms, two different adsorption sites are available for CO. The observed stretching frequencies indicate that these sites are bridge ($\nu_{C-O} \approx 242\,\mathrm{meV}$) and on-top sites ($\nu_{C-O} \approx 257\,\mathrm{meV}$), respectively.

2. The intensity ratio of almost 1:1 for Pd coverages from 0.1 ML to 0.6 ML is not reconcilable with a model, where the on-top sites are only occupied on isolated Pd atoms. Consequently, an adsorbate structure has to be supposed, where also on longer Pd chains linearly bonded CO coexists with bridge bonded molecules.

3. The changes of the CO adsorption properties of the Pd-Au(110) surfaces upon annealing can be explained by a gradual decrease of the surface Pd concentration and a concomitant removal of larger Pd clusters. The annealing effects clearly depend on the initial Pd coverage with higher coverages requiring higher annealing temperatures for certain changes to be observed.

4. The double row formation, that has been observed by STM for $\Theta_{\mathrm{Pd}} \leq 0.2$ ML after annealing at room temperature causes the CO bridge species to almost completely vanish for the lowest Pd coverage (0.1 ML), whereas for higher Pd coverages (here: 0.6 ML) no significant changes are detectable in the HREEL spectrum. The film with intermediate Pd coverage (0.3 ML) exhibits in this respect also an intermediate behaviour. It follows that in the double row structure a mixture of Pd and Au atoms is exposed to the gas phase. The local Pd concentrations depend strongly on the initial Pd coverage. However, it can not be decided, where the Pd atoms are located. Besides the possibility that they are incorporated into the top atom chains within the double rows, it can also be assumed that Pd atoms have replaced Au atoms from the added rows of the original missing row structure.

A comparison of the vibrational spectra of CO adsorbed on Pd-Au(110) surfaces with spectra from the CO/Pd(110) system (HREELS measurements by Chesters et al. [144]) reveals several differences between the CO species on Pd(110) and CO adsorbed on Pd rich areas of the bimetallic Pd-Au(110) surface. Whereas in the low CO coverage limit the agreement is rather good with a single band located around 235 meV in both cases, the CO saturated surfaces give rise to very different HREEL spectra. Low temperature (110 K) CO saturation of the

Pd(110) surface results in a strong band at 248 meV with a small shoulder at 262 meV. For intermediate CO coverages a continuous peak shift from 235 meV to 248 meV is observed. At 300 K, the behaviour of the CO/Pd(110) system is complicated by the formation of a (1×2) missing row reconstruction at intermediate CO coverages (for details see section 5.1.2). Up to three different C–O stretching modes are observed simulaneously, but their relative intensities and locations do not correspond to the douplett occuring in the case of CO/Pd-Au(110) at 242 meV and at 257 meV. Also, at 300 K only a small peak is observed in the region for linearly bonded CO (255 meV). Hence, the CO adsorption behaviour on the Pd-Au(110) surfaces that were prepared at low temperatures can not be explained by effects observed on the pure Pd(110) surface. The chemical behaviour of the annealed Pd-Au(110) surfaces is even more different to the properties of the Pd(110) surface.

In conclusion, the CO adsorption on Pd-Au(110) surfaces is still far from being well-understood. Without direct evidence for the local surface composition it can not be decided about the nature of the different observed CO species. Only for the annealed surfaces, it is plausible to ascribe the single peak around 257 meV to CO molecules on-top of single Pd atoms or on small Pd clustes within a Au environment.

5.5 Conclusions: CO adsorption on Au-Pd(111) surfaces

Since in the above sections the results obtained by TPD and HREELS measurements have been already discussed in great detail, this concluding section only briefly summarizes the information that can be obtained from a combination of the different methods. Also a short comparison with the CO adsorption properties of related bimetallic surfaces will be given.

CO adsorption on Au step edge atoms. From both methods (TPD and HREELS) it can be inferred that on Au terrace sites of Au/Pd(111) films (coverages from 0.1 ML to 4 ML Au) no stable CO adsorption is possible at 100 K. By using similar preparation procedures for both spectroscopic methods, it could be shown that Au step edge sites are considerably more active towards CO adsorption than Au terrace sites. While in the vibrational spectra only one Au related CO species is detected (C–O stretching frequency at $\sim$263 meV), TPD spectra show several different features on surfaces, where Au step edge atoms are the only possible CO adsorption sites. On completely Au covered Pd(111) surfaces the assignment of the TPD peak with the highest peak temperature (at 200 K) could be unequivocally ascribed to CO desorption from Au kink sites. Two lower temperature features might be caused by CO desorbing from regular A and B

step sites, respectively, but no direct evidence for this proposal could be obtained. From the HREELS measurements it can be concluded, that CO on Au kink sites and on regular Au step edge sites exhibit an indistinguishable C–O stretching frequency ($\Delta\nu_{C-O} \leq 1\,\mathrm{meV}$).

CO adsorption on AuPd(111) surface alloys. Here, a coherent picture for CO adsorption on surfaces with low Pd content ($c_{pd} \leq 24\%$) emerges from the comparison of TPD and HREELS data. While the former show distinct desorption peaks from Pd monomers, dimer-bridge sites, dimer-on-top sites, and threefold hollow sites, the latter method provides insight into the low temperature CO–surface interaction with distinct C–O stretching peaks for CO adsorbed in on-top, bridge, and threefold configurations depending on both surface Pd content and CO coverage. For Pd concentrations that are low enough to ensure that essentially all Pd atoms have only Au neighbour atoms, HREELS exhibits a C–O stretching vibration at 259 meV. The corresponding desorption peak is observed around 300 K. Also clear evidence is provided for Pd dimers to provide two on-top adsorption sites for CO (at high coverages) or, alternatively, one more stable brigde adsorption site at lower CO coverages. This will be clarified in the following. A direct comparison between the two experimental methods is possible for a surface with 12% Pd. On the saturated surface only linearly bonded CO is visible in the HREEL spectrum (spectrum a in fig. 5.28), while three TPD features are observed from a similar surface alloy (fig. 5.9). An STM analysis of the surface that was used for the HREELS experiment reveals that besides 9% Pd monomers already 2% twofold Pd sites are available (figs. 5.29 and 5.32). Two alternative explanations are possible: First, it can be proposed that at low CO coverages primarily the bridge sites are occupied. Only at higher coverages the molecules are forced to shift to the unfavourable on-top sites to enable a second CO molecule to adsorb on the Pd dimer. Second, in an alternative explanation the occupation of Pd bridge sites could be replaced by adsorption of CO on one of the two on-top sites of a Pd dimer. The appearance of a high temperature TPD peak (340 K) would then be the consequence of an electronic effect, namely the enhanced reactivity of a Pd atom due to an additional Pd neighbour atom. The second proposition seems to be not very plausible, considering the behaviour of CO on Pd low index crystal surfaces. On both Pd(100) and Pd(110) the bridge site is strongly favoured over the on-top site and on Pd(111) linearly bonded CO is only found in highly compressed adsorbate structures. Since the latter case is dominated by strong repulsive CO–CO interactions it can not be used as argument for the occurence of linearly bonded CO in the present case (low CO coverages on a 12% Pd surface alloy).

The strongest argument for the occupation of Pd bridge sites on Au rich AuPd(111) surface alloys is provided by a second set of measurements on surfaces with 23% Pd (HREELS, fig. 5.33) and 24% Pd (TPD, fig. 5.10), respectively. For

this surface the CO coverage dependence has been explicitly studied by HREELS. Here, clear evidence is obtained for the occupation of bridge sites at low and intermediate CO coverages. Since the amount of threefold hollow sites on this surface is very small (0.4% ML) the strong energy loss peaks around 238 meV can only be explained by CO on the abundant Pd bridge sites. The HREEL spectrum from the saturated surface allows also the conclusion that not only on Pd dimers, but at least on some of the larger linear Pd clusters on-top sites are preferred over bridge sites for CO saturation coverages. This follows from the STM observation that more than 5% ML of non-dimer Pd bridge sites are available on this surface, while for CO saturation the HREELS peak from bridge bonded CO is about one order of magnitude lower compared to the peak from linearly bonded CO. Even though vibrational peaks can not be used as a quantitative measure of adsorbate coverages and the scattering cross section possibly decreases for high coverages, the reduction of the peak intensity at 238 meV for saturation CO coverages on the 23% Pd surface alloy is too strong to be explainable by these effects. On the other hand, in TPD spectra from a 24% Pd containing surface alloy, no indication for an additional peak from CO that is linearly bonded to longer Pd chains can be found. A significant increase in the broad low temperature desorption feature could be a consequence of such locally compressed CO structures. From the CO/Pd(110) adsorption system it is known that on close-packed Pd atom chains (nn distance 2.75 Å) the CO:Pd ratio can be as high as 1. The repulsive CO–CO interaction is then accommodated by a lateral tilt of the molecule [142, 145].

Comparison with PdCu(111) and PdAg(111) alloy surfaces: electronic effects vs. geometric effects. The CO adsorption properties of $Pd_{0.75}Cu_{0.25}$ and $Pd_{0.67}Ag_{0.33}$ alloy crystals with approximately 70% and 10% Pd in the (111) oriented surface layer[22] have been studied by Noordermeer, Kok, and Nieuwenhuys (NKN) [191–193]. A comparison with these systems is interesting, because the noble metals Cu, Ag, and Au exhibit similar chemical properties with respect to CO adsorption. Unfortunately, only TPD data for CO adsorption at 250 K are available for the alloy surfaces and for each alloy only one type of surface composition was examined. While the $Pd_{0.70}Cu_{0.30}(111)$ surfaces can be compared with high Pd concentrations in AuPd(111) surface alloys, the $Pd_{0.10}Ag_{0.90}(111)$ surface allows the comparison with Au rich AuPd(111) surfaces. According to LEED, both alloys exhibit a disordered surface. On the PdAg surface mainly Pd monomers are available. Using a heating rate of 30 K/s, NKN observed a single desorption peak slightly below 400 K. From Redhead's equation they estimated an activation energy for desorption of 112 kJ mole^{-1} (assumed $\nu : 1.0 \cdot 10^{15}\mathrm{s}^{-1}$). Regarding the PdCu alloy, that contains about 70% Pd in the surface layer, a comparison of the CO TPD spectra with Pd(111) reveals three major differences:

[22] These surface Pd concentrations are only estimates based on AES data.

the maximum desorption temperature is decreased from 500 K to 450 K, the high temperature feature is more strongly reduced than the lower temperature features (300 K – 400 K), and the CO saturation coverage is only about one third of the saturation coverage on Pd(111) at 250 K. The observations that adding Cu into the surface layer causes a decrease of both the maximum desorption temperature and the relative height of the high temperature desorption peak is in good qualitative agreement to the TPD measurements from AuPd(111) surface alloys with 55% – 75% Pd. The reason for this behaviour is simply that the amount of available threefold Pd sites decreases more strongly than the Pd content of the surface. On the Ag and Au sites, respectively, an additional desorption channel becomes available which leads to an increase in the prefactor for desorption (precursor state). The drastic decrease of the CO saturation coverage by adding only 30% Cu to the surface layer might be a consequence of the relatively high CO adsorption temperature (250 K).

More interestingly, the observations on the PdAg(111) surface with only $\sim$ 10 % Pd in the surface can be quantitatively compared to the TPD measurements on AuPd(111) surfaces with 8% – 12% Pd. While in the latter case a peak temperature of 310 K – 320 K is observed for desorption from Pd monomers, the corresponding value on PdAg(111) is considerably higher (375 K). Even if the different heating rates are accounted for (10 K/s vs. 30 K/s) a substantial difference in the activation energies for desorption is found ($\Delta E_d \approx 25\,\mathrm{kJ\,mole^{-1}}$). Since the adsorption geometry is identical in both cases, this difference might be attributed to an electronic effect. However, DFT calculations by Ruban et al. show that the d band shift for Pd impurity atoms in an Ag and in a Au matrix should be almost identical (+0.14 eV for Ag and +0.17 eV for Au) [106]. Therefore, no explanation for a strongly enhanced reactivity of Pd monomers in a Ag environment vs. a Au environment is provided by theory. One reason for the disagreement between experiment and theory might be that the lattice constants for the calculations are assumed to be equal to the bulk value of the respective host metal (here: Pd), while the $Pd_{0.67}Ag_{0.33}$ bulk alloy and the AuPd surface alloys exhibit different lattice constants.

Chapter 6

C_2H_4/ Au-Pd(111) surfaces

The organization of this chapter dealing with C_2H_4 adsorption on Au-Pd(111) surfaces follows a similar outline as the previous chapter on CO adsorption. First a review on some relevant studies about C_2H_4 adsorption and reaction systems will be given. Then the experimental results that were obtained in the course of this work will be presented. Since not much measuring time was left for C_2H_4 TPD investigations, only few TPD results are available. This chapter centres on HREELS measurements, because they provide the most relevant findings for the C_2H_4/Au-Pd(111) system. In addition to experiments on bimetallic Au-Pd(111) surfaces, it was found to be necessary to clarify some aspects for the C_2H_4/Pd(111) system by careful coverage and temperature dependent HREELS measurements, even though this system has been characterized already by HREELS in the past [194–197]. XPS and STM experiments on the decomposition behaviour of C_2H_4 on different AuPd(111) surface alloys provide supplementary information to the HREELS measurements. The chapter will be concluded by a discussion of the various experimental results.

6.1 Earlier studies on C_2H_4/Pd

As an introduction to the presentation and discussion of earlier experimental investigations on the interaction between C_2H_4 and Pd surfaces, some general aspects of C_2H_4 chemisorption on metal surfaces will be considered first. The subsequent review over previous experimental studies should provide insight into the relatively broad variety of phenomena that have been encountered on different Pd surfaces. While in the case of the "simple" molecule CO a detailed theoretical understanding of various aspects of the interaction with metal sufaces could be obtained with the help of ab-initio calculations, no consistent theoretical description is available for the far more complex case of C_2H_4 chemisorption and decomposition. For instance, no accurate theoretical predictions for the reaction pathways or activation energies are available for C_2H_4 dehydrogenation

property	π bonding	di-σ bonding
scheme of adsorption geometry	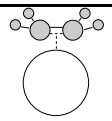	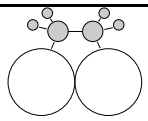
hybridization state of C atoms	sp^2	sp^3
preferred behaviour upon heating	molecular desorption	decomposition
vibrational model system	Zeise's salt $K[(C_2H_4)PtCl_3]$	1,2-dibromoethan $C_2H_4Br_2$
$\pi\sigma$ parameter	0.38	1.00
C–H_2 stretch (s)	373	366

Table 6.1: Typical properties of π and di-σ C_2H_4–metal adsorption systems. The adsorption geometry is idealized in order to illustrate the possible effects of different hybridization states of the C atoms and does not necessarily correspond to the experimentally determined adsorption sites — e. g., on Pt(111) di-σ bonded C_2H_4 is found to be adsorbed in a tilted configuration near to threefold hollow sites by "diffuse LEED" [198].

reactions on different metal surfaces. Therefore, theoretical studies concerning the C_2H_4/Pd system will only be mentioned in the course of the later discussions and are not included in this review section.

6.1.1 General aspects of C_2H_4 chemisorption and decomposition reactions

Molecular adsorption of C_2H_4 is observed on the late transition metal surfaces at low temperatures. Due to the interaction with a metal surface, the geometric and electronic structure of the C_2H_4 molecule is changed compared to the gaseous state. The most commonly employed experimental tools to characterize the properties of the adsorbed molecular form of C_2H_4 are vibrational spectroscopies (HREELS, RAIRS, SFG) and valence band photoemission spectroscopy (UPS). For both techniques it has been found convenient to discuss C_2H_4 adsorption within a simple conceptional framework. This consists in the distinction between two limiting cases of C_2H_4–metal interactions, namely π and di-σ bonding. The properties of these two adsorption modes are summarized in table 6.1. In short, π bonding is found in cases where the molecular structure is only slightly perturbed upon adsorption on a metal surface, indicating a weak C_2H_4–metal interaction. In contrast, di-σ bonding requires a strong rehybridization of the C atom valence electrons in the C_2H_4 molecule which is induced by a strong interaction with the metal surface. Consequently, surfaces that exhibit π bonded

surface	π bonding	di-σ bonding	intermediate	reference
Ni(111)		X		[199]
Ni(110)		X		[200]
C-Ni(110)	X			[200]
Pd(100)			X	[201]
O-Pd(100)	X			[201]
Pd(110)	X			[144, 202]
Pd(111)	X			[195, 197]
Pt(111)		X		[198, 203]
O-Pt(111)	X			[203]
Pt(110)(1 × 2)			X	[204]
H-Pt(110)(1 × 2)	X			[204]
Cu(111)	X			[205]
Ag(110)	X			[206]
O-Ag(110)	X			[206]

Table 6.2: Examples for C_2H_4–metal adsorption systems. The different systems are classified according to the references. Cases where the coexistence of two different species have been suggested are classified as intermediate systems.

C_2H_4 are relatively inert towards C_2H_4 dehydrogenation reactions, whereas on surfaces where di-σ bonded C_2H_4 is formed at low temperatures C_2H_4 is readily dehydrogenated at room temperature and above. While for some C_2H_4–metal systems the decision about the bonding mode is found to be unequivocal, there are also cases where an intermediate behaviour is observed. Some examples that might be relevant for the following discussions are listed in table 6.2.

Although the vibrational properties of C_2H_4–metal adsorption systems give only indirect evidence for the electronic configuration of the adsorbed species, the distinction between π and di-σ surface species has most commonly been based on HREEL spectra. Unfortunately, some of the different vibrational modes of the C_2H_4 surface species are strongly coupled, and the assignment of the vibrations is not unambiguous in all cases. This prevents the derivation of a simple correlation between the C–C stretching frequency — that should in principle contain information of the C–C bond order and hence of the hybridization state of the C atoms — and the adsorption mode. It was suggested by Stuve, Madix, and Brundle (SMB) [201] to combine the values of the two strongly coupled vibrations ν(CC) (C–C stretching) and $\delta(CH_2)$ (CH_2 scissoring) into a single number, the so-called $\pi\sigma$ parameter. This can be calculated by inserting the vibrational energies (in meV) of the two mentioned modes as band I (higher energy vibration)

and band II (lower energy vibration) into equation 6.1. The numbers 201.2 meV and 166.4 meV are the gas phase values for the ν(CC) and the $\delta(CH_2)$ modes of C_2H_4, respectively. The $\pi\sigma$ parameters for important C_2H_4 containing reference systems range from 0 for gas phase C_2H_4 (sp^2 hybridization) via 0.38 for Zeise's salt[1] to 1 for 1,2-dibromoethane (sp^3 hybridization).

$$\pi\sigma(C_2H_4) = \left(\frac{201.2 - \text{band I}}{201.2} + \frac{166.4 - \text{band II}}{166.4}\right)\frac{1}{0.366} \qquad (6.1)$$

Obviously, the $\pi\sigma$ parameter can only be applied after a careful assignment of the different vibrational modes in the region 100 meV–200 meV, which usually requires the comparison between spectra from C_2H_4 and from C_2D_4. Since on the Au-Pd(111) surfaces, that were investigated in this work, only experimental results for non-deuterated ethylene have been obtained, the $\pi\sigma$ parameter alone can not be used to describe the surface C_2H_4 species. There are other possibilities to distinguish between weakly, more π like bonded species and strongly, more di-σ like bonded species. For a number of systems, where the distortion of the C_2H_4 moleculs upon adsorption is only small (e. g., on Cu(111) [205], on O precovered Pd(100) [201], or for a π bonded C_2H_4 species formed at 150 K on Pt(111) under "high" pressure (13 mbar) conditions [208]) the out-of-plane CH_2 wagging vibration is found between 112 meV and 118 meV, and it is the most prominent peak in the HREEL spectra. Another general observation is a continuous red-shift of the C–H_2 stretching frequencies ($\nu(CH_2)$) for increasing bond strength to the metal surface. It is advantageous to monitor these high energy modes, because they can easily be identified and the vibrational coupling to other modes is negligible. However, the overall shift in the $C - H_2$ stretching frequencies is not very large ($\Delta\nu(CH_2) = 7$ meV if Zeise's salt and 1,2-dibromoethan are compared) and a good resolution in the HREEL spectra is required to make definite statements about significant peak shifts in this region. This might be the reason for the relatively little attention that has been paid to the interpretation of the $\nu(CH_2)$ peaks in the past.

6.1.2 Earlier experimental results for C_2H_4/Pd

Even though C_2H_4 adsorption on metal surfaces has not been studied to the same extent as CO adsorption, the basic properties of the interaction between C_2H_4 molecules and Pd single crystal surfaces have been revealed by several groups in the past. In the focus of these previous experiments were the related questions about the nature of the chemisorbed C_2H_4 species observed at low surface temperatures and about the competition between thermal desorption

[1] This value is given by SMB; based on a more recent vibrational analysis of Zeise's salt [207] a $\pi\sigma$ parameter of 0.33 can be calculated.

and thermal decomposition of C_2H_4. These questions were mainly addressed by HREELS and TPD measurements supplemented by some qualitative LEED investigations. Generally it is found that upon heating the sample only a fraction of a molecularly chemisorbed C_2H_4 layer on Pd low index planes is dehydrogenated while the remaining part desorbs molecularly. The details of the C_2H_4 surface reactions on Pd are still far from being completely understood. For example, it is not clear which electronic and/or geometric factors of a metal surface determine the extent of C_2H_4 decomposition. In this section, previous experimental findings concerning the interaction between C_2H_4 and different Pd low index surfaces will be summarized in order to provide some background information for the discussion of the experimental results that have been obtained in the course of this work for C_2H_4 adsorption on Pd(111) and on different bimetallic Au-Pd(111) surfaces and that will be presented below.

C_2H_4/Pd(111)

A first HREELS analysis on the vibrational properties of $C_2H_4(C_2D_4)$ on Pd(111) is reported by Kesmodel and Gates (KG). They characterized the low temperature adsorption state of C_2H_4 on Pd(111) (150 K) [195], its thermal decomposition (up to 500 K) [196], and also the species that is found upon room temperature adsorption [194]. The spectra were recorded using a primary beam energy of 3.3 eV and a resolution of typically 10 meV. Only spectra for saturation C_2H_4 coverages are reported. At 150 K the C_2H_4 molecules are π bonded to the Pd(111) surface according to KG. This is inferred from the relatively high C–C and CH_2 stretching frequencies (186 meV and 371 meV, respectively) for this adsorbate system. A second low energy CH_2 stretching band at 345 meV was ascribed to hydrogen atoms that are interacting directly with the Pd surface in a hydrogen bond-like manner. Because two CH_2 stretching bands are observed, KG propose that the hydrogen atoms of the adsorbate molecules are not equivalent. This is explained by an adsorption geometry where the molecular plane is tilted with respect to the surface plane. The assignment of the vibrational frequencies of C_2H_4/Pd(111) at 150 K are summarized in table 6.3. Heating the low temperature adsorbed C_2H_4 layer to 300 K causes the HREEL spectrum to be significantly altered. Only two distinct loss peaks remain at 113 meV and at 165 meV, which are characteristic frequencies for ethylidyne (CCH_3) [194]. Since no other surface species was observed by KG in the temperature range between 150 K and 300 K, they concluded that ethylidyne is the first stable intermediate decomposition product of C_2H_4 on Pd(111). However, only a small part of the molecules that are bonded to the surface at low temperatures are dehydrogenated. The major part desorbs molecularly upon heating the sample to 300 K. This is inferred by KG from the finding that the ethylidyne loss peaks are much weaker after heating a C_2H_4 saturated Pd(111) surface from 150 K to 300 K than in the case of direct adsorption

assignment	Pd(111)[a]	Pd(110)[b]	Pd(100)[c]	Pt(111)[d]	Zeise's salt[e]	$C_2H_4Br_2$[f]
Me–H stretch (s)	32					
Me–C stretch (s)	42/45	42/43	48	58	50	
Me–C stretch (as)	66/56	66/66		69	61	
other M–C		33/35,47				
CH_2 rock	86/-	97/-		82	92	111
CH_2 rock		108/-			105	
CH_2 wag	113/114	112/112	114	112	128	
CH_2 wag	134/-	129/-		121	129	158
CH_2 twist	142/146	140/-		98		137
CH_2 scissor (s)	152/-	153/154	180	177	190	176
CH_2 scissor (as)	177/-	175/175			176	
C–C stretch	186/177	188/188	141	132	156	126
C–H_2 stretch (s)	372/370	372/372	369	362	373	366
C–H_2 stretch (as)	-/381	383/379		372	381	373

[a] T = 150 K; from ref. [195]/ [197].
[b] T = 90 K; from ref. [202] / T = 110 K; from ref. [144].
[c] T = 80 K; from ref. [201].
[d] T = 92 K; from ref. [203].
[e] $K[(C_2H_4)PtCl_3]$; from ref. [207].
[f] Gauge form; from ref. [209].

Table 6.3: Vibrational frequencies for different C_2H_4 saturated metal surfaces. The values for Zeise's salt and for 1,2-dibromoethan have been included as references for π and di-σ bonded C_2H_4, respectively. For Pd(111), the CH_2 bending vibrations were not broken down into the different modes in the reference; the more detailed assigments in the table were arrived at by comparison with the related system Pd(110).

at 300 K. The next species which is identified by KG is methylidyne (CH), which gives rise to loss peaks at 97 meV and at 367 meV. These peaks are found already at 300 K together with the ethylidyne peaks. After heating to 400 K, the methylidyne derived features are the only peaks in the spectrum (besides a strong peak caused by coadsorbed CO). By comparing the decomposition behaviour of C_2H_4 with that of C_2H_2 on Pd(111), KG arrive at the conclusion that the methylidyne groups are not formed primarily by decomposition of ethylidyne but rather by a parallel process. This is justified by the following arguments. C_2H_4 and C_2H_2 adsorption lead to similar intensities of the ethylidyne related peaks and therefore it seems that a similar amount of ethylidyne is formed from both molecules. After heating of these ethylidyne covered Pd(111) surfaces much stronger methylidyne derived peaks are found for the C_2H_2 prepared surface than for the C_2H_4 preparation. Therefore, ethylidyne decomposition is considered to provide at most

a minor part of the CH species observed at 400 K. However, the arguments of KG are solely based on the comparison of HREELS peak intensities and might therefore be questioned.

The effect of oxygen coadsorption with C_2H_4 and with C_2H_2 was studied by Nascente et al. using HREELS and LEED [197]. Their frequency assignments for the C_2H_4/Pd(111) system are also included in table 6.3. In the case of C_2H_4 no oxygen derived changes of the C_2H_4 HREEL spectra were observed and also the ordering behaviour of the C_2H_4 derived surface species did not change. At low temperatures (150 K) C_2H_4 adsorbs disorderedly on Pd(111) and around room temperature a $(\sqrt{3} \times \sqrt{3})R30°$ superstructure is observed, which is attributed to an ordered ethylidyne structure. These findings are in accordance with earlier LEED investigations of Gates and Kesmodel [195].

Combined molecular beam, TPD, LEED, and ARUPS investigations on the C_2H_4/Pd(111) system have been performed by Tysoe, Nyberg, and Lambert (TNL) [210]. Since no ordered structures are detected at low temperatures, only an indirect determination of the surface coverages for molecularly adsorbed C_2H_4 was possible. For C_2H_2 a $(\sqrt{3} \times \sqrt{3})R30°$ structure is observed by LEED at a coverage of 0.33 ML. From this the molecular beam source could be calibrated by TNL for C_2H_2. Assuming that for a given source pressure the molecular beam fluxes of C_2H_2 and of C_2H_4 are identical, this gives also an absolute calibration for the C_2H_4 flux. Based on this procedure the saturation coverage of C_2H_4 was determined to be $\sim$0.33 ML at 175 K. The initial sticking probability of 0.8 was found to be constant up to $\sim$0.2 ML, indicating precursor mediated adsorption kinetics. Reactive scattering of C_2H_4 at the Pd(111) surface is found to yield C_2H_6 together with C_4 and C_6 products even at room temperature. However, from low temperature adsorbed C_2H_4 layers only C_2H_4 and H_2 were observed as desorbing products. For low C_2H_4 coverages (0.05 ML) an Arrhenius analysis of the desorption peak (300 K for 20 K/s heating rate) yields an activation energy of $\sim 54\,\mathrm{kJ\,mole^{-1}}$ and a prefactor of $\sim 3{\cdot}10^9\,\mathrm{s^{-1}}$. Upon increasing the C_2H_4 dose the initial C_2H_4 desorption peak at 300 K is broadened considerably towards lower temperatures and for saturation doses it reaches down to the lowest temperatures without exhibiting any clear structures. Depending on the initial C_2H_4 coverage at 175 K, only between 2% (for saturation coverages) and 4% (for 0.05 ML C_2H_4) of the adsorbed molecules were found to be decomposed during a TPD heating cycle (20 K/s to 600 K). If the C_2H_4 dosing was carried out around room temperature, only H_2 desorption was observed in subsequent TPD experiments. From the similarity between UP spectra recorded on C_2H_4 saturated Pd(111) and spectra from gaseous C_2H_4 it was inferred by TNL that the electronic structure of the molecule is essentially unperturbed after adsorption on Pd(111) at 155 K, which is in good agreement with the above mentioned HREELS derived determination of C_2H_4 being π bonded to Pd(111) at 150 K [195]. Angular resolved UPS indicates that the molecular C–C axis lies parallel to the Pd(111) surface, which

is at variance to the earlier proposal by Kesmodel and Gates of a tilted C_2H_4 adsorption geometry.

In a more recent combined UPS, XPS, and NEXAFS study by Wang et al. the findings of TNL (π bonding of C_2H_4 with the C–C axis parallel to the surface) were essentially confirmed for C_2H_4 saturated Pd(111) at 100 K [211]. From their NEXAFS data Wang and coworkers deduced a C–C bond length of 1.43 Å. This value can be compared to the bond length of gas phase C_2H_4 (1.34 Å) and C_2H_6 (1.54 Å) molecules. The C(1s) photoemission peak for molecularly bonded C_2H_4 was found at a binding energy of 283.6 eV. Almost the same C(1s) binding energy is measured upon room temperature C_2H_4 adsorption, namely 283.1 eV. From XPS C(1s) peak areas that were calibrated against known C_2H_2 coverages, a saturation coverage of 0.42 ML C_2H_4 at 100 K was determined. For this coverage the work function is decreased by 1.08 eV indicating electron transfer from the adsorbate to the substrate. Heating of a C_2H_4 saturated layer from 100 K to 300 K causes the C(1s) peak to vanish, which shows that almost all molecules desorb from the surface without being decomposed. Monitoring the C(1s) photoemission peak in a C_2H_4 adsorption sequence at 300 K shows that the sticking coefficient at this temperature is very low ($\sim$0.01).

Sum Frequency Generation (SFG) was employed by Eichhorn, Heuer, and Zacharias to characterize the different C–H stretching modes for chemisorbed C_2H_4 on Pd(111) at 130 K [212]. The measurements were performed with a background C_2H_4 pressure of 10^{-7} mbar, which ensures a saturation adsorbate coverage. By comparing measurements with different polarization geometries of the laser beams and of the detected photons Eichhorn and coworkers could assign a resonance at 370.8 meV to the totally symmetric ν_1 mode and two features at 369.5 meV and at 371.7 meV to the two mirror-symmetric ν_{11} and ν_9 modes, respectively[2]. A room temperature RAIRS study at relatively high C_2H_4 background pressures is reported by Kaltchev, Thompson, and Tysoe [214]. Under UHV conditions (80 L C_2H_4 dose) they found a typical ethylidyne spectrum with peaks at 164.8 meV (methyl bending mode) and at 135.0 meV (C–C stretching mode). The former frequency is well separated from any infrared active gas phase vibrations of C_2H_4 and therefore it can be monitored by RAIRS also in the presence of gaseous C_2H_4. Upon increasing the C_2H_4 pressure up to 1.0 Torr only a broadening of the peak is observed, but no measurable peak shift. Therefore, ethylidyne is found to be present on Pd(111) also under conditions which are much closer to a realistic reaction environment compared to the above mentioned HREELS studies in UHV. However, it can not be excluded by Kaltchev et al. that additional C_2H_4 derived surface species are formed at higher pressures, because only a narrow frequency window was monitored.

[2]The numbering of the modes is taken from the gas phase nomenclature (see [213]).

C_2H_4/Pd(110)

Angular and coverage dependent HREELS measurements for C_2H_4 and C_2D_4 adsorption on Pd(110) at 110 K are reported by Chesters et al. [144]. They observed two types of related but distinguishable types of spectra for low and for high C_2H_4 coverages, respectively. Most of the peaks are in good agreement with the assumption of π bonded molecules being the predominant species on the surface. Only for high coverages, some additional features are ascribed to a small proportion of di-σ bonded C_2H_4. The assignment of the different loss peaks for the high coverage spectra is included in table 6.3. The thermal decomposition of C_2H_4 on Pd(110) was studied by Nishijima et al. using HREELS, LEED, and TPD [202]. At 90 K there is a mostly-disordered adsorption of C_2H_4 on Pd(110). Only for saturation coverages (0.58 ML) a weak $c(2\times2)$ LEED pattern is observed indicating the formation of some ordered patches. Heating to 260 K causes some of the molecules to desorb and a clear $c(2 \times 2)$ pattern is found. In contrast to Chesters et al. Nishijima and coworkers find no indication of a second C_2H_4 species at high coverages. From the relatively high symmetric CH_2 stretching frequency of 372 meV they infer that the molecules are π bonded to the surface. Their peak assignment can also be found in table 6.3.

Upon heating of low temperature C_2H_4 adsorbate layers, C_2H_4 and H_2 are the only desorbing species. For small C_2H_4 doses only the decomposition product H_2 is found to desorb. H_2 TPD spectra exhibit two desorption peaks at $\sim$330 K (β) and at $\sim$475 K (γ), respectively. These spectra are very similar for all C_2H_4 doses and especially the intensity ratio β:γ is found to be constant at 3:1. From a saturated C_2H_4 layer two desorption features for molecular C_2H_4 are found. A broad low temperature plateau is followed by a peak at 300 K. From a mixed C_2H_4/C_2D_4 layer also $C_2H_xD_{4-x}$ molecules are observed as desorption products in the 300 K peak, but not in the low temperature plateau. Therefore, the molecules that desorb at 300 K seem to be recombination products of H atoms and some hydrocarbon species. HREEL spectra of annealed C_2H_4 layers on Pd(110) provide evidence for the existence of ethynyl (CCH) as a stable intermediate for C_2H_4 dehydrogenation at 300 K, which is in good agreement with the stoichiometry of the adsorbate layer that should be C_2H at this temperature according to the ratio of the H_2 TPD peak intensities. Since at the same temperature C_2H_4 desorption occurs from recombination reactions it can also be assumed that vinyl species ($CHCH_2$) are formed as unstable intermediates. However, no indications for the existence of a vinyl species are detected by HREELS. After annealing at 520 K a single peak is observed in the HREEL spectra at 64 meV. It is ascribed to the stretching vibration of C adatoms against the Pd(110) surface.

Nishijima and coworkers report also a combined HREELS, TPD, and LEED study on C_2H_4 adsorption on Cs precovered Pd(110) [215] ($\theta_{Cs} \approx 0.1$ ML). Cs induces a (1×2) missing row reconstruction of the Pd(110) surface. While the low

temperature HREEL spectra of C_2H_4 are not altered markedly by the presence of Cs, several other Cs induced changes are observed:

- The C_2H_4 saturation coverage is reduced from 0.58 ML to 0.23 ML.
- For large C_2H_4 exposures some physisorbed molecules are found to exist on the surface at 90 K.
- π bonded C_2H_4 is destabilized by Cs, which manifests itself in lowered desorption temperatures.
- The fraction of molecules that are thermally decomposed is slightly reduced (from 65% to 56%).

The observed general Cs related reduction in the interaction strength between π bonded C_2H_4 and the Pd(110) surface can be explained by an electron transfer from the Cs atoms to the surface and a concomittant reduction of C_2H_4 to metal electron donation, which is considered to provide the main contribution to the π C_2H_4-metal bond.

C_2H_4/Pd(100)

Combined HREELS and TPD studies of C_2H_4 and C_2D_4 adsorption on clean Pd(100) and on oxygen precovered Pd(100) are reported by Stuve, Madix, and Brundle (SMB) [201,216,217]. In short, they find that at low temperatures (80 K) the HREEL spectra for C_2H_4 saturated Pd(100) can be explained by a di-σ bondend C_2H_4 species on the surface ($\pi\sigma$ parameter 0.7). The peak positions and assignments by SMB are listed in table 6.3. The saturation coverage was estimated to be 0.37 ML. On the clean Pd(100) surface the larger part (0.25 ML) desorbs molecularly upon heating and only about one third of the molecules undergoes decomposition. Preadsorption of oxygen atoms on the Pd(100) surface up to a coverage of $\theta_O = 0.25$ ML leads to a gradual decrease of the amount of C_2H_4 molecules that are found to decompose upon heating, but on the other hand the number of desorbing C_2H_4 molecules is not affected by the O precoverage. HREEL spectra for C_2H_4 saturated surfaces are also changed by a 0.25 ML O precoverage and show features that point to π bonding of the C_2H_4 molecules ($\pi\sigma$ parameter 0.3). As explanation for these findings, SMB propose that on clean Pd(100) two different forms of chemisorbed C_2H_4 coexist at low temperatures. The form which is more strongly bonded (di-σ species) is inhibited by preadsorption of O molecules, such that for 0.25 ML O only the more weakly bonded molecules (π species) remain. In this respect, the C_2H_4 and O coadsorption system is behaving similarly on Pd(100) as on Pt(111), where an oxygen induced change from di-σ bonding to π bonding was observed by Steininger, Ibach, and Lehwald as well [203]. As general explanation for these observations

it is proposed by SMB that di-σ bonded C_2H_4 molecules accept charge from the surface, whereas π bonded C_2H_4 is a net charge donor. Therefore, the former species compete with O adatoms for occupied electronic states at the metal surface, while the latter species is rather stabilized by coadsorbed oxygen because of an increased C_2H_4 to metal electron donation.

The above conclusions on the coexistence of two different C_2H_4 species at low sample temperatures rely on the argument that the decomposition behaviour of the C_2H_4 molecules is largely determined by their properties in the chemisorbed layer at low temperatures and that therefore C_2H_4 molecules that are π bonded at 80 K desorb upon heating while di-σ bonded molecules are dehydrogenated. Since the HREEL spectra from the clean Pd(100) surface do not give any evidence for the coexistence of two different chemisorbed species, no direct experimental proof is available for the above hypothesis. SMB explain this discrepancy by the assumption of a possibly much larger scattering cross section of di-σ bonded molecules compared to π bonded molecules within the C_2H_4 saturated layer on Pd(100) at 80 K. However, a physically sensible argument for this assumption is not given. In this context it has also to be mentioned that the resolution of the HREEL spectrometer employed by SMB (FWHM of 9 meV – 13 meV) was probably too low to distinguish between two closely related chemisorbed species.

Starting from a C_2H_4 saturated surface at 80 K, decomposition of the adsorbed molecules was found by SMB to proceed in 4 steps:

1. After annealing at 200 K a strong new peak at 66 meV is ascribed to the Pd–H stretching vibration and from this the rupture of H–C bonds is inferred by SMB. Since the overall vibrational spectrum of the adsorbate layer has otherwise not significantly changed they propose a vinyl species ($CHCH_2$) to be the first reaction intermediate of C_2H_4 dehydrogenation on Pd(100).

2. The breaking of the C–C bonds is found to occur below 275 K, since upon annealing at this temperature the strong C–C stretching peak at 141 meV is almost completely vanished. After this step the surface is covered by H, CH, and CH_2 species according to SMB.

3. From the disappearance of the CH_2 scissoring mode at 181 meV upon annealing at 300 K it is concluded that only methylidyne (CH) groups remain as carbon containing species on the surface at that temperature.

4. The last dehydrogenation step occurs between 350 K and 500 K by C–H bond scission within the methylidyne groups and manifests itself by two reaction limited H_2 features at 400 K and 460 K in the TPD spectra and by the disappearance of the CH bending (115 meV) and the C–H stretching modes in the HREEL spectra after annealing at 500 K.

As has been mentioned above, 0.25 ML of O atoms are sufficient to completely suppress C_2H_4 decomposition on Pd(100). For lower O coverages a linear relationship between the number of dehydrogenated C_2H_4 molecules and the number of O atoms on the surface has been found. Considering that on the clean Pd(100) surface 0.12 ML C_2H_4 are found to decompose, it can be concluded that two O atoms are necessary to block the decomposition of one C_2H_4 molecule. However, no information on the mechanism for the oxygen induced inhibition of C_2H_4 dehydrogenation is provided by SMB, because the geometric arrangement of the C_2H_4 molecules within the $p(2 \times 2)$ oxygen layer (for 0.25 ML O) is not known.

Jia et al. reported measurements on the oxidation of C_2H_4 on the ordered Pd(100)$c(2 \times 2)$-Mn surface alloy [218]. Employing HREELS and LEED they found that the low temperature C_2H_4 adsorbate layer exhibits a very similar vibrational spectrum as on pure Pd(100). However, in the case of the bimetallic surface no significant change of the HREEL spectra is observed upon O preadsorption. Since HREELS was the only method applied by Jia et al. no statements about possible oxygen related changes in the C_2H_4 saturation coverage or in the binding energy to the substrate could be derived.

6.2 TPD results

In principle, TPD is a very powerful method that is capable of providing information on many aspects of a reactive adsorption system like C_2H_4/Pd(111). For example, adsorption energies, saturation coverages, and the identity of volatile decomposition products can be determined by TPD. Unfortunately, the experimental setup for measuring TPD spectra in the vacuum chamber used for this study exhibited the disadvantage of a high non-linear background signal from outer parts of the Pd crystal if the C_2H_4 dose was too high (see section 2.2). As a consequence, only surfaces with a low Pd content ($c_{Pd} \leq 21\%$), where small C_2H_4 doses are sufficient to saturate the surface, were investigated by TPD. Since no indication of C_2H_4 decomposition on such Au rich surfaces could be found neither by HREELS nor by TPD, only aspects of molecular C_2H_4 adsorption and desorption will be discussed in this section.

In fig. 6.1 an overview is given for the whole range of surface compositions (2% – 21% Pd) that were analysed by C_2H_4 TPD. Apart from some small features around 150 K, that originate from C_2H_4 molecules adsorbed at Au step edge atoms, only one peak centered around 225 K is discernible in each spectrum. For the highest Pd concentration investigated (21%) a high temperature shoulder is visible around 270 K. C_2H_4 coverage dependent TPD measurements for 2%, 10%, and 21% Pd are shown in figs. 6.3–6.5. In fig. 6.2 the peak integrals of the TPD spectra from C_2H_4 saturated AuPd(111) surface alloys are plotted against the surface Pd concentrations. It is obvious that up to about 10% Pd a linear

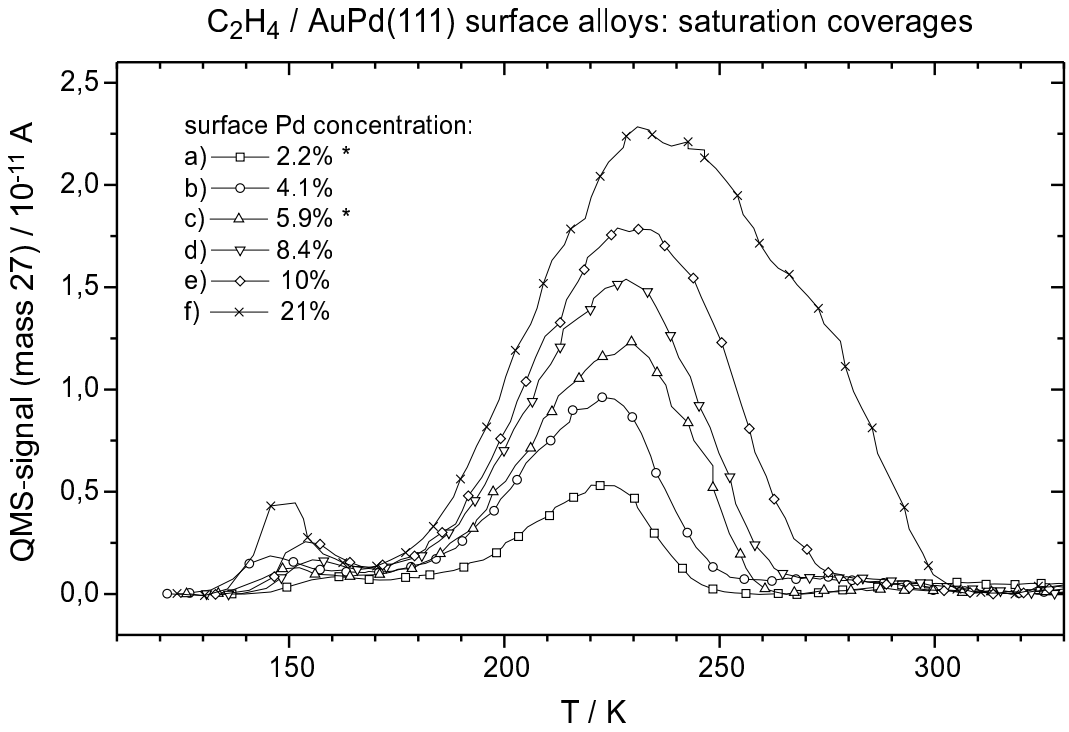

Figure 6.1: C_2H_4 TPD spectra from AuPd(111) surface alloys with Pd concentrations between 2% and 21%. The numbers marked by an "$*$" are only estimates of c_{Pd} based on CO TPD measurements; the other concentrations are derived from atomically resolved STM images. The spectra were recorded after C_2H_4 saturation of the surfaces. A linear background has been subtracted from each spectrum.

relationship between the C_2H_4 saturation coverage and the Pd concentration exists. Since for the lowest Pd concentrations exclusively isolated Pd monomers are found in the surface with an appreciable average distance between two Pd neighbouring atoms, the only rational explanation for this linearity is that each Pd atom is occupied by one C_2H_4 molecule at saturation coverage. For 10% Pd there exist already some Pd dimers in the surface. Hence, the question has to be asked, if some information concerning C_2H_4 adsorption on two neighbouring Pd atoms can be extracted from the plotted intensities. From the 10% Pd atoms about 8% are found as monomers and only 2% are part of Pd dimers or larger Pd clusters[3]. Therefore, the difference between the two possible models (only one C_2H_4 molecule per Pd dimer vs. two C_2H_4 molecules per Pd dimer) amounts to an 10% effect, which is clearly too small to enable a decision between the two possibilities based on the TPD intensities. The intensity for 21% Pd (9% monomers,

[3] The percentages that are given in this paragraph are referring to the total number of surface atoms, i. e., 100% = 1 ML.

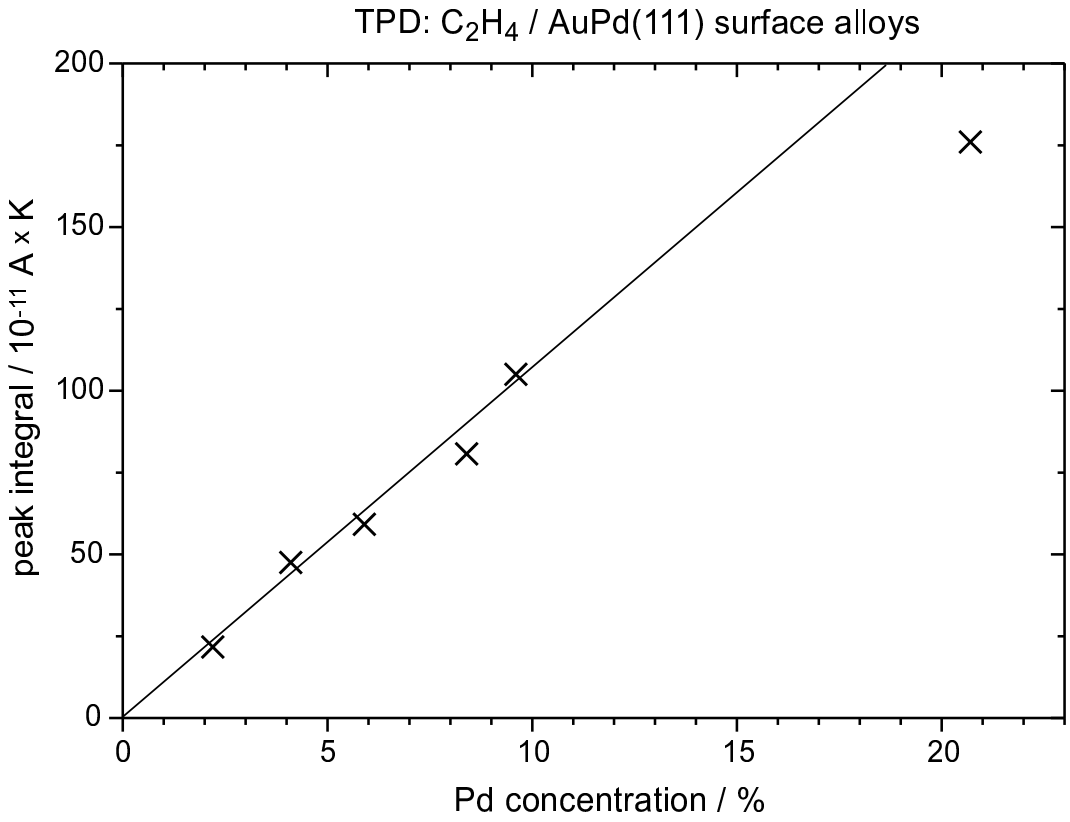

Figure 6.2: Integrated TPD peak areas from C_2H_4 saturated AuPd(111) surface alloys. A linear background has been subtracted from each spectrum prior to integration. The straight line is drawn as a guide for the eye.

3% dimers, and 6% Pd atoms in larger clusters) clearly deviates from the linear behaviour found for lower Pd concentrations. Approximately 0.17 ML C_2H_4 is stable at 100 K on this surface. This leads to the conclusion that at least for three adjacent Pd atoms and possibly already for Pd dimers the 1:1 relationship between local Pd content and C_2H_4 saturation coverage is not valid anymore. However, more precise statements are not possible because of the limited reproducibility of the TPD intensities from measurement to measurement (estimated error: $\sim$ 10%). The line drawn in figure 6.2 represents a 1:1 relation between the amount of desorbing C_2H_4 molecules and the Pd content of the surface and thereby provides an approximate calibration for C_2H_4 saturation coverages on surfaces, where the simple proportionality is not valid anymore. Specifically, it can be estimated that on the surface with 21% Pd about 0.17 ML of C_2H_4 can be adsorbed at 100 K. Compared to the C_2H_4/Pd(111) saturation coverage of only 0.42 ML at this temperature [211] this coverage appears to be quite high ($\sim$ 40% of the saturation coverage). C_2H_4 coverage dependent measurements for this surface alloy (21% Pd) are displayed in fig. 6.5. From the appearance of a

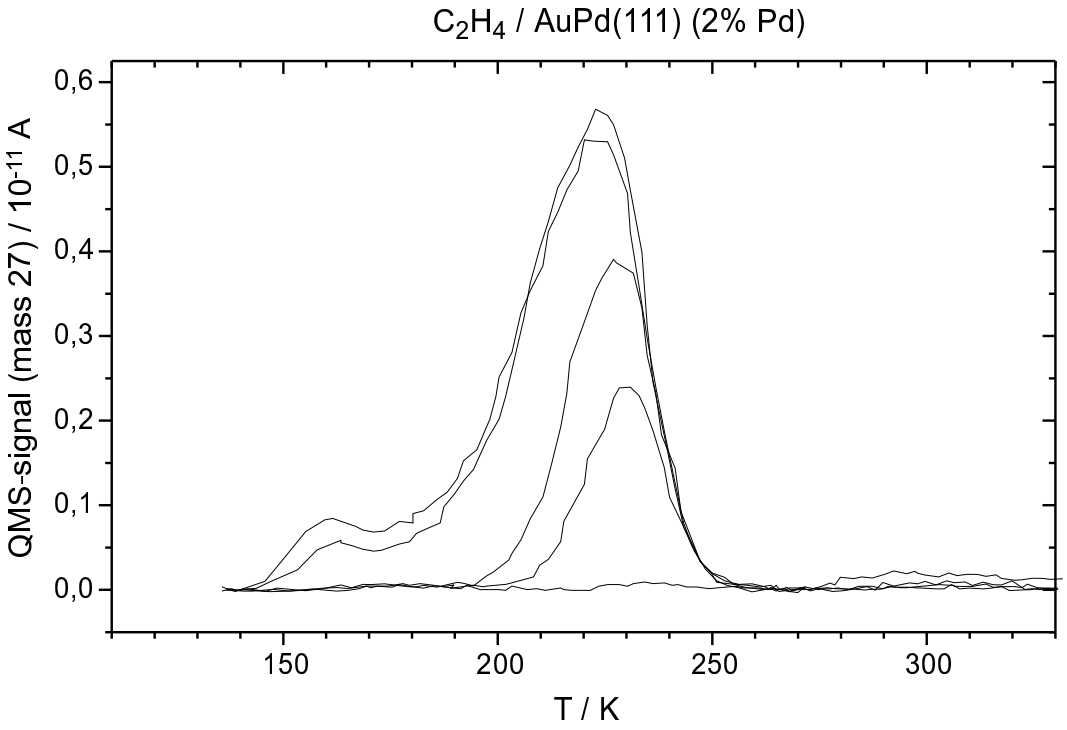

Figure 6.3: C_2H_4 TPD spectra from a AuPd(111) surface alloy with 2% Pd in the surface layer. A linear background has been subtracted from each spectrum.

high temperature shoulder around 270 K it can be inferred that on this surface two different C_2H_4 adsorption states are populated. In principle, TPD peaks and shoulders can also be caused by the formation of stable adsorbate superstructures due to adsorbate–adsorbate interactions. In the present case, however, this possible origin of the observed shoulder can be excluded, because here the arrangement of the adsorbates on the surface is determined by the surface composition (C_2H_4 is bonded only to Pd atoms for $T \geq 170$ K) and not by adsorbate–adsorbate interactions. It is not possible to determine exactly the ratio between molecules that contribute to the main peak (~ 230 K) and molecules that cause the high temperature shoulder (~ 270 K). A rough estimate yields a 3:1 ratio of these two states, i. e., approximately 0.13 ML of C_2H_4 are desorbing in the main peak and 0.04 ML in the shoulder. A comparison with the number of different Pd sites on the surface (see above) shows that the number of Pd monomers (0.09 ML) is likely to be too small for the main peak to be ascribed to desorption from only Pd monomers. Therefore, it seems that in this broad peak also C_2H_4 molecules are included that desorb from larger Pd clusters. This is a similar effect as observed for CO desorption from the same surface. The shoulder could be explained from C_2H_4 molecules adsorbed on Pd dimers (0.03 ML) and/or on other Pd bridge sites (0.04 ML).

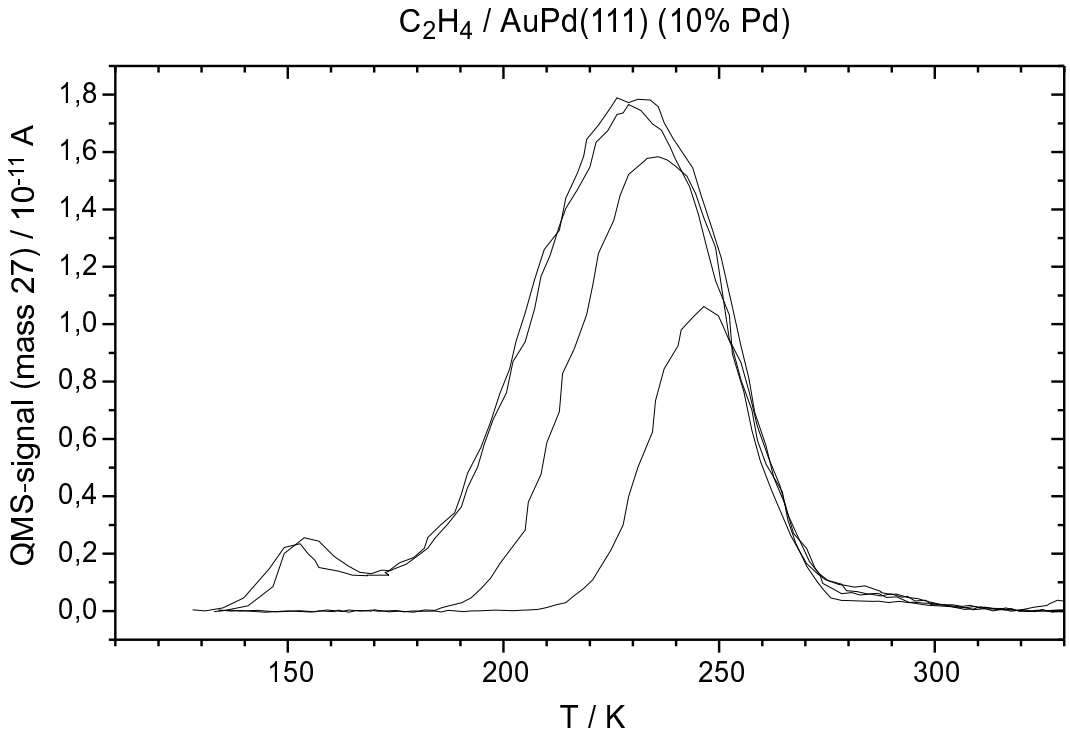

Figure 6.4: C_2H_4 TPD spectra from a AuPd(111) surface alloy with 10% Pd in the surface layer. A linear background has been subtracted from each spectrum.

A comparision between CO and C_2H_4 TPD spectra from the same surface alloys (figs. 5.6 (CO) and 6.1 (C_2H_4)) reveals that less structure is visible in the C_2H_4 spectra. While in the case of CO distinct low and high temperature features caused by CO adsorbed on Pd dimers emerge for $c_{Pd} \geq 8\%$ no such observations can be made for C_2H_4. Here only a continuous broadening of the spectra is observed. The peak widths together with the peak positions for low and high C_2H_4 coverages, respectively, are plotted in fig. 6.6 against the Pd concentration. From C_2H_4 saturated surfaces the position of the maximum desorption rate is almost constant for $2\% \leq c_{Pd} \leq 21\%$. For small C_2H_4 coverages a pronounced increase of the TPD peak position by about 50 K is observed in the same concentration range. This behaviour is in clear contrast to the CO TPD measurements, where also the saturated surfaces exhibited a strong c_{Pd} dependent peak shift. This is a first indication of qualitatively different desorption kinetics for CO and for C_2H_4 on AuPd(111) surfaces. In the case of CO the kinetic behaviour could be explained satisfactorily by the assumption of a mobile precursor state on the Au surface sites without taking any long range adsorbate–adsorbate interactions into account. The evaluation methods that are based on the precursor model described in section 5.2.4 were also applied to C_2H_4 TPD spectra. However, for none of the tested surfaces a linear Arrhenius behaviour could be obtained as it

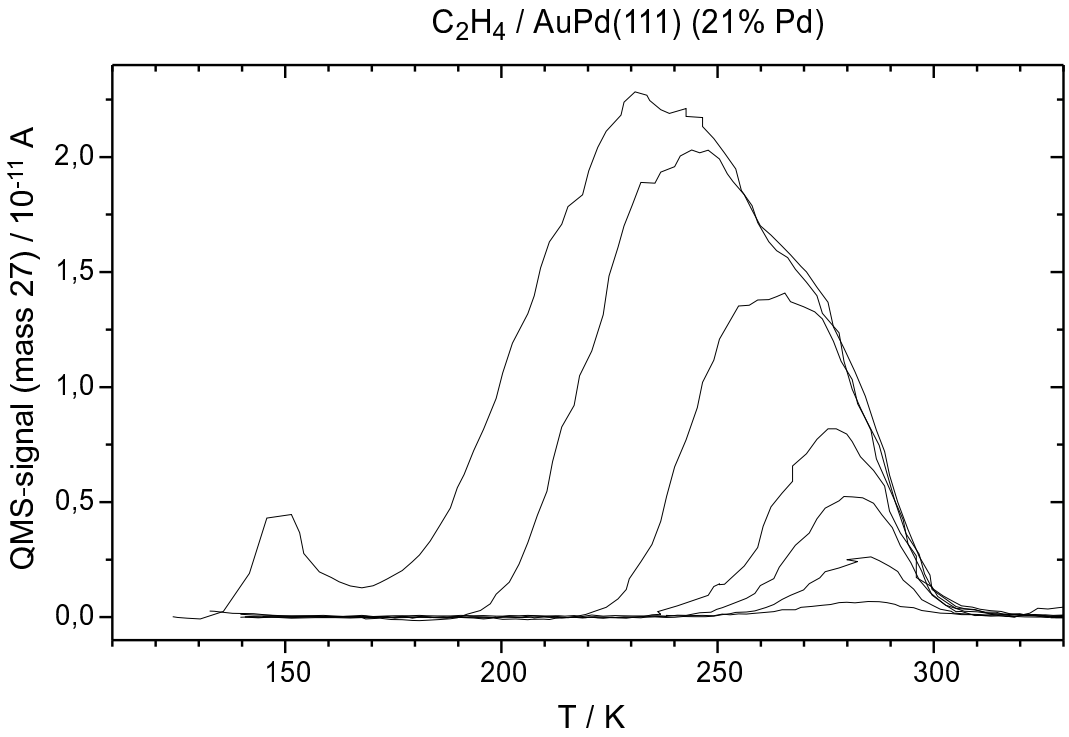

Figure 6.5: C_2H_4 TPD spectra from a AuPd(111) surface alloy with 21% Pd in the surface layer. A linear background has been subtracted from each spectrum.

is shown for CO in fig. 5.12. Also the attempt to evaluate the C_2H_4 desorption kinetics by the TTPD method was not successful, because the scatter of the data points was too large. The failure of the precursor model in the case of C_2H_4 does not necessarily imply that for this system no mobile precursor state is present on the Au surface sites. On the contrary, this state could be directly verified by the observation that for low Pd concentrations only low C_2H_4 doses were needed to saturate the Pd sites with C_2H_4. The validity of the simple rate equations for precursor mediated desorption, that were derived in section 5.2.4, depend on additional conditions other than the mere existence of a precursor state:

1. Adsorbate–adsorbate interactions have to be negligibly small.

2. The energy barriers between the strong adsorption sites (Pd sites in the present case) and the precursor sites (Au sites) have to be of the right magnitude to result in a measurable effect.

3. The model visualized in fig. 5.11 contains only two relevant energy levels (Pd sites and Au sites), whereas in reality the Au sites next to a Pd surface atom are likely to be modified. Therefore, the model described in this work is only valid if these modifications are not too large.

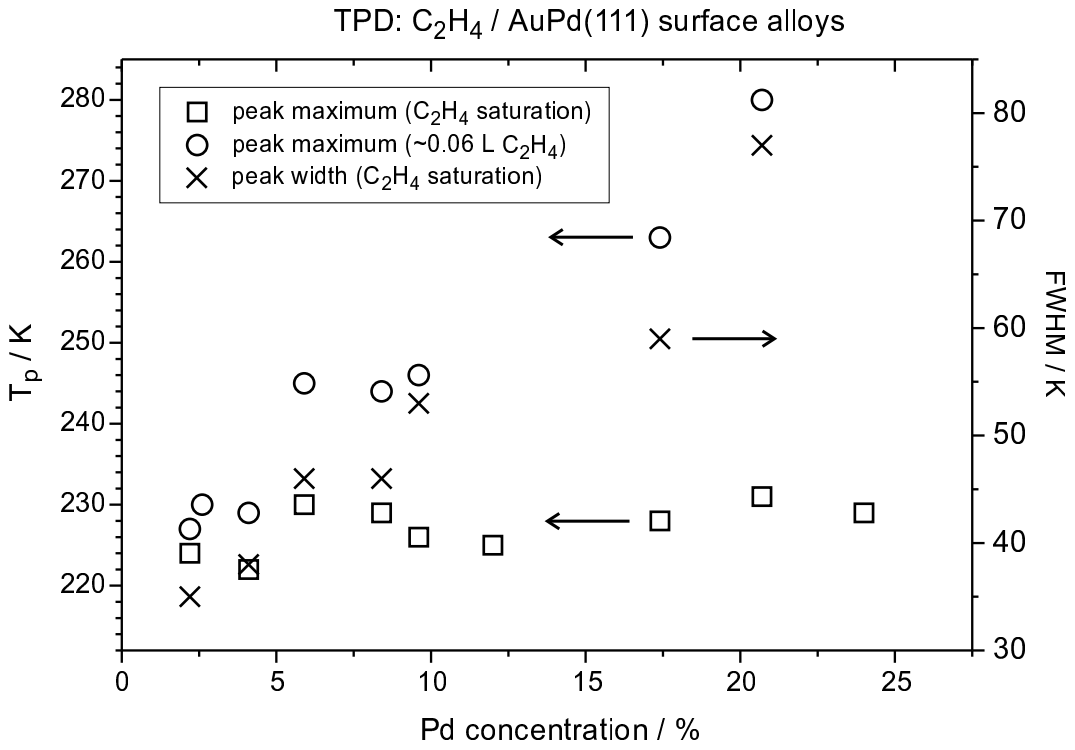

Figure 6.6: Peak positions and widths of C_2H_4 TPD spectra from AuPd(111). The peak positions (left axis) are shown for C_2H_4 saturated surfaces (squares) and for a low C_2H_4 dose ($\sim$0.06 L, circles). The peak widths (crosses, right axis) are displayed only for the saturated surfaces.

It is difficult to decide about the most relevant factor that prevents the successful application of the precursor model to the C_2H_4 TPD measurements. However, the continuous broadening of the TPD peaks with increasing Pd concentration and hence with increasing C_2H_4 saturation coverage hints to adsorbate–adsorbate interactions. These could also be the reason for the failure of the TTPD evaluation method. The adsorption energy of C_2H_4 on Pd(111) is considerably lower than the value for CO (54 kJ mole^{-1} [210] vs. 142 kJ mole^{-1} [119]) and therefore a given adsorbate–adsorbate interaction strength has a more significant relative effect for the C_2H_4/Pd(111) adsorption system than for CO/Pd(111). However, the lack of any observable ordered low temperature phases for C_2H_4 on Pd(111) seems to contradict the postulated repulsive interactions between adsorbed C_2H_4 molecules. But ordered adsorbate structures are only to be expected if the adsorbed phase is mobile enough to adopt its equilibrium configuration, which might be not the case for C_2H_4/Pd(111) at 100 K.

6.3 HREELS results

As has already been mentioned in the introduction to this chapter, some surprising findings for the C_2H_4/Pd(111) system were studied in detail before the bimetallic surfaces were analysed. In particular, a distinct C_2H_4 coverage dependence of the HREEL spectra was found at low sample temperatures (100 K), which is in contrast to a previous study by Gates and Kesmodel [195]. Angular dependent measurements as well as coadsorption experiments with preadsorbed oxygen atoms and with preadsorbed CO were performed to provide insight into the nature of the new low coverage C_2H_4 species. Its possible role as reaction intermediate in C_2H_4 decomposition reactions on Pd(111) sufaces will be one of the main themes of this chapter. Au induced changes in the reactivity of AuPd(111) surface alloys were studied both for low temperature C_2H_4 adsorption and for C_2H_4 decomposition reactions at 300 K. Besides these experiments that are closely related to the properties of bimetallic AuPd catalysts used for C_2H_4 partial oxidation reactions, the ability of pure Au overlayers on Pd(111) to bind C_2H_4 molecules was also investigated, which is rather of scientific interest. As for CO, a higher activity of undercoordinated Au island edge atoms as compared to Au terrace atoms was found for molecular adsorption of C_2H_4.

6.3.1 C_2H_4 adsorption and decomposition on Pd(111)

The presence of π bonded C_2H_4 molecules on Pd(111) at low temperatures ($T \leq 150$ K) has been revealed by different experimental methods in the past (HREELS [195], UPS [211]). However, only C_2H_4 saturated surfaces have been examined in these studies. In the following, it will be shown that at low C_2H_4 coverages significant changes in the HREEL spectra give evidence for the presence of a second C_2H_4 species, whereas at higher coverages the previously described π bonded form of C_2H_4 dominates. A characterization of the newly found C_2H_4 species will be presented in this section by angular dependent HREELS measurements and by coadsorption with atomic oxygen and with CO.

In fig. 6.7 a set of C_2H_4 coverage dependent HREEL spectra is displayed. In the region of the CH_2 deformation modes (80 meV – 150 meV) drastic changes in the relative peak intensities and also in the positions of some of the peaks are conspicuous. The most striking difference between typical low coverage spectra (e. g., spectrum c) and typical high coverage spectra (e. g., spectrum f) is that a strong peak at 107 meV for low coverage is replaced by a strong peak at 113 meV for high coverages. Since no continuous shift of the peak from the one position to the other position is observed, it has to be concluded that two different C_2H_4 surface species exist on Pd(111) at 100 K and that the relative abundance of these species depends strongly on the total C_2H_4 coverage. To facilitate the following discussions a simple nomenclature for the two species is required: The C_2H_4 species

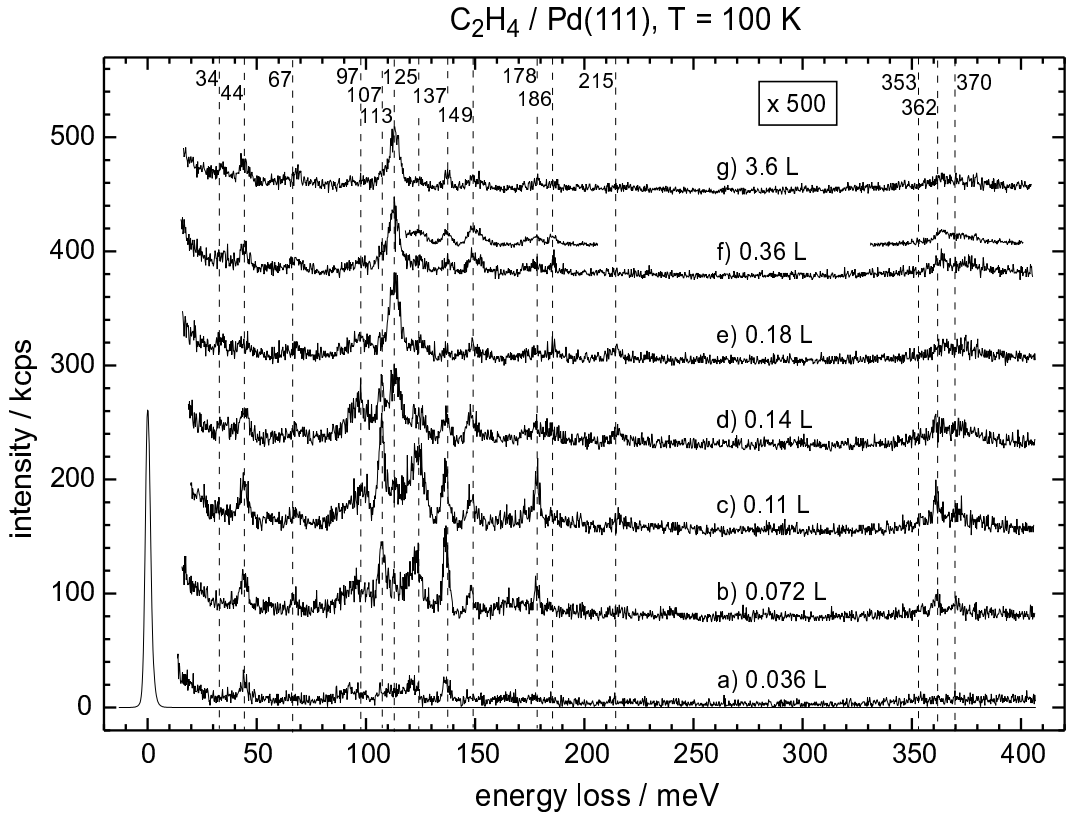

Figure 6.7: HREEL spectra of C_2H_4 adsorbed on Pd(111) at 100 K. The C_2H_4 doses are given in the figure. For spectrum f (0.36 L) two regions have been recorded with a slower scan rate resulting in a better signal to noise ratio. All spectra are normalized to equal height of the elastic peak; $E_p = 6$ eV.

giving rise to typical low coverage spectra will be called "species A" and the other species, that is identical to the well-known π bonded C_2H_4/Pd(111) surface complex, will be termed "species B". As the peak intensities in HREEL spectra do not provide direct information on the coverages of the respective species it can not be decided if species A is still present on the surface at higher coverages or not. Therefore, no statement on a possible interconversion process between the two species can be made.

The identified loss peaks are listed in table 6.4. Since no comparison with spectra of C_2D_4 is available for these measurements a direct assignment of the peaks might be ambiguous. The previous assignment by Gates and Kesmodel (GK, see table 6.3) can be taken as reference. Even though most of the peak positions for species B are in good agreement with the values reported by GK, there are some significant differences:

- Instead of a peak at 86 meV a relatively broad feature around 97 meV is seen

	vibrational energies / meV												
species A	34	44	67	97	**107**	125	136	148	178	184(?)	**353**	**362**	**370**
species B	34	44	67	97	**113**	125	137	149/152	178	186	-	**366**	**374**

Table 6.4: Vibrational energies for the low coverage (A) and the high coverage C_2H_4 species (B) on Pd(111). The values, that exhibit a significant difference between the two species, are printed in bold numbers.

in fig. 6.7. This deviation might be due to the large width and the relatively low intensity of the peak. In a later publication GK report HREEL spectra, where this peak is missing completely [196].

- While two peaks at 125 meV and at 137 meV are found in fig. 6.7, only one peak at 134 meV is reported by GK in this spectral region. In their spectra the strong peak at 113 meV is likely to cover the 125 meV peak and also the position of the small 134 meV peak might be shifted by a high inhomogeneous background.

- In fig. 6.7 no peak is visible around 142 meV. The spectra in [195] show this peak only as shoulder of a broad feature containing also the 152 meV peak and therefore its identification by GK seems to be questionable.

- GK report a strong peak around 345 meV and attribute it to a C–H stretching vibration that is modified by a hydrogen-bond like interaction between H and the Pd surface. This feature is not visible in fig. 6.7, but in other spectra (see, for instance, fig. 6.9) a broad and weak hump is found between 300 meV and 350 meV. Also in the laboratory of GK the intensity of this feature fluctuates strongly from measurement to measurement, which can be seen by comparing the spectra shown in two different publications [195,196]. Hence, this vibration might be very sensitive to the scattering conditions (geometry and electron energy), but an influence of coadsorbates like hydrogen from the residual gas can also not be excluded.

In general, the listed discrepancies between the work of GK and this work can be explained by a relatively high non-linear background extending to about 200 meV in the former case, by the different resolution ($\sim$10 meV vs. $\sim$3 meV), and by a different energy of the primary electrons (3 eV vs. 6 eV). It is remarkable that the overall resemblance of the spectra for species B in fig. 6.7 with spectra reported by Nishijima for C_2H_4/Pd(110) [202] is even closer than the similarity with the above discussed work of Gates and Kesmodel on Pd(111). The comparison between the values that are listed in table 6.3 for Pd(110) and in table 6.4 for Pd(111) reveals that the deviations are not larger than 4 meV for all modes with the exception of the high energy asymmetric CH_2 stretch peak at 383 meV

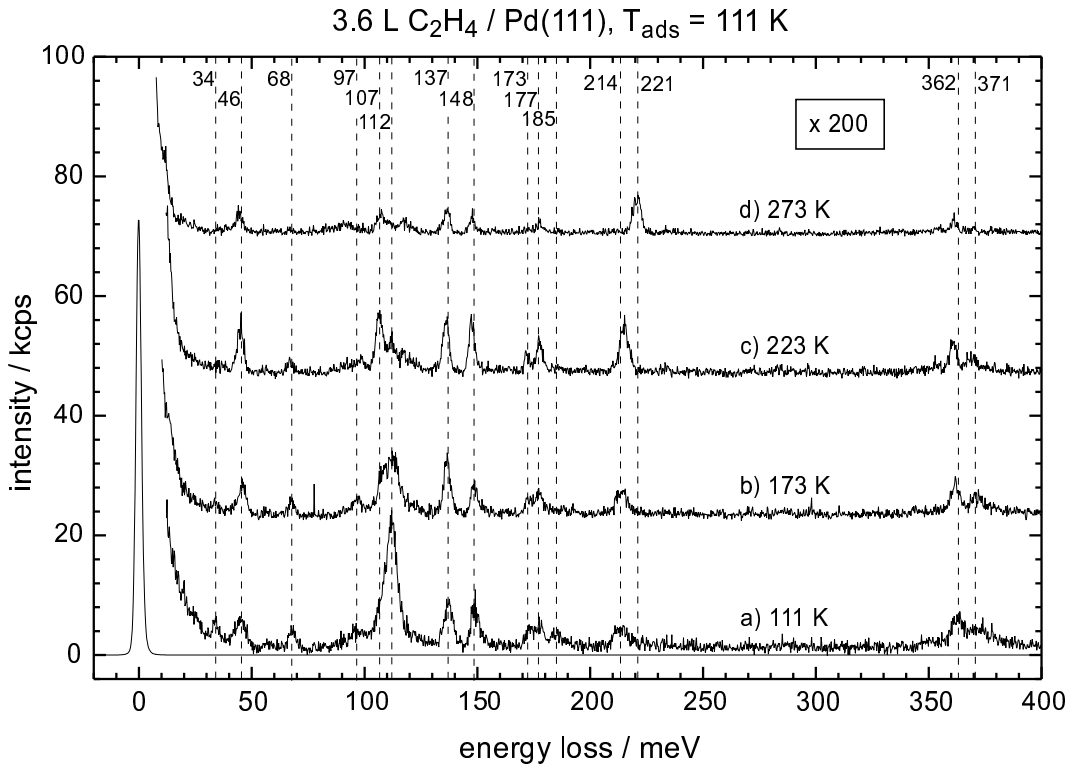

Figure 6.8: HREEL spectra of 3.6 L C_2H_4 adsorbed on Pd(111) at 111 K after short annealing at the indicated temperatures and recooling to T $\approx$ 110 K. All spectra are normalized to equal height of the elastic peak; E_p = 6 eV.

for Pd(110). Since Nishijima et al. assigned the peaks based on a careful comparison with spectra from deuterated ethylene, their assignment seems to be reliable and shall be used also for the present case of C_2H_4/Pd(111) because of the close resemblance between the HREEL spectra from the two different surfaces. It is also interesting to note that on Pd(110) the strong 112 meV peak is accompanied for high C_2H_4 coverages by a low energy shoulder around 108 meV, which corresponds to the energy of the strongest feature for the low coverage species A on Pd(111). Nishijima et al. assign this shoulder to the CH_2 rocking mode, but they did not observe a corresponding feature in C_2D_4 spectra and therefore it can not be excluded that this peak has a different origin.

The next set of spectra for C_2H_4/Pd(111) shows the thermal evolution of a low temperature C_2H_4 saturated surface (fig. 6.8). The surface was heated to 173 K, 223 K, and 273 K, respectively, within a few minutes and immediately recooled to $\sim$110 K before a HREEL spectrum was recorded. In short, no indications of new intermediate surface species are detected in these spectra. However, it is obvious that the typical features of species A reappear upon heating a C_2H_4 saturated layer to temperatures around 200 K, because a strong peak at 107 meV and a red-

shift in the CH_2 stretching peaks can be observed in spectrum c. Therefore, the existence of species A seems to be primarily dependent on the C_2H_4 coverage and not on the preparation conditions. Heating to 273 K results in a strong reduction of the intensities for all C_2H_4 derived features. Still, no additional peaks of new CH containing surface species are visible. For example, the typical CH deformation mode for ethylidyne around 165 meV is not detected. These observations can be explained by desorption of most of the adsorbed C_2H_4 molecules and only a very limited degree of decomposition reactions. This is in accordance with earlier reports stating a strong preference of molecular desorption vs. decomposition for C_2H_4 on Pd(111) [196,210,211]. An interesting observation should be mentioned concerning the C–O stretching peak caused by a small amount of coadsorbed CO. While on clean Pd(111) this peak is found only above 220 meV it is centered around 215 meV in spectra a–c. This hints to an electronic interaction between coadsorbed molecular C_2H_4 and CO. Since π bonded C_2H_4 is a net electron donor (decrease of the work function upon adsorption [211]), this effect can be explained by an increased back-donation into the π^* orbital of the CO molecules caused by C_2H_4. After annealing at 273 K most of the C_2H_4 molecules are removed and the C–O stretching peak is shifted back to a position that is typical for a very small amount of CO ($\theta_{CO} \leq 1\%$ ML) on clean Pd(111).

Some angular dependent HREELS measurements were preformed in order to gain additional information on the nature of the two low temperature C_2H_4 species. The results are displayed in fig. 6.9. For each of the species A and B a spectrum in the specular direction was recorded and compared with an off-specular measurement. The angle of 3° was found to be sufficient for the elastic peak to be reduced to about 10% – 20% of the original intensity. Therefore, also the dipole excited loss peaks should be considerably decreased in the off-specular spectra. While for species B (spectra a and b) this effect is observed for the losses at 34 meV, 46 meV, 113 meV, and 138 meV and for the broad feature between 300 meV and 350 meV, only the peak at 45 meV seems to be mainly dipole-excited in the case of species A (spectra c and d). According to the selection rule for dipole scattering at metal surfaces (s. 1.2) only totally symmetric modes of adsorbates on metals are dipole active. From this it can be inferred that the adsorbate complex of species B has a reduced symmetry compared to species A. This might be caused by a change in the adsorption site or by a tilt or rotation of the molecule upon increasing the surface coverage. However, since NEXAFS investigations on C_2H_4 saturated Pd(111) showed that the molecule is adsorbed with its C–C axis lying essentially parallel to the surface [211] the tilt angle can only be small, which is in contrast to the earlier model proposed by Gates and Kesmodel [195]. From HREELS measurements alone, no unambiguous determination of the adsorption geometry is possible. In the case of C_2H_4/Pd(111) additional structure sensitive measurements (for example by NEXAFS, LEED or photoelectron diffraction) are necessary to make definite statements on the coverage dependence of the C_2H_4

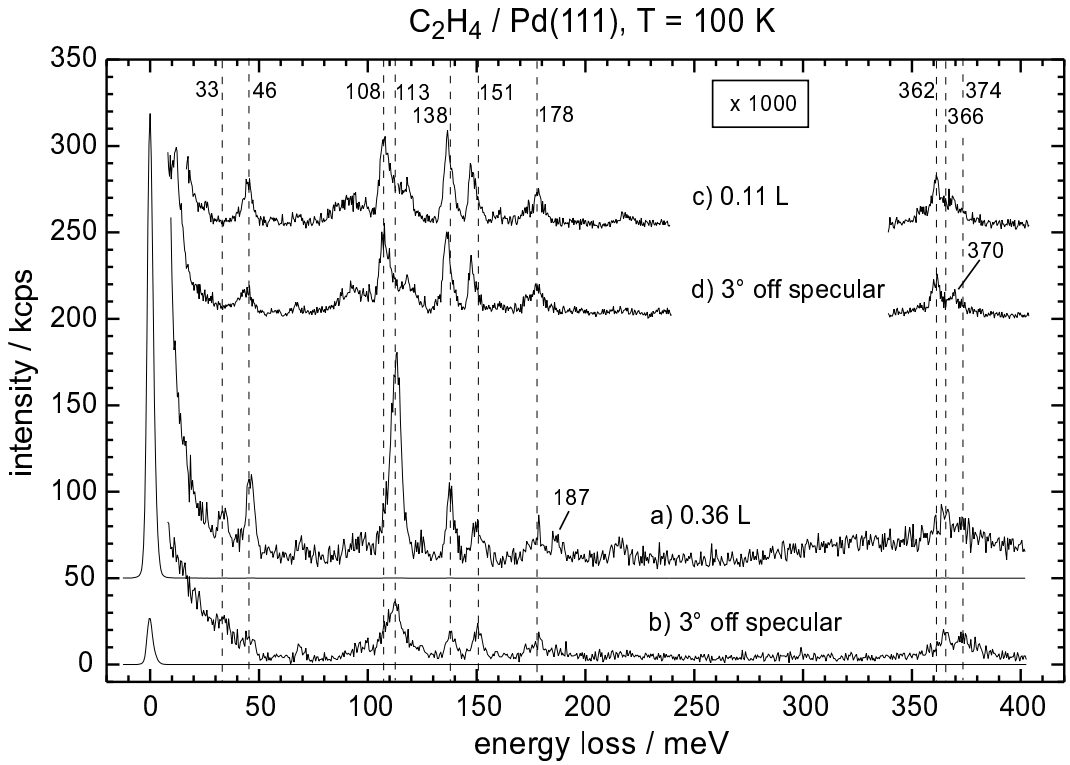

Figure 6.9: HREEL spectra of C_2H_4 adsorbed on Pd(111) at 100 K. Typical spectra representing a low C_2H_4 coverage (0.11 L, spectra c and d) and a high C_2H_4 coverage (0.36 L, spectra a and b), respectively, have been recorded with the analyzer both in the specular direction and rotated 3° towards the surface normal ("off-specular"). The spectra are displayed without any normalization; $E_p = 6$ eV.

adsorption geometry.

On surfaces, where C_2H_4 is found to be adsorbed as a di-σ species and where accordingly the degree of thermal decomposition is quite high, oxygen preadsorption is able to change the adsorption mode from di-σ to π bonding and consequently to suppress the decomposition reactions This effect is reported e. g., for Pt(111) [203] and for Pd(100) [201]. This is explained by the fact that di-σ bonded C_2H_4 as an electron acceptor is competing with the coadsorbed O atoms for the metal d electrons. Therefore, the di-σ surface species is destabilized by O atoms, whereas π bonded C_2H_4 molecules are rather stabilized. Coadsorption with CO should produce the same effect, although to a lesser degree. In fig. 6.10 HREEL spectra for C_2H_4 coadsorbed with atomic oxygen and with CO on Pd(111) are displayed. In the case of CO preadsorption the coverage can be estimated to be around 0.3 ML from the C–O stretching peak position found at 230 meV prior to C_2H_4 dosing. A red-shift by 7 meV to 223 meV is observed

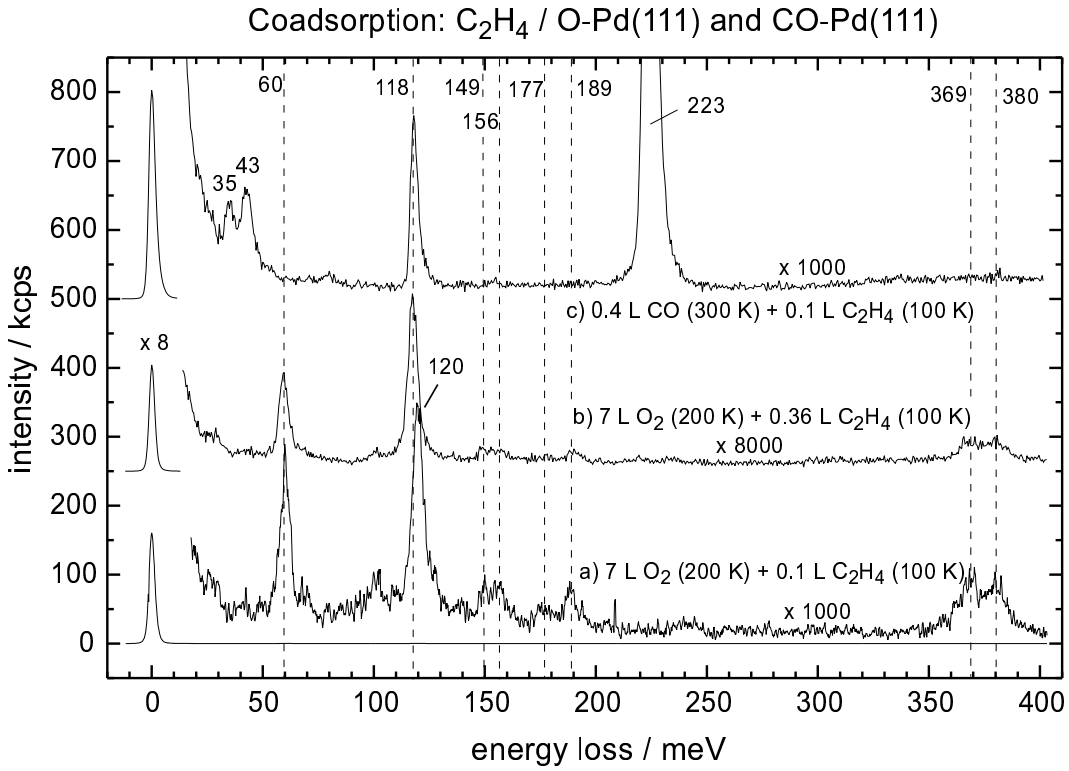

Figure 6.10: HREEL spectra of C_2H_4 adsorbed on O and on CO precovered Pd(111) at 100 K. The doses for the different adsorbates are given in the figure. The CO coverage is 0.3 ML. $E_p = 6$ eV.

upon C_2H_4 coadsorption and has been identified already above as a typical effect of electronic interactions between CO and C_2H_4 molecules on Pd(111). For atomic oxygen it is not possible to determine the coverage, because the Pd–O stretching peak position (59 meV) does not strongly depend on the O coverage. Also the coverage of O atoms might change during the experiment because of reactions between these atoms and coadsorbed surface species like H atoms or CO. The purpose of these coadsorption experiments is to check if species A does also exist on such strongly modified Pd(111) surfaces. Therefore, only relatively small C_2H_4 doses were applied (0.1 L for both coadsorbates and additionally 0.36 L on the oxygen precovered surface). In both cases no indication is found for the C_2H_4 species A. The vibrational spectra are also very different compared to species B. While on CO precovered Pd(111) only two features at 35 meV and at 119 meV can be ascribed to adsorbed C_2H_4, several different losses are observed in the case of an oxygen precoverage. From the relatively high CH_2 stretching frequencies at 369 meV and at 381 meV it can be concluded that the C_2H_4 molecules on O-Pd(111) are π bonded to the surface. Also the strong peak at 118 meV (CH_2 wagging) is an indication for such a weakly bonded species (it is found,

for instance, also on O-Pd(100) [201]). The nature of the C_2H_4 species on CO-Pd(111) is probably quite similar because of the clear dominance of the spectrum by the CH_2 wagging mode at 119 meV. As a conclusion to the coadsorption experiments, it can be stated that preadsorption of CO and of O causes major changes in the adsorption behaviour of C_2H_4 and neither species A nor species B can be identified on these surfaces. The HREEL spectra indicate that the C_2H_4–Pd interaction is considerably weakened by the preadsorbed atoms/molecules.

As a conclusion to the HREELS measurements on the C_2H_4/Pd(111) adsorption system, the following observations, that have not been reported in previous studies, should be recalled:

1. Besides the well-known π bonded C_2H_4 species on Pd(111) (species B) a second molecular C_2H_4 species (species A) has been observed. It is characterized by an intense peak at 107 meV, and it is found on Pd(111) surfaces with a relatively low C_2H_4 coverage.

2. Species A is more strongly bonded to Pd(111) than species B, which follows from the adsorption sequence (preferential population of species A states at low coverages) and also from the desorption behaviour (species A molecules are found on the surfaces up to higher temperatures than species B molecules).

3. Off-specular HREELS measurements indicate that the adsorbate complex of species B has a lower symmetry than that of species A.

4. Preadsorption of atomic oxygen or of CO leads to a reduction of the Pd–C_2H_4 interaction strength, which manifests itself in molecular vibrations of C_2H_4 that are closer to the gas phase values compared to either of the two C_2H_4 species found on clean Pd(111).

Since no direct structural or electronic information on the nature of the new C_2H_4 species A is available, no definite characterization of this species is possible. From the evidence provided by the vibrational spectra it is found, however, that species A is more strongly bonded to Pd than species B and that the CH_2 stretching vibrations are shifted towards values that are typical for di-σ bonded C_2H_4. Therefore, it can be stated that, within the framework defined by the distinction between π and di-σ bonded C_2H_4 molecules, species A is closer to a di-σ configuration than species B, that has been already identified as essentially π bonded C_2H_4 [211].

6.3.2 C_2H_4 adsorption and decomposition on AuPd(111) surface alloys

In the above section it has been shown that the C_2H_4 adsorption properties of Pd(111) can be strongly altered by preadsorption of a relatively large amount of

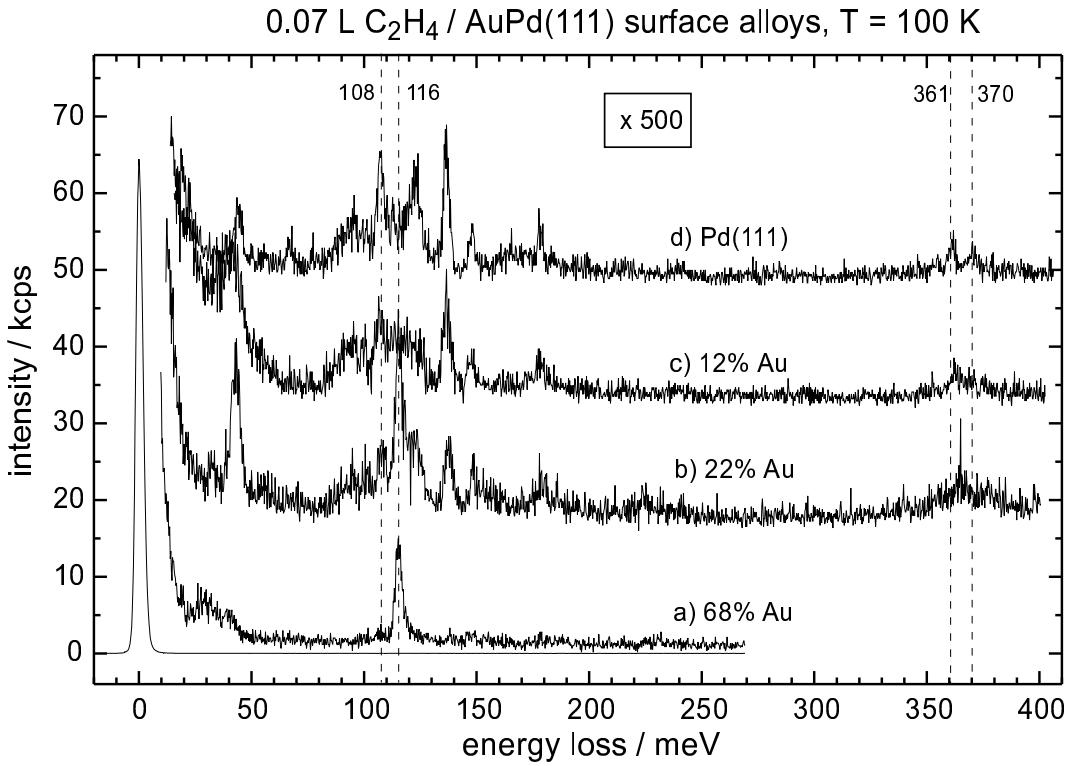

Figure 6.11: HREEL spectra of 0.07 L C_2H_4 adsorbed on different AuPd(111) surface alloys at 100 K. All spectra are normalized to equal height of the elastic peak; $E_p = 6\,eV$.

CO or of atomic oxygen. More subtle changes are to be expected if the substrate itself is modified by replacing a small part of surface Pd atoms by atoms of a different kind. The choice of Au as the second metallic component for this model adsorption reaction can be justified by the fact that PdAu catalysts exhibit better preformance than pure Pd catalysts regarding activity and selectivity for certain partial oxidation products of C_2H_4; e. g., the production rate of vinyl acetate from C_2H_4, CH_3COOH, and O_2 is found to be enhanced on bimetallic AuPd catalysts compared to pure Pd catalysts [5]. It is also found that the unwanted total oxidation of C_2H_4 is efficiently suppressed by the presence of Au surface atoms [4]. Consequently, from the practical point of view there is a great interest in the revelation of the factors that determine the balance between partial and complete oxidation reactions of C_2H_4 on Pd and PdAu alloy surfaces. An important class of partial oxidation reactions consists in the replacement of one hydrogen atom by a different chemical component leading to a vinylic product ($X–CHCH_2$). Therefore, as soon as the C–C bond of the molecule is broken or, alternatively, as soon as a CH_3 containing group is formed during the reaction, the molecule is lost for the production of the desired vinylic product. In the case

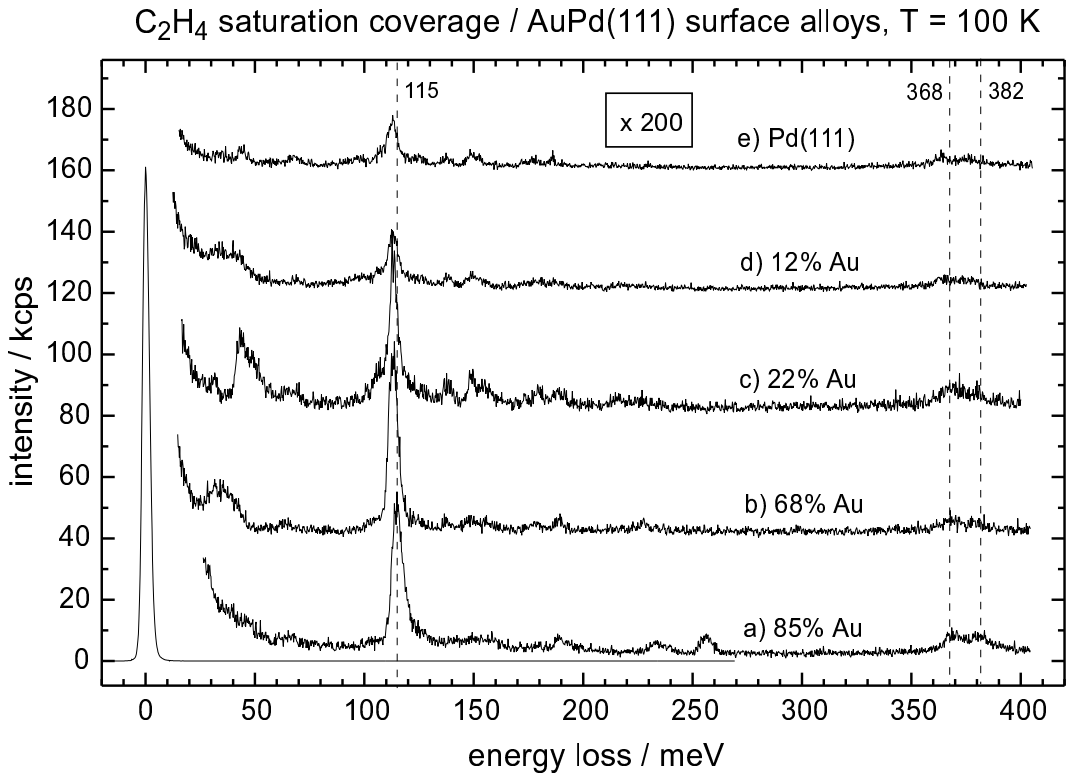

Figure 6.12: HREEL spectra of C_2H_4 saturated AuPd(111) surface alloys at 100 K. All spectra are normalized to equal height of the elastic peak; $E_p = 6$ eV.

of C_2H_4 reactions on Pd(111) surfaces, ethylidyne (CCH_3) and methylidyne (CH) were identified as decomposition intermediates, where Gates and Kesmodel point out that they do not necessarily belong to the same dehydrogenation pathway but that there is some evidence for methylidyne being formed directly from C_2H_4 molecules [196].

In any case, it is obvious that the observation of ethylidyne or methylidyne derived features can be taken as a rough estimate for the propensity of the surface to promote complete C_2H_4 decomposition. Besides the general question to what extent C_2H_4 decomposition takes place on a given AuPd(111) surface alloy at room temperature and above it is also interesting to ask about the corresponding molecular C_2H_4 adsorption behaviour at low temperatures. The following HREELS measurements were intended to give some information for answering both of these questions. Hence, at low temperatures it was investigated by C_2H_4 coverage dependent measurements if the two molecular C_2H_4 species A and B are formed on the AuPd(111) surface alloys. Then, the surfaces were annealed at 300 K and additional C_2H_4 was dosed until no further changes in the spectra were noticed.

In fig. 6.11 an C_2H_4 dose of 0.07 L is compared on pure Pd(111) and on

AuPd(111) surfaces with 12%, 22%, and 68% Au, respectively. For this dose the strong peak at 108 meV and the low energy CH_2 stretching modes at 361 meV and at 370 meV give clear evidence for the presence of species A on Pd(111) (spectrum d). On a surface with 12% Au (spectrum c) the general appearance of the spectrum is very similar to the spectrum recorded on Pd(111) (d). Even though the signal to noise ratio of this spectrum is not very good, the following trends for Au induced changes can be recognized :

- The peak intensity of the CH_2 wagging mode at 108 meV is decreased.
- The intensity detected around 116 meV is increased, but no distinct peak is visible.
- The CH_2 stretching modes are shifted somewhat to higher energies.

These changes become more obvious if the Au content is increased to 22% (spectrum b). As a new feature a strong loss at 116 meV is observed. The two strongest CH_2 stretching modes are now found rather at 365 meV and at 375 meV than at 361 meV and at 370 meV as on Pd(111). On surfaces where Pd represents the minority species (here: 68% Au, spectrum a) only one intense peak at 116 meV is detected. In this case a major change of the C_2H_4 adsorption geometry is likely to be the reason for the drastic alteration of the HREEL spectrum. In short, the HREEL spectra in fig. 6.11 reveal that for low C_2H_4 doses a surface with 68% Au exhibits a completely different adsorption behaviour than pure Pd(111). Already 22% Au are sufficient to cause major changes of the vibrational spectrum, which corresponds rather to a species B type spectrum than to a species A type spectrum despite the low C_2H_4 dose. For 12% Au, species A seems still to be present for low C_2H_4 doses, but first indications of a transition from species A to species B are evident even for this low Au content.

HREEL spectra recorded after a low temperature saturation dose of C_2H_4 on different AuPd(111) surface alloys (fig. 6.12) show less pronounced Au related modifications in the vibrational behaviour of the C_2H_4 adsorbate layer than the changes noticed in the above paragraph for a low C_2H_4 dose. Only some rather gradual peak shifts are observed for the CH_2 wagging mode from 113 meV (Pd(111), spectrum e) to 115 meV (85% Au, spectrum a) and for the two prominent CH_2 stretching peaks from 366/374 meV (Pd(111), spectrum e and fig. 6.7) to 368/382 meV (85% Au, spectrum a). These shifts point to a weakening of the interaction between the C_2H_4 adsorbates and the substrate caused by the Au atoms. But compared to the spectra that were obtained after O and after CO preadsorption with the dominating CH_2 wagging mode at 118 meV – 120 meV, the Au induced changes appear to be smaller. In the next section it will be shown that on a pure Au overlayer no C_2H_4 adsorption takes place on terrace sites at 100 K. Therefore, C_2H_4 adsorption on AuPd(111) surface alloys is likely to occur only on Pd sites. Increasing the Au content should change mainly the

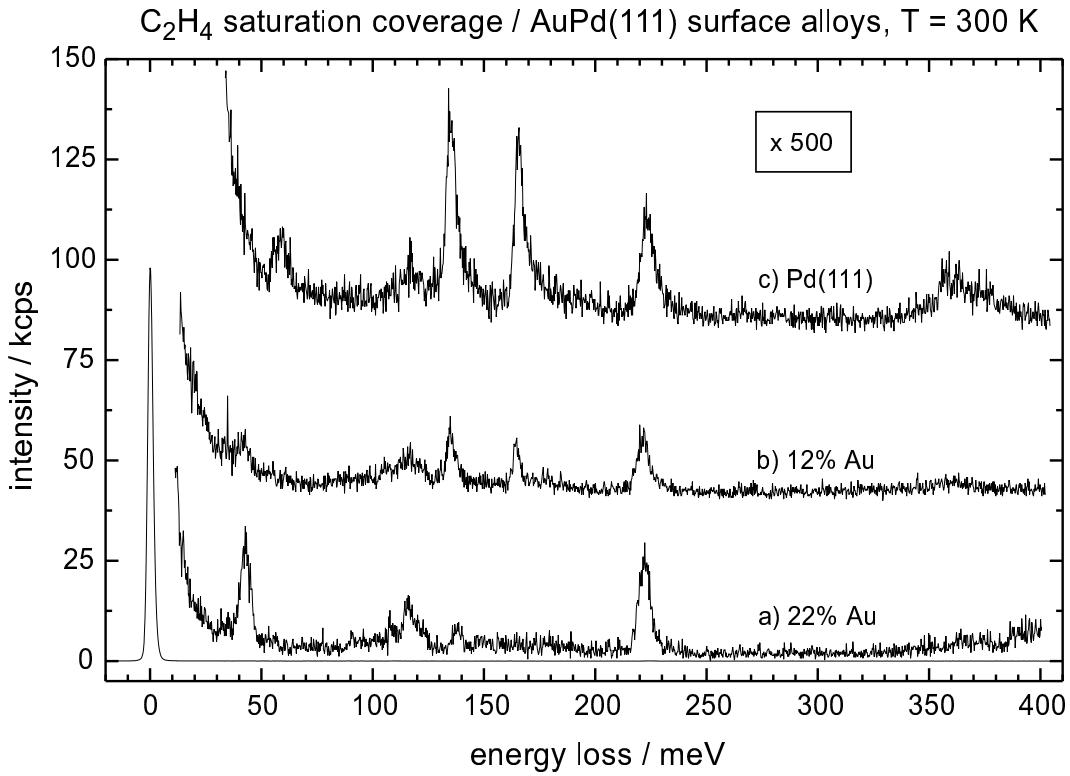

Figure 6.13: HREEL spectra of C_2H_4 saturated AuPd(111) surface alloys at 300 K. All spectra are normalized to equal height of the elastic peak; $E_p = 6$ eV.

environment of the C_2H_4-Pd adsorption complexes and not the adsorption sites themselves. This is also suggested by the TPD results presented in the previous section, where even single Pd atoms within a Au matrix are shown to exhibit rather "Pd like" C_2H_4 adsorption properties with molecular desorption occuring only above 180 K. On the other hand, it is surprising to notice some rather drastic Au related changes at low C_2H_4 coverages even for only 22% Au. This point will be discussed in some more detail below.

As has been mentioned in the introduction to this section, the formation of ethylidyne on the Pd(111) surface around 300 K can be judged as a precursor reaction to complete decomposition of C_2H_4. Even though it is possible that other, parallel reaction pathways exist, that do not contain an ethylidyne intermediate, ethylidyne represents a very important dehydrogenation product of C_2H_4 on Pd(111). Some of the AuPd(111) surface alloys that have been characterized above regarding their low temperature C_2H_4 adsorption behaviour were also used for 300 K adsorption experiments to check the formation of C_2H_4 dehydrogenation products. The results are shown in fig. 6.13. Since the Pd(111) surface itself is relatively inert regarding transformation reactions from molecularly adsorbed C_2H_4 to ethylidyne [196,210,211] by heating a C_2H_4 layer prepared at low temperatures

— even for low temperature C_2H_4 saturation the ethylidyne features are hardly detectable after heating to room temperature — , it is not useful to compare annealing experiments on the different surfaces. Instead, the direct adsorption and decomposition of C_2H_4 at 300 K is providing a better measure for the reactivity of the surface towards C_2H_4 decomposition. Three features of the spectrum from Pd(111) (spectrum c in fig. 6.13) can be ascribed unequivocally to an ethylidyne surface species: the C–C stretching mode at 134 meV, the CH_3 symmetric deformation mode ("umbrella mode") at 166 meV, and the CH_3 stretching modes around 360 meV. In the literature there has been some discussion about the nature of the 113 meV peak and about the question whether or not it belongs to the ethylidyne surface species. Gates and Kesmodel concluded from comparative C_2H_4/C_2D_4 measurements that it is derived from a CH_3 deformation mode [196]. On the other hand, this peak is considered to constitute *not* a genuine feature of ethylidyne on Pt(111) [25], but no conclusive alternative assignment was given for this mode, that is occasionally observed also on Pt(111). The peaks around 40 meV and 220 meV in fig. 6.13 are caused by metal–CO and C–O stretching vibrations of coadsorbed CO. From the relatively low C–O stretching frequency it can be estimated that only about 1% of a ML CO was present on these surfaces during the HREELS measurements. For pure Pd(111) also almost completely CO free spectra were obtained. Spectrum c with a significant amount of CO was intentionally chosen for the comparison with the AuPd(111) surface alloys, because thus the CO coverage is approximately constant for all spectra shown in fig. 6.13.

The comparison of the spectra shown in fig. 6.13 clearly demonstrates that the Au containing surfaces are considerably less reactive concerning C_2H_4 dehydrogenation to ethylidyne. Already 12% Au (spectrum b) are sufficient to cause a substantial decrease of the three ethylidyne derived bands at 134 meV, 166 meV, and around 360 meV. With 22% Au in the surface (spectrum a) the peak at 166 meV is completely absent, while a small feature remains at 134 meV. It is surprising to find some intensity around 390 meV, which is a significantly higher energy than expected for C–H stretching vibrations. Since this feature was not observed in other spectra for this adsorption system, it is likely to be caused by an artefact. An alternative explanation could be found in the formation of OH containing surface species by reactions between CO and the coadsorbed hydrocarbons, but this suggestion seems to be too speculative. A more significant observation is the occurence of a peak around 115 meV, that has about the same intensity on all three surfaces. This demonstrates that on the AuPd(111) surface alloys — including pure Pd(111) as limiting case — the feature at 115 meV has to be explained by a surface species other than ethylidyne. However, it can not be excluded that ethylidyne also contributes to this peak. It is difficult to make any statements about the origin of the peak in question, because it does not seem to be part of a distinct pattern containing additional modes, that could

provide some hints to identify the surface species. Only a small peak at 134 meV, which has been ascribed to the C–C stretching mode of ethylidyne and which is detected also on the surface with 22% Au, can be taken as indication for the presence of some C_2 containing surface species in spectrum a. As has been shown above, a CH_2 wagging peak between 113 meV and 120 meV is typical for weakly adsorbed C_2H_4 molecules on different surfaces. But it is unlikely that such a molecular species still exists at 300 K. Another possibility to explain the peak at 115 meV can be derived from the comparison with HREEL spectra recorded by Nishijima et al. from C_2H_4 decomposition products on Pd(110) [202]. After heating of a C_2H_4 saturated Pd(110) surface to 350 K they observed a dominating peak at 115 meV that is accompanied by a peak of medium intensity at 57 meV and by small peaks at 50 meV, 156 meV, and 367 meV. This spectrum is ascribed to ethynyl (CCH) groups on the surface. By comparison with spectra from C_2D_4/Pd(110) the mode at 115 meV could be determined to correspond to the in plane CH bending mode. The presence of a small amount of CCH groups on the Pd(111) and the AuPd(111) surfaces could account for the observed peak around 115 meV and could also explain the variations of the relative intensities of this peak compared to the ethylidyne peak. However, it has to be stated, that only a comparison with deuterated ethylene can lead to a conclusive determination of the origin of the feature in question.

Even though there remain some open questions on the nature of some features detected at 300 K for the C_2H_4/AuPd(111) system the following important conclusions can be drawn from the above presented HREELS measurements: A relatively low Au concentration of 22% in the surface layer is sufficient to cause two distinct effects. First, at low sample temperatures ($\sim$100 K) the C_2H_4 coverage dependence of the HREEL spectra is modified with the result that species A is no longer detectable. Second, at 300 K almost no ethylidyne formation is observed. It is tempting to infer from these observations that species A is a precursor state to ethylidyne formation on Pd(111). For this suggestion two additional arguments can be put forward. First, species A was shown in section 6.3.1 to exhibit some features that are typical for a more "di-σ" like bonding configuration (e. g., the lower CH_2 stretching frequencies). Since on the geometrically related Pt(111) surface ethylidyne formation proceeds from di-σ bonded molecules, it is conclusive that also on Pd(111) a similar reaction pathway could be possible. Secondly, it was shown by Tysoe et al. that the relative amount of C_2H_4 decomposition upon heating a low temperature adsorbate layer depends on the initial C_2H_4 coverage with the higher decomposition tendency found for lower C_2H_4 coverages [210]. Hence, a consistent picture for C_2H_4 decomposition reactions on Pd(111) and on AuPd(111) surface alloys can be developed from the HREELS results and from earlier studies on pure Pd(111). However, no direct proof for species A being a di-σ bonded precursor state for the ethylene to ethylidyne dehydrogenation reaction has been presented so far. Further experiments (e. g., UPS or NEXAFS

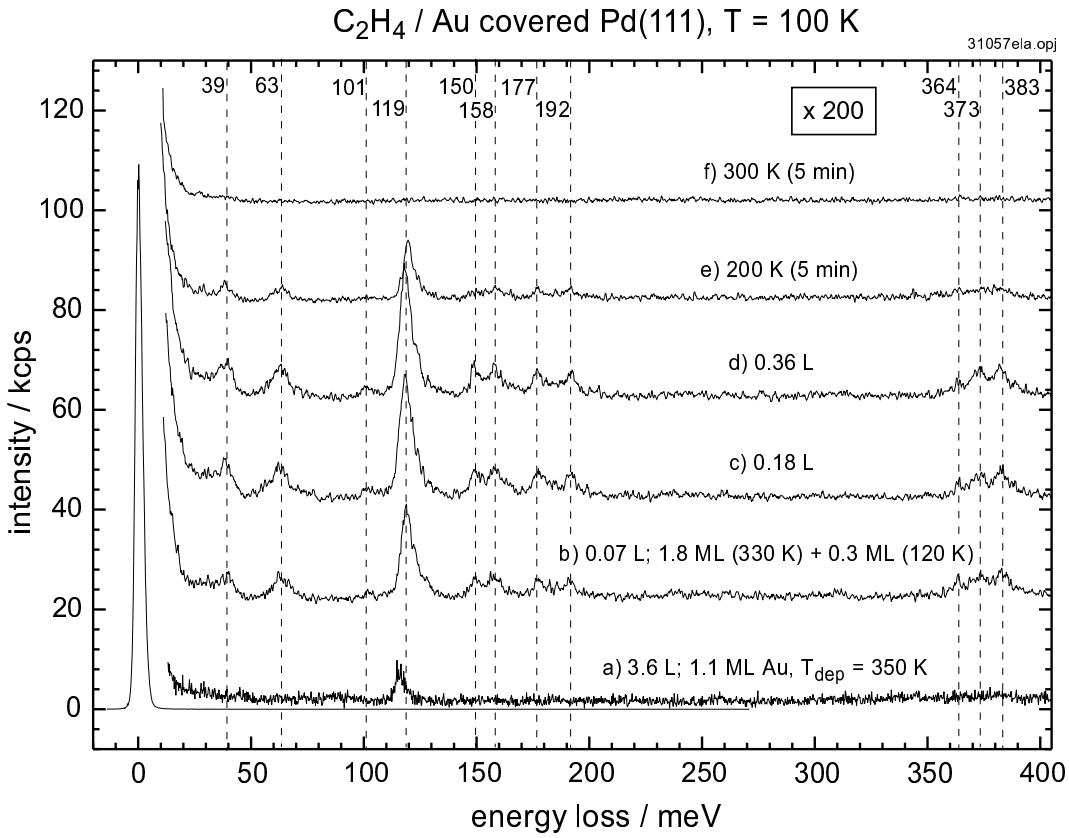

Figure 6.14: HREEL spectra of C_2H_4 on completely Au covered Pd(111) at 100 K. The C_2H_4 doses are given in the figure. Spectrum a has been recorded on a different Au film (1.1 ML Au deposited at 350 K) than the other spectra. The latter were recorded on a surface with a high fraction of Au step edge atoms, which was prepared by a two step Au deposition procedure (1.8 ML at 330 K + 0.3 ML at 120 K). All spectra are normalized to equal height of the elastic peak; $E_p = 6$ eV.

studies for different C_2H_4 coverages) and theoretical studies are necessary to settle the question about the mechanism of C_2H_4 decomposition on Pd(111) and on related bimetallic surfaces. The present work provides some important hints for where an answer to this question might be found.

6.3.3 C_2H_4 adsorption on completely Au covered Pd(111)

In chapter 5 it was demonstrated that the ability of Au/Pd(111) films to adsorb CO depends critically on the amount of undercoordinated Au step edge and Au kink atoms. Similar observations have been made for the C_2H_4 adsorption system. Where on flat Au films on Pd(111) no chemisorbed C_2H_4 was found

vibrational energy / meV	mode assignment
39	Me–C stretch(s)
63	Me–C stretch(as)
101	CH_2 rock
119	CH_2 wag
150	CH_2 twist
158	C–C stretch
177	CH_2 scissor(as)
192	CH_2 scissor(s)
364	CH_2 stretch(as)
373	CH_2 stretch(s)
383	CH_2 stretch(as)

Table 6.5: Mode assignment for C_2H_4/Au/Pd(111) based on the comparison with Zeise's salt (see table 6.3).

at temperatures as low as 100 K, relatively strong loss features appear in the HREEL spectrum if C_2H_4 is dosed on a Au/Pd(111) surface with a high amount of Au step edge and Au kink atoms. This is demonstrated in the sequence of HREEL spectra shown in fig. 6.14. Spectrum a was recorded after dosing 3.6 L C_2H_4 on a 1.1 ML Au film, that was prepared at 350 K. Since Au growth on Pd(111) does not proceed in a perfect layer-by-layer mode, there are still some areas of uncovered Pd available for C_2H_4 adsorption. This is the reason for the small peak around 115 meV. No C_2H_4 adsorption is detected on the Au covered regions at 100 K. Spectra b – f were recorded on a surface that have been prepared by a two step Au deposition procedure. First 1.8 ML Au was deposited at 330 K, which results in a completely Au covered surface. By the second Au deposition step at 120 K many relatively small and irregularly shaped Au islands are created on the Au layer. Therefore, the vibrational peaks found in spectra b – e can be ascribed to a C_2H_4 species on Au island edge atoms. It is remarkable that the peaks are saturated already after the small dose of 0.18 L, which hints to the existence of a mobile precursor state on the Au covered terraces and on the Au islands. The loss peaks of this species are found to be quite intense. They have about the same intensity as the peaks recorded for C_2H_4/Pd(111). Since the C_2H_4 saturation coverage on the Au covered surface is certain to be considerably lower than on Pd(111), the observed molecular vibrations are likely to exhibit large components of the dynamic dipole moment in the direction perpendicular to the surface. This can be interpreted as indication for a tilted adsorption geometry of C_2H_4 on Au step edge atoms.

The positions of the loss peaks for C_2H_4 on Au/Pd(111) are in very good agreement with the vibrations of Zeise's salt, the model complex for π bonded C_2H_4 (see table 6.3 for Zeise's salt and table 6.5 for C_2H_4/Au/Pd(111)). The

coupled C–C stretching and CH_2 scissoring modes and the CH_2 stretching modes are found at almost identical positions for both systems. For this C_2H_4 surface species, there is no doubt about the C_2H_4–surface interaction consisting of pure π bonding. For example, the $\pi\sigma$ parameter is found to be 0.26, which is even below the value for Zeise's salt. This view is supported by the fact that heating to 300 K results in a complete extinction of all loss features, i. e., all of the C_2H_4 molecules desorb molecularly from this surface. The reversible adsorption of C_2H_4 on evaporated Au films was already reported by Trapnell at relatively high pressures [219]. Equally, Chesters and Somorjai found no indication of C_2H_4 decomposition on Au(111) and on stepped Au(111) at elevated temperatures [220]. These reports are in good agreement with the described behaviour of ultra-thin Au films on Pd(111). A theoretical study by Paul and Sautet using extended Hückel calculations was directed to the problem of C_2H_4 bonding to differently coordinated Pt atoms on Pt(111) surfaces with surface defects like steps, kinks, and adatoms [221]. Since Pt and Au surfaces show the same tendency regarding the enhancement of activity for CO adsorption at step and kink sites, the work on Pt can give some insight into the possible effects of the presence of undercoordinated surface atoms also on Au surfaces. In short, Paul and Sautet compared the binding energy of di-σ and of π bonded C_2H_4 molecules at Pt surface sites with coordination numbers between 9 (regular surface site) and 3 (Pt adatom on the surface; only π bonding possible). In agreement with experiment they find on the flat terraces the di-σ species to be more stable than the π species. Decreasing the coordination number of the Pt atoms leads to only a small increase of the binding energy for di-σ bonded molecules, whereas for π bonded molecules a drastic stabilization is observed. Consequently, at a Pt step edge site (coordination number 7) the π configuration is more strongly bonded to the surface than the corresponding di-σ configuration. An optimization of the adsorbate geometry leads for π bonded C_2H_4 at Pt(111) step sites to a tilt of about 27° of the molecular plane with respect to the surface plane, where the molecular axis is perpendicular to the step and is pointing towards the lower terrace. For several vibrational modes the components of the dynamic dipole moment perpendicular to the surface are larger in the case of tilted C_2H_4 molecules than for molecules adsorbed flat on the surface. Therefore, the number of relatively intense dipole-active modes in specular HREEL spectra should be increased for tilted molecules. Since this is observed for the C_2H_4/Au/Pd(111) system, the calculated geometry for C_2H_4 at Pt(111) step edges can be taken as a good model also for the present case.

6.4 XPS results

It has been pointed out in the above discussion of the HREELS results for C_2H_4 adsorption on Pd(111) and on AuPd(111) surface alloys, that the C_2H_4 decomposition reactions taking place on those surfaces are very sensitive to the presence of Au atoms in the surface layer. It has been shown that at 300 K the formation of ethylidyne on the surface is almost completely suppressed by 22% Au. The vibrational spectra at T $\geq$ 400 K show only a weak feature around 92 meV (assigned to the bending mode of methylidyne (CH) by Gates and Kesmodel [196]) even for C_2H_4 saturation doses on pure Pd(111), and therefore HREELS was found to be not the appropriate method to investigate C_2H_4 surface reactions at elevated temperatures. Since TPD is not capable of providing information about surface species that are left on the surface after adsorption-decomposition reactions carried out at temperatures, where a part of the molecules are able to leave the surface during the reaction, it was decided to study some aspects of the C_2H_4 – AuPd(111) interaction by XPS. In the following the formation of C containing surface species at 400 K will be analysed on the basis of XPS measurements. Tysoe et al. showed that upon heating of a low temperature C_2H_4 layer on Pd(111) most of the available H atoms desorb below 400 K [210]. Gates and Kesmodel identified methylidyne as the only hydrocarbon species on this surface at 400 K. It can not be excluded that besides these CH groups carbon atoms are also present in the form of C adatoms or of clusters of C atoms. The signal to noise ratio and the resolution of the XP spectra displayed below are clearly not good enough to allow the distinction between different carbon species (e. g., C adatoms and CH groups) and therefore only the total C coverage on the surface will be examined.

In fig. 6.15 XP spectra (Al($K\alpha$)) of saturation doses (72 L) of C_2H_4 on Pd(111) and on AuPd(111) surface alloys with 17% and with 29% Au, respectively, are displayed. The surface temperature during adsorption was held constant at 400 K. During the XPS measurements the surface was allowed to cool down towards room temperature. The observed C(1s) peaks are centered around 284 eV, which is slightly above the values observed for low temperature C_2H_4 adsorption on Pd(111) (283.2 eV from spectra that were recorded under similar conditions as the spectra in fig. 6.15 and 283.6 eV reported by Wang et al. [211]). The amount of C atoms present on the different surfaces was estimated by comparing the C(1s) peak integrals with spectra from C_2H_4 saturated Pd(111) at 100 K, where $\theta^{sat}_{C_2H_4} = 0.42$ ML ($\rightarrow \theta_C = 0.84$ ML) has been reported by Wang et al. [211]. The results are displayed in fig. 6.16 for a low C_2H_4 dose (3.6 L) and for a saturation dose (72 L). While for 17% Au only a slight decrease in the amount of accumulated C atoms on the surface is noticed a more significant change occurs if 29% of the surface Pd atoms are replaced by Au. Only about half of the C(1s) intensity is recorded on the latter surface compared to Pd(111). However, the surface seems

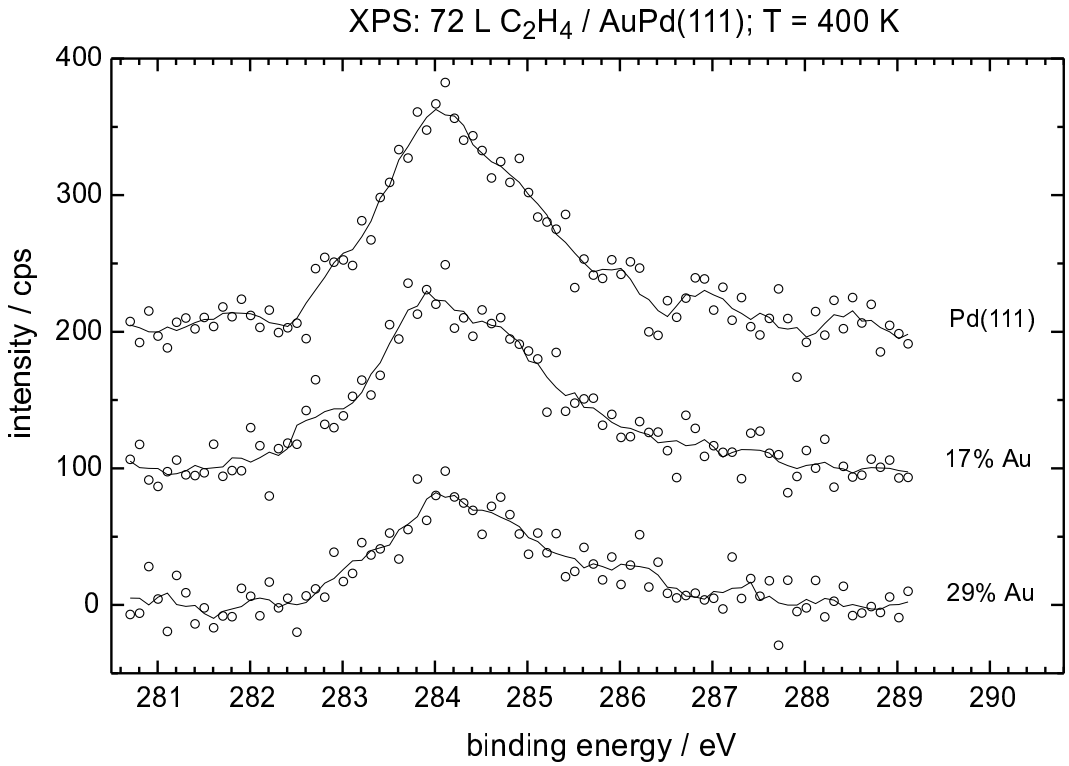

Figure 6.15: XPS (Al($K\alpha$)) spectra for C_2H_4/AuPd(111) surface alloys (T = 400 K). The lines represent spectra that were smoothed by averaging over 5 adjacent points.

to be still far from being inert towards C_2H_4 decomposition reactions at 400 K. Together with the HREELS experiments that showed at 300 K only very little ethylidyne formation on a surface with 22% Au, it seems to be likely that at least two different decomposition channels exist for C_2H_4 dehydrogenation on Pd(111) and on AuPd(111) surface alloys.

6.5 STM results

STM imaging of adsorbate covered surfaces has been used in the past to gain insight into surface reactions. As an example, the transformation from molecularly bonded C_2H_4 via ethylidyne to graphitic overlayers has been observed on Pt(111) by Land et al. [222] using STM. However, if the adsorbates are mobile on the surface and the STM scanning rate is slow compared to typical diffusion rates, it is not possible to obtain STM images from the adsorbed species. For the present system C_2H_4/Pd(111) it was attempted to record STM images from differently prepared surfaces. Unfortunately, neither the molecularly adsorbed species at low temperatures nor the ethylidyne species at room temperature could be detected

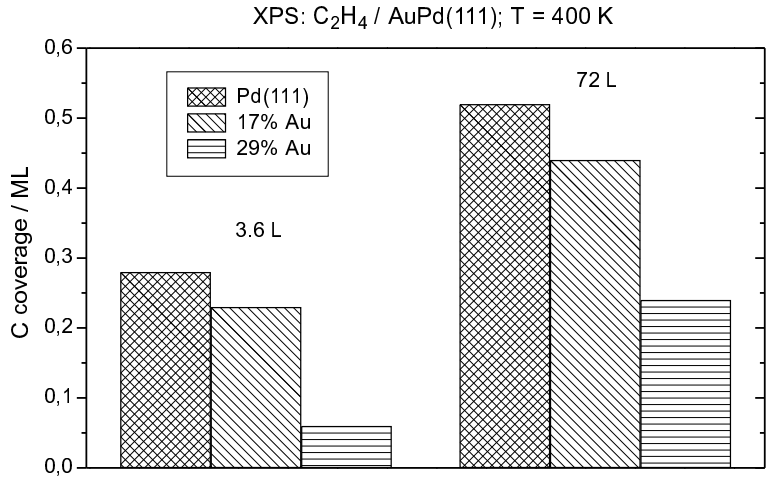

Figure 6.16: C coverages for C_2H_4/AuPd(111) surface alloys; 400 K. The coverage of atomic C was calibrated against XPS spectra from C_2H_4 saturated Pd(111) at 100 K with 0.42 ML C_2H_4 (= 0.84 ML C atoms) taken from [211].

in STM images. In the former case the noise caused by vibrations from the liquid N_2 cooling lines was preventing images of sufficiently high resolution. In the latter case it seemed that ethylidyne is too mobile at room temperature to be imageable by a relatively slowly scanning STM ($\sim$20 s per frame). On the other hand, immobile surface species could be prepared by annealing the surface at 400 K and above. In the following some examples for the resulting adsorbate layers on Pd(111) and on a AuPd(111) surface alloy with 17% Au will be presented.

The morphological changes caused by the interaction with C_2H_4 at 400 K have been analysed by STM for Pd(111) and for AuPd(111) with 17% Au. The results are shown in figs. 6.17 and 6.18, respectively. The C_2H_4 doses were sufficiently high for the C(1s) peak in XP spectra to have reached its maximum value at 400 K. The following observations can be derived from the STM images on Pd(111):

- In overview images (see fig. 6.17(a)) the distribution of adsorbate structures is found to be homogeneous over the surface, i. e., surface steps do not seem to play a significant role in the C_2H_4 decomposition process.
- A clear $(\sqrt{3} \times \sqrt{3})R30°$ superstructure is visible in relatively small domains with a typical size of a few tens of Å.
- The ordered $(\sqrt{3} \times \sqrt{3})R30°$ domains comprise about 40% of the total surface area.
- Between the ordered domains the (1×1) structure of the substrate atoms is weakly visible. Judging from the hazy contrast in these areas, it is likely that they are also covered by some mobile adsorbate species.

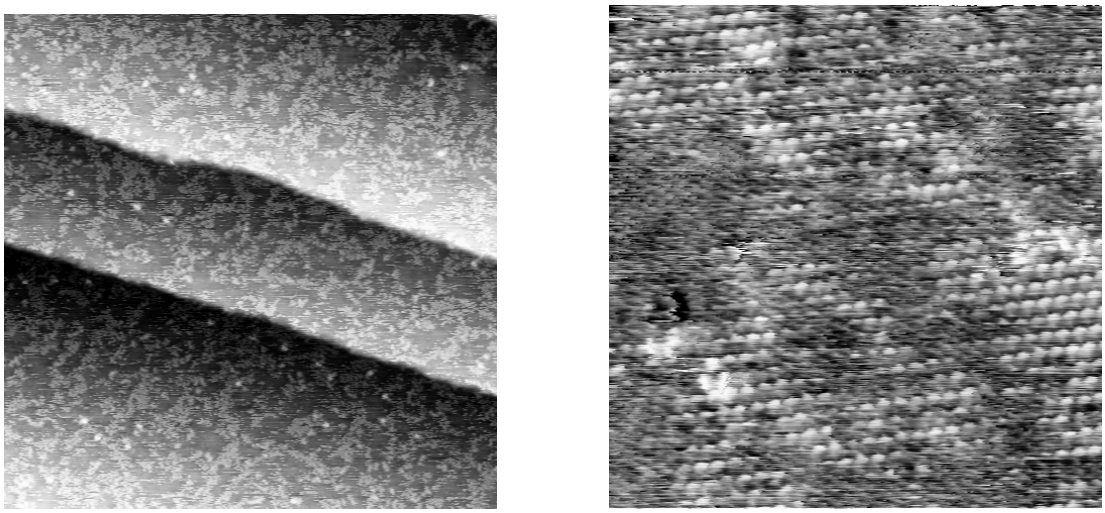

(a) 840 Å × 840 Å

(b) 140 Å × 140 Å

Figure 6.17: STM images of 110 L C_2H_4/Pd(111) (T_{ads} = 400 K).

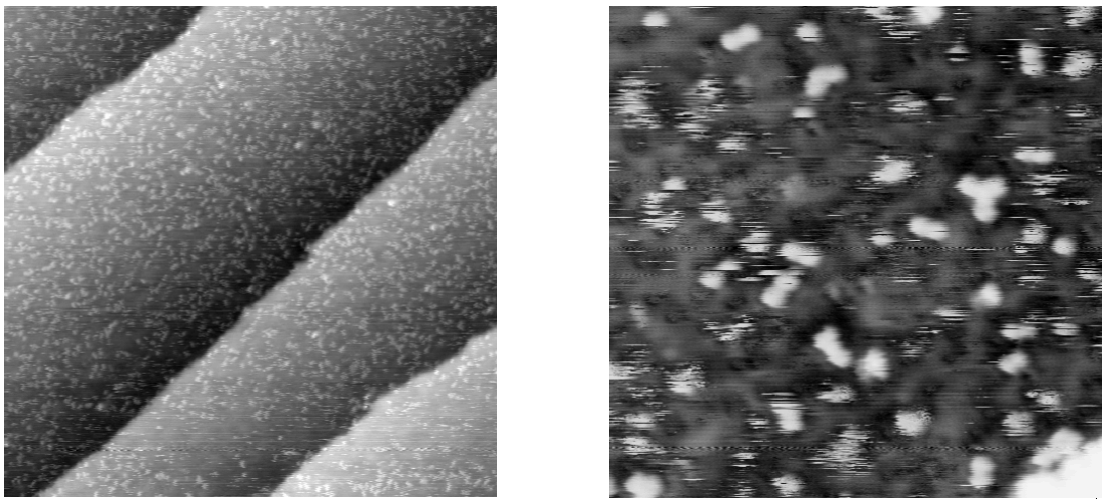

(a) 840 Å × 840 Å

(b) 135 Å × 135 Å

Figure 6.18: STM images of 72 L C_2H_4/AuPd(111) (17% Au; T_{ads} = 400 K).

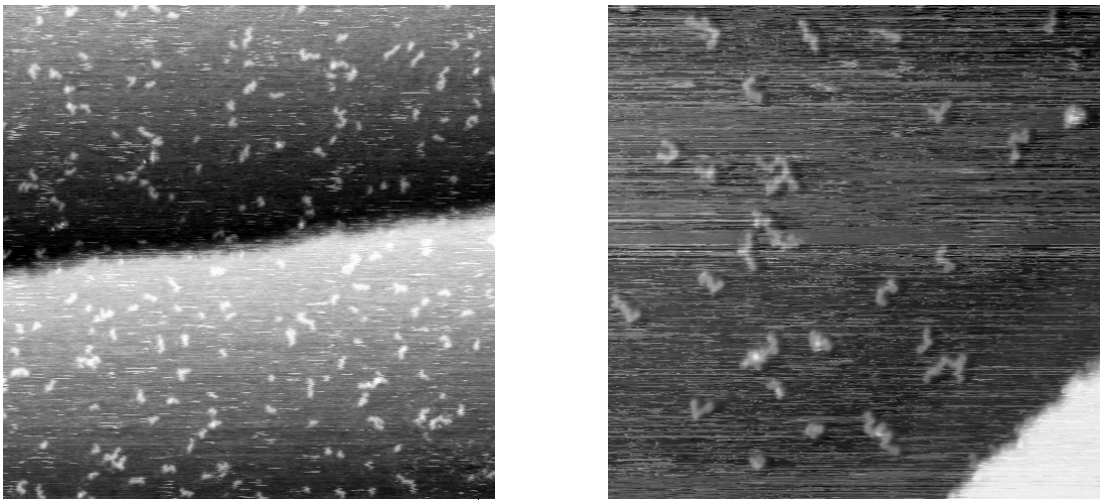

(a) 840 Å × 840 Å

(b) 360 Å × 360 Å

Figure 6.19: STM images of 180 L C_2H_4/Pd(111) (T_{ads} = 300 K) annealed at 500 K for 5 min.

- The adsorbates that are forming the $(\sqrt{3} \times \sqrt{3})R30°$ structure are not mobile at 300 K (STM operating temperature), because no changes in the adsorbate positions were noticed in consecutive STM images.

On a AuPd(111) surface alloy with 17% Au STM images taken after dosing 72 L C_2H_4 at 400 K (fig. 6.18) allow the following points to be noted:

- The adsorbate morphology is homogeneous across the surface. Steps are not preferentially covered by adsorbates.
- No indication for ordering within the adsorbate layer can be detected.
- Some small (typical size $\approx$ 10 Å; typical height $\approx$ 1 Å) islands are homogeneously distributed over the surface.
- The substrate structure could not be resolved in any area of the surface. This indicates that also between the islands adsorbates are covering the surface.

From the above listed points it can be concluded that the interaction of C_2H_4 with Pd(111) at 400 K is qualitatively different compared to the behaviour on a AuPd(111) surface alloy with 17% Au in the surface layer. Especially, the absence of ordered areas in the latter case shows that the composition of the adsorbate layer is considerably different in both cases. On the other hand, the

above presented XPS data did not suggest a large difference between the two surfaces, since the carbon coverage was determined to be only slightly lower on the Au containing surface. While for pure Pd(111) the ordered phase most likely consists of methylidyne (CH) groups, that have been identified by HREELS [196], the nature of the C containing species on the AuPd(111) surface alloy is not known. If it is assumed that on Pd(111) 40% of the surface is covered by CH groups in a $(\sqrt{3} \times \sqrt{3})R30°$ structure (local coverage = 0.33 ML), only about 0.13 ML of C atoms are found in these ordered areas. From XPS measurements (see fig. 6.16) it was estimated that about 0.5 ML C atoms should be present on this surface. Even if it is taken into account that the precision of a coverage determination by XPS might be quite inaccurate, it is evident that not all of the C atoms are found in the ordered methylidyne areas. Similarly, on the Au containing surface the total area of the islands is far too small to be able to account for all of the C atoms that should be present on the surface according to XPS ($\sim$0.45 ML). Hence, the existence of C containing adspecies, that are not visible in the STM images, has to be postulated for both surfaces.

On Pd(111) additional STM experiments were performed to investigate the surface species that is formed upon annealing at 500 K. In fig. 6.19 two STM images of different sizes are shown for a Pd(111) surface that have been exposed to 180 L C_2H_4 at 300 K and annealed at 500 K for 5 min. This preparation should result in a complete desorption of hydrogen from the surface [210]. Therefore, carbon is supposed to be the only constituent of the adsorbate structures that are visible in the STM images. Again, no aggregations are found at surface steps. On the terraces irregularly shaped, branched islands are detected. Most of them are about 0.8 Å high, but some show a small protrusion of about 1.6 Å height in the island centre. Unlike to the C_2H_4 decomposition reaction on Pt(111) surfaces [222], no graphitic overlayers are formed on Pd(111), which is due to the dissolution of C atoms in bulk Pd. This process is observed by XPS to occur at $T \geq 450$ K and therefore on the STM images shown in fig. 6.19 a considerable part of the carbon atoms that have been contained in the adsorbate layer at 300 K have already disappeared from the surface. The possibility of C dissolution prevents STM being a suitable tool for the quantification of carbon atoms on Pd surfaces, that have been annealed at elevated temperatures.

6.6 Discussion and concluding remarks

In this section, which concludes the chapter on experimental results for C_2H_4 adsorption and decomposition processes on Pd(111) and on Au-Pd(111) surfaces, the following questions will be addressed:

1. What is the nature of C_2H_4 species A, that is found for relatively low coverages on Pd(111)?

2. What is the role of species A in C_2H_4 decomposition reactions on Pd(111) and AuPd(111) surfaces?

3. How do Au atoms in the surface of AuPd(111) alloys influence C_2H_4 adsorption and decomposition reactions?

4. Which conclusions can be drawn for the catalytic properties of AuPd alloys with respect to C_2H_4 conversion reactions?

Ad 1. The nature of species A. In the introduction to this chapter the distinction between two limiting cases of C_2H_4 adsorption on metal surfaces, namely π and di-σ bonding, has been outlined. It was emphasized that no clear-cut dividing line between these two classes is defined. Consequently, there are C_2H_4/metal systems where the experimental characterization does not give evidence for an unequivocal decision about the bonding mode. In the following it will be investigated, if enough support can be derived from the experimental results to justify the classification of species A as di-σ bonded to the Pd(111) surface in contrast to the earlier determination of species B being π bonded [195, 211].

First, it should be noted that the transition from species A to species B takes place at about half of the saturation coverage of C_2H_4 which can be derived from XPS measurements. With 0.42 ML as saturation coverage (from [211]) it follows that up to 0.2 ML of species A molecules exist on the surface. This clearly shows that the occurence of the new species is not an effect of surface defects like Pd step edges. This was confirmed by additional HREELS experiments, where the Pd step edges had been decorated by a small amount of Au prior to C_2H_4 adsorption and no significant changes were observed in the spectra.

The most direct way to classify a C_2H_4/metal adsorption system as a case of di-σ bonding is to show that the hybridization state of the C atoms is close to sp^3. The analysis of the C_2H_4 valence band structure (by UPS) and the determination of the C–C bond length (e. g., by NEXAFS) could provide a reliable characterization of the hybridization state. In principle, an estimate of the C–C bond order could also be derived from the C–C stretching energy and hence vibrational spectroscopic methods could also be used to extract information about the C hybridization. However, since the C–C stretching mode (ν(CC)) is strongly coupled to at least one other mode (CH_2 scissoring; $\delta(CH_2)$) the measured frequencies do not reflect the force constant of the C–C bond directly, as was emphasized by Stuve et al. [201]. The calculation of the so-called $\pi\sigma$ parameter (equation 6.1) from both values, ν(CC) and $\delta(CH_2)$, is suggested by Stuve and coworkers in order to obtain a better estimate of the C–C bond order. However, the application of the $\pi\sigma$ parameter requires that both relevant modes are unequivocally identified. Since in this work no experiments using deuterated ethylene have been carried out, the peak assignments have to be obtained by comparison with spectra from

literature. For C_2H_4/Pd(111) the work of Gates and Kesmodel [195,196] and for the closely related system C_2H_4/Pd(110) the studies of Nishijima et al. [202] are possible references for the peak assignments.

C_2H_4 species on Pd(111)	$\delta(CH_2)$/meV	ν(CC)/meV	$\pi\sigma$ parameter
A	148.0	184.2	0.533
B	148.6/152	186.0	0.499/0.443

Table 6.6: $\pi\sigma$ parameters for C_2H_4/Pd(111). The values for the different modes have been derived from the spectra shown in fig. 6.7; for details see text.

The values that can be extracted for the ν(CC) and $\delta(CH_2)$ vibrational modes from the coverage dependent spectra shown in fig. 6.7 are collected in table 6.6. The $\pi\sigma$ parameters follow immedately from equation 6.1, but the validity of these numbers might be questioned for two reasons. First, for the $\delta(CH_2)$ vibration only a single peak can be clearly detected between 148 meV and 149 meV and a shift of about 0.6 meV is visible. For the higher coverages the peak seems to be broadened and in spectrum f even a second component might be present as a shoulder around 152 meV, which would correspond to the value reported by Gates and Kesmodel. Therefore, the $\pi\sigma$ parameter is determined for both values (148.6 meV and 152 meV) of the $\delta(CH_2)$ mode for species B. The spectra shown in fig. 6.9 (on and off specular measurements) support a $\delta(CH_2)$ frequency difference of about 3 meV between the two species, whereas in fig. 6.8 (annealing series) hardly any peak shift is visible for this mode. Second, the ν(CC) mode is a very weak feature in spectra from species A. It is only visible in a part of the spectra (e. g., in spectrum b of fig. 6.7). The interpretation of the $\pi\sigma$ parameters given in table 6.6 might lead to doubtful results because of the uncertainties that are encountered in the determination of the peak positions. As a concluding statement to the comparison of $\pi\sigma$ parameters for species A and species B, it can be said that a small tendency towards di-σ bonding is observed for species A compared to the π bonded species B but this characterization is far from being a final answer.

Since the $\pi\sigma$ parameter has been found to be only of very limited use in the present considerations, other indicators for changes in the adsorption mode of C_2H_4 upon increasing the coverage on Pd(111) have to be sought in the vibrational spectra. Two features will be discussed in this respect: The CH_2 wagging modes around 110 meV and the CH_2 stretching modes in the region above 350 meV. While the former are very intense and show the most distinct coverage dependent changes for C_2H_4/Pd(111), the latter exhibit the advantages of being closely related to the hybridization state of the C atoms and of being easily identifiable in the vibrational spectra. In table 6.7 the frequencies of these modes are collected for different systems to facilitate the comparative classification of C_2H_4/Pd(111). For the CH_2 wagging modes there is obviously no clear trend observable if π

	system	CH_2 wag	CH_2 stretch (s)	CH_2 stretch (as)	reference
di-σ	Pt(111)	112 (121)	362	372	[203]
	Ni(111)	136	366		[199]
	$C_2H_4Br_2$		366	373	[209]
π	Cu(111)	112	370	382	[205]
	Ag(110)	120			[206]
	Pd(110)	112	372	383	[202]
	O-Pd(111)	118	369	380	this work
	Au/Pd(111)	119	373	383	this work

Table 6.7: Vibrational energies of selected C_2H_4 adsorption systems, that have been classified as cases of π or di-σ bonding.

bonded molecules are compared to di-σ bonded molecules. It has also to be noted that the intensity patterns of the CH_2 deformation modes and the C–C stretching mode, i. e. the modes between 80 meV and 200 meV, are very different for the di-σ bonded sytems compared to the π bonded systems. The latter exhibit the CH_2 wagging mode as most intense peak between 112 meV and 120 meV, which therefore can be taken as fingerprint for weakly π bonded C_2H_4 molecules. Since several other modes are found in the close vicinity of the CH_2 wagging mode, there might be some doubt if all of the assignments cited in table 6.7 are correct. For example in the case of Pt(111) the inspection of the HREEL spectra in [203] shows that the value given by the authors for the CH_2 wagging mode (121 meV) corresponds to a very weak shoulder of a more intense peak centred at 112 meV, which might be a better choice for the CH_2 wagging mode. In short, from the lowering of the CH_2 wagging frequency from 113 meV (species B) to 107 meV (species A) no conclusions can be derived concerning the hybridization state of species A C_2H_4 molecules.

It remains the possibility to compare the CH_2 stretching modes of species A with reference values for other systems. Here, a clear trend can be recognized from the values in table 6.7. The CH_2 stretching frequencies of di-σ bonded C_2H_4 molecules are significantly below the values for the π bonded species. This finding agrees with the fact that for gaseous C_2 hydrocarbons also a negative shift is observed if the hybridization is changed from sp^2 (C_2H_4; $\nu(CH_2)(s) = 374$ meV) to sp^3 (C_2H_6; $\nu(CH_3)(s) = 359$ meV) [213]. Even though the peak shifts that are visible in the C_2H_4 coverage dependent HREEL spectra in fig. 6.7 are certainly not spectacular, they are still significant and reproducible (see also the spectra in figs. 6.8 and 6.9) with the frequencies for the two strongest CH_2 stretching modes shifted by about 4 meV to lower values for species A compared to species B. This finding has to be considered the best available proof of species A being indeed more "di-σ like" than species B.

Finally, is shall be explored if theoretical investigations also provide indica-

tions for the possible existence of di-σ bonded C_2H_4 on Pd(111) or if there are strong theoretical arguments agains this proposition. In a study using extended Hückel calculations Wong and Hoffmann investigated the bonding of C_2H_4 to the (111) oriented crystal faces of Ni, Pd, and Pt [223]. They compared the chemisorption energy for C_2H_4 molecules adsorbed at on-top sites (π bonding) to the respective value for 2-fold bonded molecules (di-σ bonding). For Ni(111) and Pt(111) they find a preference of di-σ bonding by 0.55 eV and 0.14 eV, respectively, and for Pd(111) a higher stability for π bonded molecules by 0.09 eV. While for Ni(111) the energy separation between the two states is quite high, for Pt(111) and for Pd(111) it can not be excluded according to the authors that also the less favourable adsorption state is populated. In the case of Pt(111) experimental evidence exists for a π bonded species at very low temperatures ($T \leq 52$ K) [224], while for Pd(111) no indications of the occurence a di-σ species have been recorded so far. Wong and Hoffmann suggest explicitly that a di-σ species on Pd(111) might be found experimentally because of the energy difference between the two species being even smaller than for Pt(111), where both states have been identified by measurements.

By ab initio calculations employing the density functional method, Fahmi and van Santen studied the interaction of C_2H_4 with Pd_n clusters ($n = 1 - 6$). Depending on cluster size either π or di-σ bonding is energetically more favourable. For $n = 1$ only the π bonded state is possible and for $n = 2$ it is still the more stable configuration. But for $n = 3 - 5$ di-σ bonding is slightly preferred. The largest cluster that has been investigate ($n = 6$) exhibits again a higher binding energy for C_2H_4 in a π bonded configuration (82 kJ mole^{-1} vs. 57 kJ mole^{-1}). The cluster size dependent oscillations of the preferable C_2H_4 adsorption mode might be reflected in the structure sensitivity of C_2H_4 adsorption on Pd single crystal surfaces, where for saturation coverages di-σ bonding has been found on the (100) oriented plane [201] and π bonding on (110) [202] and (111) [195] surfaces.

From the two theoretical studies that have been referred to above neither a conclusive argument *for* the existence of di-σ bonded C_2H_4 on Pd(111) could be extracted nor followed any strong evidence *against* this possibility. Since in the HREEL experiments the variation of the C_2H_4 adsorption mode is observed as an effect of the adsorbate coverage, calculations that take into account direct and through metal adsorbate–adsorbate interactions are necessary to provide information about the nature of the two observed species.

As a conclusion to the question about the nature of C_2H_4 species A it can be stated that vibrational spectroscopy provides some evidence (relatively low CH_2 stretching frequencies) for species A being rather di-σ bonded than π bonded to the Pd(111) surface. However, a final answer to this question requires additional experimental and theoretical studies on the effects of C_2H_4 coverage variations on Pd(111).

Ad 2. The role of species A in C_2H_4 decomposition reactions. Independent of the answer to the former question about the nature of species A, it is worthwhile to discuss whether this C_2H_4 species is found to play an important role for C_2H_4 reactions on Pd(111) and AuPd(111) surfaces. First of all, it has to be noted that besides the different vibrational properties of the two species A and B also the binding energy to the surface is found to be considerably different, with species A being more strongly bonded for low C_2H_4 coverages. This can be inferred from the fact that this species is preferably populated at low coverages and that after partial desorption of C_2H_4 from saturated Pd(111) it is found to be present on the surface up to higher temperatures than species B. Molecules of the latter kind are either desorbing or are being converted to species A molecules by heating the crystal, because the vibrational peaks of species B have vanished before any indications for C_2H_4 decomposition products can be detected in the spectra (see fig. 6.8). Therefore, the small amount of ethylidyne that is found after heating low temperature C_2H_4 saturated Pd(111) surfaces to temperatures around 300 K is originating from species A molecules. Hence, it can be stated that species A is a precursor state for the partial C_2H_4 dehydrogenation to ethylidyne and that for species B molecular desorption is strongly favoured compared to decomposition. However, only a small fraction of the species A molecules are found to be dehydrogenated. From the TPD studies of Tysoe et al. it can be inferred that even for low C_2H_4 coverages only about 4% of the molecules are decomposed [210].

An additional indirect argument for the above proposition of species A being a precursor state to ethylidyne formation can be derived from the HREELS measurements on the interaction between C_2H_4 and AuPd(111) surface alloys. It was clearly shown that the abilitiy of the bimetallic surfaces to adsorb C_2H_4 as species A is reduced with about the same dependence on the Au concentration as the ability to convert ethylene to ethylidyne (see figs. 6.11 and 6.13). I. e., on AuPd(111) surface alloys where no species A molecules are found at low temperatures also no ethylidyne formation is detected at 300 K.

Ad 3. The role of Au atoms in C_2H_4 adsorption and decomposition reactions on AuPd(111) surface alloys. The characterization of the role that the Au atoms play for the interaction between C_2H_4 and AuPd(111) surface alloys is closely related to Au derived modifications of molecular C_2H_4 adsorption. These were already determined in the previous paragraph to consist mainly in the complete suppression of species A by about 22% Au in the surface layer and a concomitant inhibition of ethylidyne formation. Here the additional aspect of C_2H_4 decomposition processes at elevated temperatures (400 K) has to be discussed.

The XPS measurements presented in fig. 6.15 and 6.16 show that with 29% Au in the surface layer of AuPd(111) the maximum C coverage obtainable by

C_2H_4 decomposition at 400 K is reduced to about 50%. Taking into account that even for the lower Au concentration of 22% virtually no ethylidyne formation is detectable at 300 K, it seems to be plausible to postulate a second C_2H_4 decomposition pathway for C_2H_4 on Pd(111) and on AuPd(111) surfaces besides ethylidyne formation. From the HREELS measurements on different AuPd(111) surface alloys at 300 K (fig. 6.13) some hints can be derived for ethynyl groups (CCH) being stable intermediates in this alternative pathway. Since the formation of ethylidyne requires not only the abstraction of a hydrogen atom from the ethylene molecule but also the transfer of another hydrogen atom from one C atom to the other, it is plausible that this complex reaction makes higher demands on the reactivity of the surface than a simple hydrogen transfer to the surface. Therefore, the substitution of relatively reactive surface atoms (Pd) by inert atoms (Au) is likely to affect primarily the complex ethylidyne formation reaction.

It can be asked whether the effect of Au can be described by a simple "site-blocking" model, where the Pd atoms within AuPd(111) surfaces are assumed not to be altered significantly in their electronic properties by neighbouring Au atoms. The site-blocking effect might indeed play a role in the inhibition of ethylidyne formation, because this reaction certainly proceeds in several steps, which probably require the interplay between different types of Pd(111) surface sites. On the other hand, in the above considerations, that were emphasizing the role of species A, geometric arguments can be shown not to play an important role. The reason for this is that for the adsorption of molecular C_2H_4 in an arbitrary configuration a maximum of three Pd atoms are required to be located in the direct vicinity of the molecule. For the "classical" π (on-top site) and di-σ (bridge site) bonding configurations only one or two Pd atoms are required, respectively. Since on a surface with 22% Au enough pure Pd threefold sites are available, it can not be argued that a certain bonding mode (here: species A) is inhibited only because of the lack of suitable adsorption sites. On the contrary, the strong influence of a relatively small amount of Au atoms can only be explained by "electronic effects", i. e., the electronic structure of the Pd atoms is modified by neighbouring Au atoms in a manner that considerably affects their reactivity towards C_2H_4 adsorption and decomposition.

Ad 4. Consequences for catalytic reactions of C_2H_4 on AuPd surfaces. Since one important aim of surface science studies on gas–metal interactions is to improve the understanding of the processes that determine the performance of supported metal catalysts, it has to be asked to what extent new insight into C_2H_4 reactions over AuPd catalysts has been gained by this study. First of all, several points have to be listed that make it difficult to draw conclusions for catalytic reactions from results that are obtained under UHV conditions on single crystalline metal surfaces using only a single gaseous species as reactant:

- In real catalysts the metal particles exhibit surfaces with various different orientations and with a relatively high amount of defects like edge or corner atoms. Hence, on these metal particles a large variety of different reaction sites coexists and due to surface diffusion of molecular species the processes on all of these sites might in principle be coupled.

- The support of the catalyst and additional promoters might play an important role for heterogeneous catalytic reactions.

- Catalytic reactions mostly require the presence of different molecules in the gas phase. Consequently, on catalyst surfaces also different adsorbed species might be present and might compete for distinct adsorption and reactions sites.

- The partial pressures of reactants is many orders of magnitude higher in real systems compared to the model investigations using UHV methods. The population of energetically unfavourable states might become possible at elevated pressures.

- Regarding the reaction temperatures it can be stated that it is in principle possible to chose the same values for UHV studies as applied in real catalytic reactions. However, the temperature dependence of certain processes might be completely different in UHV than in a high pressure environment.

In short, many parameters exist, that are likely to influence the performance of a real catalyst and that are not under control in surface science studies like the present one. Having said this, it has to be emphasized that in the description of the mechanisms for catalytic reactions one still has to recur to the combination of many single steps, which have to be justified by experiments on well-defined — and therefore idealized — systems. Therefore, a detailed insight into the interaction between the reactants with well-defined metal surfaces is a necessary, but not a sufficient condition for the understanding of processes in industrial catalytic reactions.

Coming back to the present case, it can be stated that several important aspects have been revealed for C_2H_4 adsorption and decomposition on both Pd(111) and AuPd(111) surfaces. The detection of a new molecular species at low sample temperatures, which exhibits features of di-σ bonding, shows that the simple picture of C_2H_4 being π bonded to Pd(111), that is reported in the previous literature, is not adequate for a realistic description of the C_2H_4/Pd(111) system. Coadsorption experiments with CO and O, which might be relevant for the understanding of the above mentioned synthesis reaction of vinyl acetate from C_2H_4, CH_3COOH, and O_2, yield the general result that both coadsorbates weaken the interaction between C_2H_4 and the Pd surface. For bimetallic AuPd(111) surfaces

it was revealed that the subtle balance between the two molecular C_2H_4 species is drastically altered compared to Pd(111). Another, possibly related effect of the Au surface atoms was shown to consist in the modification of the C_2H_4 decomposition pathways with ethylidyne formation being strongly suppressed by 22% Au. Two consequences of this effect for catalytic reactions can be suggested. First, ethylidyne is likely to poison the catalyst because it is relatively stable (under UHV conditions it is existing up to 350 K on Pd(111)). If its formation can be avoided the activity of the catalyst might increase. Second, for the formation of vinylic products ($XCHCH_2$) ethylidyne is part of an unwanted side reaction that decreases the selectivity of the catalyst. Hence, the latter might be improved if the C_2H_4 decomposition pathway via ethylidyne is blocked by Au.

Resume

The growth and alloying behaviour of Au on Pd(111) was studied by variable temperature STM and by AES. CO and C_2H_4 adsorption was analysed on different types of well-defined Au-Pd(111) surfaces mainly by HREELS and by TPD.

The first layer of Au grows pseudomorphically. In the second Au layer an irregular pattern of strain relief stripes appears, and from the third Au layer on the stripes become denser and the degree of order in the stripe pattern increases. Atomically resolved STM images show that the surface layer consists of an almost undistorted hexagonal lattice and therefore dislocations in deeper layers are determined to be responsible for the strain relief pattern. From the temperature dependence of Au island densities on Pd(111) a Au adatom diffusion barrier of (222 ± 22) meV could be calculated. The initial intermixing mechanisms of Au and Pd in the surface layer of Au-Pd(111) films strongly depend on the film thickness: As long as a part of the Pd substrate atoms are not Au covered, two types of alloying processes dominate at moderate temperatures (550 K – 700 K). First, detachment of Au atoms from Au step edges followed by diffusion on the terraces and exchange with Pd substrate atoms leads to a relatively homogeneous distribution of Au atoms in the former Pd terraces. Second, during the equilibration of the dendritically shaped Au step or island edges step edge assisted exchange processes between Au step atoms and Pd substrate atoms leave imprints of the original shapes of the Au islands in the terrace. On completely Au covered Pd(111) surfaces the interdiffusion of Au and Pd is not influenced by step edges or by the strain relief stripes mentioned above.

CO adsorption on layered Au/Pd(111) is possible at open Pd terrace sites and at Au step edges sites (for $T \geq 100$ K). The CO species at Au step edges gives rise to a C–O stretching peak in the HREEL spectra at 263 meV, which is a typical value for CO adsorbed linearly on Au sites. In TPD spectra different types of Au step edge sites can be identified with the kink sites providing the most favourable CO adsorption site ($T_{des} = 200$ K). On AuPd(111) surface alloys several different types of CO adsorption sites can be determined by combined STM, TPD, and HREELS measurements: CO is linearly bonded to Pd monomers. On Pd dimers, bridge bonded CO is observed for low CO coverages and two linearly bonded CO molecules are accommodated on Pd dimers for higher CO coverages. CO in threefold hollow sites is observed on compact Pd trimers. These assignments are

possible for relatively low Pd concentrations in the surface, while for higher Pd concentrations the differentiation between the various CO adsorption configurations is not possible. TPD measurements showed that the existence of a mobile CO precursor state on Au terrace sites has to be postulated in order to explain the observed peak shifts. In the limit of low Pd concentrations, the CO TPD peak from Pd monomers is shifted by about 40 K to lower temperatures due to the precursor mediated desorption.

For the interaction of C_2H_4 with Pd(111) and AuPd(111) surfaces a new low coverage species ("species A") is reported at low temperatures. Evidence is provided that this species is more "di-σ like" than the previously examined π bonded species, which is found at higher coverages. On AuPd(111) surface alloys the formation of species A is strongly reduced by only 22% Au in the surface layer. Since the formation of ethylidyne on these surface alloys is also disfavoured, species A is determined to constitute a precursor state to ethylidyne formation. On completely Au covered Pd(111) only the adsorption of a weakly bonded form of C_2H_4 is observed at Au step edges.

The present study could reveal interesting aspects of the interaction between CO/C_2H_4 and Au-Pd(111) surfaces by combining STM, TPD, and HREELS in one UHV apparatus. It has become obvious, that the benefit of a reliable characterization of a bimetallic surface based on real space imaging by STM can not be overestimated. However, several questions remain open because they could not be answered by the experimental methods that were applied. With the very detailed atomic-scale investigations on the Au-Pd(111) growth and alloying system and particularly with the STM derived correlation between CO TPD and surface composition, the door is wide open for future adsorption and reaction studies on Au-Pd(111) surfaces, since CO TPD is readily available in many surface science laboratories. Therefore, future synchrotron photoemission studies or high resolution vibrational investigations — to name some interesting examples — can be based on the available STM characterization of the surfaces.

Zusammenfassung

In der vorliegenden Arbeit wurden die lokalen chemischen Eigenschaften von nanostrukturierten Au-Pd Modellkatalysatoren untersucht. Die Grundidee besteht darin, auf wohldefinierten, bimetallischen Einkristalloberflächen Adsorptions- und Reaktionsexperimente durchzuführen, um daraus grundlegende Erkenntnisse über die Wechselwirkung zwischen Molekülen und bimetallischen Oberflächen zu gewinnen. Der Erfolg dieses Ansatzes hängt in großem Maße von der Genauigkeit ab, mit der die Struktur und die chemische Zusammensetzung der untersuchten Oberflächen bestimmt werden. Mit Hilfe der Rastertunnelmikroskopie (Scanning Tunneling Microscopy, STM) ist es möglich, Metalloberflächen mit atomarer Präzision abzubilden. Ein Ziel dieser Arbeit war es zu zeigen, wie STM mit anderen Analysemethoden[4] in einer Ultrahochvakuum-Apparatur kombiniert werden kann und welche Vorteile und neuen Erkenntismöglichkeiten sich aus dieser Kombination ergeben.

Als Untersuchungssystem wurde Au-Pd ausgewählt. Erstens weist dieses System interessante katalytische Eigenschaften auf. So werden Au-Pd-Katalysatoren in industriellen Partialoxidationsreaktionen von C_2H_4 eingesetzt [2–5]. Außerdem sind Au-Pd-Anoden-Katalysatoren vielversprechende Kandidaten für die H_2-Oxidation in Brennstoffzellen, die mit CO verunreinigtem H_2-Gas betrieben werden [6]. Zweitens hat die Kombination eines inerten Metalls (Au) mit einem reaktiven Metall (Pd) den Vorteil, dass die Interpretation der Adsorptionsmessungen an diesem bimetallischen System einfacher ist als im Falle zweier ähnlich reaktiver Metalle. Deshalb war es möglich, sichere und detaillierte Erkenntisse über verschiedene elementare Chemisorptionsvorgänge zu gewinnen. Die Präparation der bimetallischen Oberflächen erfolgte durch Aufdampfen von kleinen Mengen von Au auf einen (111)-orientierten Pd-Einkristall. Zur Herstellung der Oberflächenlegierungen wurde der Kristall anschließend geheizt.

CO stellt sicherlich das am besten untersuchte Adsorbat auf Metalloberflächen dar [102]. Da seine Adsorptionseigenschaften auf reinen Pd-Oberflächen schon gut bekannt sind (s. Abschnitt 5.1.2) eignet es sich sehr gut als Ausgangspunkt für

[4] Röntgen-Photoelektronenspektroskopie (X-ray Photoelectron Spectroscopy, XPS), Auger-Elektronenspektroskopie (Auger Electron Spectroscopy, AES), Thermodesorptionsspektroskopie (Temperature Programmed Desorption, TPD) und hochaufgelöste Elektronen-Energieverlustspektroskopie (High Resolution Electron Energy Loss Spectroscopy, HREELS).

die Untersuchung der chemischen Eigenschaften von komplexen bimetallischen Oberflächen. Sowohl CO als auch C_2H_4 sind zudem von großem Interesse aus einer anwendungsorientierten Sicht, da die katalytische Umsetzung dieser beiden Moleküle eine große wirschaftliche Bedeutung hat (für CO in der katalytischen Reinigung von Abgas- bzw. Brennstoffgasströmen; für C_2H_4 in der Herstellung von Grundstoffen für die chemische Industrie).

Es wurde schon betont, dass bei der Untersuchung von Adsorbaten auf bimetallischen Oberflächen die Struktur und Zusammensetzung der Oberfläche sehr gut bekannt sein müssen, um überhaupt die spektroskopischen Messungen interpretieren zu können. Für viele der Oberflächen, auf denen die Adsorption von CO und von C_2H_4 in dieser Arbeit spektroskopisch untersucht wurde, konnten atomar aufgelöste STM-Bilder gewonnen werden, so dass die genannte Anforderung für die meisten der gezeigten Messungen gut erfüllt ist. Außerdem wurden einige Messreihen zur Untersuchung des Wachstums von Au auf Pd(111) und zur AuPd(111)-Oberflächenlegierungsbildung durchgeführt, aus denen sich interessante Erkenntisse über die beteiligten atomaren Elementarprozesse ergaben.

Der experimentelle Aufbau ist in Abb. 2.2 schematisch dargestellt. Als wichtigste Eigenschaft dieser UHV-Apparatur kann herausgestellt werden, dass die Probe unter ständiger Temperaturkontrolle zu den verschiedenen Analysemethoden transferiert werden kann. Insbesondere ist es möglich, vor oder nach HREELS- bzw. TPD-Messungen STM-Aufnahmen von der Probenoberfläche zu gewinnen. Die Probe kann mit flüssigem Stickstoff gekühlt werden (bis ca. 100 K) und mittels Elektronenstoßheizung geheizt werden.

Im folgenden werden die wichtigsten Ergebnisse aus den einzelnen Kapiteln zusammenfassend vorgestellt.

Wachstum von Au auf Pd(111) (Kapitel 3). Das Wachstum von Au auf Pd(111) wurde im Bedeckungsbereich 0.1 ML – 3 ML bei $100\,\mathrm{K} \leq \mathrm{T} \leq 400\,\mathrm{K}$ und mit Au-Flüssen um 0.01 ML/s mittels STM untersucht. Bei kleinen Au-Bedeckungen ($\Theta_{\mathrm{Au}} \leq 0.4\,\mathrm{ML}$) findet man Au-Inseln auf den Pd(111) Terrassen, die ab ca. 180 K dendritische Formen annehmen (Abb. 3.1 und 3.3). Aus der Temperaturabhängigkeit der Inseldichte zwischen 120 K und 225 K kann mit Hilfe der Nukleationstheorie eine Au-Adatomdiffusionsbarriere auf Pd(111) von $(222 \pm 22)\,\mathrm{meV}$ abgeleitet werden (Abb. 3.6). Das Wachstum der ersten Au-Atomlagen erfolgt relativ flach, es wird aber kein perfektes Lagenwachstum erreicht. Der Vergleich zwischen verschiedenen Messungen mit $\Theta_{\mathrm{Au}} \approx 1\,\mathrm{ML}$ ergibt, dass durch Tieftemperatur-Deposition (110 K) von Au und anschließendes Tempern bei 400 K die Au-Schichten mit dem geringsten Anteil von Löchern in der ersten und Inseln in der zweiten Lage erzielt werden (Abb. 3.7 und 3.8). Während die erste Au-Lage pseudomorph aufwächst, sind mehrlagige Au-Filme durch spannungsinduzierte Versetzungsmuster gekennzeichnet. Diese erscheinen als dunkle Linien in den STM-Bildern (Abb. 3.9). Atomar aufgelöste STM-Bilder von diesen

Linien weisen auf Versetzungen in tieferen Lagen hin (Abb. 3.10), wie sie auch in anderen heteroepitaktischen Systemen gefunden wurden (Ag/Ru(0001) [61] und Ag/Pt(111) [63]).

AuPd(111)-Oberflächenlegierungsbildung (Kapitel 4). Während bei Substrattemperaturen unterhalb von 400 K reine Au-Schichten auf dem Pd(111)-Substrat aufwachsen, findet man Legierungsbildung bei höheren Wachstumstemperaturen bzw. durch Heizen von Au/Pd(111)-Filmen auf $T \geq 550$ K. Es wurden umfangreiche STM- und AES-Messungen zur Legierungsbildung bei verschiedenen Au-Bedeckungen und Heizparametern durchgeführt. Insbesondere die Fähigkeit, in atomar aufgelösten STM-Bildern zwischen Au- und Pd-Atomen unterscheiden zu können, erlaubt eine sehr genaue Beschreibung der Oberflächen.[5] Es konnte gezeigt werden, dass die Legierungsstruktur und die atomaren Prozesse, die zur Legierungsbildung führen, stark von der anfänglichen Au-Bedeckung abhängen. Relativ homogene Pd- bzw. Au-Verteilungen in der Oberfläche findet man nach dem Heizen von Au-Filmen, bei denen das Pd-Substrat vollständig von Au bedeckt ist. In diesem Fall hängt zwar die lokale Pd-Konzentration von der lokalen Au-Schichtdicke ab, es gibt aber keine großen Variationen der Legierungszusammensetzung innerhalb dieser Bereiche. Insbesondere spielen Stufenkanten (Abb. 4.13) oder die oben erwähnten Versetzungslinien in der zweiten und in höheren Au-Lagen (Abb. 4.14) keine besondere Rolle.

Im Fall von $\Theta_{Au} \leq 1$ ML, wo je nach Bedeckung dendritische Inseln oder trigonale Löcher vor dem Heizen existieren, bilden sich bei nicht zu hoher Temperatur (bis 700 K) sehr inhomogene Legierungsoberflächen. Aus der Analyse der Elementverteilung in den verschiedenen untersuchten Oberflächen lassen sich interessante Schlüsse in bezug auf die atomaren Austauschprozesse, die zur Legierungsbildung führen, ziehen. Die ersten Anzeichen für eine Durchmischung der beiden obersten Atomlagen findet man in STM-Bildern nach Heizen auf 550 K (Abb. 4.1). In Übersichtsaufnahmen lassen sich in der Nähe von Inseln und von Au-dekorierten Stufenkanten Abdrücke entdecken, deren Form den Au-Strukturen ähneln, die vor dem Heizen vorhanden waren (Abb. 4.1, 4.2 und 4.6). Die Inseln selber nehmen durch das Heizen eine kompaktere Form an, wobei kleinere Inseln durch Ostwald-Reifung verschwinden. Atomar aufgelöste STM-Bilder zeigen, dass die Abdrücke durch die Einlagerung von Au-Atomen in die Kristalloberfläche erzeugt werden (Abb. 4.7). Außerdem findet man auch in den Terrassen-Gebieten, die weit von den Abdrücken entfernt sind, einzelne Au Atome (Abb. 4.8). Die Zusammensetzung der Inseln und der Au-Anlagerungen an den Stufenkanten ändert sich durch Heizen auf $T \geq 600$ K (Abb. 4.8 und 4.9). Mindestens drei verschiedene Arten von atomaren Austauschprozessen sind

[5] In der Regel werden Au-Atome dunkler (d. h. tiefer) abgebildet als Pd-Atome, was entweder auf einen elektronischen Effekt zurückzuführen ist, oder durch eine direkte Wechselwirkung zwischen der STM-Spitze und den Substratatomen erklärt werden kann.

nötig, um die experimentellen Beobachtungen zu erklären (Abb. 4.10): Erstens, ein stufenkanten-unterstützter Austauschprozess während der Umformung der verzweigten Au-Inseln; zweitens, ein Austausch zwischen Pd-Terrassenatomen und einzelnen Au-Adatomen, die sich zuvor von Stufenkanten abgelöst haben; drittens, ein direkter (vermutlich fehlstellen-induzierter) Interlagen-Austauschmechanismus. Nach Heizen auf $T \geq 600\,K$ findet man runde Legierungsinseln, die auf eine niedrige Bildungsenergie von Kinken schließen lassen. Durch eine statistische Analyse von atomar aufgelösten STM-Bildern konnte die theoretische Vorhersage bestätigt werden, wonach Au-Oberflächenatome von mehr Pd-Atomen umgeben sind als bei einer rein zufälligen Verteilung erwartet und umgekehrt (Abb. 4.19 und 4.20) [98]. Für die Herstellung von homogenen Oberflächenlegierungen für nachfolgende Adsorptionsexperimente wurden zwei Standard-Verfahren entwickelt. Niedrige Pd-Konzentrationen lassen sich erzielen durch Anlassen von 2 ML – 3 ML Au/Pd(111) bei $T \geq 600\,K$. Hohe Pd-Konzentrationen wurden erzeugt durch Aufdampfen einer kleinen Menge Au und anschließendes kurzes Heizen auf $T \approx 780\,K$.

Die Durchmischung der obersten Kristalllagen wurde auch mittels AES beobachtet (Abb. 4.21 und 4.22). Mit Hilfe von nummerischen Simulationen, die auf einem einfachen Modell zur Beschreibung der Interdiffusion zwischen Au und Pd beruhen, konnten einige kinetische Aspekte der Legierungsbildung analysiert werden.

CO-Adsorption auf Au-Pd(111)-Oberflächen (Kapitel 5). Die Adsorptionsexperimente wurden auf zwei verschiedenen Typen von bimetallischen Au-Pd(111) Oberflächen durchgeführt: Zum einen auf Au/Pd(111)-Schichtsystemen, bei denen jede Atomlage aus nur einer Atomsorte besteht (Präparation: s. Kapitel 3). Zum anderen auf AuPd(111)-Oberflächenlegierungen, deren Herstellung in Kapitel 4 beschrieben wurde. Als zentrale Fragestellung bei den Schichtsystemen wurde der Einfluss von Au-Stufenatomen auf das CO-Adsorptionverhalten untersucht. Während auf glatten Au/Pd(111)-Filmen bei 100 K und darüber keine CO-Adsorption nachgewiesen wurde, stellt man sowohl mit HREELS als auch mit TPD fest, dass CO auf "rauen" Filmen haftet, die durch Au-Deposition bei tiefen Temperaturen hergestellt wurden. In HREEL-Spektren findet man eine C–O Streckschwingungsbande bei 263 meV, die mit linear an Au-Stufenatome gebundenem CO erklärt werden kann (Abb. 5.20, 5.22 und 5.23). In TPD-Spektren[6] von vollständig Au-bedecktem Pd(111) mit einem hohen Au-Stufenanteil treten CO-Desorptionspeaks bei 140 K und bei 200 K auf (Abb. 5.2). Diese können CO-Adsorptionsplätzen auf Au-Stufenatomen bzw. auf Au-Kinkatomen zugeordnet werden. Es konnte also gezeigt werden, dass die CO-Adsorptionsenergie auf Au-Oberflächenatomen stark von deren Koordinationszahl abhängt.

[6]Die Heizrate betrug in allen TPD-Experimenten 10 K/s.

Von den Messungen zur CO-Adsorption auf AuPd(111)-Oberflächenlegierungen sind die Ergebnisse für kleine Pd-Konzentrationen ($c_{Pd} \leq 25\%$) besonders interessant. Aufgrund der Tatsache, dass bei den untersuchten Temperaturen ($T \geq 100\,K$) CO nicht auf Au-Oberflächenatomen haftet[7] können die spektroskopisch gewonnenen Daten gut den verschiedenen in STM-Bildern identifizierten Pd-Adsorptionsplätzen zugeordnet werden. Bei sehr kleinen Pd-Konzentrationen gibt es nur Pd-Monomere in der Oberfläche. An diese bindet CO linear ($\nu_{CO} = 259\,meV$, Abb. 5.27) mit einer Adsorptionsenergie von $(82 \pm 6)\,kJ\,mole^{-1}$ (Abb. 5.16). In den TPD-Spektren findet man sowohl CO-bedeckungsabhängige (Abb. 5.8) als auch Pd-konzentrationsabhängige (Abb. 5.6) Peak-Verschiebungen, die beide mit Hilfe von Simulationsrechnungen durch ein Precursor-Modell erklärt werden können (Abb. 5.11, 5.13 und 5.14). Auf Pd-Dimeren, die ab ca. 8% Pd auftreten, bindet CO zunächst an den Brückenplatz (1 CO-Molekül pro Dimer, $\nu_{CO} = 238\,meV$), um bei höheren CO-Dosen auf die "on-top" Plätze auszuweichen ($\nu_{CO} = 259\,meV$), so dass dann zwei CO Moleküle an ein Pd-Dimer binden können (Abb. 5.33). In den TPD-Spektren findet man bei $8\% \leq c_{Pd} \leq 12\%$ neben dem Desorptionssignal von Pd-Monomeren bei $\sim 300\,K$ zwei zusätzliche Peaks bei 250 K (Dimer-on-top-Platz) und bei 340 K (Dimer-Brückenplatz) (Abb. 5.6 und 5.9). Reine Pd-Muldenplätze treten ab $c_{Pd} \approx 24\%$ auf und stellen die stabilsten CO-Adsorptionsplätze auf den AuPd(111) Oberflächenlegierungen dar (Desorption bei $T \geq 450\,K$ (Abb. 5.10) und $\nu_{CO} = 227\,meV$ bei kleinen CO-Bedeckungen, Abb. 5.34).

C_2H_4-Adsorption und Zersetzung auf Au-Pd(111)-Oberflächen (Kapitel 6). Zunächst wurde die Adsorption von C_2H_4 auf der reinen Pd(111)-Oberfläche mit Hilfe von HREELS untersucht. Im Gegensatz zu älteren Messungen von Kesmodel und Gates [195, 196] wurde eine ausgeprägte Bedeckungsabhängigkeit der Schwingungsspektren von chemisorbiertem C_2H_4 bei tiefen Temperaturen gefunden. Während die Spektren für hohe Bedeckungen gut mit den älteren Messungen übereinstimmen und mit π-gebundenem C_2H_4 erklärt werden können ("Spezies B"), treten bei kleinen Bedeckungen andere Schwingungsfrequenzen auf ("Spezies A", Abb. 6.7). Insbesondere fällt auf, dass die "CH_2-wagging"-Schwingung statt bei 113 meV (Spezies B) bei 107 meV gefunden wird. Außerdem liegen die CH_2-Streckschwingungen bei kleinen C_2H_4-Bedeckungen niedriger als bei hohen Bedeckungen. Daraus kann geschlossen werden, dass die Wechselwirkung zwischen den C_2H_4-Molekülen und der Oberfläche bei kleinen Bedeckungen intensiver ist und zu größeren Störungen der Molekülstruktur führt als bei großen Bedeckungen. Es kann gefolgert werden, dass Spezies A auf einer Skala zwischen π-gebundenem und di-σ-gebundenem C_2H_4 etwas näher in Richtung "di-σ" liegt als Spezies B.

[7] Abgesehen von den Au-Stufenatomen, deren Anteil bei den glatten Legierungsfilmen aber vernachlässigbar klein ist.

Auf AuPd(111)-Oberflächenlegierungen wurde festgestellt, dass schon relativ geringe Mengen von Au ausreichen, um sowohl die Tieftemperaturadsorption von C_2H_4 als auch die C_2H_4-Zersetzung bei höheren Temperaturen stark zu beeinflussen. Auf einer Oberfläche mit 22% Au werden praktisch keine Spezies A-Moleküle mehr nachgewiesen (Abb. 6.11). Außerdem findet auf dieser Oberfläche im Gegensatz zu reinem Pd(111) keine Bildung von Ethylidin statt (Abb. 6.13). Dieses Verhalten lässt es wahrscheinlich erscheinen, dass die neu entdeckte Tieftemperatur-Spezies A eine besondere Rolle bei der Zersetzung von C_2H_4 zu Ethylidin spielt. Im Hinblick auf die Umsetzung von C_2H_4 auf AuPd-Katalysatoren kann eine wesentliche Funktion der Au-Atome in der Unterdrückung der unerwünschten Nebenreaktion zu Ethylidin gesehen werden, so dass eine detaillierte Untersuchung des Tieftemperatur-Adsorptionsverhaltens von C_2H_4 auf Pd(111)- und auf AuPd(111)-Oberflächen mit weiteren experimentellen und mit modernen theoretischen Methoden lohnenswert erscheint.

Bei den C_2H_4-TPD Messungen wurde der Schwerpunkt auf Oberflächenlegierungen mit hohem Au-Anteil gelegt. Ähnlich wie bei CO konnte auch hier die Adsorption von C_2H_4 an Pd-Monomeren in einer Au-Umgebung nachgewiesen werden (Abb. 6.3). Allerdings findet man für C_2H_4 keine zusätzlichen Desorptionspeaks bei Oberflächen, die eine nennenswerte Anzahl von Pd-Dimeren aufweisen. Dafür ergibt sich eine kontinuierliche Verschiebung des Desorptionspeaks für kleine C_2H_4-Bedeckungen zu höheren Temperaturen hin, falls der Pd-Anteil steigt (230 K bei $c_{Pd} \leq 5\%$ und 280 K bei 21% Pd, s. Abb. 6.6).

Schlussbemerkung. In der vorliegenden Arbeit konnten einige interessante Aspekte der Wechselwirkung von CO und von C_2H_4 mit bimetallischen AuPd(111)-Oberflächen durch die Kombination der experimentellen Methoden STM, HREELS und TPD aufgeklärt werden. Insbesondere bei den Untersuchungen auf den ungeordneten AuPd(111)-Oberflächenlegierungen ist deutlich geworden, dass die Vorteile, die die direkte Abbildung von Oberflächen auf atomarer Skala mittels STM bietet, kaum überschätzt werden können. Es bleiben freilich noch Fragen offen, die mit den angewendeten Methoden nicht beantwortet werden konnten. Jedoch kann festgestellt werden, dass durch die in dieser Arbeit ermittelte Korrelation zwischen CO-TPD-Spektren und der mittels STM ermittelten Oberflächenzusammensetzung es in Zukunft relativ einfach sein sollte, eine zuverlässige Charakterisierung von AuPd(111)-Oberflächenlegierungen allein durch CO-TPD durchzuführen. Da diese Methode in vielen Laboratorien zur Verfügung steht, ist zu hoffen, dass diese Arbeit auch einen Beitrag dazu leistet, zusätzliche Informationen zu diesem interessanten System beispielsweise durch Photoelektronen-Spektroskopie am Synchrotron oder durch hochaufgelöste Vibrationsspektroskopie zu gewinnen.

Acknowledgments/Danksagung

Für die Unterstützung, die ich während der Anfertigung dieser Arbeit von vielen Seiten erhalten habe, möchte ich mich herzlich bedanken. Insbesondere bei:

- Herrn Prof. Behm für die Möglichkeit, diese Arbeit in der Abteilung Oberflächenchemie und Katalyse der Universität Ulm anzufertigen.
- Markus Hugenschmidt für die Betreuung der Arbeit in der mühevollen Anfangsphase.
- Andreas Hitzke für die gewissenhafte und solide Einarbeitung in die UHV-Technik, in das Geheimnis, wie man mit scharfen W-Drahtspitzen Atome "sehen kann", sowie in die Welt der Computer.
- Bernhard Gleich für viele nützliche und originelle Tipps im Umgang mit Drähten, Klebstoff, Puderzucker(!) und sonstigen UHV-Bastelmaterialien. Seine Ratschläge zum Programmieren in C haben sich in besonderer Weise bezahlt gemacht!
- Michael Pitter für das Verfechten des Grundsatzes, dass Probleme dazu da sind gelöst zu werden und dass ein Physiker dabei grundsätzlich Spass hat.
- Uli Schöffel und Jürgen Braun — natürlich auch Andreas und Bernhard — dafür, dass die Abteilungs-Rechner (fast) immer problemlos funktionierten.
- Thomas Häring und Gerd Bräth für vielfältige technische Unterstützung in Sachen Mechanik und Elektronik (meist auf dem "kleinen Dienstweg").
- Sonja Egle und Renate Schupp für das Verbreiten des Biberacher Charmes im Sekretariat und als unentbehrliche Schnittstelle zur Verwaltung.
- Überhaupt allen Mitgliedern der Abteilung Oberflächenchemie und Katalyse für eine ausgezeichnete Arbeitsatmosphäre!
- Special thanks to Amy Neises for the professional "online support" in English grammar questions.

- Meinen Eltern für die Unterstützung während meines Studiums und für die Möglichkeit, diese Zeit auch für andere Dinge als das Fachstudium zu nutzen.

- Schließlich — last but not least — Anita, Paul und Leo, die mir immer wieder zeigen, dass der Reiz des Lebens nicht im Zählen von Atomen besteht.

Bibliography

[1] R. M. Lambert. *Chemisorption and Reactivity on Supported Clusters and Thin Films*, chapter Introduction to Heterogeneous Catalysis, pages 285–351. Kluwer, 1997. Edited by R. M. Lambert and G. Pacchioni.

[2] H. R. Gerberich and W. K. Hall. Oxidation of ethylene over palladium and palladium-gold alloys. *Nature*, 213:1120, 1967.

[3] W. Kroenig and G. Scharfe. Verfahren zur herstellung von vinylacetat. Deutsches Patentamt, Patentschrift 1668088, 1968.

[4] H. R. Gerberich, N. W. Cant, and W. K. Hall. Catalytic oxidation: I. the oxidation of ethylene over Pd and Pd-Au alloys. *J. Catal.*, 16:204, 1970.

[5] W. D. Provine, P. L. Mills, and J. J. Lerou. Discovering the role of Au and KOAc in the catalysis of vinyl acetate synthesis. Baltimore, 1996. ICC.

[6] T. J. Schmidt, H. A. Gasteiger, and R. J. Behm. CO-tolerance mechanism on PEM fuel cell anode catalysts. In *Third International Symposium on Electrocatalysis: Advances and Industrial Application*, 1999.

[7] M. Haruta, S. Tsubota, T. Kobayashi, H. Kageyama, M. J. Genet, and B. Delmon. Low-temperaturer oxidation of CO over gold supported on TiO_2, $\alpha - Fe_2O_3$, and Co_3O_4. *J. Catal.*, 144:175, 1993.

[8] G. Binnig, H. Rohrer, C. Gerber, and E. Weibel. Surface studies by scanning tunneling microscopy. *Phys. Rev. Lett.*, 49:57, 1982.

[9] R. Wiesendanger. *Scanning probe microscopy and spectroscopy.* Cambridge University Press, Cambridge, 1994.

[10] J. Tersoff and D. R. Hamann. Theory and application of the scanning tunneling microscope. *Phys. Rev. Lett.*, 50:1998, 1983.

[11] L. Ruan, F. Besenbacher, I Stensgaard, and E. Lægsgaard. Atom resolved discrimination of chemically different elements on metal surfaces. *Phys. Rev. Lett.*, 70:4079, 1993.

[12] C. Nagl, O. Haller, E. Platzgummer, M. Schmid, and P. Varga. Submonolayer growth of Pb on Cu(111): surface alloying and de-alloying. *Surf. Sci.*, 321:237, 1994.

[13] C. Nagl, E. Platzgummer, O. Haller, M. Schmid, and P. Varga. Surface alloying and superstructures of Pb on Cu(100). *Surf. Sci.*, 331-333:831, 1995.

[14] S. Robert, S. Gauthier, R. Bocquet, S. Rousset, J. L. Duvault, and J. Klein. An STM study of the adsorption of Pb on Cu(100): formation of an ordered surface alloy. *Surf. Sci.*, 350:136, 1996.

[15] D. D. Chambliss and S. Chiang. Surface alloy formation studied by scanning tunneling microscopy: Cu(100) + Au-$c(2 \times 2)$. *Surf. Sci. Lett.*, 264:L187, 1992.

[16] M. Ruff. Untersuchungen zu Austausch- und Wachstumsphänomenen beim epitaktischen Wachstum von Cu auf Au-Oberflächen. Master's thesis, Universität Ulm, 1995.

[17] L. P. Nielsen, F. Besenbacher, I. Stensgaard, E. Lægsgaard, E. Engdahl, P. Stoltze, et al. Initial growth of Au on Ni(110): surface alloying of immiscible materials. *Phys. Rev. Lett.*, 71:754, 1993.

[18] J. Jacobsen, L. P. Nielsen, F. Besenbacher, I. Stensgaard, and E. Lægsgaard. Atomic-scale determination of misfit dislocation loops at metal-metal interfaces. *Phys. Rev. Lett.*, 75:489, 1995.

[19] F. Besenbacher, L. P. Nielsen, and P. T. Sprunger. *Growth and Properties of Ultrathin Epitaxial Layers*, volume 8 of *The Chemical Physics of Solid Surfaces*, chapter 6, Surface Alloying in Heteroepitaxial Metal-on-metal Growth, pages 207–257. Elsevier, Amsterdam, 1997. Edited by D. A. King and D. P. Woodruff.

[20] A. Hitzke, M. Hugenschmidt, and R. J. Behm. Low temperature Ni atom adsorption on the Au(110)(1×2) surface. *Surf. Sci.*, 389:8, 1997.

[21] P. W. Murray, I. Stensgaard, E. Lægsgaard, and F. Besenbacher. Mechanism of initial alloy formation for Pd on Cu(100) studied by STM. *Phys. Rev.*, B52:R14404, 1995.

[22] A. B. Aaen, E. Lægsgaard, A. V. Ruban, and I. Stensgaard. Submonolayer growth of Pd on Cu(111) studied by scanning tunneling microscopy. *Surf. Sci.*, 408:43, 1998.

[23] P. T. Wouda, B. E. Nieuwenhuys, M. Schmid, and P. Varga. Chemically resolved STM on a PtRh(100) surface. *Surf. Sci.*, 359:17, 1996.

[24] W. A. Hofer, G. Ritz, W. Hebenstreit, M. Schmid, P. Varga, J. Redinger, and R. Podloucky. Scanning tunneling microscopy of binary-alloy surfaces: is chemical contrast a consequence of alloying? *Surf. Sci. Lett.*, 405:L514, 1998.

[25] H. Ibach and D. L. Mills. *Electron Energy Loss Spectroscopy and Surface Vibrations.* Academic Press, New York, 1982.

[26] B. N. J. Persson. Theory of inelastic scattering of slow electrons by molecules absorbed on metal surfaces. *Sol. St. Comm.*, 24:573, 1977.

[27] Z. Lenac, M. Sunjic, D. Sokcevic, and R. Brako. Low-energy scattering by molecules adsorbed on metal surfaces. *Surf. Sci.*, 80:602, 1979.

[28] H. Rauscher. *Wechselwirkung, Zerfall und Synthese von Molekülen in heterogenen Adsorbatsystemen auf Ru(001).* PhD thesis, Technische Universität München, 1992.

[29] H. Pfnür, D. Menzel, F. M. Hoffmann, A. Ortega, and A. M. Bradshaw. High resolution vibrational spectroscopy of CO on Ru(001): the importance of lateral interactions. *Surf. Sci.*, 93:431, 1980.

[30] G. Ertl and J. Küppers. *Low Energy Electrons and Surface Chemistry.* VCH, Weinheim, 1985.

[31] D. Briggs and M. P. Seah, editors. *Practical Surface Analysis by Auger and X-ray Photoelectron Spectroscopy.* Wiley, New York, 1983.

[32] S. Günther. *Mikroskopische Aspekte beim Wachstum dünner Metallfilme.* PhD thesis, Universität Ulm, 1995.

[33] C. Günther. *Metallfilmwachstum auf reinen und sauerstoffvorbedeckten Ru(0001)-Oberflächen.* PhD thesis, Universität Ulm, 1994.

[34] K. Besocke. An easily operable scanning tunneling microscope. *Surf. Sci.*, 181:145, 1987.

[35] H. Ibach. *Electron Energy Loss Spectrometers.* Springer, 1991.

[36] H. Dannetun, I. Lundström, and L.-G. Petersson. The relative ionization gauge sensitivity of some unsaturated hydrocarbons. *Appl. Surf. Sci.*, 361:381, 1987.

[37] A. Hitzke. *Untersuchungen zu Depositionsprozessen und Legierungsbildung an Gold-Einkristalloberflächen.* PhD thesis, Universität Ulm, 1999.

[38] B. Gleich. Untersuchungen zu Struktur und lokalem Adsorptionsverhalten an bimetallischen, epitaktischen Au/Pd Modellkatalysatoren. Master's thesis, Universität Ulm, 1996.

[39] F. Besenbacher. Scanning tunnelling microscopy studies of metal surfaces. *Rep. Prog. Phys.*, 59:1737, 1996.

[40] H. Brune and K. Kern. *Growth and Properties of Ultrathin Epitaxial Layers*, volume 8 of *The Chemical Physics of Solid Surfaces*, chapter 5, Heteroepitaxial Metal Growth: the Effect of Strain, pages 149–206. Elsevier, Amsterdam, 1997. Edited by D. A. King and D. P. Woodruff.

[41] H. Brune. Microscopic view of epitaxial metal growth: nucleation and aggregation. *Surf. Sci. Rep.*, 31:121, 1998.

[42] J. Wintterlin and R. J. Behm. *Scanning Tunneling Microscopy I. General Principles and Applications to Clean and Adsorbate-Covered Surfaces*, volume 20 of *Springer Series in Surface Science*, chapter 4, Adsorbate Covered Metal Surfaces and Reactions on Metal Surfaces, pages 39–82. Elsevier, Berlin, 1992. Edited by H.-J. Güntherodt and R. Wiesendanger.

[43] J. A. Meyer and R. J. Behm. Place-exchange as a mechanism for adlayer island nucleation during epitaxial growth and resulting scaling behavior. *Surf. Sci. Lett.*, 322:L275, 1995.

[44] Y. Kuk, L. C. Feldman, and P. J. Silverman. Transition from the pseudomorphic state to the nonregistered state in epitaxial growth of Au on Pd(111). *Phys. Rev. Lett.*, 50:511, 1983.

[45] R. C. Jaklevic. Epitaxial growth and electronic structure of Au films on fcc(111) metals studied by electron reflection spectroscopy. *Phys. Rev.*, B30:5494, 1984.

[46] B. Eisenhut. *Wachstum und Struktur dünner Silber- und Gold-Filme auf Palladium(111)- und Silber(111)-Oberflächen.* PhD thesis, Ludwig-Maximilians-Universität München, 1992.

[47] G. Ehrlich and F. G. Hudda. Atomic view of surface self-diffusion: tungsten on tungsten. *J. Chem. Phys.*, 44:1039, 1966.

[48] R. L. Schwoebel and E. J. Shipsey. Step motion on crystal surfaces. *J. Appl. Phys.*, 37:3682, 1966.

[49] J. A. Meyer, J. Vrijmoeth, H. A. v. d. Vegt, E. Vlieg, and R. J. Behm. Importance of the additional step-edge barrier in determining film morphology during epitaxial growth. *Phys. Rev.*, B51:14790, 1995.

[50] H. Brune, C. Romainczyk, H. Röder, and K. Kern. Mechanism of the transition from fractal to dendritic growth of surface aggregates. *Nature*, 369:469, 1994.

[51] H. Brune, H. Röder, K. Bromann, K. Kern, J. Jacobsen, P. Stoltze, K. Jacobsen, and J. Nørskov. Anisotropic corner diffusion as origin for dendritic growth on hexagonal substrates. *Surf. Sci. Lett*, 349:L115, 1996.

[52] M. Hohage, M. Bott, M. Morgenstern, Z. Zhang, T. Michely, and G. Comsa. Atomic processes in low temperature Pt-dendrite growth on Pt(111). *Phys. Rev. Lett.*, 76:2366, 1996.

[53] S. C. Wang and G. Ehrlich. Atom incorporation at surface clusters: an atomic view. *Phys. Rev. Lett.*, 67:2509, 1991.

[54] S. Ovesson, A. Bogicevic, and B. I. Lundqvist. Origin of compact triangular islands in metal-on-metal growth. *Phys. Rev. Lett.*, 83:2608, 1999.

[55] J. A. Venables, G. D. T. Spiller, and M. Hanbücken. Nucleation and growth of thin films. *Rep. Prog. Phys.*, 47:399, 1984.

[56] J. A. Venables. Rate equation approaches to thin film nucleation kinetics. *Phil. Mag.*, 27:1973, 1973.

[57] H. Brune, H. Röder, C. Boragno, and K. Kern. Strain relief at hexagonal-close-packed interfaces. *Phys. Rev.*, B49:2997, 1994.

[58] A. Steltenpohl. *Wachstum von Palladium auf Palladium(111)*. PhD thesis, Universität Bayreuth, 1999.

[59] E. Bauer. Phänomenologische Theorie der Kristallabscheidung an Oberflächen. I & II. *Z. Kristallographie*, 110:372 & 395, 1958.

[60] C. Günther, J. Vrijmoeth, R. Q. Hwang, and R. J. Behm. Strain relaxation in hexagonally close-packed metal-metal interfaces. *Phys. Rev. Lett.*, 74:754, 1995.

[61] R. Q. Hwang, J. C. Hamilton, J. L. Stevens, and S. M. Foiles. Near-surface buckling in strained metal overlayer systems. *Phys. Rev. Lett.*, 75:4242, 1995.

[62] G. Rangelov, T. Fauster, U. Strüber, and J. Küppers. Stacking of Ag layers on Pt(111). *Surf. Sci.*, 331-333:948, 1995.

[63] H. Röder, K. Bromann, H. Brune, and K. Kern. Strain mediated two-dimensional growth kinetics in metal heteroepitaxy. *Surf. Sci.*, 376:13, 1997.

[64] J. V. Barth, H. Brune, G. Ertl, and R. J. Behm. Scanning tunneling microscopy observations on the reconstructed Au(111) surface: Atomic structure, long-range superstructure, rotational domains, and surface defects. *Phys. Rev.*, B42:9307, 1990.

[65] B. Predel. *Landolt-Börnstein, Numerical Data and Functional Relationships in Science and Technology*, volume 5a. Springer, Berlin, 1991. edited by O. Madelung.

[66] J. A. Meyer, I. D. Baikie, E. Kopatzki, and R. J. Behm. Preferential island nucleation at the elbows of the Au(111) herringbone reconstruction through place exchange. *Surf. Sci. Lett.*, 365:L647, 1996.

[67] W. G. Cullen and P. N. First. Island shapes and intermixing for submonolayer nickel on Au(111). *Surf. Sci.*, 420:53, 1999.

[68] A. W. Stephenson, C. J. Baddeley, M. S. Tikhov, and R. M. Lambert. Nucleation and growth of catalytically active Pd islands on Au(111)-22$\times\sqrt{3}$ studied by scanning tunnelling microscopy. *Surf. Sci.*, 398:172, 1998.

[69] M. B. Hugenschmidt, A. Hitzke, and R. J. Behm. Island assisted surface alloying observed after Ni deposition on Au(110)(1 $\times$ 2). *Phys. Rev. Lett.*, 76:2535, 1996.

[70] M. B. Hugenschmidt, M. Ruff, A. Hitzke, and R. J. Behm. Rotational epitaxy versus missing-row reconstruction: Au/Cu/Au(110). *Surf. Sci. Lett.*, 388:L1100, 1997.

[71] M. Wuttig, Y. Gauthier, and S. Blügel. Magnetically driven buckling and stability of ordered surface alloys: Cu(100)$c(2 \times 2)$Mn. *Phys. Rev. Lett.*, 70:3619, 1993.

[72] T. Flores, S. Junghans, and M. Wuttig. Atomic mechanisms for the diffusion of Mn atoms incorporated in the Cu(100) surface: an STM study. *Surf. Sci.*, 371:1, 1997.

[73] T. Flores, S. Junghans, and M. Wuttig. Atomic mechanisms for the formation of an ordered surface alloy: an STM invetigation of Mn/Cu(100). *Surf. Sci.*, 371:14, 1997.

[74] S. H. Kim, K. S. Lee, H. G. Min, J. Seo, S. C. Hong, T. H. Rho, and J.-S. Kim. Subsurface growth of Ni atoms deposited on a Cu(001) substrate. *Phys. Rev.*, B55:7904, 1997.

[75] S. C. Wu, S. H. Lu, Z. Q. Wang, C. K. C. Lok, J. Quinn, Y. S. Li, et al. Cu(001)$c(2 \times 2)$-Pd: An ordered surface alloy. *Phys. Rev.*, B38:5363, 1988.

[76] P. T. Sprunger, E. Lægsgaard, and F. Besenbacher. Growth of Ag on Cu(100) studied by STM: From surface alloying to Ag superstructures. *Phys. Rev.*, B54:8163, 1996.

[77] P.Schieffer, M.-H. Tuilier, M.-C. Hanf, C. Krembel, G. Gewinner, D. Chandesris, and H. Magnan. Atomic structure of the surface alloy formed by a room-temperature-deposited Mn monolayer on Ag(100). *Phys. Rev.*, B57:15507, 1998.

[78] S.-L. Chang, J.-M. Wen, P. A. Thiel, S. Günther, J. A. Meyer, and R. J. Behm. Initial stages of metal encapsulation during epitaxial growth studied by STM: Rh/Ag(100). *Phys. Rev.*, 53:13747, 1996.

[79] L. Porte, M. Phaner-Goutorbe, J. M. Guigner, and J. C. Bertolini. Structuring and catalytic activity of palladium thin layers deposited on the Ni(110) surface. *Surf. Sci.*, 424:262, 1999.

[80] S. Rousset, S. Chiang, D. E. Fowler, and D. D. Chambliss. Intermixing and three-dimensional islands in the epitaxial growth of Au on Ag(110). *Phys. Rev. Lett.*, 69:3200, 1992.

[81] M. Parschau and K. Christmann. Cobalt on rhenium(0001) — an example of thermally activated layer intermixing and surface alloying. *Surf. Sci.*, 423:303, 1999.

[82] M. Scherer. Untersuchungen zu Wachstums und Oberflächenlegierungsbildung von Pt/Ru(0001) Schichtsystemen als Modell für bimetallische Pt/Ru-Katalysatoren mit STM und AES. Master's thesis, Universität Ulm, 1997.

[83] A. F. Lee, C. J. Baddeley, M. S. Tikhov, and R. M. Lambert. Structural and electronic properties of Sn overlayers and Pd/Sn surface alloys on Pd(111). *Surf. Sci.*, 373:195, 1997.

[84] A. Ramstad, R. Strisland, S. Raaen, T. Worren, A. Borg, and C. Berg. Growth and alloy formation studied by photoelectron spectroscopy and STM. *Surf. Sci.*, 425:57, 1999.

[85] M. C. Saint-Lager, R. Baudoing-Savois, M. De Santis, P. Dolle, and Y. Gauthier. Thickness effect on alloying of ultrathin Co films on Pt(111): a real time and in situ UHV study with synchrotron X-ray diffraction. *Surf. Sci.*, 418:485, 1998.

[86] H. Röder, R. Schuster, H. Brune, and K. Kern. Monolayer-confined mixing at the Ag-Pt(111) interface. *Phys. Rev. Lett.*, 71:2086, 1993.

[87] M. T. Paffett and M. T. Windham. Surface modification of Pt(111) by Sn adatoms: evidence for the formation of ordered overlayers and surface alloys. *Surf. Sci.*, 208:34, 1989.

[88] M. Galeotti, A. Atrei, U. Bardi, G. Rovida, and M. Torrini. Surface alloying at the Sn-Pt(111) interface: a study by X-ray photoelectron diffraction. *Surf. Sci.*, 313:349, 1994.

[89] U. Schröder, R. Linke, J.-H. Boo, and K. Wandelt. Adsorption properties and formation of Pt/Cu surface alloys. *Surf. Sci.*, 352:211, 1996.

[90] C. Nagl, E. Platzgummer, M. Schmid, P. Varga, S. Speller, and W. Heiland. Direct observation of a new growth mode: Subsurface island growth of Cu on Pb(111). *Phys. Rev. Lett.*, 75:2976, 1995.

[91] C. Nagl, E. Platzgummer, M. Schmid, P. Varga, S. Speller, and W. Heiland. Subsurface islands and superstructure of Cu on Pb(111). *Surf. Sci.*, 352:540, 1996.

[92] D. L. Weissman-Wenocur, P. M. Stefan, B. B. Pate, M. L. Shek, I. Lindau, and W. E. Spicer. Photoemission study of Au overlayers on Pd(111) and the formation of a Pd-Au(111) alloy surface. *Phys. Rev.*, B27:3308, 1983.

[93] R. Schuster, H. Röder, K. Bromann, H. Brune, and K. Kern. Stress relief via island formation of an isotropically strained bimetallic surface layer: The mesocopic morphology of the Ag/Pt(111) surface alloy. *Phys. Rev.*, B54:13476, 1996.

[94] M. I. Haftel and M. Rosen. New ballistically and thermally activated exchange processes in the vapor deposition of Au on Ag(111): a molecular dynamics study. *Surf. Sci.*, 407:16, 1998.

[95] G. Tréglia, B. Legrand, A. Saúl, T. Flores, and M. Wuttig. Theoretical study fo surface alloy formation through generation and annihilation of vacancies. *Surf. Sci.*, 352–354:552, 1996.

[96] B. Sadigh, M. Asta, V. Ozoliņš, A. K. Schmidt, N. C. Bartelt, A. A. Quong, and R. Q. Hwang. Short-range order and phase stability of surface alloys: PdAu on Ru(0001). *Phys. Rev. Lett.*, 83:1379, 1999.

[97] C. J. Baddeley, C. J. Barnes, A. Wander, R. M. Ormerod, D. A. King, and R. M. Lambert. Surface crystallography of three catalytically important structures in the Au(111)-Pd system. *Surf. Sci.*, 314:1, 1994.

[98] A. Christensen, A. V. Ruban, P. Stoltze, K. W. Jacobsen, H. L. Skriver, and J. K. N/orskov. Phase diagrams for surface alloys. *Phys. Rev.*, B56:5822, 1997.

[99] O. Madelung and H. Mehrer, editors. *Landolt-Börnstein, Numerical Data and Functional Relationships in Science and Technology*, volume 26. Springer, Berlin, 1990.

[100] S. Tanuma, C. J. Powell, and D. R. Penn. Calculations of electron inelastic mean free paths. *Surface and Interface Analysis*, 17:911, 1991.

[101] Gmelin-Institut, editor. *Gmelins Handbuch der anorganischen Chemie.* Verlag Chemie, 1941.

[102] J. C. Campuzano. *Chemisorption Systems*, volume 3 of *The Chemical Physics of Solid Surfaces*, chapter 4, The Adsorption of Carbon Monoxide by the Transition Metals, page 389. Elsevier, Amsterdam, 1990. Edited by D. A. King and D. P. Woodruff.

[103] K. Kordesch and G. Simader. *Fuel cells and their applications.* VCH, 1996.

[104] G. Blyholder. Molecular orbital view of chemisorbed carbon monoxide. *J. Phys. Chem.*, 68:2772, 1964.

[105] B. Hammer, Y. Morikawa, and J. K. Nørskov. CO chemisorption at metal surfaces and overlayers. *Phys. Rev. Lett.*, 76:2141, 1996.

[106] A. Ruban, B. Hammer, P. Stoltze, H. L. Skriver, and J. K. Nørskov. Surface electronic structure and reactivity of transition and noble metals. *J. Mol. Catal.*, A115:421, 1997.

[107] B. Hammer, O. H. Nielsen, and J. K. Nørskov. Structure sensitivity in adsorption: CO interaction with stepped and reconstructed Pt surfaces. *Catal. Lett.*, 46:31, 1997.

[108] R. P. Eischens, W. A. Pliskin, and S. A. Francis. Infrared spectra of chemisorbed carbon monoxide. *J. Chem. Phys.*, 22:1786, 1954.

[109] R. P. Eischens, S. A. Francis, and W. A. Pliskin. The effect of surface coverage on the spectra of chemisorbed CO. *J. Phys. Chem.*, 60:194, 1956.

[110] R. P. Eischens and W. A. Pliskin. The infrared spectra of adsorbed molecules. *Advan. Catalysis*, 10:1, 1958.

[111] R. P. Eischens. Infrared spectra of chemisorbed molecules. *Z. Elektrochem.*, 60:782, 1956.

[112] H. Aizawa and S. Tsuneyuki. First-principles study of CO bonding to Pt(111): validity of the Blyholder model. *Surf. Sci. Lett.*, 399:L364, 1998.

[113] B. Hammer and J. K. Nørskov. *Chemisorption and Reactivity on Supported Clusters and Thin Films*, chapter Theory of Adsorption and Surface Reactions, pages 285–351. Kluwer, 1997. Edited by R. M. Lambert and G. Pacchioni.

[114] H. Conrad, G. Ertl, J. Koch, and E. E. Latta. Adsorption of CO on Pd single crystal surfaces. *Surf. Sci.*, 43:462, 1974.

[115] P. S. Bagus and G. Pacchioni. The contribution of metal sp electrons to the chemisorption of CO: theoretical studies of CO on Li, Na, and Cu. *Surf. Sci.*, 278:427, 1992.

[116] M. Weinert and R. E. Watson. Core-level shifts in bulk alloys and surface adlayers. *Phys. Rev.*, B51:17168, 1995.

[117] J. A. Rodriguez and D. W. Goodman. The nature of the metal-metal bond in bimetallic surfaces. *Science*, 257:897, 1992.

[118] O. K. Andersen, O. Jepsen, and D. Glötzel. *Highlights of Condensed Matter Theory LXXXIX Corso Soc. Italiana di Fisica*, page 59. 1985.

[119] G. Ertl and J. Koch. Adsorption von CO auf einer Palladium(111)-Oberfläche. *Z. Naturforsch.*, 25a:1906, 1970.

[120] H. Conrad. *Wechselwirkung von Gasen mit einer Pd(111)-Oberfläche.* PhD thesis, Ludwig-Maximilians-Universität München, 1976.

[121] A. M. Bradshaw and F. M. Hoffmann. The chemisorption of carbon monoxide on palladium single crystal surfaces: IR spectroscopic evidence for localized site adsorption. *Surf. Sci.*, 72:513, 1978.

[122] A. Ortega. *Infrarotspektroskopische Untersuchungen der Chemisorption von Kohlenmonoxid und Stickstoffmonoxid auf Palladium- und Ruthenium-Einkristalloberflächen.* PhD thesis, Technische Universität Berlin, 1980.

[123] F. M. Hoffmann. Infrared reflection-absorption spectroscopy of adsorbed molecules. *Surf. Sci. Rep.*, 3:107, 1983.

[124] W. K. Kuhn, J. Szanyi, and D. W. Goodman. CO adsorption on Pd(111): the effects of temperature and pressure. *Surf. Sci. Lett.*, 274:L611, 1992.

[125] J. S. Szanyi, W. K. Kuhn, and D. W. Goodman. CO adsorption on Pd(111) and Pd(100): Low and high pressure correlations. *J. Vac. Sci. Technol. A*, 11:1969, 1993.

[126] T. Gießel, O. Schaff, C.J. Hirschmugl, V. Fernandez, K.-M. Schindler, et al. A photoelectron diffraction study of ordered structures in the chemisorption system Pd(111)-CO. *Surf. Sci.*, 406:90, 1998.

[127] H. Ohtani, M.A. Van Hove, and G.A. Somorjai. LEED intensity analysis of the surface structures of Pd(111) and of CO adsorbed on Pd(111) in a $(\sqrt{3} \times \sqrt{3})R30^\circ$ arrangement. *Surf. Sci.*, 187:372, 1987.

[128] D. Loffreda, D. Simon, and P. Sautet. Dependence of stretching frequency on surface coverage and adsorbate–adsorbate interactions: a denstiy-functional theory approach of CO on Pd(111). *Surf. Sci.*, 68:68, 1999.

[129] X. Guo and J. T. Yates, Jr. Dependence of effective desorption kinetic parameters on surface coverage and adsorption temperature: CO on Pd(111). *J. Chem. Phys.*, 90:6761, 1989.

[130] B. Bourguignon, S. Carrez, B. Dragnea, and H. Dubost. Vibrational spectroscopy of imperfect CO/Pd(111) surfaces obtained by adsorption between 150 and 230 K. *Surf. Sci.*, 418:171, 1998.

[131] M. Šnábl, O. Borusík, V. Cháb, M. Ondřejček, W. Stenzel, H. Conrad, and A. M. Bradshaw. Surface diffusion of CO molecules on Pd(111) studied with photoelectron emission microscopy. *Surf. Sci. Lett.*, 385:L1016, 1997.

[132] M. P. Kiskinova and G. M. Bliznakov. Adsorption and coadsorption of carbon monoxide and hydrogen on Pd(111). *Surf. Sci.*, 123:61, 1982.

[133] G.A. Kok, A. Noordermeer, and B.E. Nieuwenhuys. Decomposition of methanol and the interaction of coadsorbed hydrogen and carbon monoxide on a Pd(111) surface. *Surf. Sci.*, 135:65, 1983.

[134] W. Eberhardt, S.G. Louie, and E.W. Plummer. Interaction of hydrogen with a Pd(111) surface. *Phys. Rev.*, B28:465, 1983.

[135] T.E. Felter and R.H. Stulen. An experimental study of the order-disorder transitions for hydrogen on Pd(111). *J. Vac. Sci. Technol.*, A3:1566, 1985.

[136] T.E. Felter, S.M. Foiles, M.S. Daw, and R.H. Stulen. Order-disorder transitions and subsurface occupation for hydrogen on Pd(111). *Surf. Sci. Lett.*, 171:L379, 1986.

[137] T.E. Felter, E.C. Sowa, and M.A. Van Hove. Location of hydrogen adsorbed on palladium(111) studied by low-energy electron diffraction. *Phys. Rev.*, B40:891, 1989.

[138] G.D. Kubiak and R.H. Stulen. Electron-stimulated desorption as a probe of hydrogen adsorption on and diffusion into Pd(111). *J. Vac. Sci. Technol.*, A4:1427, 1986.

[139] R. Raval, S. Haq, M.A. Harrison, G. Blyholder, and D.A. King. Molecular adsorbate-induced surface reconstruction: CO/Pd(110). *Chem. Phys. Lett*, 167:391, 1990.

[140] P. Hu, L. Moralez de la Garza, R. Raval, and D.A. King. A LEED structural study of the CO induced reconstruction on Pd(110): evidence for a missing row structure. *Surf. Sci.*, 249:1, 1991.

[141] J.-W. He and P.R. Norton. Interaction of CO with a Pd(110) surface, studied by low energy electron diffraction, thermal desorption spectroscopy, and $\Delta\Phi$. *J. Chem. Phys.*, 89:1170, 1988.

[142] A. Locatelli, B. Brena, G. Comelli, S. Lizzit, G. Paolucci, and R. Rosei. Structural determination of the Pd(110)$(2 \times 1)p2mg$-CO system by means of high-energy x-ray photoelectron diffraction. *Phys. Rev.*, B54:2839, 1996.

[143] A. Wander, P. Hu, and D.A. King. Ambiguities in adsorbate site assignment from vibrational frequencies. A TLEED structural study of (2×1)CO-Pd(110). *Chem. Phys. Lett.*, 201:393, 1993.

[144] M.A. Chesters, G.S. McDougall, M.E. Pemble, and N. Sheppard. The chemisorption of CO on Pd(110) at 110 and 300 K studied by electron energy loss spectroscopy. *Surf. Sci.*, 164:425, 1985.

[145] H. Kato, M. Kawai, and J. Yoshinobu. Switching in the molecular orientation ruled by steric repulsion of adsorbed CO on Pd(110). *Phys. Rev. Lett.*, 82:1899, 1999.

[146] R.J. Behm, K. Christmann, G. Ertl, M.A. Van Hove, et al. The structure of CO adsorbed on Pd(100): A LEED and HREELS analysis. *Surf. Sci. Lett.*, 88:L59, 1979.

[147] A. Ortega, F.M. Hoffmann, and A.M. Bradshaw. The adsorption of CO on Pd(100) studied by IR reflection absorption spectroscopy. *Surf. Sci.*, 119:79, 1982.

[148] R.L. Park and H.H. Madden. Annealing changes on the (100) surface of palladium and their effect on CO adsorption. *Surf. Sci.*, 11:188, 1968.

[149] J.C. Tracy and P.W. Palmberg. Structural influences on adsorbate binding energy. I. carbon monoxide on (100)palladium. *J. Chem. Phys.*, 51:4852, 1969.

[150] Y.Y. Yeo, L. Vattuone, and D.A. King. Calorimetric investigation of NO and CO adsorption on Pd(100) and the influence of preadsorbed carbon. *J. Chem. Phys.*, 106:1990, 1997.

[151] J.C. Tracy and P.W. Palmberg. Simple technique for binding energy determinations: CO on Pd(100). *Surf. Sci.*, 14:274, 1969.

[152] R.J. Behm, K. Christmann, and G. Ertl. Adsorption of CO on Pd(100). *J. Chem. Phys.*, 73:2984, 1980.

[153] R.D. Ramsier, K.-W. Lee, and J.T. Yates, Jr. CO adsorption on stepped Pd(112): studies by thermal desorption and electron stimulated desorption. *Surf. Sci.*, 322:243, 1995.

[154] K. Svensson, I. Rickardsson, C. Nyberg, and S. Andersson. Step site adsorption and ordering of CO on Ni(510) and Pd(510). *Surf. Sci.*, 366:140, 1996.

[155] M.L. Kottke, R.G. Greenler, and H.G. Tompkins. An infrared spectroscopic study of carbon monoxide adsorbed on polycrystalline gold using the reflection-absorption technique. *Surf. Sci.*, 32:231, 1972.

[156] A.M. Bradshaw and J. Pritchard. Infrared spectra of carbon monoxide chemisorbed on metal films: a comparative study of copper, silver, gold, iron, cobalt and nickel. *Proc. Roy. Soc. Lond.*, A316:169, 1970.

[157] D.J.C. Yates. Spectroscopic investigations of gold surfaces. *J. Colloid Interface Sci.*, 29:197, 1969.

[158] P. Dumas, R.G. Tobin, and P.L. Richards. Study of adsorption states and interactions of CO on evaporated noble metal surfaces by infrared absorption spectroscopy. *Surf. Sci.*, 171:579, 1986.

[159] J. France and P. Hollins. Interactions of CO molecules adsorbed on gold. *J. Electron Spectrosc. Relat. Phenom.*, 64/65:251, 1993.

[160] D. A. Outka and R. J. Madix. The oxidation of carbon monoxide on the Au(110) surface. *Surf. Sci.*, 179:351, 1987.

[161] A. Sandell, P. Bennich, A. Nilsson, B. Hernnäs, O. Björneholm, and N. Mårtenson. Chemisorption of CO on Cu(100), Ag(110) and Au(110). *Surf. Sci.*, 310:16, 1994.

[162] K. Dückers and H.P. Bonzel. Core and valence level spectroscopy with Y Mζ radiation: CO and K on (110) surfaces of Ir, Pt and Au. *Surf. Sci.*, 213:25, 1989.

[163] G. Elliott, J.D. Miller, and J.H. Weare. Comparison of theory and experiment for scattering of He from CO adsorbed on Au(111) at low coverage. *J. Vac. Sci. Technol.*, A3:1665, 1985.

[164] G. McElhiney and J. Pritchard. The adsorption of Xe and CO on Au(100). *Surf. Sci.*, 60:397, 1976.

[165] C. Ruggiero and P. Hollins. Adsorption of carbon monoxide on the gold(332) surface. *J. Chem. Soc., Faraday Trans.*, 92:4829, 1996.

[166] P.A. Redhead. Thermal desorption of gases. *Vacuum*, 12:203, 1962.

[167] D.D. Eley and P.B. Moore. The adsorption and reaction of CO and O_2 on Pd-Au alloy wires. *Surf. Sci.*, 111:325, 1981.

[168] X.Y. Shen, D.J. Frankel, J.C. Hermanson, G.J. Lapeyre, and R.J. Smith. Photoemission studies of ordered Pd overlayers on Au(111): Implications for CO chemisorption. *Phys. Rev.*, B32:2120, 1985.

[169] X.Y. Shen, D.J. Frankel, G.J. Lapeyre, and R.J. Smith. Photoemission and high-resolution electron-energy-loss spectroscopic studies of CO chemisorption on thin Pd films on Au(111). *Phys. Rev.*, B33:5372, 1986.

[170] A. Sellidj and B.E. Koel. Electronic and CO chemisorption properties of ultrathin Pd films vapor deposited on Au(111). *Phys. Rev.*, B49:8367, 1994.

[171] C.J. Baddeley, M. Tikhov, C. Hardacre, J.R. Lomas, and R.M. Lambert. Ensemble effects in the coupling of acetylene to benzene on a bimetallic surface: A study with Pd(111)/Au. *J. Phys. Chem.*, 100:2189, 1996.

[172] C. Nyberg and L. Westerlund. H and CO on Pd(100): coadsorption induced dissolution of hydrogen. *Surf. Sci.*, 256:9, 1991.

[173] C. Nyberg and L. Westerlund. Adsorption of CO on the Pd(100)p(1×1)H surface at low temperatures: altered CO coordination. *Chem. Phys. Lett.*, 185:445, 1991.

[174] D.E. Peebles, J.A. Schreifels, and J.M. White. The interaction of coadsorbed hydrogen and carbon monoxide on Ru(001). *Surf. Sci.*, 116:117, 1982.

[175] E.D. Williams, P.A. Thiel, W.H. Weinberg, and J.T. Yates, Jr. Segregation of co-adsorbed species: Hydrogen and carbon monoxide on the (111) surface of rhodium. *J. Chem. Phys.*, 72:3496, 1980.

[176] J.M. White. Surface interactions in nonreactive coadsorption: H_2 and CO on transition-metal surfaces. *J. Phys. Chem.*, 87:915, 1983.

[177] D.E. Peebles, J.R. Creighton, D.N. Belton, and J.M. White. Coadsorption of hydrogen and carbon monoxide on nickel and platinum. *J. Catal.*, 80:482, 1983.

[178] H.J. Kreuzer. Kinetic lattice gas model with precursors. *Surf. Sci.*, 238:305, 1990.

[179] J.W. Niemantsverdriet and K. Wandelt. The compensation effect in thermal desorption of adsorbate systems with lateral interactions. *J. Vac. Sci. Technol.*, A6:757, 1988.

[180] E. Habenschaden and J. Küppers. Evaluation of flash desorption spectra. *Surf. Sci. Lett.*, 138:L149, 1984.

[181] J.B. Miller, H.R. Siddiqui, S.M. Gates, J.N. Russell, Jr., J.T. Yates, Jr., et al. Extraction of kinetic parameters in temperature programmed desorption: A comparison of methods. *J. Chem. Phys.*, 87:6725, 1987.

[182] H. Ibach, W. Erley, and H. Wagner. The preexponential factor in desorption - CO on Ni(111). *Surf. Sci.*, 92:29, 1980.

[183] C.-M. Chan, R. Aris, and W.H. Weinberg. An analysis of thermal desorption mass spectra. I. *Appl. Surf. Sci.*, 1:360, 1978.

[184] D.A. King. Thermal desorption from metal surfaces: a review. *Surf.Sci.*, 47:384, 1975.

[185] J.B. Taylor and I. Langmuir. The evaporation of atoms, ions and electrons from caesium films on tungsten. *Phys. Ref.*, 44:423, 1933.

[186] M. Grunze and H.J. Kreuzer, editors. *Kinetics of Interface Reactions*, page 95. Springer, 1987.

[187] D.A. King. The influence of weakly bound intermediate states on thermal desorption kinetics. *Surf. Sci.*, 64:43, 1977.

[188] R. Gorte and L.D. Schmidt. Desorption kinetics with precursor intermediates. *Surf. Sci.*, 76:559, 1978.

[189] G. Binnig, H. Rohrer, C. Gerber, and W. Weibel. (111) facets as the origin of reconstructed Au(110) surfaces. *Surf. Sci. Lett.*, 144:L379, 1983.

[190] T. Gritsch, D. Coulman, R.J. Behm, and G. Ertl. A scanning tunneling microscopy investigation of the structure of the Pt(110) and Au(110) surfaces. *Surf. Sci.*, 257:297, 1991.

[191] G. A. Kok, A. Noordermeer, and B. E. Nieuwenhuys. Effect of alloying on the adsorption of CO on palladium: a comparison of the behaviour of PdAg(111), PdCu(111) and Pd(111) surfaces. *Surf. Sci.*, 152/153:505, 1985.

[192] A. Noordermeer, G. A. Kok, and B. E. Nieuwenhuys. A comparative study of the behaviour of the PdAg(111) and Pd(111) surfaces towards the interaction with hydrogen and carbon monoxide. *Surf. Sci.*, 165:375, 1986.

[193] A. Noordermeer, G. A. Kok, and B. E. Nieuwenhuys. Comparison between the adsorption properties of Pd(111) and PdCu(111) surfaces for carbon monoxide and hydrogen. *Surf. Sci.*, 172:349, 1986.

[194] L. L. Kesmodel and J. A. Gates. Ethylene adsorption and reaction on Pd(111): An angle-dependent EELS analysis. *Surf. Sci. Lett.*, 111:747, 1981.

[195] J. A. Gates and L. L. Kesmodel. EELS analysis of the low temperature phase of ethylene chemisorbed on Pd(111). *Surf. Sci. Lett.*, 120:L461, 1982.

[196] J. A. Gates and L. L. Kesmodel. Thermal evolution of acetylene and ethylene on Pd(111). *Surf. Sci.*, 124:68, 1983.

[197] P. A. P. Nascente, M. A. Van Hove, and G. A. Somorjai. Induced ordering of ethylidyne on the Pd(111) surface by preadsorption of oxygen: a LEED and HREELS study. *Surf. Sci.*, 253:167, 1991.

[198] R. Döll, C. A. Gerken, M. A. Van Hove, and G. A. Somorjai. Structure determination of disordered ethylene adsorbed on Pt(111) analyzed by diffuse LEED: asymmetrical di-σ bonding favored. *Surf. Sci.*, 374:151, 1997.

[199] S. Lehwald and H. Ibach. Decomposition of hydrocarbons on flat and stepped Ni(111) surfaces. *Surf. Sci.*, 89:425, 1979.

[200] C. E. Anson, B. J. Bandy, M. A. Chesters, B. Keiller, I. A. Oxton, and N. Sheppard. Vibrational spectra of ethylene and acetylene on metal surfaces — an electron energy loss study of ethylene adsorbed on Ni(110) and its carbided surface, and the use of metal – cluster analogies. *J. Electron Spectrosc. Relat. Phenom.*, 29:315, 1983.

[201] E. M. Stuve, R. J. Madix, and C. R. Brundle. The adsorption and reaction of ethylene on clean and oxygen covered Pd(100). *Surf. Sci.*, 152/153:532, 1985.

[202] M. Nishijima, J. Yoshinobu, T. Sekitani, and M. Onchi. Chemisorption and thermal decomposition of ethylene on Pd(110): Electron energy loss spectroscopy and thermal desorption spectroscopy studies. *J. Chem. Phys.*, 90:5114, 1989.

[203] H. Steininger, H. Ibach, and S. Lehwald. Surface reactions of ethylene and oxygen on Pt(111). *Surf. Sci.*, 117:685, 1982.

[204] E. Yagasaki, A. L. Backman, B. Chen, and R. I. Masel. The coadsorption of ethylene and hydrogen on Pt(210), (1×1)Pt(110), and (2×1)Pt(110). *J. Vac. Sci. Technol.*, A8:2616, 1990.

[205] R. Linke, C. Becker, T. Pelster, M. Tanemura, and K. Wandelt. Adsorption of ethene on Cu(111). *Surf. Sci.*, 377–379:655, 1997.

[206] C. Backx, C. P. M. de Groot, and P. Biloen. Electron energy loss spectroscopy and its applications. *Appl. Surf. Sci.*, 6:256, 1980.

[207] C. E. Anson, N. Sheppard, and D. B. Powell. $[(\eta^2 - C_2H_4)Os(CO)_4]$ as a vibrational model for type I' ethene chemisorbed as a metallacyclopropane on metal surfaces. *J. Chem. Soc. Faraday Trans.*, 90:1449, 1994.

[208] J. Kubota, T. Ohtani, J. N. Kondo, C. Hirose, and K. Domen. IRAS study of π-bonded ethylene on a Pt(111) surface in the presence of gaseous ethylene and hydrogen. *Appl. Surf. Sci.*, 121/122:548, 1997.

[209] T. Shimanouchi, editor. *Tables of Molecular Vibrational Frequencies, Consolidated*, volume 1 of *Natl. Stand. Ref. Data Ser.* U. S. Natl. Bur. Stand., 1950.

[210] W. T. Tysoe, G. L. Nyberg, and R. M. Lambert. Structural, kinetic, and reactive properties of the palladium(111)-ethylene system. *J. Phys. Chem.*, 88:1960, 1984.

[211] L. P. Wang, W. T. Tysoe, R. M. Ormerod, R. M. Lambert, H. Hoffmann, and F. Zaera. Determination of the bonding and orientation of ethylene on Pd(111) by near-edge X-ray absorption fine structure and photoelectron spectroscopy. *J. Phys. Chem.*, 94:4236, 1990.

[212] G. Eichhorn, W. Heuer, and H. Zacharias. IR-visible sum frequency mixing in C_2H_4/Pd(111). *J. Electron Spectrosc. Relat. Phenom.*, 64/65:109, 1993.

[213] G. Herzberg. *Infrared and Raman Spectra.* Van Nostrand Reinhold, New York, 1945.

[214] M. Kaltchev, A. W. Thompson, and W. T. Tysoe. Reflection-absorption infrared spectroscopy of ethylene on palladium(111) at high pressure. *Surf. Sci.*, 391:145, 1997.

[215] T. Sekitani, J. Yoshinobu, M. Onchi, and M. Nishijima. Chemisorption and thermal decomposition of ethylene on a Pd(110)(1×2)-Cs surface: Electron energy loss spectroscopy and thermal desorption studies. *J. Phys. Chem.*, 94:6847, 1990.

[216] E. M. Stuve and R. J. Madix. Oxidation of ethylene on Pd(100); bonding of ethylene and scavenging of dehydrogenation fragments by surface oxygen. *Surf. Sci.*, 160:293, 1985.

[217] E. M. Stuve and R. J. Madix. Bonding and dehydrogenation of ethylene on palladium metal. Vibrational spectra and temperature-programmed reaction studies on Pd(100). *J. Phys. Chem.*, 89:105, 1985.

[218] J.-F. Jia, K. Wu, S.-H. Lu, R.-G. Zhao, X.-M. Wei, et al. Oxidation of ethylene on the ordered alloy surface Pd(001)c(2×2)-Mn. *Surf. Sci.*, 338:69, 1995.

[219] B. M. Trapnell. The activities of evaporated metal films in gas chemisorption. *Proc. Roy. Soc. (London)*, A218:566, 1953.

[220] M. A. Chesters and G. A. Somorjai. The chemisorption of oxygen, water and selected hydrocarbons on the (111) and stepped gold surfaces. *Surf. Sci.*, 52:21, 1975.

[221] J.-F. Paul and P. Sautet. Influence of the surface atom metallic coordination in the adsorption of ethylene on a platinum surface: A theoretical study. *J. Phys. Chem.*, 98:10906, 1994.

[222] T. A. Land, T. Michely, R. J. Behm, J. C. Hemminger, and G. Comsa. Direct observation of surface reactions by scanning tunneling microscopy: Ethylene → ethylidyne → carbon particles → graphite on Pt(111). *J. Chem. Phys.*, 97:6774, 1992.

[223] Y.-T. Wong and R. Hoffmann. A comparative study of the chemisorption of ethene on three metal surfaces: Ni(111), Pd(111) and Pt(111). *J. Chem. Soc. Faraday Trans.*, 86:4083, 1990.

[224] M. B. Hugenschmidt, P. Dolle, J. Jupille, and A. Cassuto. Ethylene π species on bare and cesiated Pt(111) surfaces. *J. Vac. Sci. Technol.*, A7:3312, 1989.

List of Figures

1.1 Illustration of STM tip effects. 6
1.2 Illustration for XPS and AES. 14

2.1 UHV chamber. 18
2.2 Schematic topview drawings of the UHV chamber used for this work. 19
2.3 Sketch of the "beetle-type" STM. 21
2.4 Cut through the sample holder. 23

3.1 STM: 0.1 ML Au deposited at low temperatures. 36
3.2 Model for corner diffusion on fcc(111) surfaces. 37
3.3 STM: 0.1 ML–0.4 ML Au deposited at $T \geq 298\,K$. 38
3.4 STM: 0.1 ML Au deposited at 99 K after warming up to 300 K. . . 40
3.5 STM: 0.5 ML and 0.7 ML Au deposited around room temperature. 41
3.6 Arrhenius plot of Au/Pd(111) island densities. 44
3.7 STM: $\sim$1 ML Au deposited at different temperatures. 46
3.8 STM: 1.1 ML Au, $T_{dep} = 110\,K$, after annealing at 400 K for 5 min. 47
3.9 STM: Au multilayers deposited at temperatures above 300 K. . . . 51
3.10 STM: Atomically resolved strain relief patterns. 53
3.11 Hard sphere model for strain relief pattern. 54

4.1 STM: 0.2 ML Au, $T_{dep} = 303\,K$, after annealing at 550 K. 61
4.2 STM: 0.1 ML Au, $T_{dep} = 303\,K$, after annealing at 600 K. 62
4.3 STM: $\sim$1 ML Au annealed at 600 K. 64
4.4 STM: 0.4 ML Au, $T_{dep} = 400\,K$, after annealing at $T \geq 600\,K$. . . 65
4.5 STM: Submonolayer Au films annealed at 780 K. 67
4.6 STM: 0.2 ML Au, $T_{dep} = 307\,K$, after annealing at $T \geq 600\,K$. . . 69
4.7 STM: 0.2 ML Au, $T_{dep} = 307\,K$, after annealing at $T \geq 600\,K$. . . 71
4.8 STM: 0.1 ML Au, $T_{dep} = 303\,K$, after annealing at $T \geq 600\,K$. . . 73
4.9 STM: 0.4 ML Au, $T_{dep} = 400\,K$, after annealing at $T \geq 600\,K$. . . 75
4.10 Elementary processes in AuPd(111) surface alloy formation. . . . 76
4.11 STM: $\sim$1 ML Au annealed at 600 K. 78
4.12 STM: Structure of multilayer Au films annealed at $T \geq 625\,K$. . . 82
4.13 STM: Influence of steps on the AuPd(111) surface alloy composition. 84

4.14 STM: Influence of the strain relief stripes on the AuPd(111) surface alloy composition. 85
4.15 STM: 0.1 ML Au, $T_{dep} = 600$ K. 87
4.16 Statistical analysis of the Au atom distribution. 88
4.17 STM: 1.2 ML Au, $T_{dep} = 550$ K. Overview images. 90
4.18 STM: 1.2 ML Au, $T_{dep} = 550$ K. Atomically resolved image. 91
4.19 Statistical analysis of monomer densities on AuPd(111) surface alloys. 93
4.20 Statistical analysis of the Pd chain lengths for 42% Pd. 95
4.21 Au-Pd(111) interdiffusion monitored by AES (0.9 ML Au). 97
4.22 Au-Pd(111) interdiffusion monitored by AES (2.7 ML Au). 98
4.23 Scheme of the diffusion barriers used for the simulations. 99
4.24 Calculated Au concentrations in the near-surface region of AuPd(111). 105

5.1 CO TPD spectra from Pd(111). 138
5.2 CO TPD spectra from completely Au covered Pd(111). 142
5.3 STM images of 0.2 ML Au on Au/Pd(111) (T_{dep}=120 K). 143
5.4 CO TPD spectra from partially Au (0.25 ML) covered Pd(111). . 147
5.5 CO TPD spectra from partially (0.5 ML) Au covered Pd(111). . . 149
5.6 CO TPD spectra from AuPd(111) surface alloys ($c_{Pd} \leq 24\%$). . . 152
5.7 CO TPD spectra from AuPd(111) surface alloys. 153
5.8 θ_{CO} dependent TPD spectra from AuPd(111) with $c_{Pd} = 2\%$. . . . 154
5.9 θ_{CO} dependent TPD spectra from AuPd(111) with $c_{Pd} = 12\%$. . . 155
5.10 θ_{CO} dependent TPD spectra from AuPd(111) with $c_{Pd} = 24\%$. . . 156
5.11 Potential energy diagram for precursor model. 164
5.12 Example for the analysis of CO TPD spectra employing the precursor model. 167
5.13 Simulation of CO TPD from a AuPd(111) surface alloy with $\theta_{CO} = 2\%$. 169
5.14 Simulation of CO TPD from AuPd(111) surface alloys with $1\% \leq c_{Pd} \leq 9\%$. 170
5.15 TPD peak positions: experiment and simulations. 171
5.16 E_d for CO/AuPd(111) surface alloys (TTPD analysis). 175
5.17 HREEL spectra of CO adsorbed on Pd(111) at 300 K. 179
5.18 HREEL spectra of CO adsorbed on Pd(111) at 100 K. 181
5.19 STM image of 1.3 ML Au on Pd(111) ($T_{dep} = 320$ K) 185
5.20 HREEL spectra of CO adsorbed on completely Au covered Pd(111). 186
5.21 STM image of 4.2 ML Au on Pd(111) ($T_{dep} = 166$ K) 187
5.22 HREEL spectra of CO adsorbed on 4.2 ML Au/Pd(111). 188
5.23 HREEL spectra of CO adsorbed on partially Au covered Pd(111). 191
5.24 STM image of mildly Ar^+ sputtered Pd(111) 192
5.25 HREEL spectra of CO adsorbed on 0.3 ML Au/Pd(111). 193

5.26 HREEL spectra of CO on AuPd(111) surface alloys. 197
5.27 HREEL spectra of CO on a AuPd(111) surface alloy with $c_{Pd} < 1\%$. 198
5.28 HREEL spectra of CO on AuPd(111) surface alloys. 200
5.29 STM image of a AuPd(111) surface alloy with 12% Pd. 201
5.30 STM image of a AuPd(111) surface alloy with 23% Pd. 201
5.31 STM image of a AuPd(111) surface alloy with 83% Pd. 202
5.32 Size distribution of Pd ensembles on AuPd(111) surfaces. 203
5.33 HREEL spectra of CO on a AuPd(111) surface alloy with $c_{Pd} = 23\%$. 204
5.34 HREEL spectra of CO on a AuPd(111) surface alloy with $c_{Pd} = 57\%$. 206
5.35 STM images of 0.1 ML Pd on Au(110) (T_{dep}=165 K). 210
5.36 Hard sphere models for metal growth on Au(110)(1 × 2). 211
5.37 HREEL spectra of CO on Pd-Au(110) surfaces. 212

6.1 TPD: C_2H_4/AuPd(111); $c_{Pd} \leq 21\%$. 231
6.2 TPD peak areas from C_2H_4 saturated AuPd(111). 232
6.3 TPD: C_2H_4/AuPd(111); $c_{Pd} = 2\%$. 233
6.4 TPD: C_2H_4/AuPd(111); $c_{Pd} = 10\%$. 234
6.5 TPD: C_2H_4/AuPd(111); $c_{Pd} = 21\%$. 235
6.6 TPD peak positions and widths for C_2H_4/AuPd(111). 236
6.7 HREELS: C_2H_4Pd(111); 100 K. 238
6.8 HREELS: Thermal stability of C_2H_4/Pd(111). 240
6.9 HREELS: C_2H_4Pd(111); 100 K, on and off specular. 242
6.10 HREELS: C_2H_4 on O and on CO precovered Pd(111); 100 K. . . . 243
6.11 HREELS: 0.07 L C_2H_4/AuPd(111); 100 K. 245
6.12 HREELS: C_2H_4 saturated AuPd(111); 100 K. 246
6.13 HREELS: C_2H_4 saturated AuPd(111); 300 K. 248
6.14 HREELS: C_2H_4 on completely Au covered Pd(111); 100 K. 251
6.15 XPS: C_2H_4/AuPd(111) surface alloys; 400 K. 255
6.16 C coverages for C_2H_4/AuPd(111) surface alloys at 400 K. 256
6.17 STM images of C_2H_4/Pd(111) (T_{ads} = 400 K). 257
6.18 STM images of C_2H_4/AuPd(111) (17% Au; T_{ads} = 400 K). 257
6.19 STM images of C_2H_4/Pd(111) (T_{ads} = 300 K) annealed at 500 K. . 258

List of Tables

3.1 Filling of different layers for 1 ML Au 48

4.1 Metal-on-metal systems forming surface alloys. 58
4.2 Elementary processes in AuPd(111) surface alloy formation. . . . 77
4.3 Local Pd concentration on AuPd(111) surface alloys. 83
4.4 Preparation parameters for the films evaluated in fig. 4.19 94
4.5 Parameters for fitting the AES annealing series. 102
4.6 Parameters for fitting the AES annealing series. 103

5.1 Shifts in d band centres of surface impurities and overlayers. . . . 119
5.2 Kinetic parameters for CO desorption from AuPd(111) surface alloys. 168
5.3 Kinetic parameters for the CO TPD simulations. 168
5.4 Variation of the kinetic parameters. 172
5.5 Activation energies for CO desorption from different Pd sites on AuPd(111) surface alloys. 178
5.6 Preparation parameters for AuPd(111) surface alloys. 202
5.7 Statistical analysis of STM images from AuPd(111) surface alloys. 203
5.8 Vibrational properties of CO on various well-defined sites. 208

6.1 Typical properties of π and di-σ C_2H_4–metal adsorption systems. 220
6.2 Examples for C_2H_4–metal adsorption systems. 221
6.3 Vibrational frequencies for different C_2H_4 adsorption systems. . . 224
6.4 Vibrational energies for C_2H_4/Pd(111). 239
6.5 Mode assignment for C_2H_4/Au/Pd(111). 252
6.6 $\pi\sigma$ parameters for C_2H_4/Pd(111). 261
6.7 Vibrational energies of selected C_2H_4 adsorption systems. 262

List of Appreviations

AES	Auger Electron Spectroscopy/Spectrometer
ASA	Atomic Sphere Approximation
bcc	body centered cubic
CLAM	Combined Lens and Analyzer Module
CMA	Cylindrical Mirror Analyzer
cps	count per second
DFT	Density Functional Theory
EFT	Effective Medium Theory
EAM	Embedded Atom Method
EELS	Electron Energy Spectroscopy/Spectrometer
EMT	Effective Medium Theory
ES	Ehrlich Schwoebel (barrier)
ESD	Electron Stimulated Desorption
ESDIAD	ESD Ion Angular Distribution
fcc	face centered cubic
FLAPW	Full-potential Augmented Plane Waves
FWHM	Full Width at Half Maximum
GGA	General Gradient Approximation
HEIS	High Energy Ion scattering Spectroscopy
HOMO	Highest Occupied Molecular Orbital
HR...	High Resolution ...
IG	Ionization Gauge
IP	Ion Pump
ISS	Ion Scattering Spectroscopy
KMC	Kinetic Monte Carlo
LDOS	Local Density Of States
LEED	Low Energy Electron Diffraction
LMTO	Linear Muffin Tin Orbitals
LUMO	Lowest Unoccupied Molecular Orbital
ML	Monolayer
MSSR	Metal Surface Selection Rule
NEXAFS	Near Edge X-ray Absorption Fine Structure
nn	nearest neighbour

QMS	Quadrupol Mass Spectrometer
RAIRS	Reflection-Absorption Infrared Spectroscopy
SCLS	Surface Core Level Shift
SFG	Sum Frequency Generation
SG	Sputter Gun
STM	Scanning Tunneling Microscopy/Microscope
TMP	Turbo Molecular Pump
TPD	Temperature Programmed Desorption
TSP	Titanium Sublimation Pump
TTPD	Threshold TPD
UHV	Ultra High Vacuum
UPS	Ultraviolet Photoelectron Spectroscopy
VB	Valence Band
XPD	X-ray Photoelectron Diffraction
XPS	X-ray Photoelectron Spectroscopy/Spectrometer

List of STM Images

figure	data file	I_t/nA	U_t/mV[8]
1.1(a)	19121997.y06	25	+1
1.1(b)	19121997.y13	32	+2
3.1(a)	13051998.y31	1.2	+50
3.1(b)	12051998.y31	3.5	+100
3.1(c)	13051998.y12	1.2	+1700
3.1(d)	15051998.y09	6.3	+400
3.3(a)	25051998.y23	5.6	+500
3.3(b)	25051998.y02	6.3	-450
3.3(c)	01101996.y36	3.2	-400
3.3(d)	07111997.y05	3.2	+900
3.4(a)	13051998.y60	28	+20
3.4(b)	13051998.y61	8.9	+17
3.5(a)	02121996.y10	3.2	-350
3.5(b)	06101998.y05	0.63	+800
3.7(a)	21011998.y07	1.3	+650
3.7(b)	01101997.y01	1.0	-500
3.7(c)	23071998.y01	2.0	-900
3.7(d)	22071998.y05	1.8	-1000
3.8	21011998.y10	1.3	+650
3.9(a)	21101997.y08	3.2	-1700
3.9(b)	08121997.y07	1.0	+900
3.9(c)	05111997.y35	1.0	+1900
3.9(d)	05111997.y35	1.0	+1900
3.10(a)	09091997.y19	32	+4
3.10(b)	05111997.y27	10	+2
3.10(c)	05111997.y16	10	+5
4.1(a)	23041998.y01	5	+150
4.1(b)	23041998.y16	1.8	+1100
4.2	22011998.y39	6	+8

figure	data file	I_t/nA	U_t/mV[8]
4.3(a)	01101997.y30	3.2	-850
4.3(b)	21011998.y44	5.0	+1100
4.4(a)	07111997.y03	3.2	-900
4.4(b)	07111997.y40	3.2	+500
4.4(c)	10111997.y02	3.2	+750
4.4(d)	11111997.y11	3.2	+800
4.5(a)	27101997.y01	3.2	+850
4.5(b)	01111998.y03	2.0	-900
4.6(a)	23011998.y23	2.8	+200
4.6(b)	23011998.y26	2.8	+20
4.7(a)	23011998.y32	16	+1
4.7(b)	23011998.y31	22	+1
4.8	22011998.y17	22	-5
4.9(a)	07111997.y37	32	+50
4.9(b)	07111997.y31	10	+5
4.9(c)	10111997.y14	10	+1
4.9(d)	11111997.y06	10	+1
4.11(a)	01101997.y19	14	+1
4.11(b)	21011998.y46	32	-4
4.12(a)	07101997.y20	0.32	-200
4.12(b)	05111997.y49	3.2	+1300
4.12(c)	24071998.y15	16	-1200
4.12(d)	02101998.y08	0.63	+1100
4.13(a)	22101997.y05	10	-5
4.13(b)	07101997.y27	10	-3
4.13(c)	09101997.y09	3.2	-4
4.14(a)	05111997.y42	10	+1
4.14(b)	05111997.y46	10	+1
4.15	27071998.y06	45	+2
4.17	07011998.y07	3.2	+600
4.18	07011998.y28	10	+1
5.3(a)	10091998.y03	1.2	+1500
5.3(b)	11091998.y03	10	+650
5.19(a)	21041997.y01	0.32	-500
5.19(b)	21041997.y25	3.2	-650
5.21	05031997.y14	3.2	-500
5.24	21111996.y15	1.0	-30
5.29	05111997.y51	32	+3
5.30	22091997.y22	10	-12

figure	data file	I_t/nA	U_t/mV[8]
5.31	17091997.y14	32	+4
5.35(a)	01081996.y10	10	-1000
5.35(b)	01081996.y17	3.2	-1000
5.35(c)	01081996.y29	3.2	-1000
5.35(d)	02081996.y21	10	-700
6.17(a)	11121997.y03	10	+150
6.17(b)	11121997.y10	3.2	+3
6.18(a)	23121997.y10	10	+350
6.18(b)	23121997.y12	3.2	+800
6.19(a)	18121997.y06	3.2	-1700
6.19(b)	18121997.y12	3.2	-750

[8] sample bias

Curriculum Vitae

12.3.1967	geboren in Herbrechtingen/Brenz als Sohn von Artur Ruff und Irma Ruff geborene Nusser
1973 – 1977	Grundschule in Herbrechtingen
1977 – 1983	Progymnasium Herbrechtingen
1983 – 1986	Margarete Steiff Gymnasium in Giengen/Brenz
Juni 1986	Abitur
1986 – 1988	Zivildienst in der Heilpädagogischen Berufsausbildungsstätte in Heidenheim/Brenz
1988 – 1995	Physik-Studium an der Universität Ulm
1988 – 1992	Begleitstudium Philosophie an der Universität Ulm
1992 – 1993	Studienaufenthalt an der Portland State University, Portland, Oregon (USA)
1995 – 1999	Wissenschaftlicher Mitarbeiter in der Abteilung Oberflächenchemie und Katalyse, Universität Ulm
seit Oktober 1999	angestellt bei der Siemens AG

Martin Ruff